

Silicon Photonics Platforms for Sensing and Telecoms

A thesis submitted to the University of Manchester for the degree of
Doctor of Philosophy

in the Faculty of Science and Engineering.

2021

Osamah Abdullah S Alsalman

Department of Electrical and Electronic Engineering

Blank page

Table of Contents

1	Introduction	21
1.1	Silicon Photonics	22
1.2	Integrated Photonic Sensors	25
1.3	Objectives of the Research	27
1.4	Thesis Outline.....	28
1.5	References	30
2	Literature Review (Background).....	35
2.1	Optical Channel Waveguide Types	35
2.1.1	Rib Waveguide.....	36
2.1.2	Strip Waveguide.....	37
2.1.3	Slot Waveguide	38
2.2	Evanescent Wave	39
2.3	Microring Resonators (MRRs).....	42
2.4	Ring Characteristics	44
2.4.1	Free Spectral Range (FSR).....	44
2.4.2	Full Width at Half Maximum (FWHM).....	45
2.4.3	Extinction Ratio (ER).....	45
2.4.4	Finesse (F).....	46
2.4.5	Q-factor	46
2.5	Fibre to Waveguide Coupling	47
2.6	Refractive Index Sensing.....	48
2.6.1	Bulk Refractive Index (Homogeneous) Detection.....	49
2.6.2	Surface Refractive Index Detection	50
2.6.3	Limit of Detection (LOD)	51
2.7	Surface Functionalisation	52
2.7.1	Surface Modification Using Biological Materials	52
2.7.2	Surface Modification Using Large Surface Area Materials.....	54
2.8	Novel Ring Resonator Designs	58
2.8.1	Slotted Ring Resonators	58
2.8.2	Multiple Ring Resonators	59
2.8.3	Photonic Crystal Ring Resonator (PCRR).....	61
2.9	References	64

3	Simulation Methods and Optimisation	70
3.1	Simulation Methods	72
3.1.1	Finite-Difference Time-Domain (FDTD)	72
3.1.2	Finite-Difference Eigenmode (FDE).....	73
3.1.3	EigenMode Expansion (EME)	73
3.1.4	HEAT Transport (HT).....	73
3.1.5	Scattering Matrix Method (SMM)	74
3.2	Physical Layout	76
3.3	Fabrication Process.....	76
3.4	Optimisation of Passive Components.....	78
3.4.1	Grating coupler.....	78
3.4.2	Waveguides	82
3.5	References	85
4	Experimental Setup.....	86
4.1	Introduction	86
4.2	Optical Setup and Experimental Procedure.....	86
4.2.1	Gas Sensing Setup.....	86
4.2.2	Thermo-Optic Setup.....	88
4.3	Optical Measurement Components	90
4.3.1	Input Light Sources	90
4.3.2	Spectrum Analyser	93
4.4	Chip Layout Design.....	94
4.5	Spectral Analysis.....	97
4.5.1	‘Cleaning’ of Raw Data	98
4.6	Characterisation of Single MRR Devices	99
4.6.1	Q-Factor and Extinction Ratio (ER) Analysis	101
4.6.2	Extraction of Losses and Coupling Coefficients.....	105
4.7	Performance Analysis.....	108
4.8	Code Listings.....	110
4.9	References	112
5	Vapour Sensing	114
5.1	Experimental and Simulation Details.....	118
5.2	Strip Microring Resonator (Strip-MRR)	122

5.2.1	Strip-MRR Modelling	122
5.2.2	Dynamic (Real-Time) Measurements of the Strip-MRR Sensor	123
5.3	Slotted Microring Resonator (Slot-MRR)	126
5.3.1	Slot-MRR Modelling	126
5.3.2	Real-Time Measurements of Slot-MRR	127
5.4	Graphene Oxide Slotted Microring Resonator (GOMRR).....	129
5.4.1	Graphene Oxide (GO) Synthesis.....	129
5.4.2	Graphene Oxide (GO) Coating	130
5.4.3	GOMRR Modelling	132
5.4.4	Real-Time Measurements of GOMRR	133
5.5	Results and Discussion.....	135
5.6	Summary and Future Work	143
5.7	References	145
6 Novel Sensor Design based on Directional Coupler Integrated MRR (DC-MRR) with Ultra-Large FSR.....		151
6.1	Directional Couplers (DCs).....	151
6.2	DC biochemical sensing	155
6.2.1	Intensity Interrogation.....	155
6.2.2	Wavelength Interrogation.....	157
6.3	Novel DC coupled racetrack-type MRR	158
6.3.1	Single DC coupled MRR - modelling.....	160
6.4	Vernier Cascaded DCs	164
6.4.1	Double DC coupled MRR - modelling	165
6.5	Code Listings.....	169
6.6	References	170
7 Tuneable Superluminal and Slow Light in coupled ring resonators		172
7.1	Introduction	172
7.2	3×3 Coupler based dual (Coupled) Ring Resonator (CRR)	174
7.2.1	Experimental and Modelling Methods.....	175
7.2.2	Device Characterisation	179
7.2.3	Thermo-Optic Tuning	184
7.3	References	190

8	Conclusions and Future Work.....	194
8.1	Summary	194
8.2	Future Work	196
8.3	References	198

Final Word Count: 34,844

List of Figures

Figure 1.1 Incident ray vs refracted when $RI_1 > RI_2$ for (a) $\theta_1 < \theta_c$ (b) $\theta_1 = \theta_c$ and $\theta_2 = 90^\circ$ (c) total internal reflection (TIR) condition at $\theta_1 > \theta_c$	23
Figure 2.1 Optical waveguide structures (a) Rib waveguide (b) Strip waveguide (c) Slotted channel waveguide.....	36
Figure 2.2 (a) Normalised electric field profile (E_x) for 50nm slot (b) cross-sectional plot through the centre of the waveguide.....	38
Figure 2.3 Demonstration of evanescent wave in the top and bottom cladding, associated with the guided mode in the Si waveguide. The evanescent wave is typified by an exponentially decaying field profile with a ‘penetration depth’, d_p in the cladding region, typically defined by a field intensity that is $1/e$ of that at the waveguide/cladding interface.....	39
Figure 2.4 Penetration depth as a function of (a) waveguide width W and height h (b) wavelength and (c) cover refractive index n_{clad}	41
Figure 2.5 Electric field intensity for the fundamental (a) quasi-TE mode and (b) quasi-TM mode	42
Figure 2.6 Schematic view of a ring resonator	42
Figure 2.7 An intensity vs wavelength spectrum for a 25 μ m radius ring resonator ..	44
Figure 2.8 An example of Full Width at Half Maximum (FWHM) distance	45
Figure 2.9 Different techniques for coupling light from an optical source (directly or via fibre) to a sub-wavelength scale optical waveguide [10].....	47
Figure 2.10 Spectral shift due to a change in the effective refractive index of the ring resonator.....	49
Figure 2.11 Depiction of the bulk sensing showing the analytes surrounding the core of the waveguide	50
Figure 2.12 Surface sensing showing the analytes bound to specific receptors at the surface of the core of the waveguide.....	51
Figure 2.13 Process of surface functionalisation of silicon [37]. (a) the silicon surface is rinsed with piranha solution to expose hydroxyl groups on the surface (b) organo-silane agents (APTES) interact with hydroxyl groups on the surface and	

generate NH ₂ groups (c) NHS-biotin bind to NH ₂ groups to act as a receptor (d) Avidin selectively attach to biotin.....	53
Figure 2.14 Scanning Electron Microscope (SEM) images [41] of (a) P <i>Si</i> ring resonator (b) top view porosity profile of the WG (small pores) and cladding (large pores) layers, and (c) cross-section of the strip WG	55
Figure 2.15 (a) Measured transmission spectrum and (b) corresponding resonance shift for different ethanol vapour concentrations. (c) Dynamic response of the sensor for one on-off cycle upon exposure to 300 ppm ethanol [47].....	56
Figure 2.16 (a) Optical response of the hybrid photonic-MOF device to 20 minutes exposure of different VOCs with a fixed concentration of 100 ppm. (b) Enhancement factor and detection limitation of five VOCs at equilibrium [48].....	57
Figure 2.17 Slotted ring resonator configuration	59
Figure 2.18 Vernier effect in cascaded ring resonator [64] (a) schematic of the Vernier cascaded ring design for sensing application (b) output response of the filter MRR (dashed line) and sensor MRR (solid line) (c) overall spectrum of the cascaded MRR design in a larger wavelength range	60
Figure 2.19 Optical EIT-like effect [70] (a) Optical microscope image of the parallel coupled MRR design (b) spectral response corresponding to five different devices with variation in the ring to ring separations, $S =$ (i) 15.69 μm , (ii) 15.71 μm , (iii) 15.73 μm , (iv) 15.75 μm and (v) 15.77 μm	61
Figure 2.20 (a) SEM image of the photonic crystal ring resonator (PCRR), (b) magnified image of the coupling region and (c) simulation of the resonant mode profile [73]	62
Figure 2.21 An SEM image of the SWG based MRR developed by Flueckiger et al. [75]. The ring resonator was fabricated by e-beam lithography	63
Figure 3.1 Flow chart of the design process for photonic integrated circuits described in this thesis	71
Figure 3.2 Components for the theoretical description of coupling of light to a single MRR.....	74
Figure 3.3 Illustration of the fabrication process which was performed by CORNERSTONE [12]	78

Figure 3.4 Schematic illustration of delivery (from a SMF) and coupling of light to the guided mode using a focusing grating coupler fabricated in SOI	79
Figure 3.5 2D FDTD simulations of the coupling efficiency as a function of (a) grating pitch, (b) grating gap, (c) fibre position and (d) fibre rotation angel (θ)	80
Figure 3.6 S-parameter of the optimised grating coupler design using (a) 2D FDTD and (b) 3D FDTD	81
Figure 3.7 (a) 3D simulation of Electrical field distribution in the xy plane (b) snapshot of the depicted grating coupler.....	82
Figure 3.8 Mode profiles (including calculated Cf, n_{eff} values) for strip waveguides with different widths (a) W=350nm (b) W=400nm (c) W=450nm (d) W=500nm (e) W=550nm.....	83
Figure 3.9 Transmission as a function of taper length for waveguides that have 500nm width tapered down to 350, 400 and 450nm.....	84
Figure 4.1 Optical delivery and collection of light to/from the photonic chip along with bespoke setup for gas/vapour delivery.....	87
Figure 4.2 Thermo-optic sensing and imaging setup	89
Figure 4.3 The output spectrum of the fibre coupled superluminescent diode (model: S5FC1005S Single-mode, Thorlabs, Inc.) with an operating current of 600 mA [6]	91
Figure 4.4 Schematic of a Littman configuration ECL showing the gain chip, collimating lens, diffraction grating, rotatable mirror and fibre output [7].	92
Figure 4.5 The tuning range of the fibre coupled tuneable laser (model: TLK-L1550M, Thorlabs, Inc.) [7]	92
Figure 4.6 The spectral resolution of the Thorlabs Optical Spectrum Analyser OSA 203B [9]	94
Figure 4.7 The chip dimensions for (a) rib waveguide-based chip (b) MPW#6 and MPW#10	95
Figure 4.8 Snapshot images from GDS files for the chip layout (a) slotted micro-ring resonator (b) MPW#6 (c) MPW#10	96
Figure 4.9 Typical (raw) transmission spectrum of a micro-ring resonator	97
Figure 4.10 SLD fibre output and MRR device transmission spectra	98
Figure 4.11 Comparison of MRR raw transmission (red) and processed (Gaussian subtracted) data	99

Figure 4.12 Snapshot from the MPW#10 GDS file for ring with radius = $25\mu\text{m}$, $W = 400\text{nm}$ and $G = 300\text{nm}$	100
Figure 4.13 Transmission spectra (with single resonances in the insets) for $R = 25\mu\text{m}$, $W = 400\text{nm}$ and $G = 200, 250$ and 300nm for (a) silica and (b) air cladding MRRs	100
Figure 4.14 Transmission spectra (with single resonances in the insets) for $R = 25\mu\text{m}$, $W = 450\text{nm}$ and $G = 200, 250$ and 300nm for (a) silica and (b) air cladding MRRs	101
Figure 4.15 Transmission spectra (with single resonances in the insets) for $R = 25\mu\text{m}$, $W = 500\text{nm}$ and $G = 200, 250$ and 300nm for (a) silica and (b) air cladding MRRs	101
Figure 4.16 Experimental spectrum fit with Lorentzian line-shape function showing a single resonance (inset)	102
Figure 4.17 Average Q-factor for (a) silica and (b) air clad MRRs.....	103
Figure 4.18 Average extinction ratio (ER) for (a) silica and (b) air clad MRRs	103
Figure 4.19 (a) GDS image and (b) transmission spectrum of the MRR with pulley coupling structure.....	104
Figure 4.20 Dependency of transmission coefficient (t) (red line) and loss factor (α) over a 50nm spectral range for MRR with $R = 50\mu\text{m}$ $W = 450\text{nm}$ and $G = 200\text{nm}$	106
Figure 4.21 Coupling coefficient (κ) as a function of the separation gap (G) and waveguide widths (W) for (a) silica cladding (b) air cladding	106
Figure 4.22 Loss factor (α) as a function of the separation gap (G) and waveguide widths (W) for (a) silica cladding (b) air cladding.....	107
Figure 4.23 Measured and fitted transmission spectra for MRR with $W=400\text{nm}$ and $G=200\text{nm}$ with air cladding (blue curve) and water cladding (green curve).....	108
Figure 5.1 Schematic structure of (a) strip-MRR (b) slot-MRR (c) GOMRR.....	115
Figure 5.2 Flow chart of the iterative FDE simulation process for determination of the MRR device sensitivity [22]	121
Figure 5.3 Experimental transmission spectrum of the single strip-MRR with the left inset showing a close-up of the unperturbed resonance peak (black circles) and Lorentzian fit (red line). The right inset shows the simulated electric field distribution at the right bend of the $25\mu\text{m}$ strip-MRR	123

Figure 5.4 Dynamic (real-time) monitoring of spectral response and recovery of the single strip-MRR with exposure to (a) ethanol, (b) benzene and (c) hexane. The red highlighted areas indicate the time range(s) when the N_2 +VOC vapour carrier flow is opened and white regions where it was closed (only N_2 dilution flow open). The vapour-dilution flow ratio (F_v/F_d), ranging from 0.05 to 0.5, are illustrated on top of each figure..... 125

Figure 5.5 Experimental transmission spectra of the slot-MRR with left inset showing a close-up of the unperturbed resonance peak (black circles) and Lorentzian fit (red line). The right inset shows the simulated electric field distribution at the right bend of the $25\mu\text{m}$ slot-MRR..... 127

Figure 5.6 Real-time monitoring of spectral response and recovery of slot-MRR for (a) ethanol, (b) benzene and (c) hexane. The red highlighted areas indicate the time range(s) when the $N_2 + \text{VOC}$ vapour carrier flow was opened. The vapour carrier-dilution flow ratios are illustrated on top of each plot 128

Figure 5.7 (a) Optical microscope image of the GOMRR showing the etched window area highlighted by the white dashed box (b) A typical Raman spectrum obtained from the ring waveguide region, as indicated by the small white circle in (a) with I_D/I_G ratio = 1.11 (c) Raman map of the I_D/I_G ratio for the highlighted window area of the GOMRR with the darker region revealing the underlying ring structure with lower I_D/I_G ratio (d) Histograms and Gaussian fits (dashed lines) of the I_D/I_G ratio, determined from (Lorentzian) fits to the Raman spectral peaks, for each mapped spatial position [22]..... 132

Figure 5.8 Experimental transmission spectrum of the GOMRR with left inset showing a close-up of the unperturbed resonance peak (black circles) and Lorentzian fit (red line). The right inset shows the simulated electric field distribution at the right bend of the $25\mu\text{m}$ GOMRR 133

Figure 5.9 Real-time monitoring of the spectral response and recovery of GOMRR for (a) ethanol, (b) benzene and (c) hexane. The red highlighted areas indicate the time range(s) when the N_2 +VOC vapour carrier flow is opened. The vapour carrier-dilution flow ratios are illustrated on top of each plot 134

Figure 5.10 Experimental resonance wavelength shift at equilibrium ($\Delta\lambda_{\text{eq}}$) as a function of vapour-dilution flow ratio (F_v/F_d) for various VOC vapours for strip-

MRR (red) slot-MRR (blue) and GOMRR (green) with the fitting of <i>Hill-Langmuir</i> model (dashed lines)	139
Figure 5.11 Sensitivity measurements showing equilibrium resonance shift ($\Delta\lambda_{eq}$) as a function of change in refractive index (ΔRI) for various VOC vapours for strip-MRR (red) slot-MRR (blue) and GOMRR (green).....	142
Figure 5.12 <i>Hill</i> coefficient ratio ($n_{GOMRR}/n_{slot-MRR}$) as a function of the relative polarity - kinetic diameter ratio for all VOCs tested, green dashed line is a guide to the eye [22].....	143
Figure 6.1 A schematic diagram of the directional coupler	152
Figure 6.2 Effective indices of the even (red curve) and odd (blue curve) modes for directional coupler with identical waveguide dimensions (350×220nm). The coupling length (black curve) as a function of the coupling gap is displayed in the secondary y-axis. Insets show the even (upper) and odd (lower) modes profile for 50nm (left) and 800nm (right) coupling gaps	153
Figure 6.3 Through and coupled powers as a function of DC length with inset of electric field distribution of identical SOI waveguides with gap (G), width and height of 50nm, 350nm and 220nm, respectively. The dashed line indicates the coupling length L_c	154
Figure 6.4 Transmitted power for RI = 1.318 (black) and 1.338 (red) as a function of the DC length for different separation gaps, G	156
Figure 6.5 Transmitted power for RI = 1.318 (black) and 1.338 (red) as a function of wavelength for different separation gap, G.....	158
Figure 6.6 Schematic diagram of the proposed DC coupled MRR sensor illustrating input and output ports.....	159
Figure 6.7 Simulations of the attenuation losses of the fundamental mode as a function of the bend radius for different waveguide widths (circles) with its exponential fit (dashed line).....	160
Figure 6.8 Schematic illustration of the single DC coupled MRR model	161
Figure 6.9 Normalised transmission (<i>P_{out}</i>) for a DC coupled racetrack MRR with $L_{DC} = 20.7\mu m$, $t_1 = 0.95$ and (a) $\alpha = 0.80$ (b) $\alpha = 0.95$	163
Figure 6.10 Schematic diagram of the double DC coupled MRR	164
Figure 6.11 Schematic illustration of the ring with DC model	165

Figure 6.12 The transmission spectrum of the varFDTD simulation (black curve) and our model (red curve) for (a) wide wavelength range and (b) zoomed wavelength range of 1560-1595nm	166
Figure 6.13 The Vernier sensitivity, <i>SVernier</i> , (black curve) and free spectral range, <i>FSRVernier</i> , (red curve) as a function of the length of the sensor DC, <i>LDCsensor</i> . The inset shows the zoomed range of <i>LDCsensor</i>	168
Figure 7.1 Schematic illustration of pulse propagation from $Z = 0$ to $Z = L$ in Vacuum and in a medium with anomalous dispersion. The front edges of the pulses (i.e. the nonanalytical points in the leading edge of the peaks) always propagate with $V_f = c$, whereas the centre of the peak passing a medium with anomalous dispersion propagates with superluminal group velocity (i.e. $V_{g(Anomalous)} > V_{g(Vacuum)} = c$)	173
Figure 7.2 Schematic of the 3x3 coupler based CRR design, with rings (R_1, R_2), coupled via common drop port. Optical Input (In) and Output (T_1, T_2 and D_1) ports are labelled	174
Figure 7.3 Schematic diagram of the 3x3 coupler model as used in the SMM approach	176
Figure 7.4 (top) Combined experimental unperturbed drop port spectrum with (inset, bottom) IR scattered light microscope images of the CRRs (TiN electrical contacts in Gold and CRR with their shared drop port positions are illustrated by the dashed red circles and lines) at a wavelength of (a) 1545.31nm, (b) 1545.68nm and (c) 1545.94nm	180
Figure 7.5 FDTD simulation for a CRR system with rings of 5 μ m radius and a small (2nm) difference in the waveguide width. (a) D_1 output spectrum and E-field distribution in the CRR system for (b) the shorter wavelength peak, (c) the central transparency and (d) the longer wavelength peak	182
Figure 7.6 Analytical modelling of 3x3 CRR for (a) $R_1 = 25\mu\text{m}$, $n_{eff1} = n_{eff2} = 2.45$, $\alpha_{1,2} = 0.99$ and $t_{1,2,3,4} = 0.98$ (b) $R_1 = R_2 = 25\mu\text{m}$, $n_{eff1} = 2.45$, $\alpha = 0.99$ and $t_{1,2,3,4} = 0.98$ (c) $R_1 = R_2 = 25\mu\text{m}$, $n_{eff1} = n_{eff2} = 2.45$, $\alpha_{1,2} = 0.98$, $t_{1,2} = 0.99$ and $t_3 = 0.90$	183
Figure 7.7 (a) Effective index (n_{eff}) and local temperature close to the waveguide as a function of injected (heater) power and (b) thermal distribution close to the waveguide (red box) for heater powers; 0, 17 and 21mA (colour bar labels are temperature in K)	184

- Figure 7.8 Experimental vs modelled drop port (D_1) spectra as a function of R_2 heater currents in the range 0 to 12mA (as indicated in (a) to (l)). The dashed blue line indicates the original position of the transparency..... 185
- Figure 7.9 Contour plot showing the spectral intensity of the CRR as a function of heater current on R_2 . The black lines represent the uncoupled system, whereas the green and blue curves correspond to the theoretical fit of the stationary and travelling peak positions, respectively using the avoided crossing model, Equation (7.10)... 187
- Figure 7.10 Effective phase shift, Φ , (green dashed curves) and group delay, τ_g , (blue curves) of the output signal collected by the shared drop port for heater current on R_2 of $I = 0\text{mA}$ to 12mA (as indicated) 188
- Figure 7.11 Simulation of the temperature rise as function of time at the waveguide's surface 189

Abstract

This thesis presents a comprehensive study of the design, fabrication and characterisation of a variety of waveguide-based photonic integrated circuits (PICs) derived from the silicon-on-insulator (SOI) platform. Modelling and design optimisation of various PIC components, including grating couplers and tapered waveguide sections and microring resonators, were implemented along with experimental characterisation.

Detailed investigation of a graphene oxide integrated MRR (GOMRR) device, for detection of vapour phase Volatile Organic Compounds (VOCs), reveals an improved sensitivity and correspondingly lower limit of detection compared with a standard silicon (control) MRR. Careful analysis of the optical response of the GOMRR to the various VOCs tested, based on the *Hill-Langmuir* absorption isotherm, also reveals the potential for discrimination (selectivity), which is not the case for the control MRR. This is attributed to a molecular dependent capillary condensation (within the GO interlayers), which determines the degree of cooperative molecular binding. Our analysis reveals that this cooperativity (increased binding affinity) is enhanced for molecules with a polarity that is high relative to their size (kinetic diameter). This result is consistent with the current understanding of the interaction between GO and various molecules (specifically that the GO serves as an effective ‘molecular sieve’), suggesting that it may be used as a functional layer in photonic sensing applications, where molecular selectivity is critical.

A novel device based on a Directional coupler integrated MRR (DC-MRR) device was also carried out as part of this study and revealed an enhanced spectral sensitivity ($> 14000 \text{ nm/RIU}$) and extended FSR (of 223nm), both of which are key to improved sensing devices based on small footprint SOI-based PICs.

A detailed study of superluminal (fast) and subluminal (slow) light is also described using a set of coupled MRRs, whereby thermo-optic tuning of one of the rings with respect to the other was employed. This device exhibits a maximum group delay (for the slow light mode) of 16.25ps and an advance (for the fast light mode) of 239.17ps . Comprehensive analytical modelling, combined with FDTD simulations were employed to support the observed experimental characteristics (electromagnetically induced transparency (EIT)-like effects and anti-crossing behaviour in these coupled MRRs of the fabricated devices.

Blank Page

Declaration

No portion of the work referred to in this thesis has been submitted in support of an application for another degree or qualification of this or any other university or institute of learning.

Copyright statement

The author of this thesis (including any appendices and/or schedules to this thesis) owns certain copyright or related rights in it (the “Copyright”) and he has given The University of Manchester certain rights to use such Copyright, including for administrative purposes.

Copies of this thesis, either in full or in extracts and whether in hard or electronic copy, may be made only in accordance with the Copyright, Designs and Patents Act 1988 (as amended) and regulations issued under it or, where appropriate, in accordance with licensing agreements which the University has from time to time. This page must form part of any such copies made.

The ownership of certain Copyright, patents, designs, trademarks and other intellectual property (the “Intellectual Property”) and any reproductions of copyright works in the thesis, for example graphs and tables (“Reproductions”), which may be described in this thesis, may not be owned by the author and may be owned by third parties. Such Intellectual Property and Reproductions cannot and must not be made available for use without the prior written permission of the owner(s) of the relevant Intellectual Property and/or Reproductions.

Further information on the conditions under which disclosure, publication and commercialisation of this thesis, the Copyright and any Intellectual Property and/or Reproductions described in it may take place is available in the University IP Policy (see <http://documents.manchester.ac.uk/DocuInfo.aspx?DocID=24420>), in any relevant Thesis restriction declarations deposited in the University Library, The University Library’s regulations (see <http://www.library.manchester.ac.uk/about/regulations/>) and in The University’s policy on Presentation of Theses

Publications related to this thesis

- [1] Tsui, Alsalman, Mao, Alodhayb, Albrithen, Knights, et al. (2020). Graphene oxide integrated silicon photonics for detection of vapour phase volatile organic compounds. *Scientific reports*, 10(1), 1-11.

Acknowledgements

I would like to express my sincere thanks and appreciation to my academic supervisor, associate professor Iain Crowe, for sharing his immense knowledge and continuous support, guidance and patience through my entire graduate program. It would never have been possible for me to complete this degree without his incredible support and encouragement.

In addition, I would like to thank my co-supervisor, professor Matthew Halsall for sharing his lab equipment with me and for his continuous guidance in the lab.

I would like to express my profound thanks and appreciation to Dr Hei Chit Leo Tsui for all the stimulating discussions and various forms of support and continuous cooperation during my PhD journey.

I was lucky and fortunate enough to have the opportunity to get my photonic designs fabricated by the CORNERSTONE project. I want to extend my thanks and appreciation to Dr Callum Littlejohns (CORNERSTONE coordinator), who kindly guided me during my mask layout submission.

Finally, I owe my deepest and sincere gratitude to my family for their endless love, help and encouragement. I would like to present my sincere thankfulness to my parents for all their support and for believing in me and inspiring me to follow my dreams. I am especially grateful to my wife, who has been extremely encouraging and supportive of me throughout my postgraduate study and has taught me how to produce lots of schematic diagrams, which were used in this thesis, using her skills in graphical software. I am also thankful for all her innumerable sacrifices to help me get to this level. Finally, I would like to extend my gratitude to my little baby boy, Talal, who always spreads happiness and joy around the house by his contiguous smiles and laughs! Without such a team behind me, I doubt that I would be in this place today.

Blank Page

1 Introduction

Photonics is the science and technology that is concerned with the control of transmission, detection, emission, amplification and modulation of light (photons). The adjective term ‘photonic’ was chosen to replace the term ‘optical’ by The Optical Society of America [1]. The photonics term appeared in the late 1960s when Theodore Maiman brought the theoretical work of Albert Einstein’s paper “On the Quantum Theory of Radiation” into a practical working laser [2].

In the 21st century, photonic devices began to replace and complement electronic devices due to the many advantages compared with the purely electronic counterpart. The unique characteristics of photons (as carriers of information) offer enhanced bandwidth, long-distance communication, immunity against electromagnetic interference and reduced energy consumption. Modern data centres that use microelectronics for data processing suffer from huge power consumption. Recently, large companies such as Google, Apple, Amazon, Facebook and Microsoft had been investing in building their data centres in locations with cooler climates to save energy [3]. Also, Google filed a patent for a water-based data centre that uses the surrounding water to naturally cool the centre [4]. The advances in photonic technologies have already enabled lower power consumption, which along with near comparable price levels to electronics will revolutionize the future of many scientific and engineering fields, even beyond data centre/telecommunications.

Due to the increased demand for fast and efficient devices, the integration of photonics and electronics (called Optoelectronics) on a single platform has become a necessity. Major academic and industrial sectors such as Harvard, MIT, IBM and Intel had already begun to equip their labs for the fabrication of integrated photonic devices [5, 6, 7]. The ultimate goal of an optoelectronic circuit is to realise photonic components (i.e. lasers, passive/active waveguides and photodetector) with advanced microelectronics processors in the same layer or in different layers bonded together. However, the main obstacle facing optoelectronics technology is the lack of full integration of laser sources. Historically, the conventional platforms for photonics were mostly based on either III-V materials such as indium phosphide (InP) monolithic integration, which are mainly devoted for lasers integration, or silicon-based materials for most of

the passive integrated photonic components. The direct nature and size of the bandgap of such III-V-based compounds mean they have been the material of choice for on-chip laser generation [8, 9], while the compatibility of the silicon-based devices with Complementary Metal Oxide Semiconductor (CMOS) fabrication process facilities led them to be integrated with huge densities for lower prices [9]. Until today the full integration of lasers with CMOS fabrication infrastructure at the same level as other optical or electronic components is still in development [10]. Several practical approaches have been proposed to solve this issue, as will be described in the next section.

1.1 Silicon Photonics

The past decade has seen the rapid development of silicon nanophotonic devices due to their compatibility with Complementary Metal Oxide Semiconductor (CMOS), low cost and high performance. Silicon is the second most abundant element in the earth's crust after oxygen [11]. Its ability to form a stable, high-quality insulating oxide (SiO_2) led to the hugely successful development of the transistor in the 1950s [12]. To draw a comparison with this early technological success in microelectronic integrated circuits, the more recent development of mass-scalable, ultra-thin Silicon-On-Insulator (SOI) technology serves as the basis for the photonic integrated circuit (PIC). At 1550nm, the refractive indices of silicon and SiO_2 are around 3.48 and 1.44, respectively [13, 14]. This high contrast in refractive indices between the guiding layer (silicon) and surrounded cladding produces relatively large light confinement based on total internal reflection (TIR) phenomena. According to Snell's law in Equation (1.1), TIR only occurs when (i) light travels from a high refractive index (RI_1) to low refractive index material (RI_2), and (ii) angle of incident light (θ_1) is greater than the critical angle (θ_c). The critical angle is the angle that allows light to refract at $\theta_2 = 90^\circ$ degrees from the normal axis and travel along the boundary.

$$RI_1 \sin(\theta_1) = RI_2 \sin(\theta_2) \quad (1.1)$$

When $RI_1 > RI_2$ and $\theta_2 = 90^\circ$, the critical angle (θ_c) can be calculated from Equation (1.1) as follow:

$$\theta_1 = \theta_c = \sin^{-1}\left(\frac{RI_2}{RI_1}\right) \quad (1.2)$$

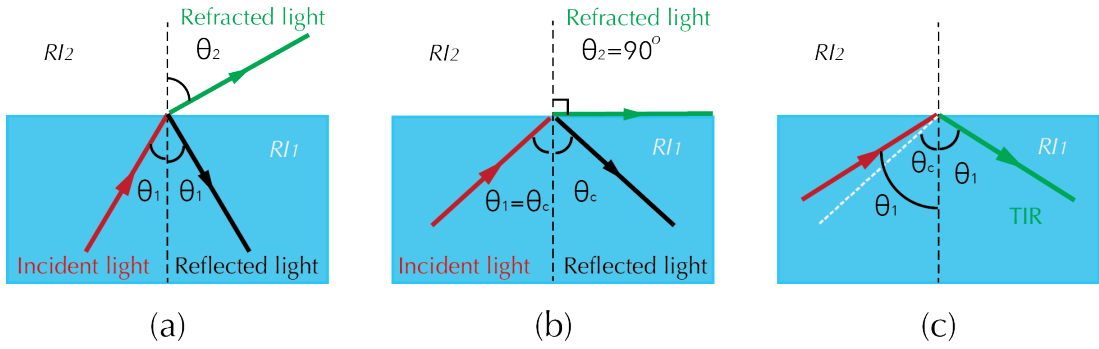


Figure 1.1 Incident ray vs refracted when $RI_1 > RI_2$ for (a) $\theta_1 < \theta_c$ (b) $\theta_1 = \theta_c$ and $\theta_2 = 90^\circ$ (c) total internal reflection (TIR) condition at $\theta_1 > \theta_c$

Increasing the refractive index contrast allows small critical angles, which enables very small waveguide bends with relatively small propagation losses. Pure silicon is transparent in the wavelength range used for telecommunications (1550nm), making it an ideal platform for guiding and manipulating photons in this range within a photonic integrated circuit. Indeed, this has led to a number of useful PIC devices such as the micro-ring resonator, Mach-Zehnder Interferometer (MZI) etc. However, the indirect nature of the silicon band gap means that it does not lend itself well to light emission due to the low probability of radiative recombination at ambient temperature, even in extremely high quality (low defect density) material [15]. Although there have been a number of intelligent attempts to circumvent this issue; e.g. the silicon Raman laser [16, 17], silicon quantum dots (QDs) [18], silicon nanocrystals [19] and more recently, tensile strained Germanium (Ge), Germanium-tin (GeSn) etc. [20, 21], as yet there remains no efficient solution that offers this versatility, which is compatible with CMOS manufacturing technology [22, 23]. Whilst III-V lasers have been integrated with silicon photonic circuits via direct transfer of III-V devices to silicon substrate

[9, 24, 25, 26], this is not sufficiently scalable to be a cost-effective solution as it still suffers from the incompatibility with CMOS foundries [10]. Despite this, the familiarization of global fabrication facilities (commonly called a fab) with silicon-based devices has led to a rapid standardization of the silicon photonics platforms which can be accessed through multi-project wafer (MPW) runs [27, 28], which help to de-risk development (and thus reduce the overall cost of) prototyping for academic and industrial research in this area. These advantages are the key enabling factors for bringing silicon photonics to a range of applications such as optical telecommunications, interconnects, and sensors on-chip.

Typically, an SOI platform comprises a thin (sub-micrometre) top silicon layer which is separated from the silicon substrate by a $2\mu\text{m}$ -thick buried oxide (BOX) layer. The top silicon layer can readily be patterned, with both extremely high accuracy and repeatability, using standard lithography techniques. Amongst these, both UV photo- and electron-beam lithography (EBL) are used to form highly precise, patterned structures, by partial or complete removal of specified regions of the top silicon layer, either by masked UV, or direct (mask-less) electron beam, exposure of a deposited resist material. In the case of EBL, feature sizes at the sub-10nm scale can be achieved [29]. However, the drawback of EBL is the relatively low throughput (and thus high cost) for scalable prototyping. In order to achieve cost-effective prototyping, UV photolithography is in most cases sufficient, with minimum feature sizes (limited by the wavelength of the UV source) on the 100nm scale [30]. Rapid, cost-effective prototyping has been further enhanced at many fabs by the multi-project wafer (MPW) philosophy, which enables multiple customers and projects to share a common mask and wafer set. The first foundries to offer silicon photonics MPW commercially were IMEC (Belgium) and CEA-Leti (France) [10]. The commercial and academic MPW service is usually offered with fixed etch depths of the top silicon layer.

The potential applications of the SOI-based photonics are determined by its optical transparency window. The transparency range for silicon is between $1.1\mu\text{m}$ and $8\mu\text{m}$ [31], whereas silica glass (SiO_2) is transparent between $0.2\mu\text{m}$ and $4\mu\text{m}$ [32]. Therefore, the transparency range of SOI platforms is restricted by the lower limit of silicon ($1.1\mu\text{m}$) and the upper limit of silica ($4\mu\text{m}$). In the range of wavelengths from approximately $1.1\mu\text{m}$ to $1.6\mu\text{m}$, SOI-based platforms are primarily utilised to demonstrate

applications for the short-haul and long-haul telecommunication systems. These include but are not limited to wavelength division multiplexing (WDM) systems for wavelength filters [33], spectroscopy-on-chip [34] and sensing applications [35]. For wavelengths longer than $2\mu\text{m}$, gas sensing and biological imaging have been demonstrated [36, 37]. The Mid-IR region is interesting as the oscillation frequency of light waves in this band corresponds to the frequency of characteristic molecular bond vibrations, which provides a method for the distinctive fingerprinting of particular gases/vapours.

1.2 Integrated Photonic Sensors

A variety of novel applications in the field of silicon photonic sensing devices have been explored in recent years. These include Light Detection and Ranging (LIDAR) technologies, which is the light equivalent of RADAR where radio waves are used to detect objects and determine their range and velocity. Interest in LIDAR technology has grown considerably in recent years because of its huge potential in automotive self-driving and augmented reality (AR) systems since it enables fast and high-resolution 3D positional mapping [38].

Another promising application in the field of silicon photonics sensors is optical gyroscopes, which can provide extremely sensitive detection in the change of position or direction [39]. The working principle of these sensors is based on the Sagnac effect [40]. If two laser beams are guided in opposite direction around a circular-shape waveguide (or fibre), any slight rotation of the device will affect the optical path length of one of the beams with respect to the other. This creates a relative phase difference between the two beams that can be used to measure the rate and degree of (or with feedback maintenance of the) orientation.

Perhaps the most common sensing application in silicon photonics in recent years has been that of chemical and biochemical detection [41]. The close integration of handheld smartphone device technologies with the human senses can perhaps be considered mature, with the exception of smell. The ability to integrate a bio-photonic ‘nose’ into our smartphones would provide significant advantages in a variety of fields such as food safety, agriculture, security and especially in healthcare. The gaseous

compounds such as nitric oxide, ammonia, carbon dioxide and isoprene, which are released by the human body, e.g. through exhaled breath, can be used to diagnose specific diseases and disorders such as cancer, asthma, diabetes, kidney failure, high blood cholesterol levels and many infections, in a non-invasive way [42, 43]. A variety of approaches have been exploited for optical detection of these, such as absorption, emission, fluorescence, Raman scattering and refractive index (RI) sensing [44]. The primary detection concept of most chip-based optical biosensors is to utilise the molecular interaction with the evanescent field of guided optical modes. These fields are extremely sensitive to changes in local refractive index (RI) within the surroundings of the light guiding material, which enables sensitive, real-time, label-free biomolecular sensors such as surface plasmon resonance (SPR) and planar waveguide types. The typical interrogation configurations applied to such transducers are wavelength or phase interrogation and intensity interrogation. The significant advances in optical biosensors have led to their rapidly being implemented in clinical practice [45]. The overall biosensors market is projected to grow from USD 21.2 billion in 2019 to USD 31.5 billion by 2024, where optical biosensors are the most lucrative application [46]. The growing demand for the fast and reliable detection of any kind of analytes has stimulated the production and design of a wide variety of optical biosensors such as the Mach–Zehnder interferometer (MZI) [47], microring resonator (MRR) [48], slotted ring resonator [49], disk resonator [50], Bragg grating resonators [51], and photonic crystals (PhCs) [52]. These sensors have been able to achieve high sensitivity, high selectivity and quick response leading to ‘real-time’ detection in a compact device. Optical biosensors can be used to detect either gases and vapours or liquids in the surrounding environment. Controlled delivery of the target analyte(s) to the photonic integrated circuit commonly involves the integration of microfluidic channels on top of the photonics sensor area in order to precisely guide the vapours or liquids to interact with the evanescent fields of the sensor. Polydimethylsiloxane (PDMS) is a frequently employed material to fabricate the microfluidic channels due to its optical transparency and straightforward, cost-effective feature definition and fabrication. Despite the high sensitivities of the refractive index-based sensors, the lack of intrinsic discrimination mechanism (selectivity) between different species is still a vital concern for medical and environmental applications. Operating in the Mid-IR spectral

regime offers inherent molecular selectivity through characteristic absorption spectra ('fingerprinting'), which enables accurate and selective analysis of different chemical and biological species [53]. However, for SOI-based technologies, the strong absorption of light by the BOX layer beyond $4\mu\text{m}$ prohibits device operation in this wavelength range. Different approaches have been proposed to tackle this limitation, such as selective under-etching of the BOX layer using hydrofluoric acid (HF) to form suspended membrane waveguides [54]. This technique can extend the device operating wavelength range up to the long wavelength limit of silicon transparency ($8\mu\text{m}$). Other approaches utilise different materials that are transparent in the Mid-IR region, such as germanium-on-silicon, chalcogenide-on-silicon and silicon-on-sapphire [55]. However, operating in the Mid-IR regime comes with its own challenges mainly due to the lack of cost-effective broadband light emitters and optical components that operate in this regime. This is because the procurement and fabrication of device structures are usually performed using less common materials that can increase the cost significantly [56]. In contrast, the availability and relatively low cost of both sources and detectors operating in the near-IR, thanks to the huge investment and development of these during the early telecoms era (1990s), means that prototyping and development of devices operating in this wavelength range have huge cost and scalability benefits. As such, the approach to device design and operation considered in this thesis is limited to the near-IR spectral range.

1.3 Objectives of the Research

The goal of this thesis is to experimentally and theoretically examine and demonstrate novel designs and techniques for sensing and telecoms applications based on optical microring resonators (MRRs). There are three primary objectives of this research. The first is to investigate the selectivity or specificity enhancement of the refractive index-based sensors by employing porous 2D materials for surface functionalisation. The second objective is to design and simulate SOI-based novel devices which are able to detect different molecules with higher sensitivity and selectivity. The third objective is to experimentally and theoretically achieve coherent manipulation of the propagat-

ing light fields in order to control the resonant line-shapes and generate electromagnetically induced transparency (EIT)-like resonances. In addition, this study aims to examine devices in which it is possible to control, by thermo-optic tuning, the group delay for both superluminal and subluminal (fast and slow) light applications.

1.4 Thesis Outline

The structure of this thesis consists of eight chapters. The first chapter provides a general introduction about the silicon photonics platform, its applications and challenges. Chapter 2 consists of the theoretical background of the microring resonators (MRRs) along with a thorough review of the current literature on state-of-the-art gas/liquid sensing technologies.

Chapter 3 describes the simulation tools and resources which were employed to provide both insight into the physics of device operation and support the experimental data derived during this work. In addition, modelling and simulation served as a guide to optimisation of the SOI-based photonic components in terms of specific performance metrics.

Chapter 4 provides a detailed explanation of the experimental setup developed and employed during the course of this work. This includes the bespoke microscope/transmission spectroscopy setup for both basic imaging and delivery and collection of light via the silicon photonic integrated circuit devices, a thermal tuning experiment for characterization of MRR based devices and a bespoke vapour sensing experiment, developed during the research. Furthermore, in this chapter, we examine the effect, on the performance of silicon MRRs (extinction ratio, cavity quality-factor and losses), of varying the separation between the waveguide and the MRR, as well as modifying the waveguide width.

Chapter 5 presents the results and analyses of the optical response of three different devices (i) a conventional microring resonator (strip-MRR), (ii) a slotted microring resonator (slot-MRR) and (iii) a graphene oxide integrated silicon microring resonator (GOMRR) when they are exposed to a range of vapour phase Volatile Organic Compounds (VOCs). This is supported by numerical (Finite-Difference Eigenmode (FDE)-Lumerical) simulations to determine device sensitivities and limits of detection.

Chapter 6 demonstrates a theoretical analysis of a novel design and approach for gas/liquid sensing using a single racetrack resonator with attached single or double directional couplers. Both free spectral range (FSR) and bulk sensitivity were significantly improved as compared to conventional microring resonator structures by exploiting the Vernier effect.

Chapter 7 demonstrates the manipulation of resonant line-shapes in coupled MRRs with integrated on-chip microheaters. Tuneable Electromagnetically Induced Transparency (EIT)-like and anti-crossing-like effects were observed experimentally and these observations are supported by both analytical models and numerical simulations in order to determine the origin of the optical transparency in the spectrum. The capability to tune EIT and generate asymmetric (Fano-like) resonant line-shapes has obvious applications in low power optical switching and modulation in telecoms as well as for optical gyroscopes and biochemical sensor applications.

Finally, chapter 8 concludes by summarizing the key findings and achievements of the research and providing some possible directions and potential for future work based on the findings of this project.

1.5 References

1. Reed. (2008). *Silicon photonics: The state of the art*: John Wiley & Sons.
2. Maiman, Maiman, & Holland. (2018). *Laser inventor*: Springer.
3. "The future of data centers." (2019). from <https://www.cbinsights.com/research/future-of-data-centers/>.
4. Clidaras, Stiver, & Hamburgren. (2009). Water-based data center. In: Google Patents.
5. Li, Lin, Qiao, Huang, Li, Michon, et al. (2018). Monolithically integrated stretchable photonics. *Light: Science & Applications*, 7(2), 17138-17138.
6. Vivien, Marris-Morini, Virot, Perez-Galacho, Rasigade, Cassan, et al. (2015). *Ultra-fast silicon-based optoelectronic devices on a 300 mm cmos platform for on-chip optical interconnects*. Paper presented at the 2015 17th International Conference on Transparent Optical Networks (ICTON).
7. Assefa, Xia, & Vlasov. (2010). Reinventing germanium avalanche photodetector for nanophotonic on-chip optical interconnects. *Nature*, 464(7285), 80-84.
8. Zhou, Yin, & Michel. (2015). On-chip light sources for silicon photonics. *Light: Science & Applications*, 4(11), e358.
9. Billah, Blaicher, Hoose, Dietrich, Marin-Palomo, Lindenmann, et al. (2018). Hybrid integration of silicon photonics circuits and inp lasers by photonic wire bonding. *Optica*, 5(7), 876-883.
10. Chrostowski, & Hochberg. (2015). *Silicon photonics design: From devices to systems*: Cambridge University Press.
11. Remello, Hirano, Kuttassery, Nabetani, Yamamoto, Onuki, et al. (2015). Visible light induced oxygenation of alkenes with water sensitized by silicon-porphyrins with the second most earth-abundant element. *Journal of Photochemistry and Photobiology A: Chemistry*, 313, 176-183.
12. Arns. (1998). The other transistor: Early history of the metal-oxide semiconductor field-effect transistor. *Engineering Science & Education Journal*, 7(5), 233-240.
13. Li. (1980). Refractive index of silicon and germanium and its wavelength and temperature derivatives. *Journal of Physical and Chemical Reference Data*, 9(3), 561-658.

14. Malitson. (1965). Interspecimen comparison of the refractive index of fused silica. *Josa*, 55(10), 1205-1209.
15. Iyer, & Xie. (1993). Light emission from silicon. *science*, 260(5104), 40-46.
16. Boyraz, & Jalali. (2004). Demonstration of a silicon raman laser. *Optics express*, 12(21), 5269-5273.
17. Rong, Liu, Jones, Cohen, Hak, Nicolaescu, et al. (2005). An all-silicon raman laser. *Nature*, 433(7023), 292-294.
18. Huang, Liu, Qin, Lü, & Xu. (2011). Nano-laser on silicon quantum dots. *Optics Communications*, 284(7), 1992-1996.
19. Pavesi, Dal Negro, Mazzoleni, Franzo, & Priolo. (2000). Optical gain in silicon nanocrystals. *Nature*, 408(6811), 440-444.
20. Pilon, Lyasota, Niquet, Reboud, Calvo, Pauc, et al. (2019). Lasing in strained germanium microbridges. *Nature communications*, 10(1), 1-8.
21. Camacho-Aguilera, Cai, Patel, Bessette, Romagnoli, Kimerling, et al. (2012). An electrically pumped germanium laser. *Optics express*, 20(10), 11316-11320.
22. Assefa, Xia, Green, Schow, Rylyakov, & Vlasov. (2010). Cmos-integrated optical receivers for on-chip interconnects. *IEEE Journal of Selected Topics in Quantum Electronics*, 16(5), 1376-1385.
23. Michel, Liu, & Kimerling. (2010). High-performance ge-on-si photodetectors. *Nature photonics*, 4(8), 527.
24. Roelkens, Liu, Liang, Jones, Fang, Koch, et al. (2010). Iii-v/silicon photonics for on-chip and intra-chip optical interconnects. *Laser & Photonics Reviews*, 4(6), 751-779.
25. Luo, Cheng, Song, Liow, Wang, & Yu. (2016). Wafer-scale dies-transfer bonding technology for hybrid iii/v-on-silicon photonic integrated circuit application. *IEEE Journal of Selected Topics in Quantum Electronics*, 22(6), 443-454.
26. Bowers, Komljenovic, Davenport, Hulme, Liu, Santis, et al. (2016). *Recent advances in silicon photonic integrated circuits*. Paper presented at the Next-Generation Optical Communication: Components, Sub-Systems, and Systems V.

27. Absil, De Heyn, Chen, Verheyen, Lepage, Pantouvaki, et al. (2015). *Imec isipp25g silicon photonics: A robust cmos-based photonics technology platform*. Paper presented at the Silicon Photonics X.
28. Lin. (2019). *Tsri silicon photonics design platform: Standardization and collaboration*. Paper presented at the 2019 International Symposium on VLSI Design, Automation and Test (VLSI-DAT).
29. Prakash, & Yeom. (2014). *Nanofluidics and microfluidics: Systems and applications*: William Andrew.
30. Schodek, Ferreira, & Ashby. (2009). *Nanomaterials, nanotechnologies and design: An introduction for engineers and architects*: Butterworth-Heinemann.
31. Kuyken, Ideguchi, Holzner, Yan, Hänsch, Van Campenhout, et al. (2015). An octave-spanning mid-infrared frequency comb generated in a silicon nanophotonic wire waveguide. *Nature communications*, 6(1), 1-6.
32. Kitamura, Pilon, & Jonasz. (2007). Optical constants of silica glass from extreme ultraviolet to far infrared at near room temperature. *Applied optics*, 46(33), 8118-8133.
33. Bogaerts, Dumon, Van Thourhout, Taillaert, Jaenen, Wouters, et al. (2006). Compact wavelength-selective functions in silicon-on-insulator photonic wires. *IEEE Journal of Selected Topics in Quantum Electronics*, 12(6), 1394-1401.
34. Baets, Subramanian, Dhakal, Selvaraja, Komorowska, Peyskens, et al. (2013). *Spectroscopy-on-chip applications of silicon photonics*. Paper presented at the Integrated optics: Devices, materials, and technologies XVII.
35. Kallepalli. (2018). *Applications of silicon photonics in sensors and waveguides*: BoD–Books on Demand.
36. Shi, Wong, He, Li, Zhang, Yung, et al. (2019). High-resolution, high-contrast mid-infrared imaging of fresh biological samples with ultraviolet-localized photoacoustic microscopy. *Nature photonics*, 13(9), 609-615.
37. Consani, Ranacher, Tortschanoff, Grille, Irsigler, & Jakoby. (2018). Mid-infrared photonic gas sensing using a silicon waveguide and an integrated emitter. *Sensors and Actuators B: Chemical*, 274, 60-65.
38. Notaros, Notaros, Raval, Poulton, Byrd, Li, et al. (2019). *Integrated optical phased arrays: Lidar, augmented reality, and beyond*. Paper presented at the Integrated Photonics Research, Silicon and Nanophotonics.

39. Wu, Yu, & Zhang. (2019). Mode-assisted silicon integrated interferometric optical gyroscope. *Scientific reports*, 9(1), 1-7.
40. Arditty, & Lefevre. (1981). Sagnac effect in fiber gyroscopes. *Optics letters*, 6(8), 401-403.
41. Steglich, Hülsemann, Dietzel, & Mai. (2019). Optical biosensors based on silicon-on-insulator ring resonators: A review. *Molecules*, 24(3), 519.
42. Bijland, Bomers, & Smulders. (2013). Smelling the diagnosis a review on the use of scent in diagnosing. *Neth. J. Med*, 71(2013), 300-307.
43. Wang, Kalyanasundaram, Stanacevic, & Gouma. (2010). Nanosensor device for breath acetone detection. *Sensor Letters*, 8(5), 709-712.
44. Lechuga. (2005). Optical biosensors. *Comprehensive analytical chemistry*, 44, 209-250.
45. Garzón, Pinacho, Bustos, Garzón, & Bustamante. (2019). Optical biosensors for therapeutic drug monitoring. *Biosensors*, 9(4), 132.
46. "Biosensors market." (2019). Retrieved 28 April 2020, from <https://www.marketsandmarkets.com>.
47. Liu, Tu, Kim, Kee, Shin, Han, et al. (2013). Highly sensitive mach–zehnder interferometer biosensor based on silicon nitride slot waveguide. *Sensors and Actuators B: Chemical*, 188, 681-688.
48. De Vos, Bartolozzi, Schacht, Bienstman, & Baets. (2007). Silicon-on-insulator microring resonator for sensitive and label-free biosensing. *Optics express*, 15(12), 7610-7615.
49. Claes, Molera, De Vos, Schacht, Baets, & Bienstman. (2009). Label-free biosensing with a slot-waveguide-based ring resonator in silicon on insulator. *IEEE Photonics journal*, 1(3), 197-204.
50. Grist, Schmidt, Flueckiger, Donzella, Shi, Fard, et al. (2013). Silicon photonic micro-disk resonators for label-free biosensing. *Optics express*, 21(7), 7994-8006.
51. Jugessur, Dou, Aitchison, De La Rue, & Gnan. (2009). A photonic nano-bragg grating device integrated with microfluidic channels for bio-sensing applications. *Microelectronic Engineering*, 86(4-6), 1488-1490.
52. Mandal, Serey, & Erickson. (2010). Nanomanipulation using silicon photonic crystal resonators. *Nano letters*, 10(1), 99-104.

-
53. Xia, Qiu, Zhang, Gao, Shu, & Xu. (2013). Suspended si ring resonator for mid-ir application. *Optics letters*, 38(7), 1122-1124.
 54. Penades, Ortega-Moñux, Nedeljkovic, Wangüemert-Pérez, Halir, Khokhar, et al. (2016). Suspended silicon mid-infrared waveguide devices with subwavelength grating metamaterial cladding. *Optics express*, 24(20), 22908-22916.
 55. Lin, Luo, Gu, Kimerling, Wada, Agarwal, et al. (2017). Mid-infrared integrated photonics on silicon: A perspective. *Nanophotonics*, 7(2), 393-420.
 56. Hou, Chen, Zhang, Zhuo, Huang, Hogg, et al. (2018). Near-infrared and mid-infrared semiconductor broadband light emitters. *Light: Science & Applications*, 7(3), 17170-17170.

2 Literature Review (Background)

This chapter is intended to reinforce some fundamental concepts of silicon photonics devices, especially those designed for sensing applications. The control and manipulation of light using integrated silicon waveguides, whilst simple in principle, can provide new and exciting device applications, beyond straightforward ‘routing’. One example of this is the control of coherent interference via ‘feedback’ between different coupled photonic resonators. This chapter aims to cover the significant advances in this area, helping to set the current work in context with that in the literature, as well as to provide insights into effective approaches to device design that could be used to further improve the technologies and widen applications.

2.1 Optical Channel Waveguide Types

Recently, optical waveguides have played an important role in communication networks and optical sensing [1]. As described in chapter 1, the common structure of the optical channel waveguides consists of a fabricated thin layer (core) between two layers with slightly lower refractive indices (cladding). These channels can be designed to confine the propagation of the electromagnetic waves (light) in two directions.

Depending on the wavelength range and the application type, various materials and platforms are used for fabricating the optical waveguides, including silicon-on-insulator (SOI) [2], silicon nitride (Si_xN_y) [3], silicon-on-sapphire (SOS) [4], suspended silicon [5] and, more recently, chalcogenides-on-silicon [6]. Among these materials, our research group have focused on the most promising platform which is SOI due to its stability, low cost, high optical confinement and high integration capabilities [7]. The SOI waveguides are commonly covered with top oxide cladding in order to allow for metal interconnects or on-chip microheaters to be deposited on top. In sensing applications, a portion of the top oxide layer needs to be removed to expose the device to the environment, allowing molecules to attach themselves to (or come in close contact with) the silicon waveguide surface.

The physical geometry of the optical waveguides can be classified into three main categories: (a) Rib waveguide, (b) Strip waveguide and (c) Slot waveguide, as illustrated in Figure 2.1.

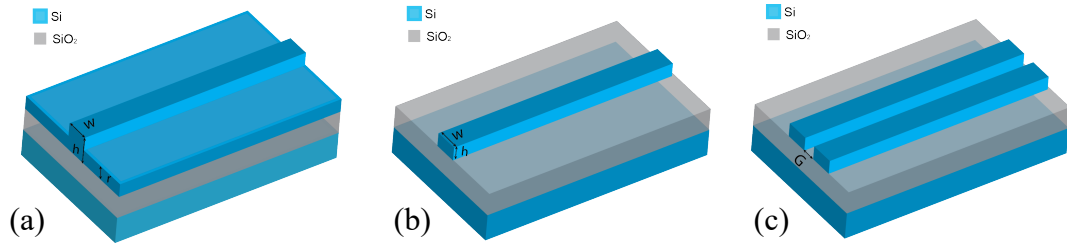


Figure 2.1 Optical waveguide structures (a) Rib waveguide (b) Strip waveguide (c) Slotted channel waveguide

2.1.1 Rib Waveguide

The structure of the SOI rib waveguide usually consists of a guiding layer (core) over SiO₂ buffer layer (lower cladding). The guiding layer is partially etched, as seen in Figure 2.1 (a) which forms the rib geometry shape.

Different parameter dimensions of the rib waveguide design lead to different applications. Most of these applications operate at the single-(fundamental) mode condition, which provides for low loss propagation [8]. The condition for achieving single-mode operation was demonstrated previously by Soref et al. [9] to be determined by the dimensions of the rib waveguide according to the following equation:

$$\frac{W}{h} \leq 0.3 + \frac{(r/h)}{\sqrt{1 - (r/h)^2}} \quad (for \ 0.5 \leq \frac{r}{h} < 1) \quad (2.1)$$

Where W is the width of the rib, h is the thickness of the guiding layer and r is the thickness of the un-etched core (slab), as illustrated in Figure 2.1 (a).

Silicon guiding layers with larger cross-sections (exceeding the limits of Equation (2.1)) can also still accomplish predominantly single-mode operation as a result of

higher-order modes tending to ‘leak’ out from the core to the surrounding slab, over sufficiently long waveguide lengths [9, 10, 11]. Therefore, employing long enough waveguides (several millimetres) enables single-mode operation for such structures.

2.1.2 Strip Waveguide

This waveguide type is obtained by fully etching the silicon guiding layer down to the (SiO₂) BOX layer, providing a ‘strip geometry’, as shown in Figure 2.1 (b). Compared with the rib waveguide, the strip structure has an inherently higher sensitivity to side-wall roughness. However, strip-based waveguides exhibit higher mode confinement because the low-index cladding completely surrounds the waveguide [12]. The high refractive index contrast allows this type of waveguide to be fabricated with very small dimensions (several hundred nanometres) whilst maintaining low propagation losses (i.e. < 2.8 dBcm⁻¹ for the TE polarisation at 1.5μm) [13].

In order to achieve single-mode operation for TE polarisation, an approximate expression was calculated by Aalto, resulting in the following equation [11]:

$$W \times h \leq 0.13 \mu m^2 \quad (2.2)$$

Timotijevic et al. carried out 2D simulations and found that the TM polarisation is critical for single-mode operation. They established a generalised analytical expression that represents the boundary between single-mode and multi-mode area [14, 15]:

$$W \leq -1.405 \times h + (0.746 \times 10^{-6}) \quad (2.3)$$

Where, the waveguide width (W) and height (h) are in μm units. Usually, strip-based waveguides are preferred in bio-sensing applications since the evanescent field of the guided mode is relatively strong on all three sides of the waveguide which increases the interaction with surrounding (target) molecules.

2.1.3 Slot Waveguide

A slotted waveguide consists of a narrow low refractive index slot between two high refractive index waveguides. The low index medium causes a large discontinuity of the electric field at the interface of the high/low index materials, which results in the guided mode being predominantly confined to the (low index) slot region. For SOI-based waveguides, the slot is usually filled with either air or silica (SiO_2). In Figure 2.2, the normalised electric field distribution (E_x) of the fundamental TE mode is shown for such a device, as obtained using 2D (Finite-Difference Eigenmode, FDE) simulations. The waveguide material is silicon and the surrounding cladding is silica. The width and height of the simulated waveguides are 500nm and 220nm, respectively. Figure 2.2 (b) shows E_x against the horizontal waveguide position, x , at half the waveguide height.

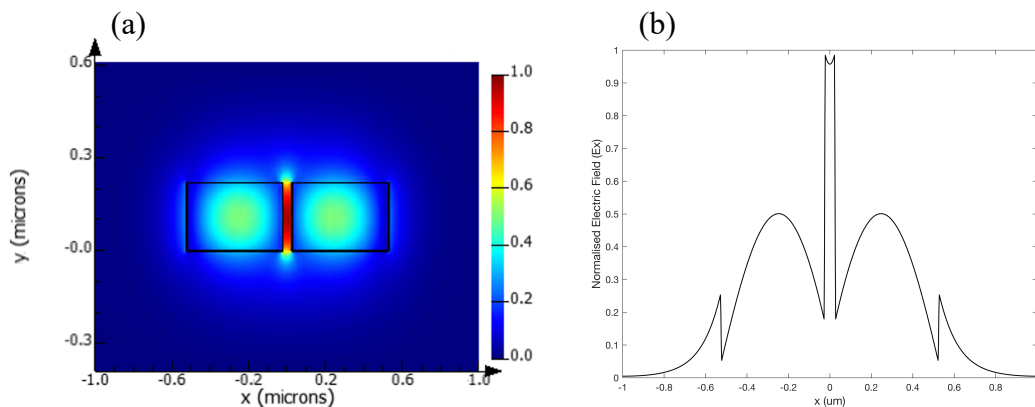


Figure 2.2 (a) Normalised electric field profile (E_x) for 50nm slot (b) cross-sectional plot through the centre of the waveguide

Both standard photolithography and electron beam (e-beam) lithography techniques enable slot widths in the sub-hundred-nanometre range. Slot waveguides with widths as low as 10nm were demonstrated by Debnath et al., albeit with a relatively large propagation loss of 13.6 dB/cm [16].

2.2 Evanescent Wave

When total internal reflection occurs in a waveguide, the light becomes confined in the core. However, some portion of the electric field of the guided light waves penetrates into the cladding materials, as shown in Figure 2.3. This is called the “evanescent wave”.

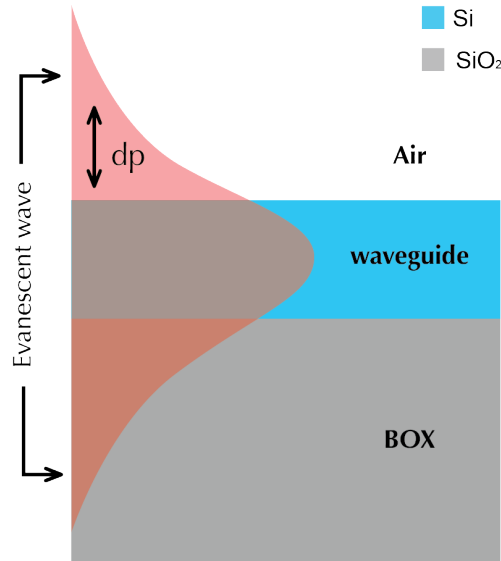


Figure 2.3 Demonstration of evanescent wave in the top and bottom cladding, associated with the guided mode in the Si waveguide. The evanescent wave is typified by an exponentially decaying field profile with a ‘penetration depth’, d_p in the cladding region, typically defined by a field intensity that is $1/e$ of that at the waveguide/cladding interface

The evanescent field amplitude decays exponentially with distance from the core/cladding interface [17], according to:

$$E = E_0 \exp\left(\frac{-y}{d_p}\right) \quad (2.4)$$

Where E_0 is the electric field at the core/clad interface, $y > 0$ is the perpendicular distance from the core/clad interface and d_p is the penetration depth extending into the

cladding layer. The penetration depth is defined as the distance at which the field amplitude decays to $1/e$ of its value at the interface (E_0) and can be written as [17]:

$$d_p = \frac{\lambda}{2\pi} \left[\frac{1}{\left(\sqrt{(n_{eff})^2 - (n_{clad})^2} \right)} \right] \quad (2.5)$$

Where, λ is the operating wavelength, n_{eff} is the effective refractive index of the guided mode and n_{clad} is the cladding refractive index. The effects of core and cladding materials along with the geometric structure of the waveguide are included in n_{eff} .

The penetration depths can be controlled by the operating wavelength, waveguide structure and the cover refractive index. The influence of these factors on penetration depth for strip-based SOI waveguides with air as cover cladding and 1550nm as the operating wavelength was investigated using Equation (2.2), where the fundamental quasi-TE effective index is obtained using simulation (refer to chapter 3 for more details). Figure 2.4 shows the penetration depth as a function of waveguide dimensions, operating wavelength and cover refractive index. The penetration depth increases with decreasing the waveguide width W and height h . However, for very small waveguide dimensions, no modes can be supported.

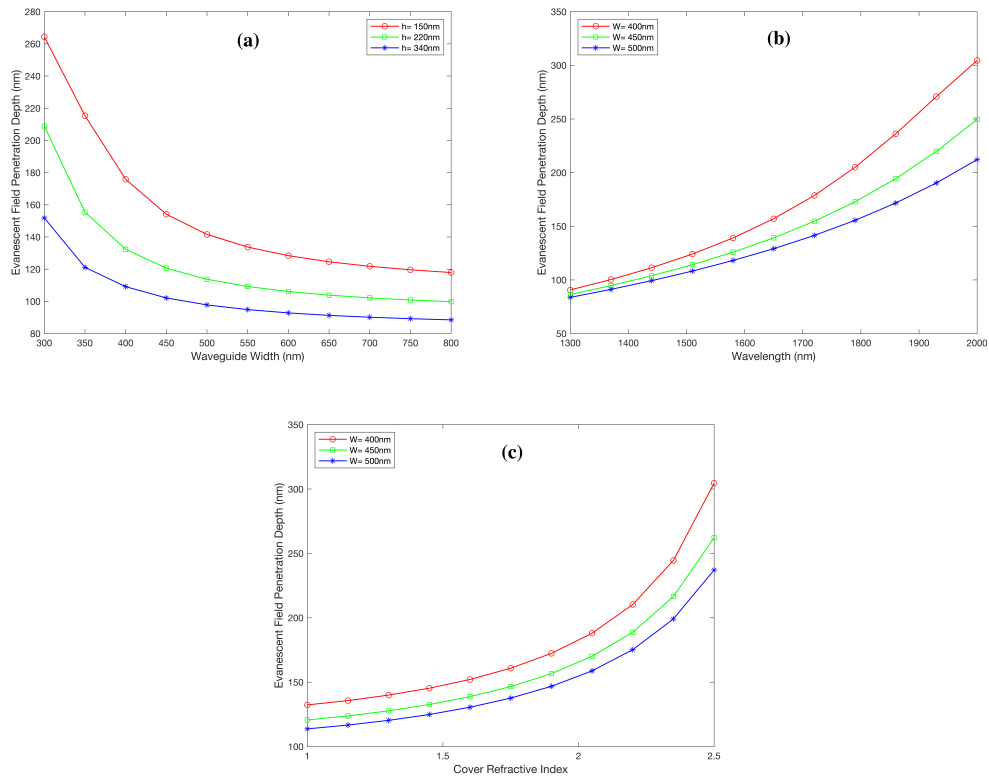


Figure 2.4 Penetration depth as a function of (a) waveguide width W and height h (b) wavelength and (c) cover refractive index n_{clad}

The evanescent field can be enhanced further by exploiting quasi-TM modes instead of the quasi-TE modes. However, quasi-TM modes usually experience higher mode losses at 1550nm which limits their applications in this spectral range [18]. Figure 2.5 shows mode profiles for the quasi-TE and quasi-TM modes in a $500 \times 220\text{nm}$ SOI waveguide with water as the cover index ($n_{clad} = 1.318$ at 1550nm). The mode confinement factors are 80.8% and 34.6% for the quasi-TE and quasi-TM modes, respectively. Although this lower mode confinement results in a much longer penetration depth for the evanescent field, this is coupled with much higher propagation loss for the quasi-TM and so only devices supporting quasi-TE modes were considered in this thesis.

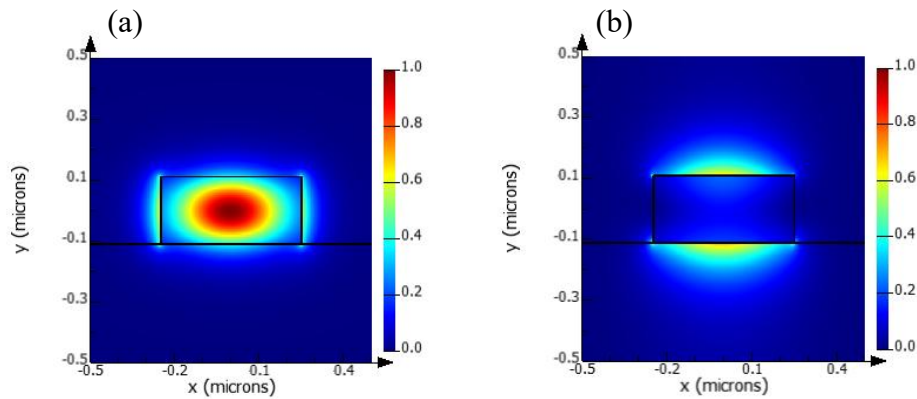


Figure 2.5 Electric field intensity for the fundamental (a) quasi-TE mode and (b) quasi-TM mode

2.3 Microring Resonators (MRRs)

In the past few years, ring resonators have been extensively explored in different silicon photonics applications because of the ultra-compact footprint and ease of fabrication. One of the most promising applications of these optical ring resonators is in the area of biochemical sensing [19].

The operating principle of a ring resonator is based on the evanescent coupling of light from a ‘bus’ waveguide to a proximate (within a few hundred nanometres), circular waveguide, as shown in Figure 2.6.

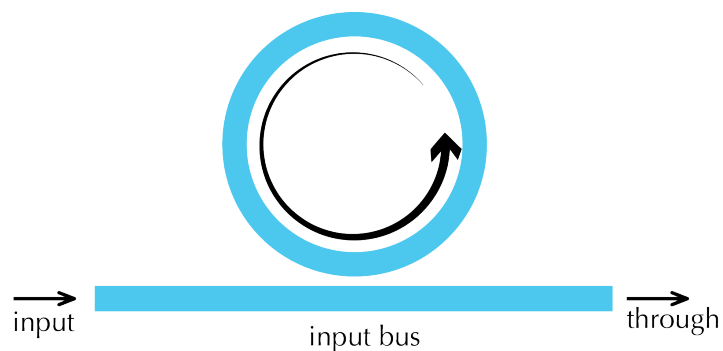


Figure 2.6 Schematic view of a ring resonator

When broadband light, or monochromatic light swept over a range of wavelengths, is injected into the input port of the bus waveguide, the evanescent coupling of this light into the ring generates an interference pattern at the through port. This interference pattern reveals deep (10s of dB), spectrally narrow (sub-nm) ‘notches’ in the transmission spectrum at wavelengths that are (in the case of dispersion-less operation) equally spaced across the entire spectral range of the device. The spectral position of these wavelengths occurs for integer multiples of 2π after each full round-trip of the ring; i.e. they represent phase-matched (resonant) wavelengths with light in the ‘bus’ waveguide. Altering the geometry (round-trip length) of the ring, either physically or ‘effectively’ (by modification of its local refractive index), results in small but discernible wavelength shifts for these resonances. For example, changes in the local effective refractive index of the ring may be achieved when an analyte concentration is attached to the physical structure, and interacts with the evanescent field associated with the resonant guided mode within the ring. With the capability of extremely high-resolution spectral detection, one can, in principle, measure extremely small wavelength shifts (on the order of 10’s of pm with current optical spectrum analysers) leading to the detection of extremely small concentrations of analytes, in a rather generic way [20]. The resonant wavelength(s) of such a device are described by the following expression [15]:

$$\lambda_{\text{res}} = \frac{2\pi R n_{\text{eff}}}{m} \quad (2.6)$$

Where, R is the radius of the ring, n_{eff} is the effective refractive index of the ring, and m is an integer.

The sharp ‘valleys’ at each resonant wavelength can be observed in the example measured output spectrum shown in Figure 2.7.

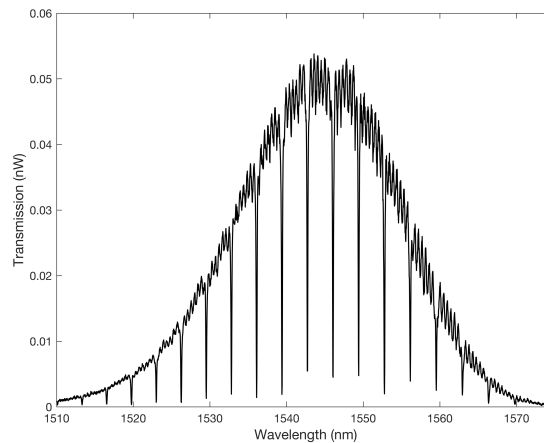


Figure 2.7 An intensity vs wavelength spectrum for a 25 μ m radius ring resonator

In Figure 2.7, the Gaussian shape results from the coupling of light into the device using a broadband superluminescent diode (SLD) via grating coupler at the ‘bus’ waveguide input. Here, the spectral bandwidth (approximately 25nm) is limited by the grating coupler, rather than the source (which is closer to 50nm). Improvements in grating coupler design to enhance the spectral bandwidth of such devices are discussed further in section 3.4.1.

2.4 Ring Characteristics

The functional behaviour of the ring resonators can be described by a number of parameters; Free Spectral Range (FSR), Full Width at Half Maximum (FWHM), Extinction Ratio (ER), Finesse (F) and Q-factor, which are explained in more detail in the following sections.

2.4.1 Free Spectral Range (FSR)

The FSR is the spectral distance between two consecutive resonant peaks in the optical transmission spectrum. The FSR is inversely proportional to the ring radius; i.e. the smaller the ring, the larger the FSR leading to further spaced resonances. The expression for FSR can be written as [15]:

$$\text{FSR} = \frac{\lambda_{\text{res}}^2}{2\pi R n_g} \quad (2.7)$$

Where, λ_{res} is the resonant wavelength, R is the ring radius, and n_g is the group index of refraction [$n_g = n_{\text{eff}} - \lambda (dn_{\text{eff}}/d\lambda)$].

2.4.2 Full Width at Half Maximum (FWHM)

The width of the resonances is normally characterised by their FWHM; i.e. the spectral distance between two points on the peak (valley) at which the intensity is half its maximum (minimum) value, as illustrated in Figure 2.8.

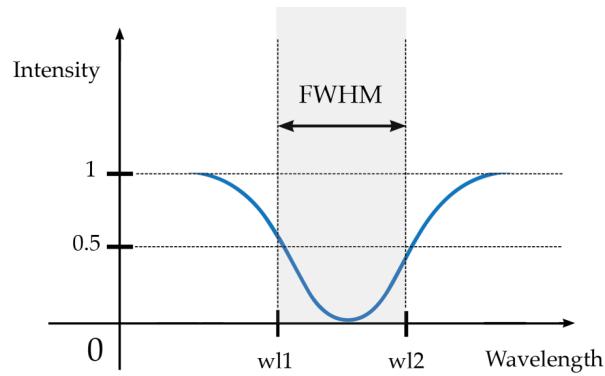


Figure 2.8 An example of Full Width at Half Maximum (FWHM) distance

2.4.3 Extinction Ratio (ER)

The ratio of the maximum to minimum transmitted power through the device is referred to as the extinction ratio (ER). It can be directly determined, experimentally or theoretically calculated using the physical parameters of an MRR coupled to a single bus waveguide. The expression of ER can be written as [21]:

$$\text{ER} = \frac{T_{\text{max}}}{T_{\text{min}}} = \left[\frac{(\alpha + t)(1 - at)}{(\alpha - t)(1 + at)} \right]^2 \quad (2.8)$$

Where, $T_{\max, \min}$ are maximum and minimum transmission of the peaks, α represents the cavity loss, including propagation (i.e. scattering, absorption and radiation) losses in the ring and losses in the couplers, and t is the transmission coefficient, which estimates the fraction of the transmitted light at each resonant peak.

2.4.4 Finesse (F)

The finesse is defined as the ratio of the FSR to the resonance FWHM, essentially describing ‘spectral purity’ (or how ‘sharp’ the resonances are relative to their spacing) [22].

$$F = \frac{\text{FSR}}{\text{FWHM}} \quad (2.9)$$

2.4.5 Q-factor

The quality (Q) factor is defined as the ratio of resonant wavelength to the FWHM. It is a measure of how sharp the peaks are relative to their central frequency [22]. It can also be calculated using n_g , α and t of an MRR with a single bus waveguide:

$$Q = \frac{\lambda_{\text{res}}}{\text{FWHM}} = \frac{\pi n_g L \sqrt{\alpha t}}{\lambda_{\text{res}} (1 - \alpha t)} \quad (2.10)$$

Where, L represents the cavity length. The Q-factor essentially represents the number of round-trips the light makes within the ring before it is consumed by (propagation and scattering) losses. It is thus a measure of the characteristic photon lifetime in the device. The Q-factor of an MRR tends to be diminished with decreases in bend radius and/or increases in sidewall roughness of the ring waveguide, non-optimised bus-to-ring coupling gap and also the materials comprising the core/cladding regions of the device. High Q-factor ring resonators are highly desirable in a wide range of applications such as narrow-bandwidth filters and extremely sensitive detection in sensing.

2.5 Fibre to Waveguide Coupling

Traditionally, there exist a variety of techniques for coupling light into and out of an optical waveguide; these include ‘prism coupling’, ‘grating couplers’, ‘butt coupling’ and ‘end-fire’ coupling [10], all of which are illustrated in Figure 2.9.

Prism coupling can couple more than 90% of light into and out of the waveguide without requiring extra process for the waveguide substrate [23]. Also, it does not involve critical alignment. However, the material of the prism should have a higher refractive index than the waveguide in order to achieve the coupling. The prism can also damage the surface of the waveguide. These limitations exclude this technique from being a good candidate for SOI technology [10].

Butt coupling and end-fire coupling is basically done by shining the laser light onto the end side of the waveguide. In contrast to prism coupling, butt coupling and end-fire coupling require extra processing steps such as cleaving the facet and using anti-reflection coating for the waveguide end. Also, alignments between the two ends play a crucial part in the efficiency of the transmitted power. The end-fire technique requires a lens to focus the light from the optical fibre to the waveguide end, whereas butt coupling is a straightforward coupling, as illustrated in Figure 2.9 (c and d).

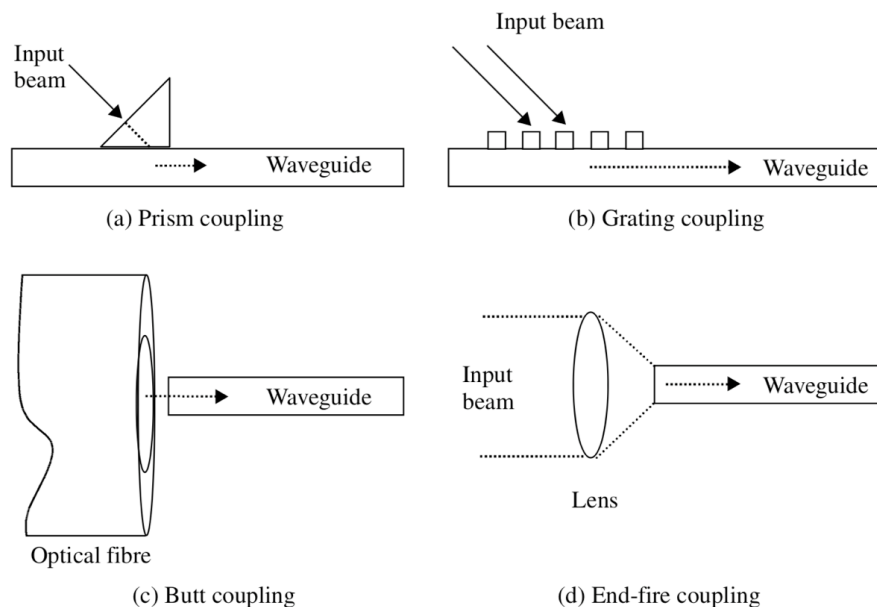


Figure 2.9 Different techniques for coupling light from an optical source (directly or via fibre) to a sub-wavelength scale optical waveguide [10]

Grating couplers are another attractive approach for coupling. The input and output gratings are fabricated by partially or fully etching the silicon waveguide at specific depth and spacing. Grating couplers offer many advantages over the other techniques, such as compatibility with wafer-level testing, ability to be placed anywhere on the chip and much wider alignment tolerance. Grating couplers can achieve coupling efficiencies greater than 80%, as illustrated by Marchetti et al. [24].

2.6 Refractive Index Sensing

Optical biochemical sensors are powerful devices since they provide portability, precise sensitivity and real-time monitoring. They have been employed in numerous important fields such as food safety, security and healthcare [25].

The optical biochemical sensors can be classified according to their functionality. The main sensing techniques incorporate light absorption, emission, scattering and alteration of the effective index. Extremely small perturbations of the effective index can be measured using a ring resonator. These changes can be used to calculate small variations in the local environment such as temperature [26], humidity [27] and strain [28]. In addition, the attachment of molecules, carried in gas/vapour or liquid environments, to the microring resonator surface alters the effective index of the propagating mode which causes a spectral shift in wavelength or variations in the resonant peak depth. The surface of the silicon can also be chemically functionalised to selectively bind to specific (target) molecules, such as proteins and DNA strands [29], in a mixed environment. This allows several different biosensors with different selectivity to be integrated on the same chip.

Various designs of microring resonator were demonstrated theoretically and experimentally, with the primary focus of detecting the presence (and concentration) of a particular molecule in the gas or liquid phase, by analysing the effective refractive index change as described in section 2.2. In Figure 2.10, the black curve corresponds to the unperturbed ring resonator peak position and the red dashed curve corresponds to the shifted resonance peak as a result of a change in the local RI, for example due to the presence of a specific concentration of analyte(s).

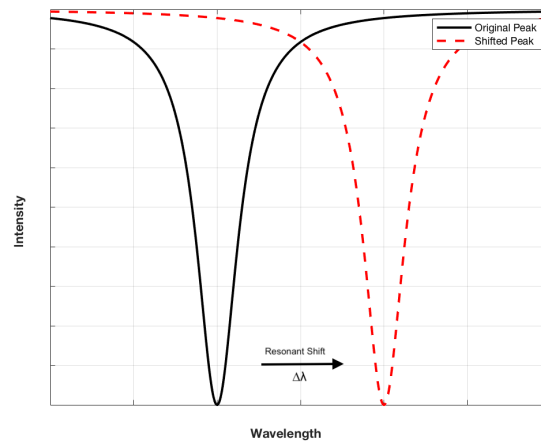


Figure 2.10 Spectral shift due to a change in the effective refractive index of the ring resonator

The sensitivity performance of the optical waveguide sensors that rely on the evanescent wave can be described by the bulk (homogeneous) sensing, surface sensing and limit of detection (LOD).

2.6.1 Bulk Refractive Index (Homogeneous) Detection

Homogeneous sensing is considered when analyte molecules are uniformly distributed in the sensor's evanescent wave surroundings. In this mechanism, bulk refractive index (RI) of the top cladding material will be modified according to the analyte concentration; hence the effective index of the guided mode will be modified. The detection of the bulk RI usually lacks specificity because all materials, including the detected analyte, can contribute to an effective index perturbation [30].

The bulk (homogeneous) sensitivity of the microring sensor can be expressed as [31]:

$$S_{\text{Bulk}} = \frac{\Delta\lambda_{\text{res}}}{\Delta\text{RI}} \quad (2.11)$$

Where, $(\Delta\lambda_{\text{res}})$ is the magnitude of the resonant wavelength shift and (ΔRI) is the RI change of the bulk (top cladding). The sensitivity is usually written in nm/RIU.

The resonant wavelength shift can be written as [31]:

$$\Delta\lambda_{res} = \frac{\Delta n_{eff}(\Delta RI, \Delta\lambda_{res})}{n_g(\lambda_{res0})} \lambda_{res0} \quad (2.12)$$

Where, $\Delta n_{eff}(\Delta RI, \Delta\lambda_{res})$ is the effective index change of the optical mode as a function of bulk refractive index change and spectral peak shift and $n_g(\lambda_{res0})$ is group index at the unperturbed resonance wavelength (λ_{res0}).

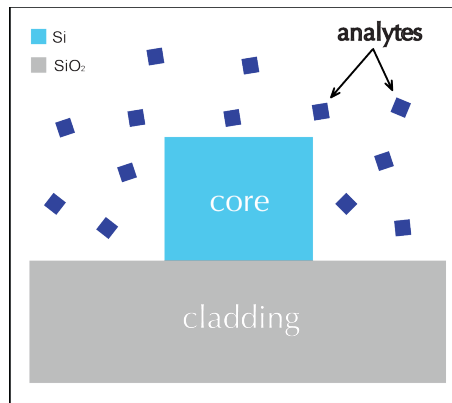


Figure 2.11 Depiction of the bulk sensing showing the analytes surrounding the core of the waveguide

2.6.2 Surface Refractive Index Detection

In surface RI detection, the surface of the waveguide is pre-treated with specific receptors (or binding sites) to capture particular molecules. Typically, a thin layer is employed to enhance sensitivity and specificity towards specific molecules [30]. The surface sensitivity can be expressed as [31]:

$$S_s = \frac{\Delta\lambda_{res}}{\Delta t} \quad (2.13)$$

Where, Δt is the thickness variation of the adsorbed layer on the sensor's surface. Similar to the homogenous sensing, the resonant wavelength shift can be written as [31]:

$$\Delta\lambda_{res} = \frac{\Delta n_{eff}(\Delta t, \Delta\lambda_{res})}{n_g(\lambda_{res0})} \lambda_{res0} \quad (2.14)$$

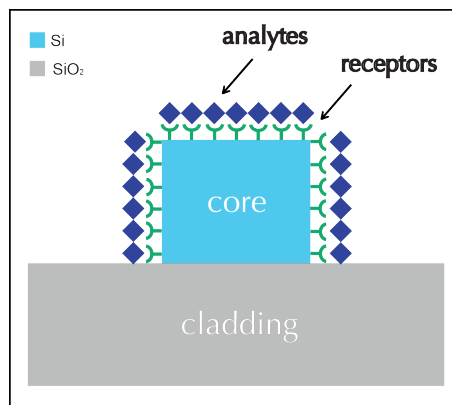


Figure 2.12 Surface sensing showing the analytes bound to specific receptors at the surface of the core of the waveguide

2.6.3 Limit of Detection (LOD)

The minimum quantity or concentration of an analyte that can be reliably distinguished and detected is called the limit of detection (LOD). For sensors based on a microring resonator, the LOD is defined as the smallest possible spectral shift ($\delta\lambda$) that can be detected using a commercial instrument (e.g. optical spectrum analyser) and is given by the following equation [32]:

$$\text{LOD} = \frac{\delta\lambda}{S} \quad (2.15)$$

Where, S is the device bulk or surface sensitivity in nm/RIU. With $\delta\lambda$ typically expressed in units of nm, the LOD is thus expressed in units of RIU. Theoretically, the wavelength shift, induced by the effective index change, is independent of the resonance shape and is limited only by the resolution of the instrument used for signal detection (e.g. optical spectrum analyser (OSA)). However, quantifying $\delta\lambda$ is not trivial because, even in the absence of analyte driven changes in the MRR resonance, the spectrum can still be perturbed by a variety of noise sources [33]. In an attempt to account for these, so as to provide a conservative practical estimate for the absolute LOD in such devices, the approach generally employed [34] is to assign $\delta\lambda \geq 3\sigma$ (i.e. the 99.7% range of uncertainty in determining the resonant peak position of the MRR), such that the LOD becomes equal to $3\sigma/S$ [34].

2.7 Surface Functionalisation

In the past few years, many researchers have reported different approaches to enhance the molecular selectivity by engineering the sensor surface chemistry. The functionalisation of the sensor surface is usually done by chemically coating different types of receptors on the surface. This allows only certain ligands (molecules) to be captured or immobilized near the surface. The binding between receptors and target analytes can then result in extremely high selectivity. The functionalised layers are usually added post (device) fabrication, which allows the possibility of employing different coatings in order to allow for simultaneous detection of several substances on one chip, as illustrated by Washburn et al. [35]. The types of surface modification depend on the target analytes and can be classified into two types: (i) sensing using biological materials and (ii) sensing using high surface area materials.

2.7.1 Surface Modification Using Biological Materials

One of the most common and efficient strategies for altering the chemical and physical properties of the surface for SOI-based bio-sensing is the silanization method [17]. Many substrates, including silica and silicon, can be silanized, which effectively coats the surface with a monolayer of silane (hydroxyl or OH groups). The surface activation

(generation of hydroxyl groups) is usually attained by cleaning the silicon with piranha solution. The surface can then be functionalised using organo-silane agents such as (3-Aminopropyl)triethoxysilane (APTES) which binds to the free OH groups and results in the formation of NH_2 groups [36]. Finally, linker molecules such as NHS-biotin can then be deposited on the surface to stabilise molecular binding [37]. Targets such as streptavidin and avidin can then be isolated (and thus) detected, even in a mixed molecular environment, as they are captured by binding to the biotin near the surface. The biotin-avidin interaction is one of the most widely used non-covalent bindings due to its extremely high specificity and affinity [36, 38]. This method is illustrated graphically in Figure 2.13 and a similar process can be employed for detection or immobilization of many proteins and analytes such as oestrogen response elements, prostate-specific antigen (PSA) and glucose [39].

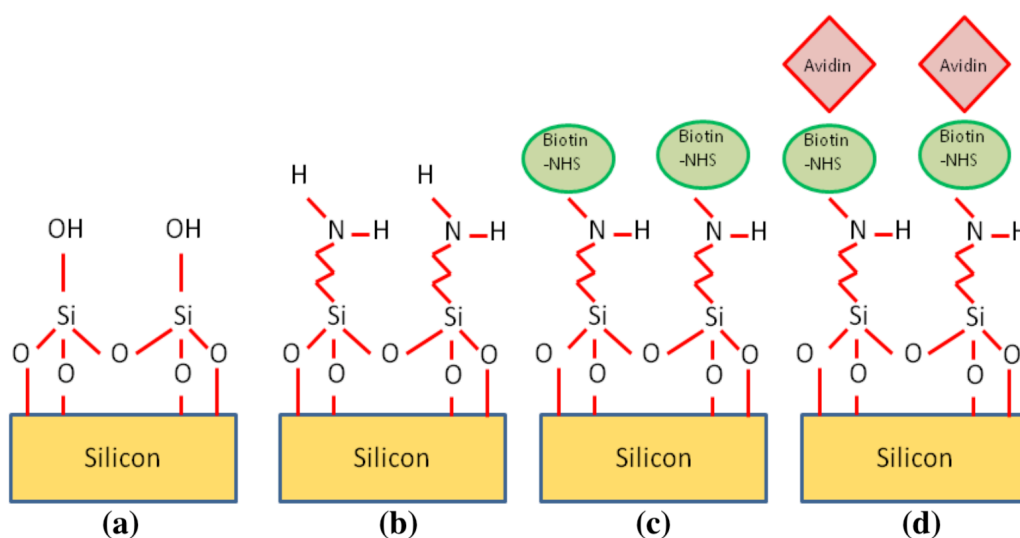


Figure 2.13 Process of surface functionalisation of silicon [37]. (a) the silicon surface is rinsed with piranha solution to expose hydroxyl groups on the surface (b) organo-silane agents (APTES) interact with hydroxyl groups on the surface and generate NH_2 groups (c) NHS-biotin bind to NH_2 groups to act as a receptor (d) Avidin selectively attach to biotin

2.7.2 Surface Modification Using Large Surface Area Materials

Another approach to enhance the performance of an optical sensor is by integrating high surface area or porous materials with the underlying silicon photonics device. The porous nature of such layers provides a method for ‘trapping’ molecules, carried in the gas or liquid phase, close to the sensor surface for improved detection sensitivity, whilst the nature (or efficiency) of pore-filling, can be limited either by the physical size of the molecules or their chemical reactivity with the functional layer to provide a subtly different route to molecular selectivity for mixed molecule environments. In the next sections, various functional materials are described, which have been employed previously to achieve such selectivity, and in the results section of this thesis, a novel approach is demonstrated using graphene oxide as the functional layer enabling the selective detection of a variety of solvents carried in the vapour phase.

2.7.2.1 Porous Silicon (PSi)

Porous structures can be formed directly on the silicon surface by electrochemical etching [40]. The remarkable development of an optical PSi biosensor was derived from the ability to precisely control the properties of the PSi, such as pore diameter, porosity and thickness of the layer. Rodriguez et al. demonstrated a PSi ring resonator with quality factors near 10,000 and detection sensitivity of 380 nm/RIU when exposed to saltwater solutions [41]. The designed 25 μ m radius ring consists of a double layer PSi WG on a silicon substrate. The guiding layer (WG) and cladding layer were fabricated by immersing the sample in a 15% solution of hydrofluoric (HF) acid in ethanol and applying 5 mA/cm² and 48 mA/cm² current density, respectively. This produces a small pore size for the guiding layer and a large pore size for the cladding layer [41], as shown in Figure 2.14 (b).

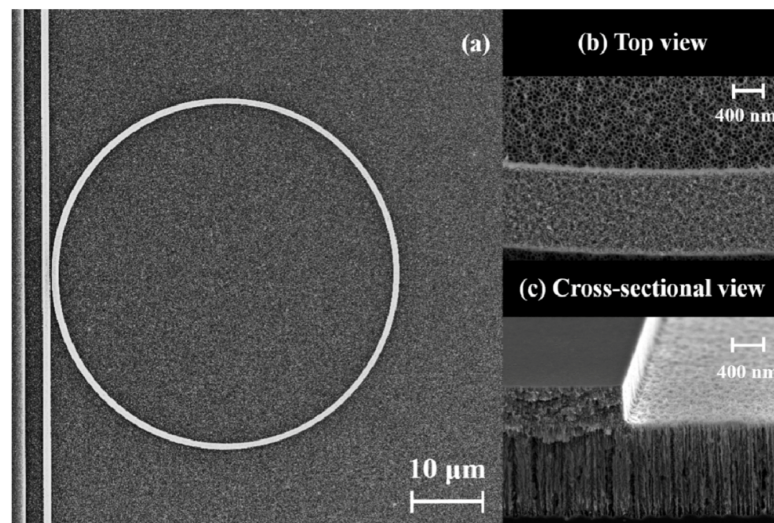


Figure 2.14 Scanning Electron Microscope (SEM) images [41] of (a) PSi ring resonator (b) top view porosity profile of the WG (small pores) and cladding (large pores) layers, and (c) cross-section of the strip WG

2.7.2.2 Metal Oxides Coating

Chemical coatings made from metal oxide nanostructures have been extensively studied for optical gas sensing applications. Metal oxide can be highly selective to one or more gas molecules, for instance, Tungsten Oxide (WO_3) functionalisation is mainly sensitive to hydrogen [42], whereas Tin dioxide (SnO_2) is sensitive to a number of other gases, including ethanol, H_2 , CO , and NH_3 [43]. One of the most widely used metal oxide coatings is Zinc Oxide (ZnO) due to its ability to detect various vapours or gases at low concentration at room temperature [44, 45, 46]. Yebo et al. reported an MRR coated with a 200nm thick nanocrystalline ZnO film in which ethanol vapour detection was demonstrated at concentrations below 100 ppm at room temperature [47]. After depositing the ZnO film, the Q-factor was shown to decrease from 26,000 (for the uncoated ring) to 15,000 for the coated ring. They experimentally show peak shift when exposed to different concentrations of ethanol c_{EtOH} in ppm. As seen in Figure 2.15 (a and b), exposure to 1500 ppm of ethanol leads to a shift of 0.5nm. Figure 2.15 (c) indicates that “on” response can be reached within 15 seconds, while “off” response is reached within 6 seconds. They attributed the incomplete recovery in the

“off” state to ethanol molecules not being released from adsorption sites on the ZnO surface.

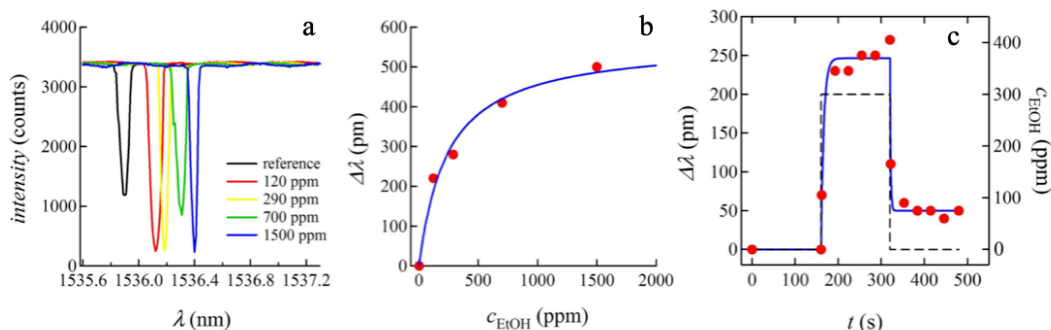


Figure 2.15 (a) Measured transmission spectrum and (b) corresponding resonance shift for different ethanol vapour concentrations. (c) Dynamic response of the sensor for one on-off cycle upon exposure to 300 ppm ethanol [47]

2.7.2.3 Metal-Organic Framework (MOF) Coating

Another novel technique to exploit porous materials for gas/vapour sensing applications was reported by Tao et al. [48]. In this work, a ZIF-8 (MOF) integrated silicon nitride (Si_3N_4) MRR, with a $40\mu\text{m}$ ring radius, exhibited sensitivity enhancements (compared with an equivalent uncoated device) of $\times 10^2$ to $\times 10^3$ for a range of volatile organic compound (VOC) vapours. The ZIF-8 was chosen as the MOF coating because of its high surface area ($1840\text{m}^2\text{g}^{-1}$), relative immunity to humidity and transparency in near IR. Spectral resonance shifts (for the uncoated device) are almost indiscernible over the vapour concentration range, but for the MOF integrated device, this is increased significantly. The gases of a fixed concentration of 100 ppm were carried by N_2 gas flow into the chip. They attributed the initial blue-shift of the resonant signal, in Figure 2.16 (a), to gas flow induced cooling of the device and the red-shift to the adsorption of the gases on the surface of the ZIF-8, which results in an increase in the local refractive index. Figure 2.16 (b) shows the limit of detection (LOD) and the sensitivity enhancement factor for the MOF integrated device for all VOCs tested.

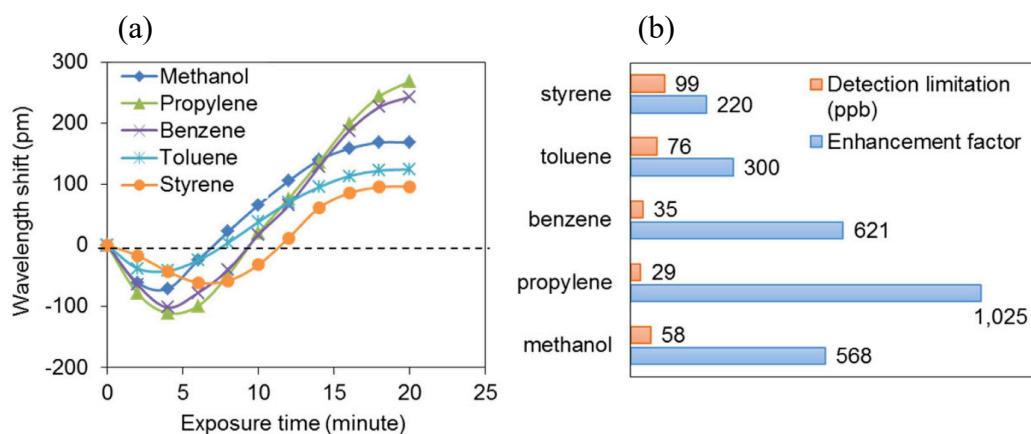


Figure 2.16 (a) Optical response of the hybrid photonic-MOF device to 20 minutes exposure of different VOCs with a fixed concentration of 100 ppm. (b) Enhancement factor and detection limitation of five VOCs at equilibrium [48]

2.7.2.4 Graphene-based coatings

After the discovery and isolation of single atomic layer carbon sheets at the University of Manchester in 2004 [49], interest in graphene-based electronic and photonic applications has been meteoric. In principle, graphene is particularly suited to sensing due to its true two-dimensional (2D) nature, leading to a colossal surface area ($2630\text{m}^2\text{g}^{-1}$), whereby every carbon atom is considered as a surface atom capable of adsorbing a gas molecule (i.e. devices incorporating graphene-based sensors should have exceptionally large sensing area per unit volume) [50]. There are different mechanisms of interaction that can contribute to graphene molecular adsorption, e.g. H-bond, van der Waals, electrostatic interaction and π - π interaction [51]. All of these can cause a measurable perturbation of the effective refractive index if employed in an optical sensor. Many researchers have also reported selective optical sensing based on graphene's derivatives; graphene oxide (GO) and reduced graphene oxide (rGO) [52, 53, 54]. The GO sheets can be deposited on the sensor's surface by chemical vapour deposition (CVD) or drop-casting and spin-coating if the GO is dispersed in a liquid.

In chapter 5 of this thesis, we show how a drop-cast layer of GO over a slotted silicon MRR can lead to both detection sensitivity enhancements and a degree of selectivity for a range of vapour phase VOCs.

2.8 Novel Ring Resonator Designs

The traditional SOI-based single MRRs can achieve typical sensitivities of up to 70 nm/RIU, using quasi-TE polarisation [55]. This is limited by the very near-surface interaction between adsorbed molecules and the guided optical mode evanescent field of the MRR [56]. Another drawback for traditional MRRs is the lack of a functionalised layer that can physically adsorb or chemically immobilize the analyte molecules, which can enhance the sensor's selectivity and specificity to detect different gases. Hence, novel configurations are being introduced in the research in order to overcome these limitations. Novel designs of silicon MRR based sensors, without such surface modification, also have the potential for high sensitivities because they can be engineered to have high Q-factors by engineering the resonance line-shape. This may be achieved, for example, by coupling two or more resonators that exhibit the optical equivalent of electromagnetically induced transparencies (EITs) and asymmetric-(Fano-like) resonant line-shapes, which can have very sharp cut-offs. A brief overview of some of these designs will be given in the next subsections.

2.8.1 Slotted Ring Resonators

Similar to the slotted waveguide, explained in section 2.1.3, the slotted ring resonators incorporate a narrow slot (of the order of 100nm) of a low-index material between two circular high-index materials, as shown in Figure 2.17. The large discontinuity of the electric field at the interface of the high index waveguides results in the light being predominantly confined within the low-index slot region. Almeida et al. demonstrated the slotted ring resonator for the first time in 2004 [57]. When employed as a sensor, the slotted MRR has superior sensitivity compared to the conventional (single ring) MRR because it provides a much stronger interaction between analytes (within the slot) and the electric field associated with the guided mode. This configuration has been shown to be capable of achieving 298 nm/RIU [212 nm/RIU] sensitivities for SOI-based [Si_3N_4 -based] MRRs [58, 59].

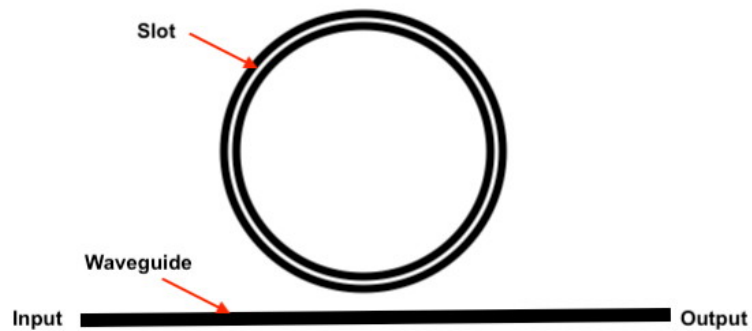


Figure 2.17 Slotted ring resonator configuration

2.8.2 Multiple Ring Resonators

Various configurations of cascaded ring resonators have been studied due to their great potentials in many applications such as filters [60], gyroscopes [61], biochemical/temperature sensing [62, 63].

In sensing applications, two cascaded ring resonators with slightly different radii are commonly utilised to generate a Vernier effect, as shown in Figure 2.18. Due to the difference in the optical round-trip length between the two rings, their free spectral range (FSR) will be slightly different, giving rise to an overall (combined) FSR that is much larger, according to where the resonances of the individual MRRs of the device overlap, as illustrated in Figure 2.18. A small wavelength shift, due to the presence of a concentration of analyte in the sensor MRR with respect to the filter MRR, results in a much larger shift in the cascaded spectrum. Claes et al. have been able to experimentally achieve bulk refractive index sensitivities up to 2169 nm/RIU and a detection limit of (LOD) of 8.3×10^{-6} RIU using this technique [64].

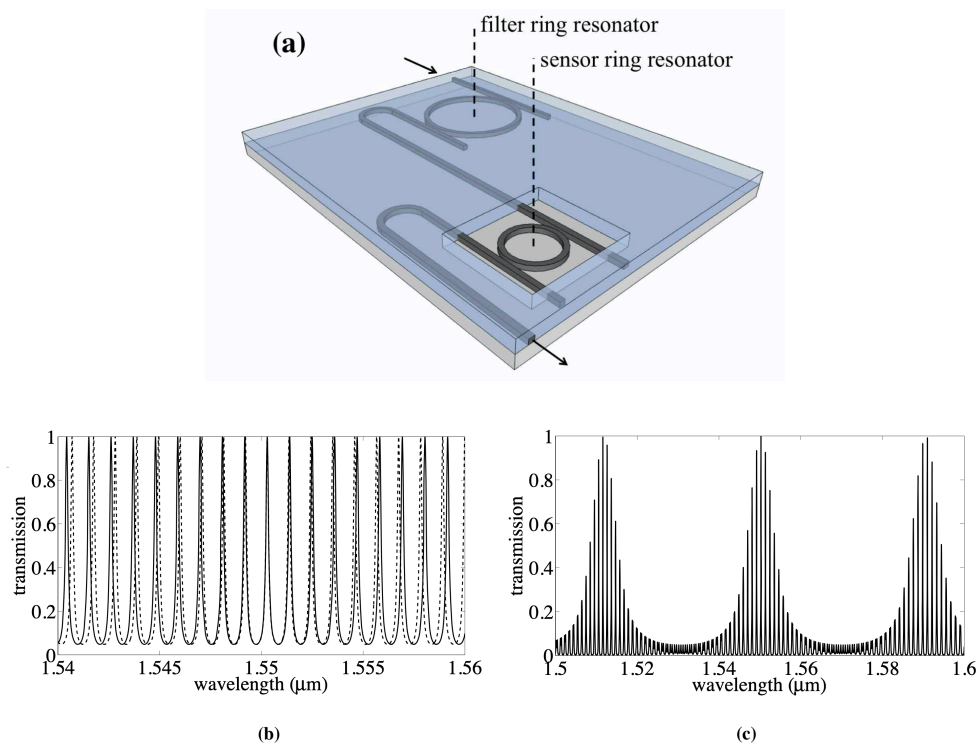


Figure 2.18 Vernier effect in cascaded ring resonator [64] (a) schematic of the Vernier cascaded ring design for sensing application (b) output response of the filter MRR (dashed line) and sensor MRR (solid line) (c) overall spectrum of the cascaded MRR design in a larger wavelength range

Another feature of multiple, cascaded MRRs is the appearance of electromagnetically induced transparency (EIT)-like phenomena. The optical EIT-like effect is analogous to that which is observed for quantum interference of optical transitions induced by coherent light in atomic systems [65]. There are a number of potential applications for these EIT-like effects, implemented in a photonic integrated circuit, ranging from sensing [66, 67] to slow light [68] and optical switches [69].

In one example of this, a parallel pair of coupled MRRs was demonstrated experimentally by Xu et al. [70]. In this case, the narrow EIT was realised using relatively small rings with radii close to $5\mu\text{m}$. A small (8nm) difference in the circumference between the rings was introduced in order to detune their resonances by just 0.4nm. All waveguide widths were chosen to be 450nm with a height of 250nm. The distance between the rings (S) was varied from 15.69 to $15.77\mu\text{m}$ in order to find the optimum EIT

response. The SEM image of the proposed design and their output spectra are shown in Figure 2.19.

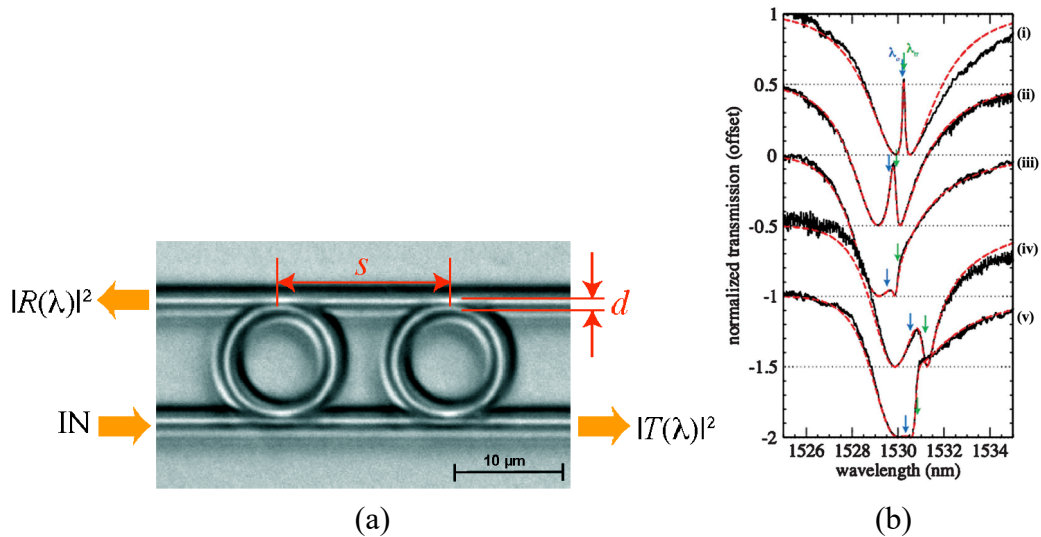


Figure 2.19 Optical EIT-like effect [70] (a) Optical microscope image of the parallel coupled MRR design (b) spectral response corresponding to five different devices with variation in the ring to ring separations, $S =$ (i) $15.69\mu\text{m}$, (ii) $15.71\mu\text{m}$, (iii) $15.73\mu\text{m}$, (iv) $15.75\mu\text{m}$ and (v) $15.77\mu\text{m}$

Figure 2.19 (b) reveals a narrow, symmetric EIT-like response from through port $|T(\lambda)|^2$ when the ring (coupling) separation is equal to $15.69\mu\text{m}$. The EIT exhibits a quality (Q-) factor ($= 11,800$), which is more than ten times that of the individual rings (~ 1000).

2.8.3 Photonic Crystal Ring Resonator (PCRR)

An attractive alternative to conventional ring resonator configuration is the photonic crystal ring resonator (PCRR). A photonic crystal comprises of periodic dielectric nanostructures (or nano-pores) that result in a distinctive photonic band gap (PBG) whereby the propagation of electromagnetic waves (light) is prohibited at certain frequencies [71]. The PCRR, shown in Figure 2.20, offers many advantages as a biosensor because target molecules can interact with the optical fields at trapping sites within

the low refractive index (usually air-filled) holes. 3D Finite-Difference Time-Domain (FDTD) simulations were used to illustrate the fraction of the electric field that penetrates the holes, as shown in Figure 2.20 (c). Unlike the nearly uniform, periodic free spectral range (FSR) in the conventional MRR spectrum, the PCRR can be designed to have non-uniform FSR, implying that the PCRR can have a much wider upper limit on the concentration of analyte because the tracked resonant peak in the spectrum can be identified, even for spectral shifts larger than one FSR, due to the non-uniform spacing. In addition, the PCRR can be designed with a very small bend radius, whilst maintaining relatively low propagation loss, compared with the traditional MRR (which typically exhibits an exponentially increasing propagation loss with inverse radii of curvature below $5\mu\text{m}$ [72]). In [73], label-free detection of DNA and proteins using a PCRR structure was reported, as shown in Figure 2.20 (a). The PCRR, fabricated using the SOI platform, was realised from a silicon ring waveguide (width = 450nm), coupled to a straight bus waveguide (width = 360nm), patterned with 100 circular, air-filled holes (radius = 135nm). The periodicity of the holes and the separation gap were $a = 450\text{nm}$ and $g = 135\text{nm}$, respectively. The experimental bulk refractive index sensitivity for this device was derived experimentally to be 248 nm/RIU .

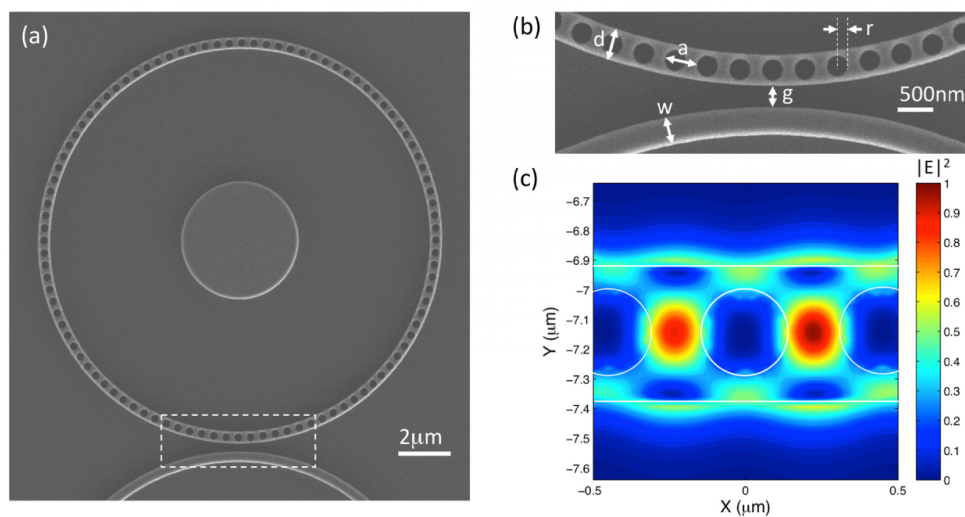


Figure 2.20 (a) SEM image of the photonic crystal ring resonator (PCRR), (b) magnified image of the coupling region and (c) simulation of the resonant mode profile [73]

Another exciting new design that employs a one-dimensional (1D) photonic crystal optical waveguide is the subwavelength grating (SWG) MRR. It is formed by periodic silicon pillars (with a period much smaller than the operating wavelength), with a low index (air or silica) cladding, as shown in Figure 2.21. The shape of these pillars can greatly affect the performance of the SWG MRR, with trapezoidal pillar structures exhibiting lower bend losses and consequently higher Q-factors, compared with rectangular pillars [74]. This structure is promising in biochemical sensing because it allows significant interaction between the propagating optical fields and the cladding materials, as demonstrated by Flueckiger et al. [75]. Engineering the effective refractive index and mode profile in this way, a Q-factor of 7000 and bulk sensitivity of 490 nm/RIU was demonstrated. The drawbacks of SWG and PCRR type devices is the additional leakage losses and fabrication complexity.

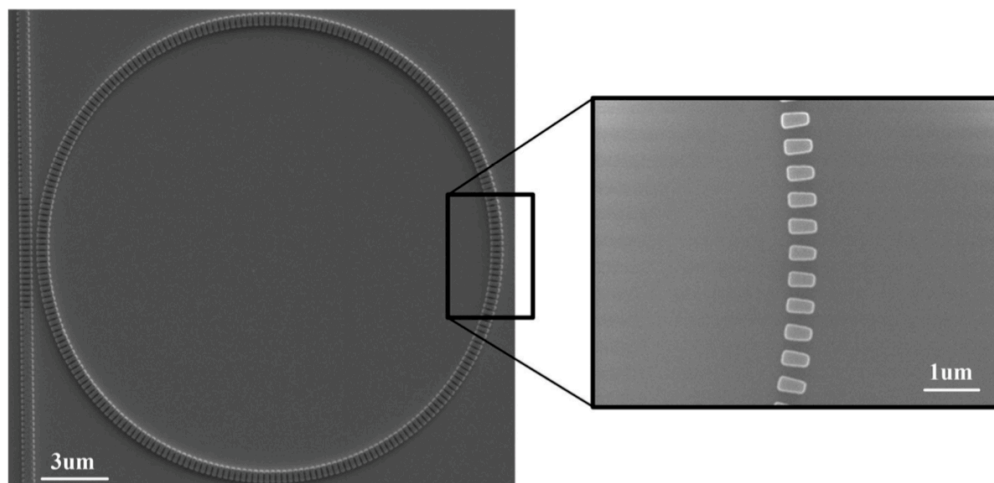


Figure 2.21 An SEM image of the SWG based MRR developed by Flueckiger et al. [75]. The ring resonator was fabricated by e-beam lithography

2.9 References

1. Prajzler, Klapuch, Lyutakov, Hüttel, Špírková, Nekvindová, et al. (2011). Design, fabrication and properties of rib poly (methacrylimide) optical waveguides.
2. Zou, Chakravarty, Chung, Xu, & Chen. (2018). Mid-infrared silicon photonic waveguides and devices. *Photonics Research*, 6(4), 254-276.
3. Hu, Dong, Luo, Liow, Song, Lee, et al. (2017). Silicon photonic platforms for mid-infrared applications. *Photonics Research*, 5(5), 417-430.
4. Baehr-Jones, Spott, Ilic, Spott, Penkov, Asher, et al. (2010). Silicon-on-sapphire integrated waveguides for the mid-infrared. *Optics express*, 18(12), 12127-12135.
5. Cheng, Chen, Wong, Xu, & Tsang. (2012). Mid-infrared suspended membrane waveguide and ring resonator on silicon-on-insulator. *IEEE Photonics journal*, 4(5), 1510-1519.
6. Ma, Choi, Yu, Gai, Yang, Debbarma, et al. (2013). Low-loss chalcogenide waveguides for chemical sensing in the mid-infrared. *Optics express*, 21(24), 29927-29937.
7. Miller, Yu, Ji, Griffith, Cardenas, Gaeta, et al. (2017). Low-loss silicon platform for broadband mid-infrared photonics. *Optica*, 4(7), 707-712.
8. Leblanc-Hotte, Delisle, Lesage, & Peter. (2016). The importance of single-mode behavior in silicon-on-insulator rib waveguides with very large cross section for resonant sensing applications. *IEEE Journal of Selected Topics in Quantum Electronics*, 22(6), 241-248.
9. Soref, Schmidtchen, & Petermann. (1991). Large single-mode rib waveguides in gesi-si and si-on-sio/sub 2. *IEEE Journal of Quantum Electronics*, 27(8), 1971-1974.
10. Reed, & Knights. (2004). *Silicon photonics: An introduction*: John Wiley & Sons.
11. Aalto. (2004). *Microphotonic silicon waveguide components*: VTT Technical Research Centre of Finland.
12. Vivien, Grillot, Cassan, Pascal, Lardenois, Lupu, et al. (2005). Comparison between strip and rib soi microwaveguides for intra-chip light distribution. *Optical materials*, 27(5), 756-762.

13. Tsuchizawa, Yamada, Fukuda, Watanabe, Takahashi, Takahashi, et al. (2005). Microphotonic devices based on silicon microfabrication technology. *IEEE Journal of Selected Topics in Quantum Electronics*, 11(1), 232-240.
14. Timotijevic, Reed, Jones, Liu, Michaeli, & Mashanovich. (2006). *Optical filters in silicon-on-insulator: Design considerations for devices based upon strip and rib waveguides*. Paper presented at the Workshop on Optical Components for Broadband Communication.
15. Reed. (2008). *Silicon photonics: The state of the art*: John Wiley & Sons.
16. Debnath, Khokhar, Reed, & Saito. (2017). *Fabrication of silicon slot waveguides with 10nm wide oxide slot*. Paper presented at the 2017 IEEE 14th International Conference on Group IV Photonics (GFP).
17. Zourob, Elwary, & Turner. (2008). *Principles of bacterial detection: Biosensors, recognition receptors and microsystems*: Springer Science & Business Media.
18. Schmidt, Flueckiger, Wu, Grist, Fard, Donzella, et al. (2014). *Improving the performance of silicon photonic rings, disks, and bragg gratings for use in label-free biosensing*. Paper presented at the Biosensing and Nanomedicine VII.
19. Sun, & Fan. (2008). Analysis of ring resonators for chemical vapor sensor development. *16*(14), 10254-10268.
20. Ramachandran, Wang, Clarke, Ja, Goad, Wald, et al. (2008). A universal biosensing platform based on optical micro-ring resonators. *23*(7), 939-944.
21. McKinnon, Xu, Storey, Post, Densmore, Delâge, et al. (2009). Extracting coupling and loss coefficients from a ring resonator. *17*(21), 18971-18982.
22. Bogaerts, De Heyn, Van Vaerenbergh, De Vos, Kumar Selvaraja, Claes, et al. (2012). Silicon microring resonators. *6*(1), 47-73.
23. Sarid, Cressman, & Holman. (1978). High-efficiency prism coupler for optical waveguides. *Applied Physics Letters*, 33(6), 514-515.
24. Marchetti, Lacava, Khokhar, Chen, Cristiani, Richardson, et al. (2017). High-efficiency grating-couplers: Demonstration of a new design strategy. *Scientific reports*, 7(1), 1-8.
25. Kintzios. (2017). *Portable biosensors and point-of-care systems*: Institution of Engineering & Technology.

26. Singha, & Bhowmik. (2018). *On-chip photonic temperature sensor using micro ring resonator*. Paper presented at the 2018 Fifteenth International Conference on Wireless and Optical Communications Networks (WOCN).
27. Guo, Wang, & Hu. (2014). *A high sensitivity humidity sensor based on micro-ring resonator with three coupling points*. Paper presented at the International Symposium on Optoelectronic Technology and Application 2014: Laser and Optical Measurement Technology; and Fiber Optic Sensors.
28. Abdulla, Harmsma, Nieuwland, Pozo, Lemmen, Sadeghian, et al. (2012). *Soi based mechano-optical pressure sensor using a folded microring resonator*. Paper presented at the Proc. 9th Nanomechan. Sensing Workshop.
29. Yan, Huang, Xu, Chakravarty, Tang, Tian, et al. (2016). Unique surface sensing property and enhanced sensitivity in microring resonator biosensors based on subwavelength grating waveguides. *Optics express*, 24(26), 29724-29733.
30. Chao, & Guo. (2006). Design and optimization of microring resonators in biochemical sensing applications. 24(3), 1395-1402.
31. Barrios. (2009). *Analysis and modeling of a silicon nitride slot-waveguide microring resonator biochemical sensor* (Vol. 7356): SPIE.
32. Wang. (2012). *Advances in chemical sensors: BoD–Books on Demand*.
33. Saponara, & De Gloria. (2019). *Applications in electronics pervading industry, environment and society*: Springer.
34. Guider, Gandolfi, Chalyan, Pasquardini, Samusenko, Pederzolli, et al. (2015). Sensitivity and limit of detection of biosensors based on ring resonators. *Sensing and bio-sensing research*, 6, 99-102.
35. Washburn, Luchansky, Bowman, & Bailey. (2010). Quantitative, label-free detection of five protein biomarkers using multiplexed arrays of silicon photonic microring resonators. *Analytical chemistry*, 82(1), 69-72.
36. Steglich, Hülsemann, Dietzel, & Mai. (2019). Optical biosensors based on silicon-on-insulator ring resonators: A review. *Molecules*, 24(3), 519.
37. Scullion, Krauss, & Di Falco. (2013). Slotted photonic crystal sensors. *Sensors*, 13(3), 3675-3710.
38. Claes, Molera, De Vos, Schacht, Baets, & Bienstman. (2009). Label-free biosensing with a slot-waveguide-based ring resonator in silicon on insulator. *IEEE Photonics journal*, 1(3), 197-204.

39. De Smet, Ullien, Mescher, & Sudhölter. (2011). Organic surface modification of silicon nanowire-based sensor devices. *Nanowires-Implementations and Applications*, 267-288.
40. Korotcenkov. (2016). *Porous silicon: From formation to application: Biomedical and sensor applications, volume two*: CRC Press.
41. Rodriguez, Hu, & Weiss. (2015). Porous silicon ring resonator for compact, high sensitivity biosensing applications. *Optics express*, 23(6), 7111-7119.
42. Yebo, Taillaert, Roels, Lahem, Debliquy, Van Thourhout, et al. (2009). Silicon-on-insulator (soi) ring resonator-based integrated optical hydrogen sensor. *IEEE photonics technology letters*, 21(14), 960-962.
43. Wu, Li, & Sun. (2010). Nano sn₂ gas sensors. *Current Nanoscience*, 6(5), 525-538.
44. Tsai, Chang, Ji, Hsiao, Tang, Lu, et al. (2018). High sensitivity of no gas sensors based on novel ag-doped zno nanoflowers enhanced with a uv light-emitting diode. *ACS omega*, 3(10), 13798-13807.
45. Paliwal, Sharma, Tomar, & Gupta. (2017). Carbon monoxide (co) optical gas sensor based on zno thin films. *Sensors and Actuators B: Chemical*, 250, 679-685.
46. Zhu, & Zeng. (2017). Room-temperature gas sensing of zno-based gas sensor: A review. *Sensors and Actuators A: Physical*, 267, 242-261.
47. Yebo, Lommens, Hens, & Baets. (2010). An integrated optic ethanol vapor sensor based on a silicon-on-insulator microring resonator coated with a porous zno film. *Optics express*, 18(11), 11859-11866.
48. Tao, Wang, Sun, Cai, Wang, Lin, et al. (2017). Hybrid photonic cavity with metal-organic framework coatings for the ultra-sensitive detection of volatile organic compounds with high immunity to humidity. *Scientific reports*, 7, 41640.
49. Novoselov, Geim, Morozov, Jiang, Zhang, Dubonos, et al. (2004). Electric field effect in atomically thin carbon films. *science*, 306(5696), 666-669.
50. Yuan, & Shi. (2013). Graphene-based gas sensors. *Journal of Materials Chemistry A*, 1(35), 10078-10091.
51. Yu, Wang, Xu, Chen, Fu, Wu, et al. (2018). Adsorption of vocs on reduced graphene oxide. *Journal of Environmental Sciences*, 67, 171-178.

-
52. Zhu, Sun, Liu, Zhuang, & Zhao. (2017). Room-temperature nh 3 sensing of graphene oxide film and its enhanced response on the laser-textured silicon. *Scientific reports*, 7(1), 1-8.
 53. Balaji, Yang, Wang, & Zhang. (2019). Graphene oxide-based nanostructured DNA sensor. *Biosensors*, 9(2), 74.
 54. Sehrawat, Islam, Mishra, & Ahmad. (2018). Reduced graphene oxide (rgo) based wideband optical sensor and the role of temperature, defect states and quantum efficiency. *Scientific reports*, 8(1), 1-13.
 55. De Vos, Bartolozzi, Schacht, Bienstman, & Baets. (2007). Silicon-on-insulator microring resonator for sensitive and label-free biosensing. *Optics express*, 15(12), 7610-7615.
 56. Caroselli, Ponce-Alcántara, Quilez, Sánchez, Morán, Barres, et al. (2017). Experimental study of the sensitivity of a porous silicon ring resonator sensor using continuous in-flow measurements. 25(25), 31651-31659.
 57. Almeida, Xu, Barrios, & Lipson. (2004). Guiding and confining light in void nanostructure. 29(11), 1209-1211.
 58. Claes, Molera, De Vos, Schacht, Baets, & Bienstman. (2009). Label-free biosensing with a slot-waveguide-based ring resonator in silicon on insulator. 1(3), 197-204.
 59. Barrios, Banuls, Gonzalez-Pedro, Gylfason, Sanchez, Griol, et al. (2008). Label-free optical biosensing with slot-waveguides. *Optics letters*, 33(7), 708-710.
 60. Little, Chu, Absil, Hryniewicz, Johnson, Seiferth, et al. (2004). Very high-order microring resonator filters for wdm applications. *IEEE photonics technology letters*, 16(10), 2263-2265.
 61. Ciminelli, Campanella, Dell'Olio, Campanella, & Armenise. (2012). *Multiple ring resonators in optical gyroscopes*. Paper presented at the 2012 14th International Conference on Transparent Optical Networks (ICTON).
 62. Jin, Li, & He. (2011). Highly-sensitive silicon-on-insulator sensor based on two cascaded micro-ring resonators with vernier effect. *Optics Communications*, 284(1), 156-159.
 63. Kim, & Yu. (2016). Cascaded ring resonator-based temperature sensor with simultaneously enhanced sensitivity and range. *Optics express*, 24(9), 9501-9510.

64. Claes, Bogaerts, & Bienstman. (2010). Experimental characterization of a silicon photonic biosensor consisting of two cascaded ring resonators based on the vernier-effect and introduction of a curve fitting method for an improved detection limit. *18(22)*, 22747-22761.
65. Fleischhauer, Imamoglu, & Marangos. (2005). Electromagnetically induced transparency: Optics in coherent media. *Reviews of modern physics*, *77(2)*, 633.
66. Du, Li, Yang, & Lu. (2019). High-performance optical sensing based on electromagnetically induced transparency-like effect in tamm plasmon multilayer structures. *58(17)*, 4569-4574.
67. Tomita, Totsuka, Hanamura, & Matsumoto. (2009). Tunable fano interference effect in coupled-microsphere resonator-induced transparency. *26(4)*, 813-818.
68. Li, & Bogaerts. (2017). Tunable electromagnetically induced transparency in integrated silicon photonics circuit. *25(25)*, 31688-31695.
69. Scheuer, Sukhorukov, & Kivshar. (2010). All-optical switching of dark states in nonlinear coupled microring resonators. *Optics letters*, *35(21)*, 3712-3714.
70. Xu, Sandhu, Povinelli, Shakya, Fan, & Lipson. (2006). Experimental realization of an on-chip all-optical analogue to electromagnetically induced transparency. *96(12)*, 123901.
71. Ruda, & Matsuura. (2017). Nano-engineered tunable photonic crystals. In *Springer handbook of electronic and photonic materials* (pp. 1-1): Springer.
72. Robinson, & Nakkeeran. (2013). Photonic crystal ring resonator-based add drop filters: A review. *Optical Engineering*, *52(6)*, 060901.
73. Lo, Hu, Gaur, Kostoulas, Weiss, & Fauchet. (2017). Photonic crystal microring resonator for label-free biosensing. *Optics express*, *25(6)*, 7046-7054.
74. Wang, Xu, Fan, Wang, & Chen. (2016). High quality factor subwavelength grating waveguide micro-ring resonator based on trapezoidal silicon pillars. *Optics letters*, *41(14)*, 3375-3378.
75. Flueckiger, Schmidt, Donzella, Sherwali, Ratner, Chrostowski, et al. (2016). Sub-wavelength grating for enhanced ring resonator biosensor. *24(14)*, 15672-15686.

3 Simulation Methods and Optimisation

Many optical simulation tools and software packages are commercially available to help engineers and scientists investigate the behaviour of the electromagnetic waves in such systems. The increasing interest in modelling the photonic integrated circuit components and systems has led to major developments in optical simulation tools, such as Lumerical MODE/FDTD Solutions [1], COMSOL Multiphysics (wave optics module) [2], Photon Design FIMMWAVE/OmniSim [3] and Synopsys RSoft FemSIM/FullWAVE [4].

Much of the work described in this thesis involved the use of Lumerical [1] for the simulation of electromagnetic waves (light) at the component level, using 2D/3D Finite-Difference Time-Domain (FDTD), Finite-Difference Eigenmode (FDE) and EigenMode Expansion (EME) methods. Furthermore, circuit or system-level simulation was carried out using INTERCONNECT (photonic integrated circuit) simulator. This tool also provides for modelling of the thermal effects in such photonic integrated circuits, using the Heat Transport (HEAT) solver. In addition, Matlab software [5] was employed to model the MRRs, mathematically, using the Scattering Matrix Method (SMM).

In this thesis, the results of Lumerical simulation are validated and tested by performing the following steps:

- 1- Develop a mathematical model, using SMM approach for MRRs, and compare it with the simulation results.
- 2- Simulate similar devices from literature (if available) and compare their experimental results with the simulation, as demonstrated in section 5.1.

This verification process is important since it ensures that the default optical material database, that includes refractive index data, and the simulation physics are an accurate representation of the real world.

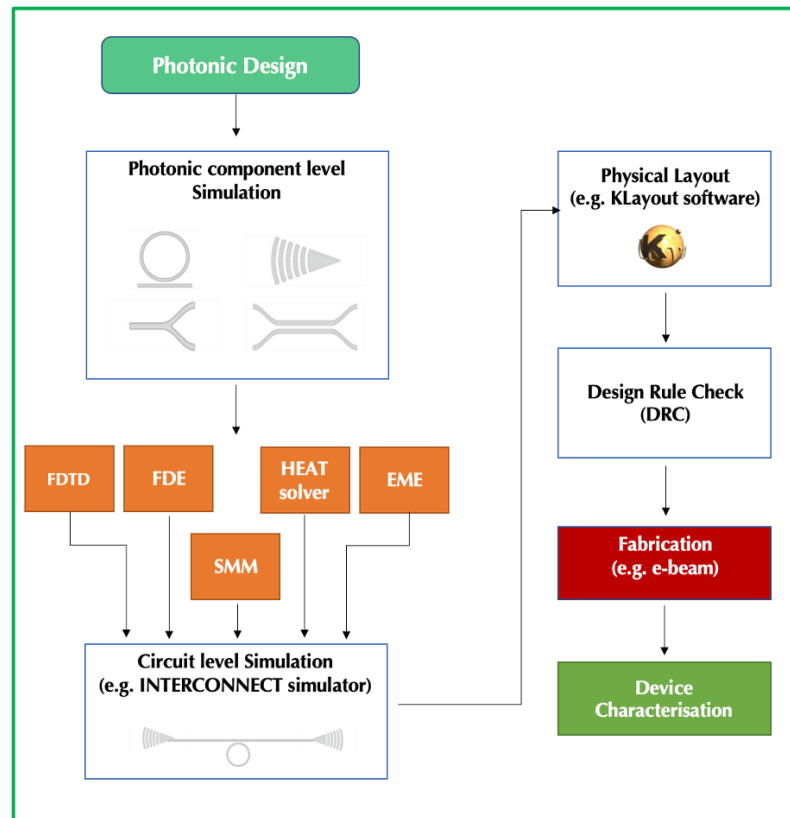


Figure 3.1 Flow chart of the design process for photonic integrated circuits described in this thesis

In this chapter, the photonic integrated circuit design process flow is described in detail, from photonic component through to full device fabrication, in a semiconductor foundry. The flow chart in Figure 3.1 illustrates this process, beginning with the various component simulations (e.g. for the MRR, grating coupler, y-splitter, directional coupler, etc.) using the appropriate simulation tools. The simulation results (scattering or S-parameters) from each method are then exported to the circuit level simulator (INTERCONNECT) where several photonic components can be connected and analysed as a single optical circuit. INTERCONNECT deals with the photonic components as building blocks connected together. After optimising the full circuit design, this is then implemented schematically using a layout editor software (such as K-layout). The layout software packages allow the user to either construct the optical circuit using scripting commands or manually by drawing the mask layout, layer by layer. Once the physical layout is completed, this is run through a design rule check (DRC)

to ensure it meets the foundry submission requirements, prior to sending the full chip design for fabrication. When the chips are delivered, several optical and thermo-optic characterisations are performed to check the device functionality. The experimental setups which are employed here are explained in detail in Chapter 4.

3.1 Simulation Methods

Each of the simulation methods undertaken during the design phase provides different information about the device functionality. An overview of the simulation methods employed here (e.g. FDTD, FDE, HT, EME and SMM) are presented in the following subsections.

3.1.1 Finite-Difference Time-Domain (FDTD)

The FDTD numerical method is the most widely used tool for simulating electromagnetic propagation in a dielectric medium [6]. The technique is based on numerically solving Maxwell's equations and finding an exact solution in the temporal and spatial domains. The electric and magnetic field components of the solution are obtained by applying Fourier transform (FT) analysis to decompose a time-domain function into its constituent frequencies. This allows the user to visualise mode propagation in the dielectric (e.g. waveguide) structures as a function of frequency or wavelength. The Lumerical FDTD simulator automatically constructs a rectangular mesh over the full structure (or sub-structure) to be simulated (including the background of the structures), with each mesh point containing information on the material properties (e.g. real and imaginary components of the refractive indices) to derive solutions for the electric and magnetic field components [7]. The simulation can be used in either 2D or 3D domains, allowing the user to run initial (fast) simulations (in a 2D grid) to optimise the design before running the full 3D simulation, which is computationally more demanding. The simulation boundary conditions utilised a perfectly matched layer (PML) to absorb incident light, minimising reflections back into the device. The PML boundary condition is necessary for certain simulations, specifically those involving radiative loss, for example, when modelling waveguide bends.

3.1.2 Finite-Difference Eigenmode (FDE)

The FDE solver is part of the MODE solution from Lumerical. Similar to the FDTD tool, FDE solves Maxwell's equations to determine the spatial profiles and frequency dependence of the waveguide modes. The solver requires the material types and waveguide dimensions in order to calculate transverse electric (TE) and transverse magnetic (TM) mode profiles, effective indices, and loss. The PML boundary condition is typically employed where purely imaginary effective indices or loss are required (e.g. for waveguide bends). Metal boundary conditions are employed in cases where only negligible modal fields exist at the edge of the simulation region (e.g. for straight waveguides) since these provide much quicker simulation (than for PML) [7].

3.1.3 EigenMode Expansion (EME)

This simulator extends the functionality of the FDE solver. First, it uses the FDE solver to find the supported optical modes at many consecutive non-uniform cross-sections [7]. Second, the solution of the TE and TM fields from each cross-section is utilised to propagate the light along the waveguide. It is particularly suitable for simulating the behaviour of light over long propagation distances because it offers a significant enhancement in simulation time as compared to the FDTD solver. This method is appropriate for structures with only bi-directional propagation such as directional coupler, waveguide taper and spot size converter.

3.1.4 HEAT Transport (HT)

Most foundry facilities now offer integrated on-chip micro-heaters that can be deposited over the waveguide structures in order to allow for thermo-optic tuning. In our experimental setup, we utilise electrical contact probes to inject current into these surface integrated (resistive) components that result in highly localised heating of the device, e.g. directly above a waveguide structure. This alters the effective index of the propagating modes, as will be explained in detail in chapter 4. The heat profile from the micro-heater to the waveguide (usually buried within a top cladding) can be modelled using the Lumerical HEAT Transport (HT) module. The simulation interface

allows the user to inject variable heating power (in Watts) at a defined position (according to the dimensions of the micro-heater) above the buried waveguide such that it acts as a uniform heat source. The temperature profile for each input power can be obtained by placing a temperature monitor around the waveguide. This profile is then imported in FDE solver where it converts the temperature grid to a variation of refractive index, depending on the material thermo-optic coefficient. This allows the user to simulate the change in effective index as a function of the injected power which can be useful, e.g. for calculating device sensitivity in nm/RIU or for determining phase shift as a function of heating power.

3.1.5 Scattering Matrix Method (SMM)

Almost two decades ago, Yariv et al. proposed the first matrix models incorporating unidirectional coupling between bus and ring waveguides in a MRR structure [8]. SMM is a powerful mathematical modelling approach that can describe the behaviour of a guided wave in dielectric media (e.g. waveguides or fibres).

The configuration of a single MRR is shown in Figure 3.2 where $E(1,3)$ and $E(2,4)$ are the input and output electric fields, respectively. The input light can either be transmitted through the waveguide according to the value of its transmission coefficient “ t ” or coupled to the adjacent ring structure corresponding to the value of its coupling coefficient “ κ ”. All losses (scattering and propagation) in the MRR are incorporated in the loss factor “ α ” [9].

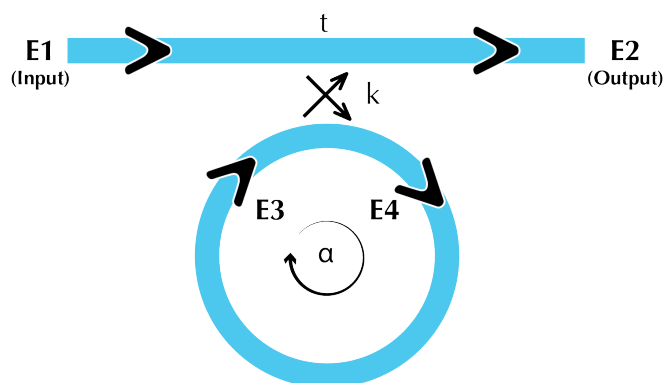


Figure 3.2 Components for the theoretical description of coupling of light to a single MRR

The propagation of the guided light in a single MRR can be described, in SMM form, according to [8, 10]:

$$\begin{vmatrix} E2 \\ E4 \end{vmatrix} = \begin{vmatrix} t & i\kappa \\ i\kappa & t \end{vmatrix} \begin{vmatrix} E1 \\ E3 \end{vmatrix} \quad (3.1)$$

With the aid of power conservation, the relation between the coupling and transmission coefficients is defined as [10]:

$$\kappa^2 + t^2 = 1 \quad (3.2)$$

Normalising all fields to E1, transmission within the ring, E3 can be written:

$$E3 = \alpha e^{i\theta} E4 \quad (3.3)$$

Where, the loss factor α is a real number between 0 and 1 where so-called ‘lossless’ propagation determined with $\alpha = 1$ and 100% loss represented by equating α to zero. The phase delay around the ring (θ) is described by:

$$\theta = \frac{2\pi n_{eff}}{\lambda} \times 2\pi R \quad (3.4)$$

Where, n_{eff} is the mode effective index, R is the radius of the ring and λ is the input wavelength of light. The output field, after passing the ring resonator, is given as:

$$E2 = E1 \frac{t - \alpha e^{i\theta}}{1 - t\alpha e^{i\theta}} \quad (3.5)$$

The power transmission output from the ring is given by:

$$T = \left| \frac{E2}{E1} \right|^2 = \left| \frac{t - \alpha e^{i\theta}}{1 - t\alpha e^{i\theta}} \right|^2 \quad (3.6)$$

Critical coupling occurs when $|t| = \alpha$, leading to $T = 0$ at resonance. This condition indicates that all the power goes into the ring and is stored there until dissipated by the

loss. The spectrum, loss factor and transmission coefficient for any single ring resonator can be determined using this simple model.

3.2 Physical Layout

After optimising the photonic devices at both component and system level, they must all be combined and constructed schematically in a specified area (and, where appropriate, layers) using a layout editor software in order to submit the chip design to the semiconductor fabrication facility. The free open-source software “K-Layout” was used to graphically design the optical chip [11]. The dimensions of the drawn structures (mainly, the minimum width) and minimum separation between them must comply with the design rules which are provided by the semiconductor foundry through their process design kit (PDK). The PDK includes a documentation set describing the key information regarding the fabrication process, boundaries of the design area, layer names, optical standard devices (e.g. grating couplers), etc. Once the chip layout is complete, the design rule check (DRC) step, which is embedded in K-layout, is performed. The DRC detects any design errors prior to sending the layout to the foundry. Usually, the designs are required to be submitted in Graphic Design System (GDS) format. During the course of this research, the CORNERSTONE rapid prototyping foundry at Southampton University was utilised to fabricate our devices via a multi-project wafer (MPW) service [12]. A GDS template file was provided by CORNERSTONE foundry which consists of layer names, standard devices and chip boundaries.

3.3 Fabrication Process

The SOI photonic chips were fabricated using high-resolution UV photo- or electron beam (e-beam) lithography. The sample fabrication process flow was provided by the CORNERSTONE [12] according to the different MPW runs usually defined by the fixed etch depth of the top silicon waveguide layer and the SiO₂ BOX. The depths for all of the devices described in this work are 220nm for silicon waveguides and 2µm for the BOX. The 220nm is the thinnest commercial SOI platform, although further reduction of this top silicon layer can enhance the device sensitivity as explained in

section 2.2 and in Figure 2.4 (a). CORNERSTONE offered three silicon etches for the 220nm platform [12]:

- 1- Shallow etch of $70\text{nm} \pm 10\text{nm}$, typically used for grating couplers.
- 2- Intermediate etch of $120\text{nm} \pm 10\text{nm}$.
- 3- Additional etch of 100nm to the BOX layer.

The strip waveguides with 220nm depth are formed by utilising the intermediate and the additional etch. After forming the waveguides, a top SiO_2 cladding with a thickness of $1\mu\text{m} \pm 100\text{nm}$ can be deposited over the waveguides which allows for the later deposition of the metal layers for integrated micro-heaters. The first metal layer above the oxide cladding consists of thin (60nm thick) titanium nitride (TiN) heater filaments. The second layer is assigned for the heater contact pads which consist of 30nm of titanium (Ti) and 200nm of gold (Au). The Ti layer is deposited to improve the adhesion strength to the Au, which acts as the low resistivity conductive layer. The full detailed process flow is shown in Figure 3.3.

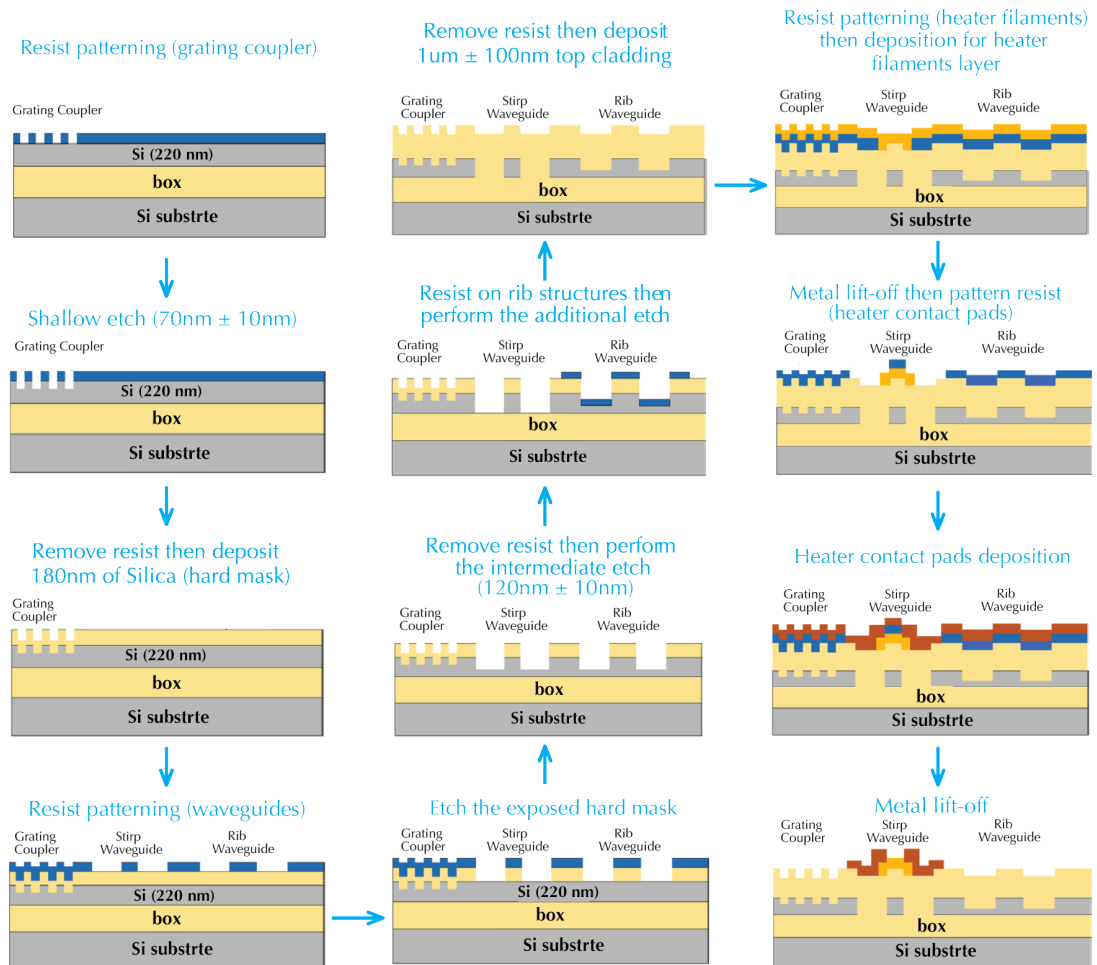


Figure 3.3 Illustration of the fabrication process which was performed by CORNER-STONE [12]

3.4 Optimisation of Passive Components

The basic photonic components (e.g. grating couplers, tapers and waveguides) were optimised using Lumerical. The performance of these components was tailored to fit our sensing applications.

3.4.1 Grating coupler

The grating couplers were used to couple light from single-mode fibre (SMF) to the SOI waveguides in all of our fabricated chips. Unlike the edge coupling techniques

(explained in chapter 2) which require further treatment (cleaving and polishing) of the sample edges, the grating couplers can be fabricated anywhere on the chip without the need for extremely precise alignment.

The focusing grating coupler configuration was utilised to harvest the quasi-TE fundamental mode and suppress the quasi-TM mode. The depiction of the grating coupler is shown in Figure 3.4 where the yellow cylindrical shape represents the fibre (not to scale) position above the grating. The red dashed line (x-axis) represents the guided mode propagation direction.

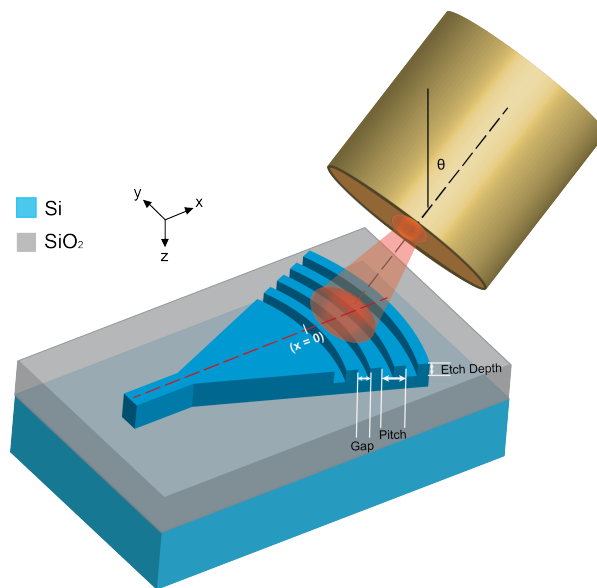


Figure 3.4 Schematic illustration of delivery (from a SMF) and coupling of light to the guided mode using a focusing grating coupler fabricated in SOI

The bandwidth and coupling efficiency between the optical fibre and grating coupler are highly sensitive to the grating design. In addition, the angle and position of the fibre can greatly affect the device spectrum. The optimisation was carried out by firstly running fast initial 2D FDTD simulations followed by a final optimisation using 3D FDTD. The goal of the optimisation is to maximise the coupling efficiency and bandwidth simultaneously. Since the etch depth (70nm) was fixed by the CORNERSTONE design rules [12], the 2D simulation sweeps were applied only on the gap and pitch of the grating coupler for various fibre positions and angles. The 3D FDTD was utilised to run a final optimisation only on the fibre position because it requires long simulation

times. Figure 3.5 (a and b) show that only small variations (few nanometres) on the grating pitch and gap can greatly affect the output spectrum of the 2D grating coupler. The pitch and gap parameters that maximise the coupling efficiency at the 1550nm wavelength were found to be 612nm and 306nm, respectively. In addition, the fibre position along the x-axis (red dashed line in Figure 3.4), and angle (θ) with respect to the vertical (z-axis), can also affect the coupling efficiency and bandwidth of the output spectrum, as shown in Figure 3.5 (c and d). The simulations showed that the efficiency can be optimised when the centre of the fibre is positioned at $x = 3.7\mu\text{m}$ and tilted by 6.96° from the vertical. Since the grating is symmetric with respect to the y-axis, the fibre position was kept at $y = 0$ during all the sweeps.

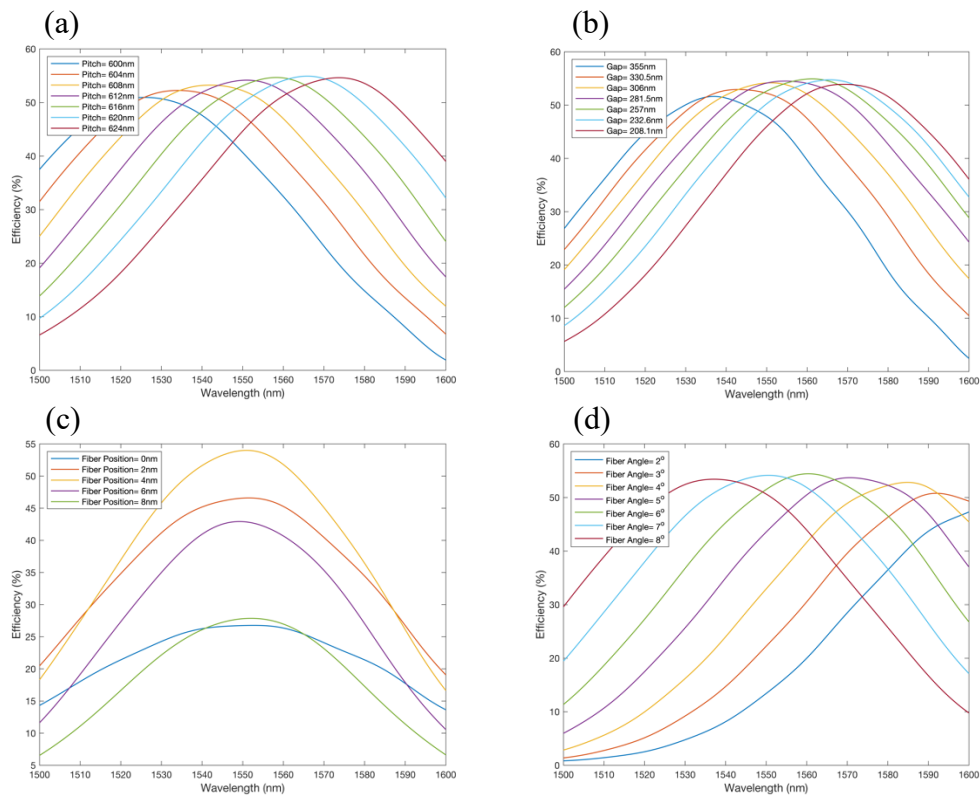


Figure 3.5 2D FDTD simulations of the coupling efficiency as a function of (a) grating pitch, (b) grating gap, (c) fibre position and (d) fibre rotation angle (θ)

The efficiency of the transmitted and reflected light can be described in terms of the scattering- (or S-) parameters of a two-port network:

$$\begin{pmatrix} S_{11} & S_{12} \\ S_{21} & S_{22} \end{pmatrix} \quad (3.7)$$

Where, S_{11} and S_{21} are the input reflection and transmission coefficients, respectively (i.e. for light coupled from the fibre to the grating) and S_{12} and S_{22} are the transmission and reflection coefficients in the reverse direction (i.e. for light coupled from the grating to the fibre). The S-parameters were obtained for the optimum design using 2D and 3D simulations with the former indicating a coupling efficiency of almost 55% at 1550nm (for both S_{12} and S_{21}) whereas almost negligible light (less than 5%) was reflected as indicated by S_{11} and S_{22} curves in Figure 3.6 (a). The coupling efficiencies, derived from the 3D FDTD simulations, showed a similar trend, as shown in Figure 3.6 (b). However, the S_{12} and S_{21} exhibit coupling efficiencies of nearly 40% at the centre wavelength. These relatively lower efficiencies (as compared to 2D results) were expected since only the fibre position was optimised in the 3D FDTD where all other design parameters were adapted from the 2D simulations.

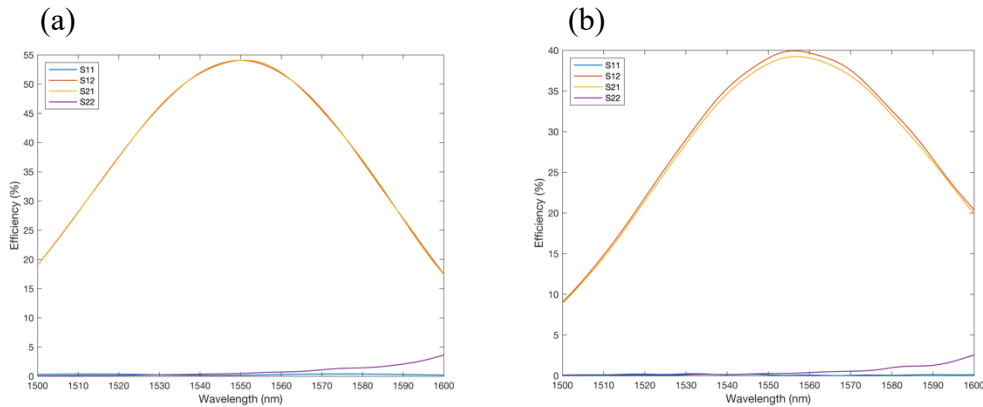


Figure 3.6 S-parameter of the optimised grating coupler design using (a) 2D FDTD and (b) 3D FDTD

The grating coupler design is shown in Figure 3.7 (a), where the blue area represents the tapered silicon waveguide with a height of 220nm and the red area represents the

periodic grating structure created in the top silicon layer using the shallow (70nm) etch. A plan view (x-y plane) of the simulated electric field distribution (3D FDTD), for coupling from fibre to grating (injection at $x = 3.4\mu\text{m}$), reveals the focussing effect of the grating, as shown in Figure 3.7 (b).

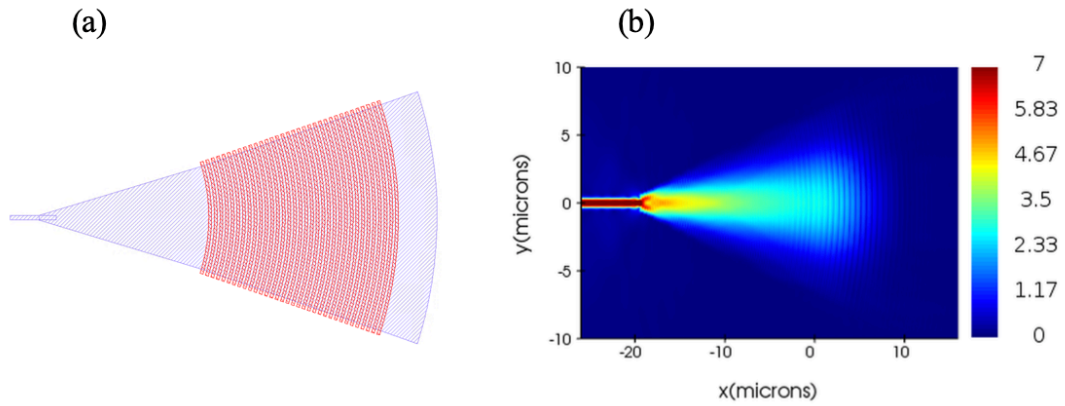


Figure 3.7 (a) 3D simulation of Electrical field distribution in the xy plane (b) snapshot of the depicted grating coupler

3.4.2 Waveguides

The waveguides described in this work were designed with a view to balancing propagation losses with penetration of the evanescent wave outside the waveguide core, for sensing purposes. Both design goals can be achieved in the same circuit with the help of the waveguide tapers. Since narrow waveguide widths lead to larger penetration depths of the evanescent wave (as illustrated in Figure 2.4 (a)), they were utilised in the regions where light-analyte interaction occurs (e.g. ring resonators). Losses were minimised in all other circuit regions by tapering up to slightly wider waveguide widths (achieving a higher mode confinement factor (Cf)), as illustrated in Figure 3.8. The effective indices (n_{eff}) and Cf of the fundamental mode at the wavelength of $1.55\mu\text{m}$ also shown for each of the waveguide widths in the same figure.

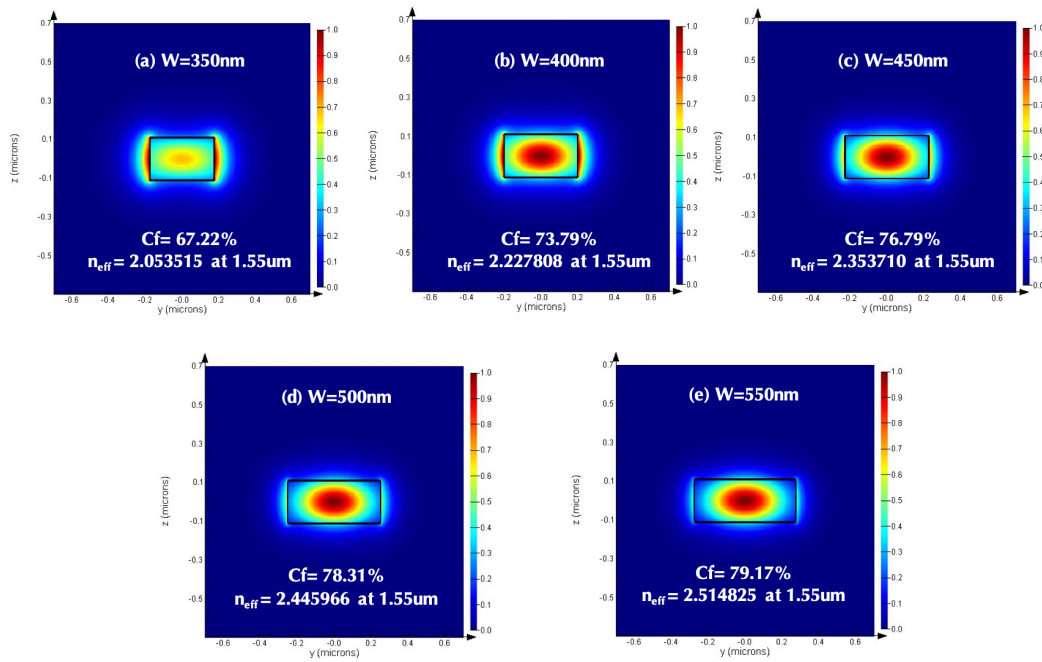


Figure 3.8 Mode profiles (including calculated Cf, n_{eff} values) for strip waveguides with different widths (a) W=350nm (b) W=400nm (c) W=450nm (d) W=500nm (e) W=550nm

The standard strip waveguide width of 500nm [13] was used as the low loss waveguide, tapering gradually to 350nm for the sensing regions of the device. The minimum taper length that ensures adiabatic transmission was acquired using the EME solver. Figure 3.9 shows the transmission efficiency as a function of the taper length when connecting a 500nm wide waveguide to the narrower waveguides with width of 350nm, 400nm and 450nm. This modelling revealed that just 8 μ m taper length was required in order to achieve near lossless transmission for all the aforementioned widths.

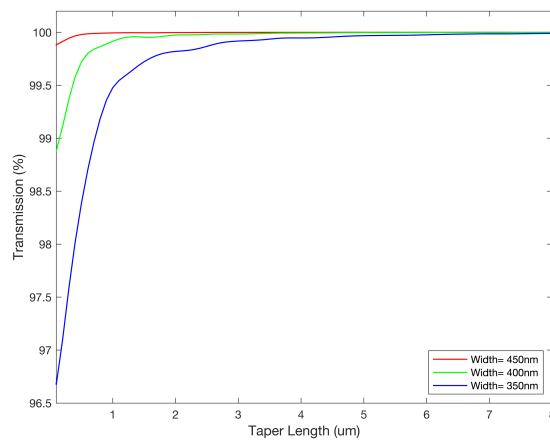


Figure 3.9 Transmission as a function of taper length for waveguides that have 500nm width tapered down to 350, 400 and 450nm

3.5 References

1. "Lumerical inc.". from <https://www.lumerical.com/products/>
2. "Comsol multiphysics." from <https://www.comsol.com>.
3. "Photon design ltd." from <https://www.photond.com>.
4. "Synopsys photonic solutions." from <https://www.synopsys.com/photonic-solutions/rsoft-photonic-device-tools/rsoft-products.html>.
5. "Matlab software." Retrieved 02 June 2020, from <https://mathworks.com/products/matlab>.
6. Das. (2012). *Optical communication*: BoD–Books on Demand.
7. "Lumerical support." Retrieved 30 May 2020, from <https://support.lumerical.com>.
8. Yariv. (2000). Universal relations for coupling of optical power between microresonators and dielectric waveguides. *36*(4), 321-322.
9. Rabus. (2007). *Integrated ring resonators*: Springer.
10. Rabus. (2007). Ring resonators: Theory and modeling. *Integrated Ring Resonators: The Compendium*, 3-40.
11. "Klayout layout viewer and editor." Retrieved 31 May 2020, from <https://www.klayout.de>.
12. "Cornerstone service." Retrieved 2 September 2019, from <http://www.cornerstone.sotonfab.co.uk/>.
13. Vivien, & Pavesi. (2016). *Handbook of silicon photonics*: Taylor & Francis.

4 Experimental Setup

4.1 Introduction

In this chapter, the photonic component design, layout of the overall photonic integrated circuit along with the experimental setup for the optical characterisation of, and vapour detection using, the fabricated devices are described. In addition, the transmission characteristics of the basic building blocks (e.g. ring resonator) are analysed.

4.2 Optical Setup and Experimental Procedure

Two experimental systems were used to characterise and analyse the performance of the fabricated devices: 1- gas sensing setup and 2- thermo-optic setup.

4.2.1 Gas Sensing Setup

The gas sensing setup was designed such that the PIC could be housed within a gas cell enabling real-time delivery of vapour phase volatile organic compounds (VOCs). This necessitates ‘free-space’ (rather than fibre optic) delivery and collection of laser light to the PIC, which was achieved using a bespoke arrangement of mirrors and focussing optics, as shown in Figure 4.1. An external light source (described in section 4.3) and a single-mode fibre were employed to generate and guide the laser beam to a 50:50 beam-splitter. The beam-splitter was tilted at an angle that reflects the light towards the chip at $\sim 7^\circ$ degrees from the vertical axis. Slightly off-normal operation reduces the back-reflection from the grating couplers [1] and shifts the peak wavelength spectral position to the desired location (as shown in the simulation results in section 3.4.1). A wide field of view, long working distance microscope objective (OCT scan) lens (LSM03-BB, Thorlabs, Inc.) [2] was used for both delivery and collection of light to the optical chip through a quartz window in the gas cell. The chip can be repositioned using a 3-axis stage in order to align the input grating coupler

beneath the laser spot. An infrared camera was used to image the position of the grating coupler during the alignment procedure. Light from the output grating couplers of the photonic devices is collected via the same OCT scan lens, a beam splitter and rotatable (alignment) mirror and a final beam splitter, allowing for both imaging (with the infrared camera) and focussing of the light onto a single-mode fibre coupled to a spectrometer. Once coarse alignment is achieved, fine positioning for maximum signal into the spectrometer is achieved by careful repositioning of the chip using the 3-axis stage.

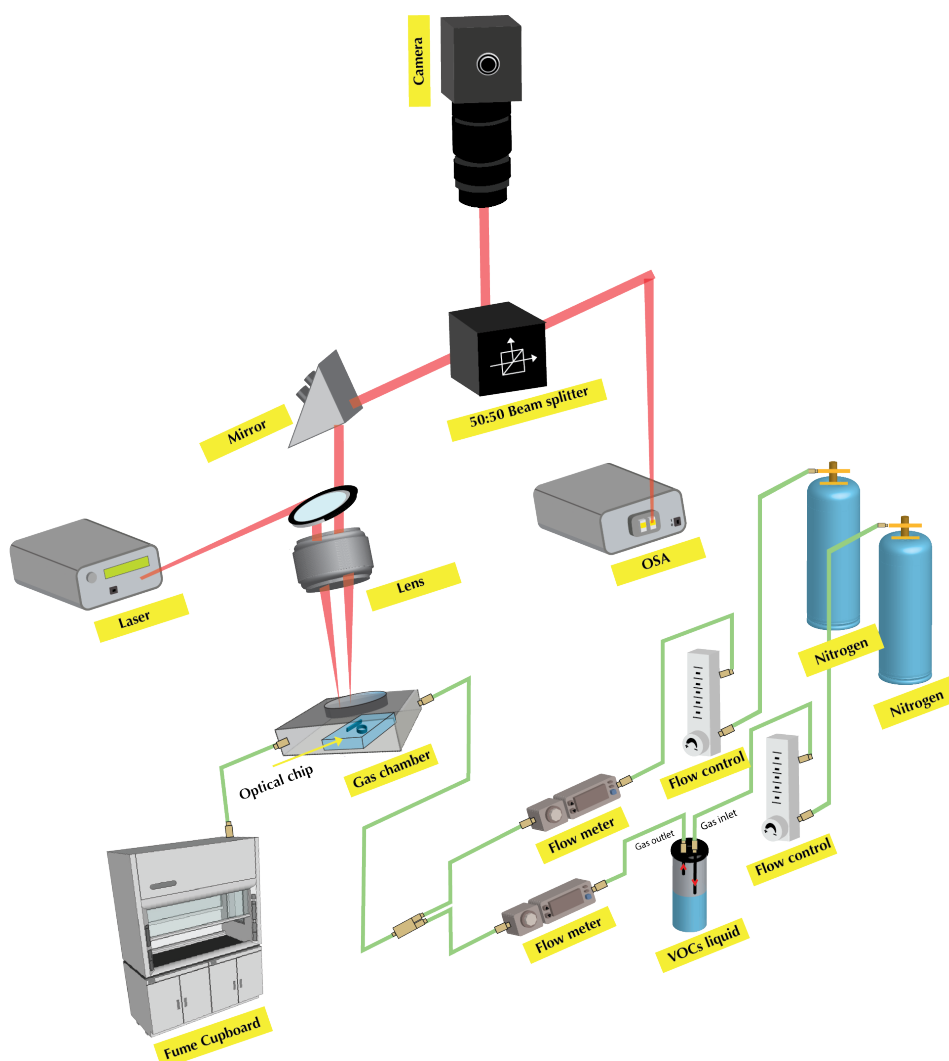


Figure 4.1 Optical delivery and collection of light to/from the photonic chip along with bespoke setup for gas/vapour delivery

The VOC vapour sensing was achieved by the careful delivery of a pure carrier gas (nitrogen, 99.998% purity) to the sealed gas cell using two separate N₂ cylinders. The flow rates from each cylinder were controlled using separate gas flow meters. One of the gas delivery lines is used to generate, control and carry VOC vapours to the gas cell. Solvent-based VOCs were evaporated at room temperature (20°C) in a vial that includes the N₂ inlet and vapour outlet tubes. The high vapour pressure of the VOCs and the adjustable pressure from the inlet tube produce a controllable vapour concentration above the surface of the liquid which can be picked up by the outlet tube. The flow rates from the outlet were monitored using a precise digital flow meter (model: SMC PFM710S-C4-B-W). The second gas flow line was used to dilute the vapour concentrations and for purging the gas cell before and after VOC delivery. This dilution flow is maintained and monitored using a separate digital flow meter (model: SMC PFM750S-C8-A-W). The vapour and dilution flow lines were combined just before entrance to the gas cell and the gas cell outlet was connected to a fume cupboard in order to exhaust hazardous gases.

4.2.2 Thermo-Optic Setup

The second setup (shown in Figure 4.2) has almost the same functionality as the gas sensing setup but with the addition of two electrical probes which allow thermo-optic tuning via integrated on-chip microheaters. The tips of the electrical probes can be brought into contact with microheaters using a 3-axis stage. The first probe is connected to the negative (-) or common terminal of the power supply (THURLBY 30V-2A, RS Components Ltd.) [3] and the second probe is connected to the positive (+) terminal of the same power supply. A multi-meter was employed to continuity (i.e. no open circuit) between the on-chip contact pads. Before establishing the electrical connection, the input and output grating couplers were aligned (using the 3-axis stage) with the fibre-coupled laser source and spectrometer. High precision alignment of the probes was achieved using a combination of zoom lens (with magnification range 2x to 24.5x) from a working distance of 86mm (models: 1-50486, 1-62831, 1-6270 and 1-6010, Navitar, Inc.) [4] and an extended range (400-1700nm) infrared camera

(model: OW1.7-VS-CL-LP-640, Raptor Photonics Ltd.) [5]. The combination of camera and zoom lens permit the imaging of the chip and observation of scattered near-IR light inside the waveguides for improved alignment.

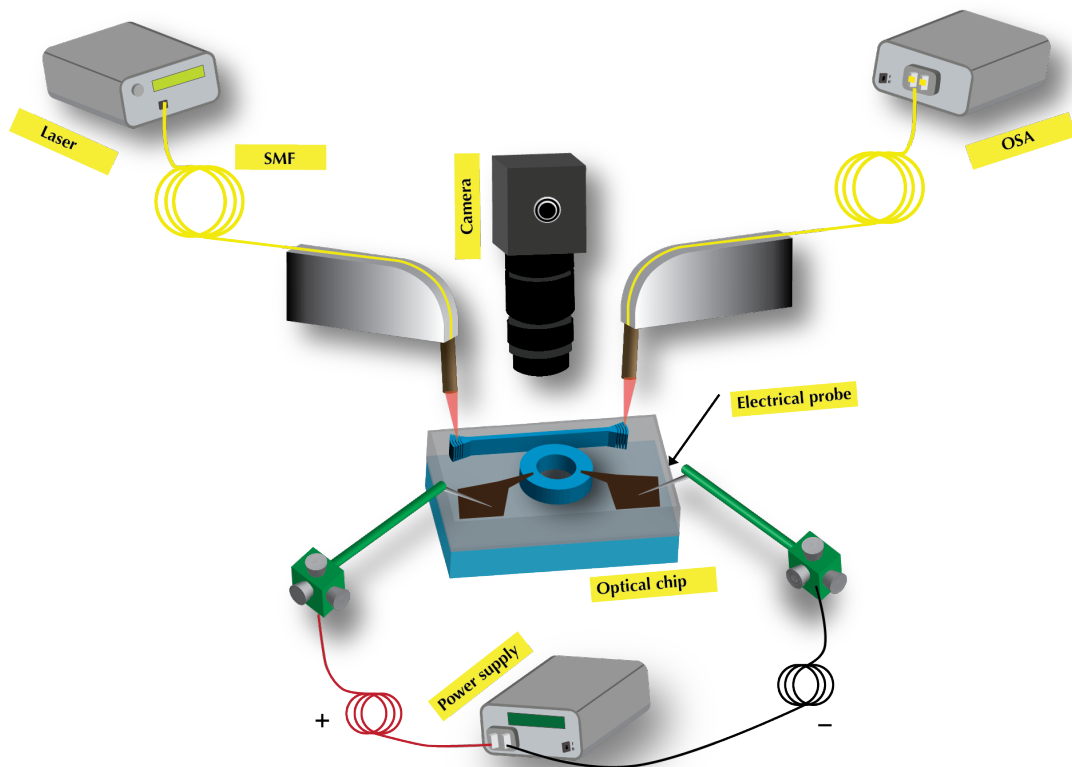


Figure 4.2 Thermo-optic sensing and imaging setup

This setup allows the user to study the resonant peak shift of MRR and MZI type devices as a function of the injected power (or current) due to the thermo-optic changes in the refractive index.

4.3 Optical Measurement Components

The gas sensing and thermo-optic setups are both equipped with single-mode fibres at their input and output which makes them compatible with the same external laser sources and spectrometer. Since both laser source and spectrometer play a critical role in determining the optical response of our fabricated devices, their capabilities and limitations will be described in details in the next subsections.

4.3.1 Input Light Sources

Two external light sources were utilised in this research. The first one is a broadband superluminescent diode (SLD) which was extensively used for many of the characterisation measurements described in this thesis. The second source is a tuneable laser which was employed in cases that required narrow-linewidths, as will be shown in chapter 7.

4.3.1.1 Superluminescent Diode (SLD)

The Superluminescent Diode (model: S5FC1005S Single-mode, Thorlabs, Inc.) [6] was used as a source of broadband infrared light. This light source is an indium phosphide (InP)-based device that incorporates an integrated thermoelectric cooler (TEC) to stabilise the operating temperature between 15 and 35 °C. SLD output is determined through user control of the TEC temperature and operating current of the SLD. With the SLD operated at its maximum current and power (600mA, 22mW) and at ambient temperature (25 °C), the spectral profile of the SLD is near-Gaussian with centre wavelength of 1550nm and optical (3dB) bandwidth of 50nm, as shown in Figure 4.3.

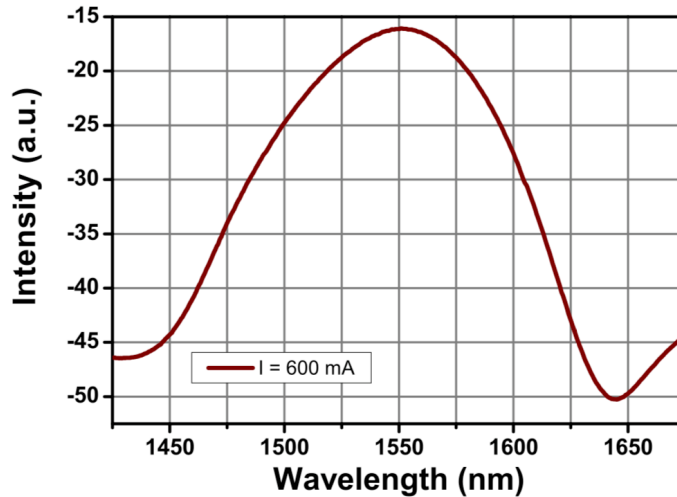


Figure 4.3 The output spectrum of the fibre coupled superluminescent diode (model: S5FC1005S Single-mode, Thorlabs, Inc.) with an operating current of 600 mA [6]

4.3.1.2 Tuneable Laser

The tuneable laser (model: TLK-L1550M, Thorlabs, Inc.) [7] is also coupled to a single-mode fibre (SMF) with a centre wavelength of 1550 nm but offers slightly higher and tuneable output power (35mW). This external cavity laser (ECL) features a half-butterfly gain chip (model: SAF1176S, Thorlabs, Inc.) and is based on a Littman configuration [8] with a fixed grating angle and an adjustable mirror, as shown in Figure 4.4. The light emitted from the gain element is first collimated using a collimating lens. Then a fixed grating is used to diffract the incident light to a rotatable mirror which reflects the beam back to the grating again. Since the beam experiences diffraction twice before coupling back into the gain element, the output linewidth is typically narrow (for this particular model, equal to 100 kHz). An external controller was also used for the laser diode and TEC (model: ITC4000, Thorlabs, Inc.). The 10-dB wavelength tuning range for this device is 120nm, as shown in Figure 4.5, with a tuning resolution of 3pm.

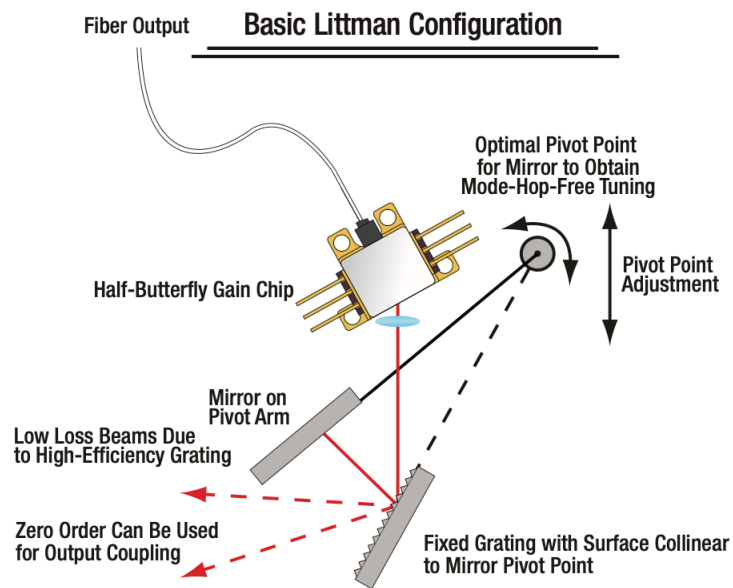


Figure 4.4 Schematic of a Littman configuration ECL showing the gain chip, collimating lens, diffraction grating, rotatable mirror and fibre output [7].

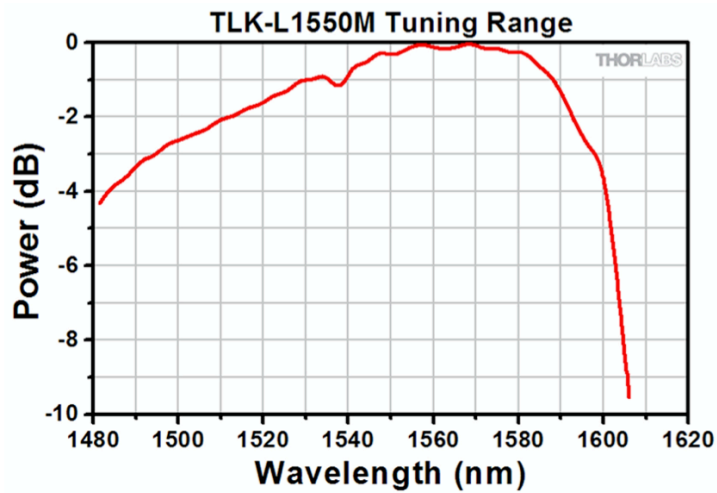


Figure 4.5 The tuning range of the fibre coupled tuneable laser (model: TLK-L1550M, Thorlabs, Inc.) [7]

4.3.2 Spectrum Analyser

The Optical Spectrum Analyser (model: OSA203B, Thorlabs, Inc.) was used to analyse the transmission spectra from the devices described in this thesis. The OSA operates in the range of 1.0 – 2.6 μm and offers variable spectral resolution and sensitivity. As the resolution and sensitivity increase, the data acquisition time also increases, as shown in Table 4.1. The ability to control the acquisition time is very helpful since fast spectrum updates are required in real-time sensing measurements, while accurate results are important in standard (non-dynamic) measurements.

Table 4.1 Spectrum update times for variable sensitivity and resolution

Time Between Updates		
Sensitivity	Low Resolution	High Resolution
Low	0.5 seconds	1.8 seconds
Medium Low	0.8 seconds	2.9 seconds
Medium High	1.5 seconds	5.2 seconds
High	2.7 seconds	9.5 seconds

The resolution is a function of wavelength in which it improves with decreasing the wavelength, as shown in Figure 4.6. The maximum sensitivity is -70 dBm/nm, whereas the highest resolution at 1550nm is around 60pm [9]. This OSA features fibre-coupled input that is compatible with the aforementioned optical setups. The OSA is connected to a Windows laptop via USB 2.0 in order to transfer the optical spectrum to the provided OSA software.

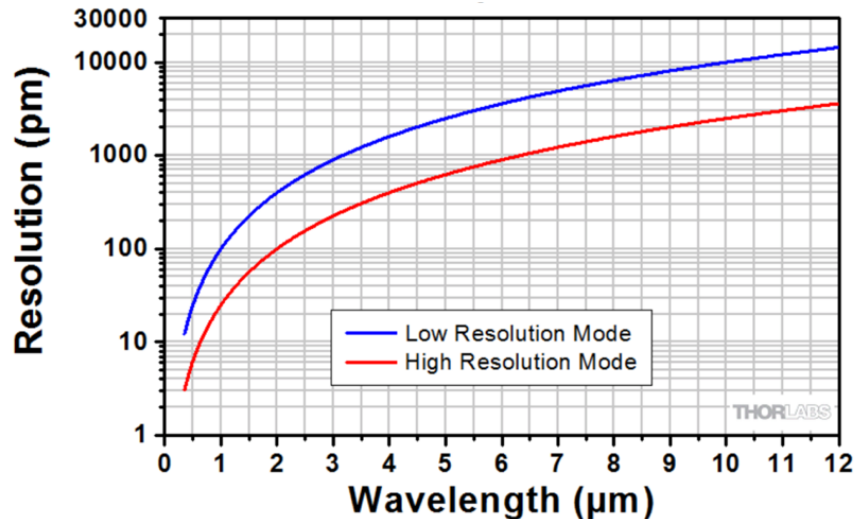


Figure 4.6 The spectral resolution of the Thorlabs Optical Spectrum Analyser OSA 203B [9]

4.4 Chip Layout Design

All the designed and fabricated devices described here are based on silicon on insulator (SOI) waveguides with grating couplers designed to couple input/output light with a central wavelength of 1550nm. Microring resonators were used as the basic building blocks due to their capacity for a variety of functions and applications. Three different chips were used to investigate different devices.

The first chip consists of rib waveguide-based slotted ring resonator configuration, the design for which was adapted from that originally developed by a former PhD student in our group [10]. The rib waveguide structures were designed for TE operation, with a rib height of 130nm on a slab of 90nm thickness giving a total waveguide height of 220nm, as shown in Figure 4.7 (a). The silicon guiding layer is fabricated on top of a 2000nm buried oxide (BOX) layer. This chip will be referred to as rib waveguide-based chip.

The second (hereinafter referred to as MPW#6) and third chip (referred to as MPW#10) were designed by the author and fabricated by CORNERSTONE rapid prototyping foundry at the University of Southampton [11]. They include numerous devices that are all strip waveguide-based structures with waveguide depth of 220nm, as

shown in Figure 4.7 (b). Although slotted ring resonator configurations are an attractive design for many applications, only conventional ring resonator structures were considered for all devices in these latter two chips. This is because slotted waveguides require either narrow slot widths or narrow waveguide widths in order to confine the light in the slot, the requirement for which could not be met under the MPW rapid prototyping rules offered by CORNERSTONE. The designed devices include single, eye-like, pulley-type, dual-ring-assisted Mach–Zehnder and multiple serial and parallel coupled ring resonators. A select number of these devices were investigated in detail, while many are beyond the scope of this thesis but provide for future research work in this area.

All ring resonators were designed with 25 or 50 μm radius with various coupling gaps to ensure some exhibit critical coupling (i.e. no light passes through the bus waveguide at the resonant wavelength due to the complete destructive interference between the transmitted fields in the bus waveguide and cavity). Each design was fabricated twice on the same chip. One is containing a 1- μm silica top cladding with integrated metallic heater contacts, while the other has an etched top cladding in order to allow gas/liquid sensing. The etching process was done using hydrofluoric acid (HF) for the rib waveguide-based chip. Strip waveguide-based devices require extra care during the cladding etch because HF might continue to etch into the BOX layer as well, culminating in inadvertent lift-off the strip waveguides. Therefore, dry plasma etching, followed by HF etching of the last 50nm was performed for chips containing strip waveguide structures. The optical chip layouts are illustrated in Figure 4.8, where the different schematic colours represent the different material and etch layers.

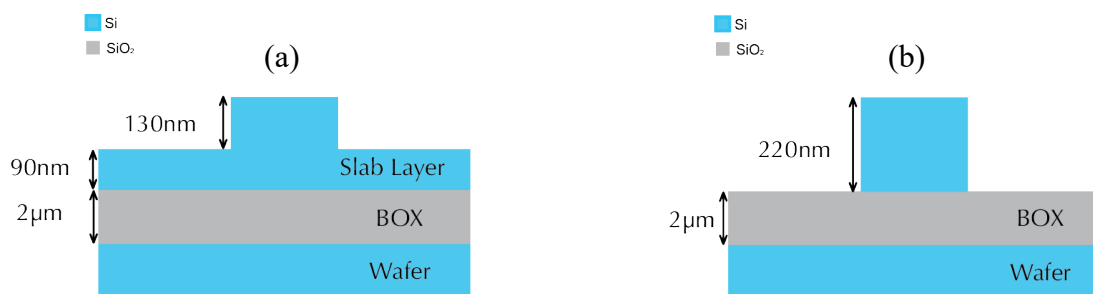


Figure 4.7 The chip dimensions for (a) rib waveguide-based chip (b) MPW#6 and MPW#10

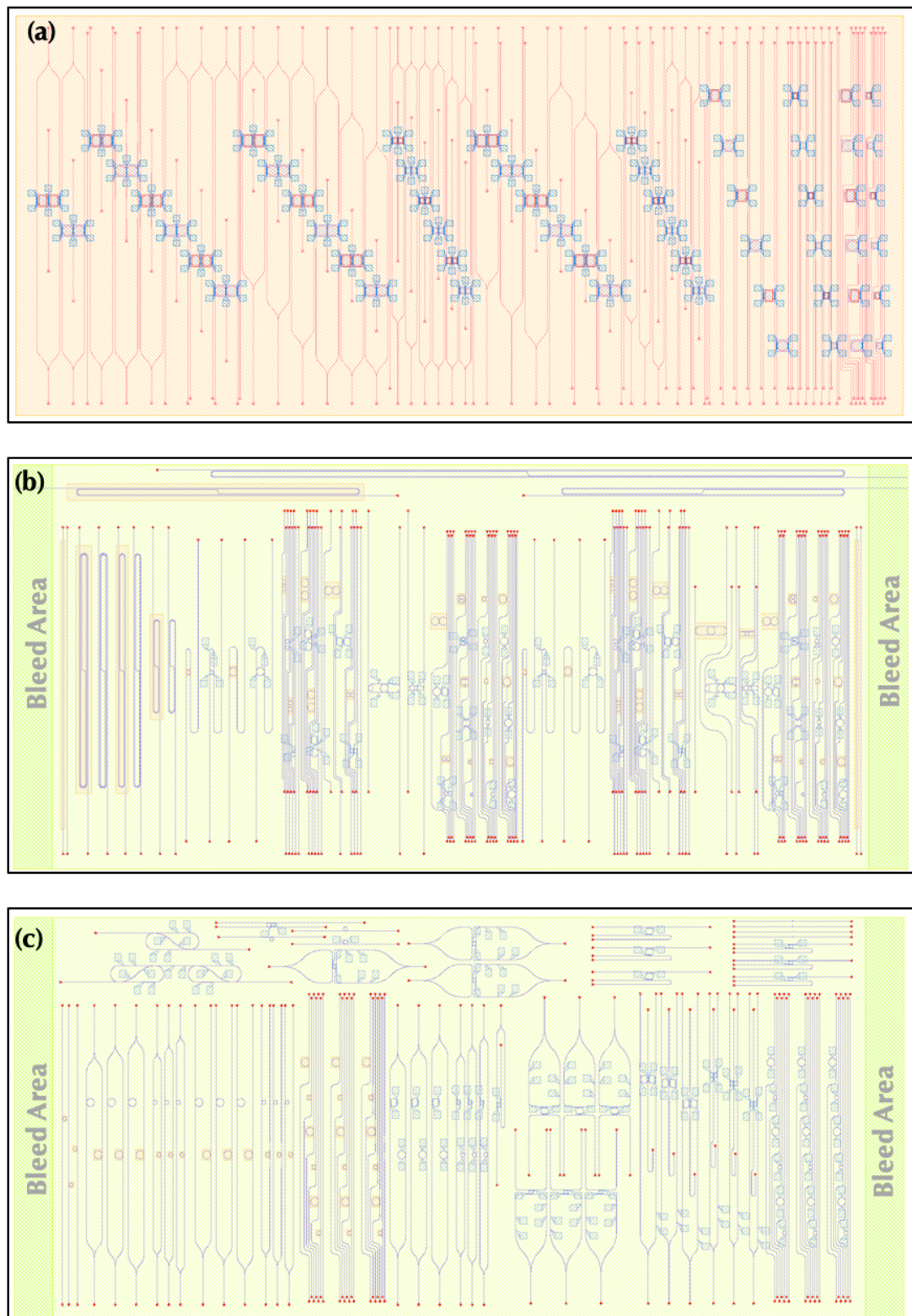


Figure 4.8 Snapshot images from GDS files for the chip layout (a) slotted micro-ring resonator (b) MPW#6 (c) MPW#10

4.5 Spectral Analysis

After aligning the grating couplers with the input and output fibres (from the light source and to the spectrometer), the transmission spectra were collected. When performing real-time measurements, the spectrometer was programmed to continuously save a specific wavelength range of the output transmission spectra in a target folder (directory) until terminated by the user. The scan sensitivity and resolution of the spectrometer were set to “medium-low” and “high”, respectively providing a good balance for speed and accuracy. As a result, the spectrum updates rapidly (every ~ 3 seconds), as illustrated in Table 4.1. This permits monitoring of transient changes (in e.g. resonant wavelengths, intensity etc.) that happen during a particular experiment (e.g. flowing gases/vapours with different concentrations). On the other hand, high sensitivity and resolution settings were used with all other standard measurements in order to collect the most accurate data-sets. In addition, five accumulations (spectral averaging) was used to reduce the random noise level. Figure 4.9 shows a standard measurement of micro-ring resonator having a radius (R), waveguide width (W) and gap (G) of $25\mu\text{m}$, 450nm and 300nm , respectively.

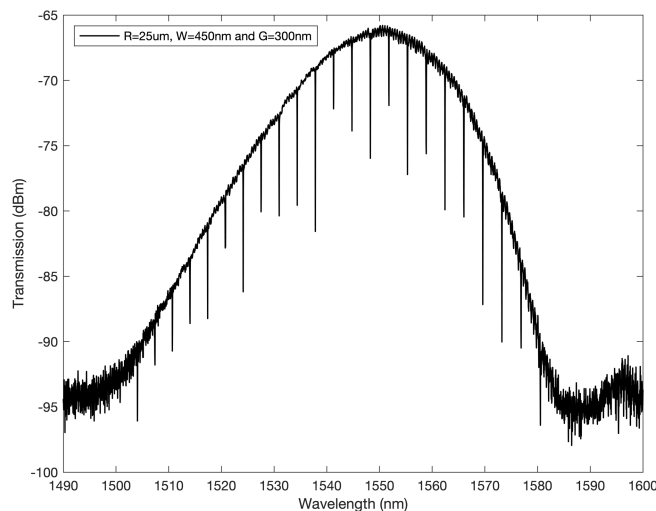


Figure 4.9 Typical (raw) transmission spectrum of a micro-ring resonator

4.5.1 ‘Cleaning’ of Raw Data

All acquired raw spectra had a near-Gaussian optical spectrum with restricted spectral bandwidth. This can be attributed to the limited bandwidth of either the SLD light source or the designed grating couplers. In order to investigate this further, the optical spectrum of the fibre-coupled SLD source was collected by connecting it directly to the spectrometer. This was compared with the output transmission of a ring resonator which was obtained by aligning the same SLD source and spectrometer with input and output gratings. Figure 4.10 shows that SLD raw spectrum (black curve) has a wider bandwidth as compared to the microring resonator output (red curve). This indicates that the grating couplers are the main factor that controls the spectral line shape of our transmitted spectra. Here the noise level for the SLD spectrum is higher than the MRR because no spectral averaging was used for the SLD data whereas five spectra (averaged) were used to produce the MRR spectrum as mentioned in the previous section. Losses associated with the coupling of light into/out of the device are described in section 3.4.1.

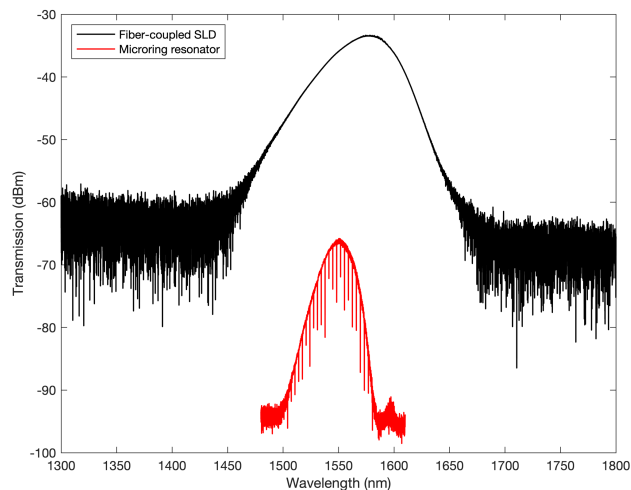


Figure 4.10 SLD fibre output and MRR device transmission spectra

The transmission spectral data was processed, for comparative analysis of the MRR resonant peak depth/extinction ratio (ER), by removal of the background Gaussian spectral shape via polynomial fit to the raw data, using a code written in Matlab

R2019b [12]. This curve flattening process does not affect the properties (e.g. wavelength position, Q-factor and ER) of the MRR individual notches. The curve fitting code is written in Listing 4.7.1 in section 4.7. In Figure 4.11, the raw transmission data (red curve) is plotted together with the processed (Gaussian removed) data (black curve).

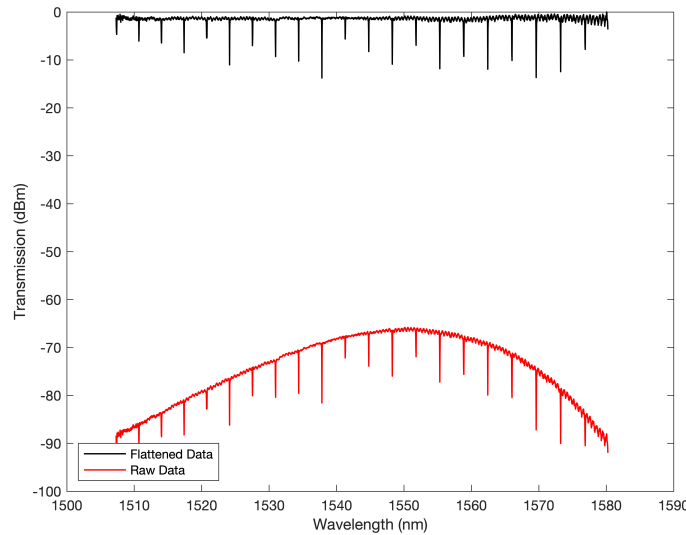


Figure 4.11 Comparison of MRR raw transmission (red) and processed (Gaussian subtracted) data

4.6 Characterisation of Single MRR Devices

This section aims to investigate the effect of waveguide widths (W) and bus-to-ring coupling gaps (G) on the performance (Q-factor and ER) of single MRR devices. Eighteen strip waveguide-based single MRRs were fabricated under CORNERSTONE MPW#10 with various W , G combinations to determine the optimum device characteristics. For W : 400, 450 and 500nm, each MRR was designed with $G = 200, 250$ and 300nm. Two sets of these nine MRR devices were fabricated; one with a top silica cladding completely covering the whole chip and the other with etched windows (i.e. air cladding) over the MRR structures. This latter design enables access to the MRRs for, i.e. integration of graphene Oxide (GO) for vapour sensing experiments,

described in the following chapter. All MRRs were designed with a mean radius of $25\mu\text{m}$ to the centre of the waveguide. The dimensions of the etched windows are $50\mu\text{m}$ by $70\mu\text{m}$ over the ring waveguide, as shown in the GDS file image in Figure 4.12 (orange area reveals the position of the etched window relative to the ring structure).

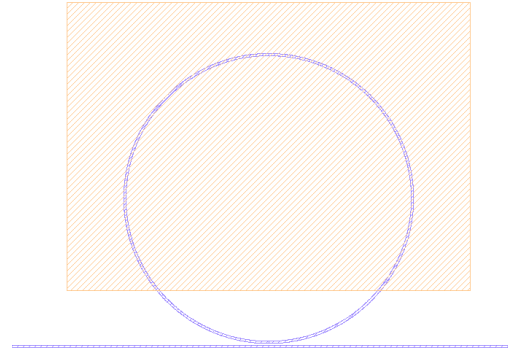


Figure 4.12 Snapshot from the MPW#10 GDS file for ring with radius = $25\mu\text{m}$, $W = 400\text{nm}$ and $G = 300\text{nm}$

The processed transmission spectra for all eighteen MRR devices are plotted in Figure 4.13 to Figure 4.15. The red, green and blue transmission curves correspond to devices with separation gap of 200, 250 and 300nm.

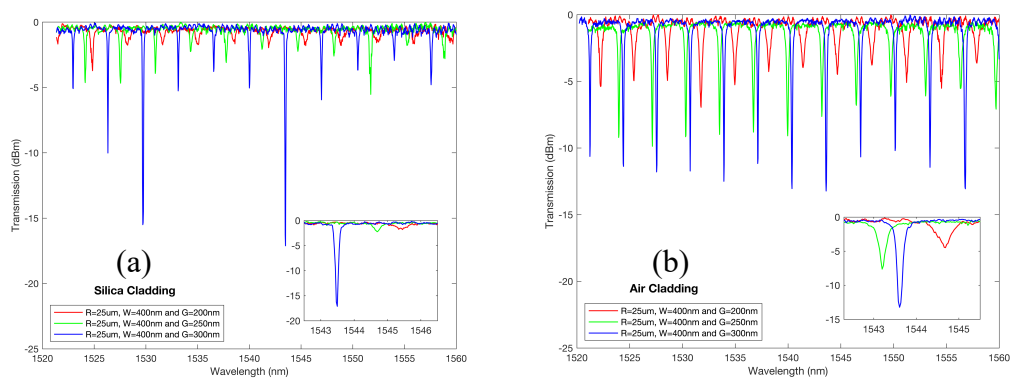


Figure 4.13 Transmission spectra (with single resonances in the insets) for $R = 25\mu\text{m}$, $W = 400\text{nm}$ and $G = 200, 250$ and 300nm for (a) silica and (b) air cladding MRRs

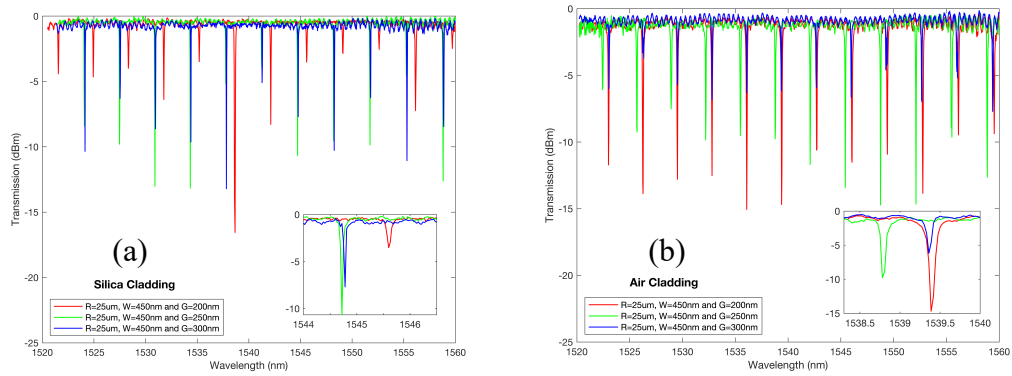


Figure 4.14 Transmission spectra (with single resonances in the insets) for $R = 25\mu\text{m}$, $W = 450\text{nm}$ and $G = 200, 250$ and 300nm for (a) silica and (b) air cladding MRRs

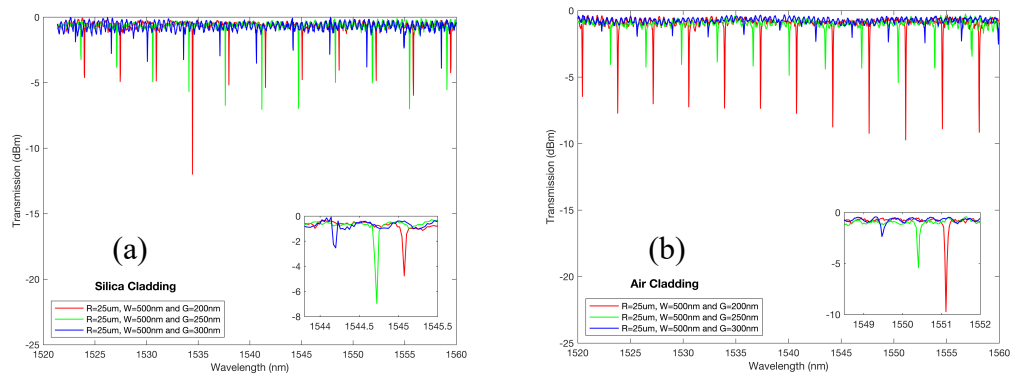


Figure 4.15 Transmission spectra (with single resonances in the insets) for $R = 25\mu\text{m}$, $W = 500\text{nm}$ and $G = 200, 250$ and 300nm for (a) silica and (b) air cladding MRRs

4.6.1 Q-Factor and Extinction Ratio (ER) Analysis

In order to obtain reliable values of Q-factor and ER, all resonance peaks were fit with a Lorentzian line-shape function [13]:

$$L(\lambda) = y_0 + \frac{2A(FWHM)}{\pi [4(\lambda - \lambda_{\text{res}})^2 + FWHM^2]} \quad (4.1)$$

Where, y_0 is the baseline of the peak (offset), A is the area under the peak, $FWHM$ represents the full width at half maximum of the peak and λ_{res} is the centre wavelength of the peak. The Q-factor and ER were calculated for each peak using the below equations:

$$Q\text{-factor} = \frac{\lambda_{res}}{FWHM} \quad (4.2)$$

$$ER = -\left(y_0 + \frac{2A}{FWHM \times \pi}\right) \quad (4.3)$$

The fitting process was automated using Matlab code, as shown in Listing 4.7.2. Any peaks that were not well fit (i.e. not converged) to the experimental data were neglected during the calculation of the average values. An example of the fitting is shown in Figure 4.16 for a silica cladding MRR with $W=500\text{nm}$ and $G=300\text{nm}$. The average Q-factor and ER results for all MRRs are shown in Figure 4.17 and Figure 4.18, respectively. For each device, the vertical error bars represent the standard deviation of the analysed peaks in the whole spectrum.

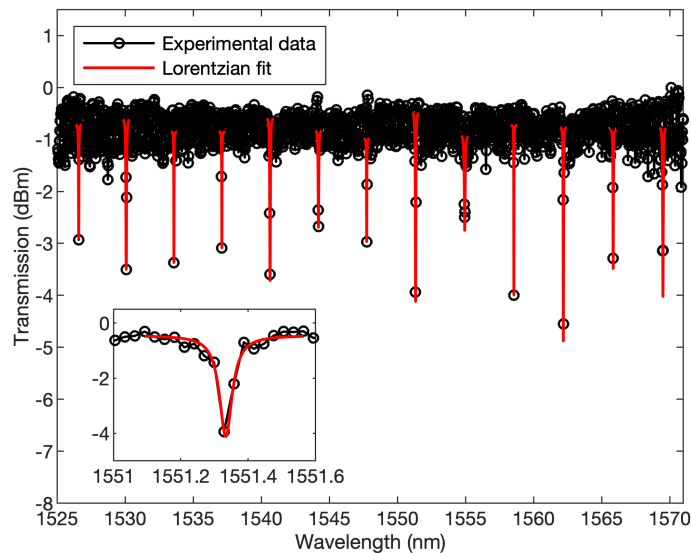


Figure 4.16 Experimental spectrum fit with Lorentzian line-shape function showing a single resonance (inset)

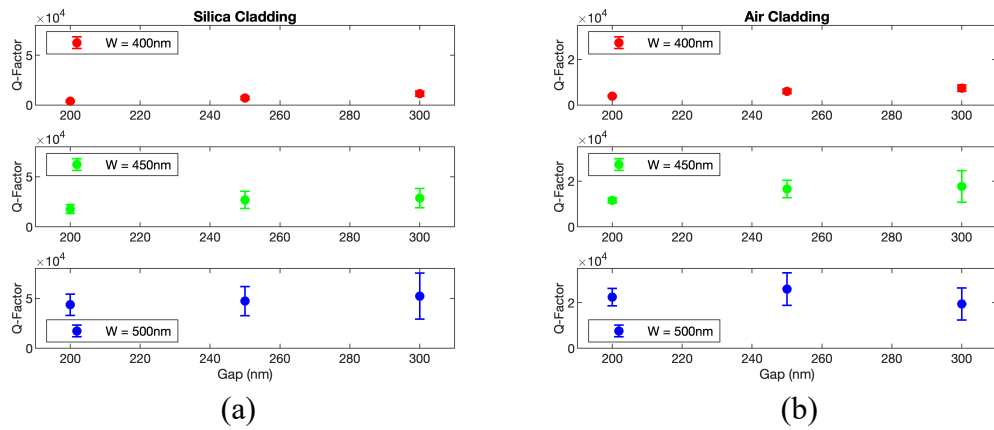


Figure 4.17 Average Q-factor for (a) silica and (b) air clad MRRs

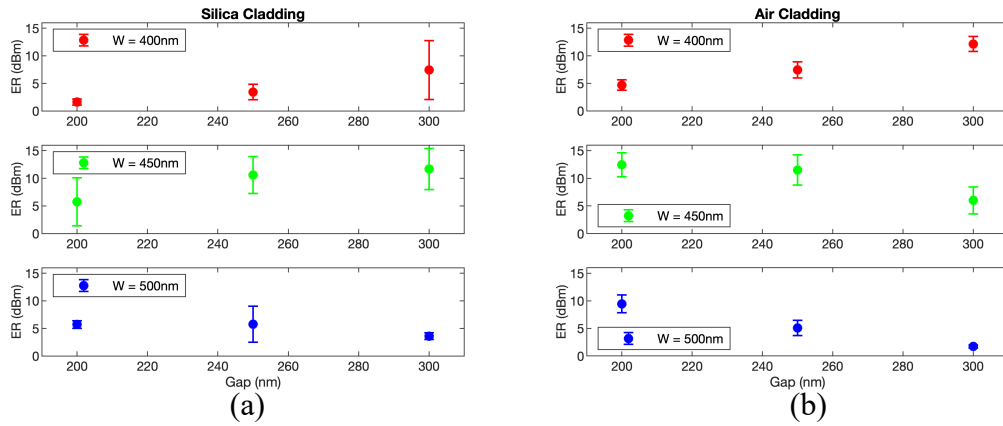


Figure 4.18 Average extinction ratio (ER) for (a) silica and (b) air clad MRRs

The Q-factor increases with both W and G for both silica and air clad devices for almost all MRRs. Theoretically, air clad devices have higher index contrast as compared to the silica clad counterparts, leading to stronger light confinement. However, the fabricated air clad devices exhibit lower Q-factors, which is likely attributable to the surface roughness caused by the dry etching [14]. The ER (or peak depth) reflects the relationship between the transmission coefficient (t) or coupling coefficient (κ) and the overall cavity loss (α) where the highest ER is achieved for ‘critical coupling’ (when $t = \alpha$) [15]. A more detailed analysis of coupling and loss coefficients is described in the next subsection.

For each device structure with a specific waveguide W , there is an optimum G that can achieve critical coupling. Figure 4.18 shows that waveguides with $W = 400\text{nm}$ can achieve near critical coupling condition with relatively large $G (= 300\text{nm})$, which does not require sophisticated fabrication facilities, whereas for $W = 500\text{nm}$, a much smaller $G (< 200\text{nm})$ is required to achieve similar ER. Alternatively, the ER can be enhanced by increasing the bus-to-ring coupling efficiency. This can be achieved by increasing the coupling length, for instance by using racetrack resonators. Another design that offers longer coupling lengths for circular resonators is the pulley-type coupling structures, where the bus waveguide is partially wrapped around the ring, as shown in Figure 4.19 (a). This type of structure, with $W = 500\text{nm}$ and $G = 300\text{nm}$, was fabricated in MPW#6 with silica cladding. This design achieved an average ER = 5.78 dBm and Q-factor = 7.8×10^4 . This represents a near 65% enhancement of ER and 50% increase of Q-factor, compared with an identical device (i.e. same radius, width and gap) but with single point coupling. The transmission spectrum for the pulley-type device is shown in Figure 4.19 (b).

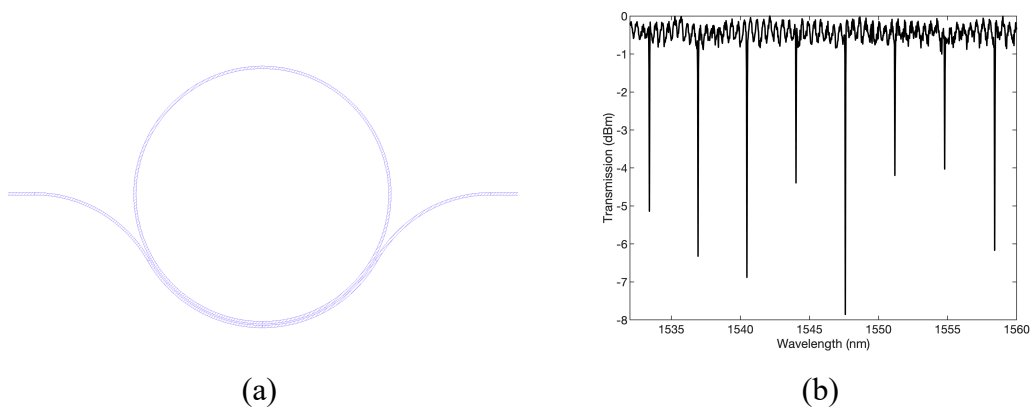


Figure 4.19 (a) GDS image and (b) transmission spectrum of the MRR with pulley coupling structure

4.6.2 Extraction of Losses and Coupling Coefficients

The MRR performance is typically determined by three quantities:

- 1- The transmission coefficient (t)
- 2- The coupling coefficient (κ)
- 3- The loss factor (α)

The transmission coefficient (t) determines the amount of transmitted light through a bus waveguide, whereas the coupling coefficient (κ) specifies the fraction of the coupled light into the ring resonator. The loss factor (α), which includes both transmission and scattering losses, determines the amount of light remaining after a complete round trip of the ring. Extraction of these coefficients is achieved by first calculating the free spectral range (FSR), the full width at half maximum (FWHM) and extinction ratio (ER) for each resonance [16]. The FSR is calculated by measuring the separation wavelength(s) between adjacent resonant peaks (assuming near zero dispersion across relatively small wavelength ranges), then determining the average. The FWHM and ER were directly obtained from the Lorentzian fitting. The loss factor and transmission coefficient can be estimated using the following equations [16]:

$$A = \left(\frac{\cos(\pi/F)}{1 + \sin(\pi/F)} \right) \quad (4.4)$$

$$B = 1 - \left[\frac{1 - \cos(\pi/F)}{1 + \cos(\pi/F)} \right] \frac{1}{ER} \quad (4.5)$$

$$(\alpha, t) = \left(\frac{A}{B} \right)^{1/2} \pm \left(\frac{A}{B} - A \right)^{1/2} \quad (4.6)$$

Where, F is the finesse ($F=FSR/FWHM$). The values of α and t are interchangeable in Equation (4.6). In order to distinguish between α and t , they are plotted against a wide range of wavelengths. The transmission coefficient tends to exhibit a much stronger wavelength dependence (across relatively small spectral ranges), compared with the

loss coefficient [16, 17] and so they may be distinguished. Figure 4.20 illustrates the dependence of α and t on wavelength for a single ring resonator with $R = 50\mu\text{m}$, $W = 450\text{nm}$ and $G = 200\text{nm}$.

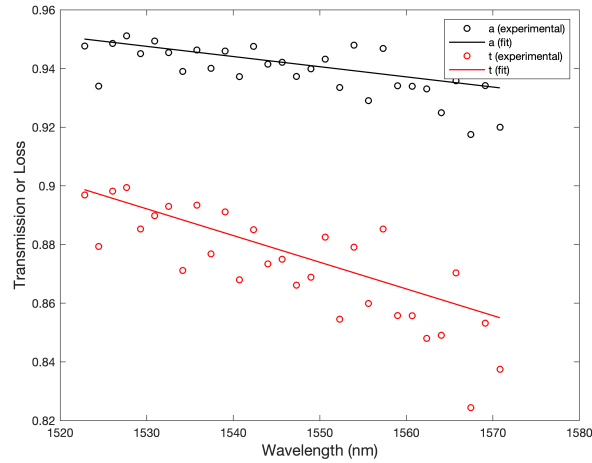


Figure 4.20 Dependency of transmission coefficient (t) (red line) and loss factor (α) over a 50nm spectral range for MRR with $R = 50\mu\text{m}$ $W = 450\text{nm}$ and $G = 200\text{nm}$

The coupling coefficient (κ) can be then calculated from t as $\kappa = \sqrt{1 - t^2}$. Figure 4.21 and Figure 4.22 show the average and standard deviation of coupling coefficient (κ) and loss factor (α) as a function of both G and W for the eighteen-strip waveguide-based single MRRs.

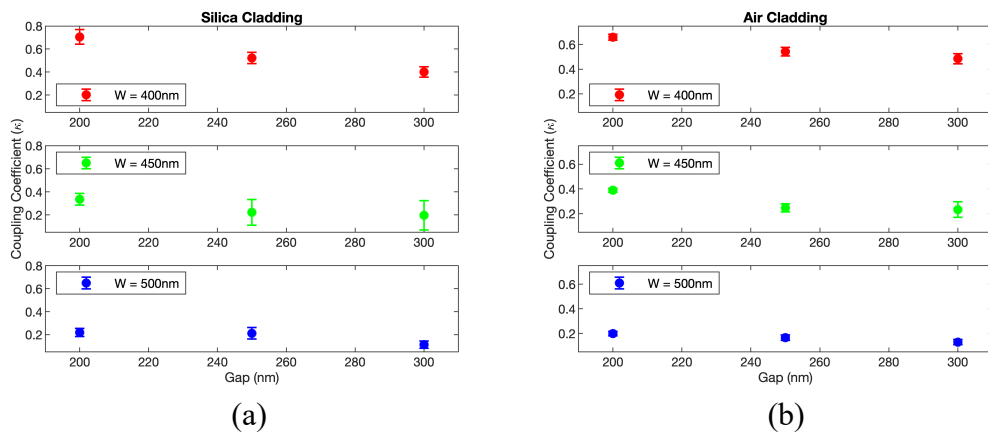


Figure 4.21 Coupling coefficient (κ) as a function of the separation gap (G) and waveguide widths (W) for (a) silica cladding (b) air cladding

As W decreases, the evanescent wave extends further outside the core of the waveguide, which leads to higher coupling efficiency. Furthermore, the coupling coefficients can be controlled by adjusting the design G , for a given W .

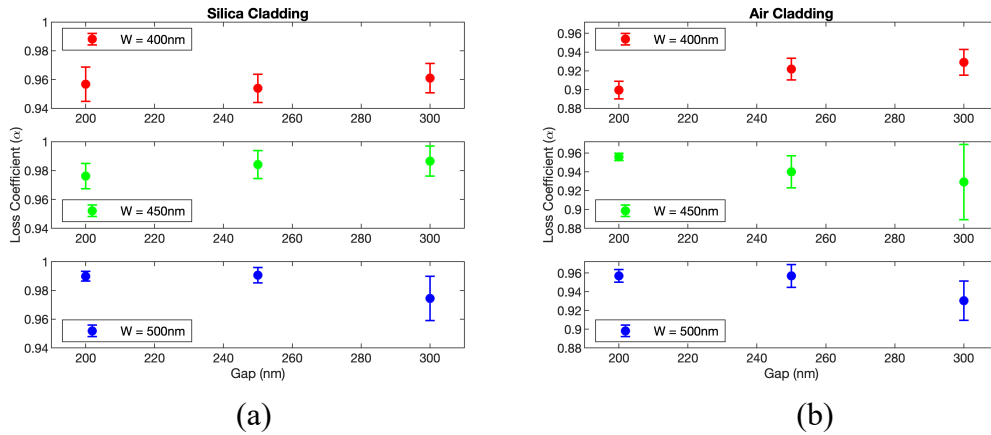


Figure 4.22 Loss factor (α) as a function of the separation gap (G) and waveguide widths (W) for (a) silica cladding (b) air cladding

The loss factor exhibited a random behaviour with G but an increase of α as a function of W was observed for almost all measured data which indicates lower cavity losses, as shown in Figure 4.22.

All MRRs with silica cladding exhibited over-coupled (i.e. $\alpha > t$) condition except for the MRR with $W = 500\text{nm}$ and $G = 300\text{nm}$ which was functioning in under-coupled ($\alpha < t$) state. MRRs with etched windows have showed over-coupled behaviour for all $W = 400$ data, as well as the MRR with $W = 450\text{nm}$ and $G = 200\text{nm}$ while the rest of the air cladded MRRs were operated in under-coupled regime.

The over-coupled resonators with fixed coupling coefficients (i.e. coupling region is protected, as shown in Figure 4.12) are suitable for applications that require exposing the MRR to extra losses (e.g. implantation, high RI sensing and surface functionalisation) because the increase of the optical loss changes the coupling conditions towards critical coupling regime ($\alpha = t$). However, excessive loss moves the resonator beyond the critical point and towards the under-coupled regime. In Figure 4.23, deionised (DI) water was drop cast on the surface of the over-coupled MRR (with $W = 400$ and $G = 200\text{nm}$) in order to increase the cavity losses.

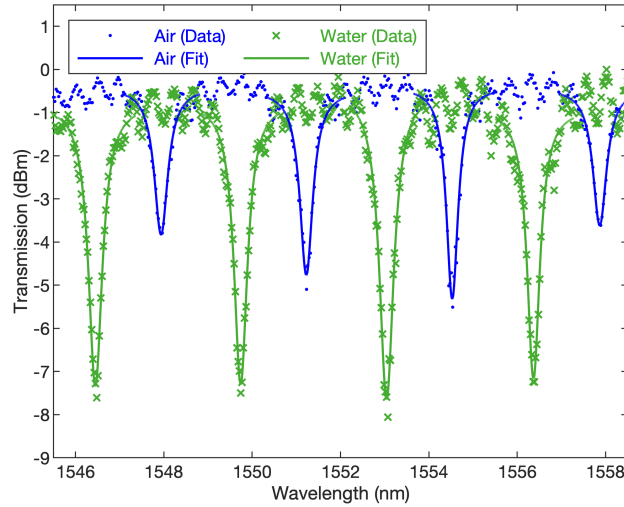


Figure 4.23 Measured and fitted transmission spectra for MRR with $W=400\text{nm}$ and $G=200\text{nm}$ with air cladding (blue curve) and water cladding (green curve)

In this case, the average ER increases by approximately 3.3 dBm, going from air cladding to water cladding. On the other hand, the q-factor decreases slightly from 3.9×10^3 to 3.4×10^3 . This suggests that the strong power coupling (κ^2), due to the small bus-to-ring gap, G , requires a relatively large power loss in the cavity in order to approach critical coupling point (i.e. $1 - \alpha^2 \approx \kappa^2$ or $\alpha \approx t$) [18].

4.7 Performance Analysis

One of the most vital characteristics of a photonic component is the loss, or attenuation, that light waves experience during their propagation or coupling process. In MRR devices, the amount of losses are directly reflected in the MRR's q-factor. Almost all optical applications including narrow-bandwidth filters, lasers and highly sensitive sensors require high q-factors. In this study, we have been able to produce q-factors ranging from 3.8×10^3 , for standard MRR with $W = 400\text{nm}$, $G = 200\text{nm}$ and silica cladding, to 7.8×10^4 , using pulley-type MRR. All MRRs fabricated using CORNERSTONE foundry without any special surface treatments. These values are considered above average as compared to similar SOI devices [19, 20]. Our devices can be further

improved by performing additional surface smoothing steps during the lithography process in order to reduce the sidewall roughness [21, 22] especially for devices with an etched upper cladding.

Mature foundries such as IMEC demonstrated that their typical value of loss, for a straight strip-based waveguide with $W = 450\text{nm}$ operating at 1550nm , is less than 2 dB/cm [23] whereas CORNERSTONE declared, in the chip delivery report of MPW#10, that a similar device (i.e. $W = 450\text{nm}$) has achieved 4.3 dB/cm [11, 24].

However, ultra-low loss waveguides and thus extremely high q -factors (ranging from 10^5 to 2.2×10^7 [25, 26]) have been reported in the past few years. These devices are usually fabricated using non-standard SOI process and relatively large waveguide dimensions in order to minimise the sidewall interaction with the fundamental mode [26]. This prevents such devices to operate as highly sensitive evanescent sensors due to the reduced interaction between the surrounded cladding and the evanescent tails.

4.8 Code Listings

Listing 4.7.1 Curve flattening

```

%Flatten MRR Curve

% First import raw data from a text or csv file
% Choose small wavelength range for better poly fit
cut_xdata=Wavelength (1000:3500);
cut_ydata=Intensity (1000:3500);

% Apply 4th degree polynomial curve fit
p = polyfit(cut_xdata,cut_ydata,4);
% Evaluates the polynomial p at each point in x
y_polyfit = polyval(p,cut_xdata);
% Flatten the curve
y_flat= (cut_ydata - y_polyfit)- max (cut_ydata - y_polyfit);

% Plot results
figure(1)
plot (cut_xdata, y_flat,'k', 'DisplayName','Flattened Data','lin-
ewidth',1)
hold on
plot (cut_xdata,cut_ydata,'r', 'DisplayName','Raw Data','lin-
ewidth',1)
xlabel('Wavelength (nm)','fontweight','normal','FontSize', 11)
ylabel('Transmission (dBm)','fontweight','normal','FontSize', 11)
legend

```

Listing 4.7.2 Lorentzian curve fitting

```

% Lorentzian fit

% First import raw data from a text or csv file
% Lorentzian Function
lorentzian = @(a, x) a(1) + (2*a(4)/pi)*(a(3)./(4.*(x-a(2)).^2 +
a(3).^2))

%Loop for fitting all peaks in the spectrum
for i=1:length(peak_row)
    Range=6; % Recommended number between 6 and 30

% Choose peak:
peak_no=i;
x= cut_xdata(loc_row(peak_no)-Range:loc_row(peak_no)+Range,:);
y= y_flat(loc_row(peak_no)-Range:loc_row(peak_no)+Range,:);

```

```

% Increase number of points in x-axis to smooth the fit
x1 = linspace(min(x), max(x), 800);
% Make initial guess of the parameters:
init_area= 1.57*width(peak_no);
a0 = [max(y) locations(peak_no) width(peak_no) init_area];
% Perform a least-squares fitting to the measured data
a = lsqcurvefit(lorentzian, a0, x, y);

plot(x1, lorentzian(a, x1), 'r-', 'linewidth', 1);
xlabel ('Wavelength (nm)', 'fontweight', 'normal', 'FontSize', 11)
ylabel ('Transmission (dBm)', 'fontweight', 'normal', 'FontSize',
11)
legend('Data', 'Lorentzian fit', 'Location', 'Best');

% store each fitted peak in a matrix
y1=lorentzian(a, x1);
Lor_x(i,:)= x1;
Lor_y(i,:)=lorentzian(a, x1);

%%% peak analysis
ER = - (a(1)+2*a(4)/(a(3)*pi));
% Peak analysis
ER = - (a(1)+2*a(4)/(a(3)*pi));
Wavelength(i,:)= a(2);

% Normalise data
max_norm= max(10.^(y1./10));min_norm= min(10.^(y1./10));
y1_norm= ((10.^(y1./10))-min_norm)./(max_norm-min_norm);

halfHeight= max(y1_norm)/2;
y11=y1_norm';
x11=x1';
% Find left edge
index1 = find(y11 <= halfHeight, 1, 'first');
xa = x11(index1);
% Find right edge
index2 = find(y11 <= halfHeight, 1, 'last');
xb = x11(index2);
% Compute the full width, half max.
FWHM = xb - xa;
Q_factor= a(2)/FWHM;

%save ER and Q only if the fitting is reasonable (converged)
if ( ER < 20) && (ER > 0) && Q_factor>100
ER_tbl(i,:)= ER_W400_G200_OpenWindow;
Q_factor_tbl(i,:)=Q_factor;
FWHM_tbl(i,:)=FWHM;
end
end

%Remove zeros from the array
ER_tbl_corrected = ER_tbl(ER_tbl~=0);
Q_factor_tbl_corrected = Q_factor_tbl(Q_factor_tbl~=0);
number_of_peaks= size(ER_tbl_corrected,1);

%calculate the average
avg_ER_tbl = mean(ER_tbl_corrected);
avg_Q_factor_tbl = mean(Q_factor_tbl_corrected);

```

4.9 References

1. Son, Han, Park, Kwon, & Yu. (2018). High-efficiency broadband light coupling between optical fibers and photonic integrated circuits. *Nanophotonics*, 7(12), 1845-1864.
2. "Thorlabs, inc." Retrieved 10 Jan 2020, from <https://www.thorlabs.com/thorproduct.cfm?partnumber=LSM03-BB>.
3. "Rs components ltd.". Retrieved 12 Jan 2020, from <https://uk.rs-online.com/web/c/test-measurement/bench-power-and-power-measurement/>.
4. "Navitar, inc.". Retrieved 14 June 2020, from <https://navitar.com/products/imaging-optics/high-magnification-imaging/12x-zoom/12x-body-tubes/>.
5. "Raptor photonics ltd.". Retrieved 14 June 2020, from https://www.raptorphotonics.com/wp-content/uploads/2016/01/OWLMini_UM_REV1.pdf.
6. "Thorlabs, inc. (sm benchtop sld source)." Retrieved 12 Jan 2020, from <https://www.thorlabs.com/thorproduct.cfm?partnumber=S5FC1005S>.
7. "Thorlabs, inc. (tunable laser)." Retrieved 15 June 2020, from <https://www.thorlabs.com/catalogpages/Obsolete/2018/TLK-L1550M.pdf>.
8. Mroziewicz. (2008). External cavity wavelength tunable semiconductor lasers-a review. *Opto-Electronics Review*, 16(4), 347.
9. "Thorlabs inc (osa 203b)." Retrieved 17 June 2019, from <https://www.thorlabs.com/catalogpages/Obsolete/2017/OSA203B.pdf>.
10. Lydiate. (2016). *Novel method of biosensing using a temperature invariant microring resonator*. The University of Manchester (United Kingdom),
11. "Cornerstone service." Retrieved 2 September 2019, from <http://www.cornerstone.sotonfab.co.uk/>.
12. "Matlab software." Retrieved 02 June 2020, from <https://mathworks.com/products/matlab>.
13. "Lorentzian function." from <https://www.originlab.com/doc/LabTalk/ref/Lorentz-func>.
14. Chremmos, Schwelb, & Uzunoglu. (2010). *Photonic microresonator research and applications* (Vol. 156): Springer.

15. Bogaerts, De Heyn, Van Vaerenbergh, De Vos, Kumar Selvaraja, Claes, et al. (2012). Silicon microring resonators. *Laser & Photonics Reviews*, 6(1), 47-73.
16. McKinnon, Xu, Storey, Post, Densmore, Delâge, et al. (2009). Extracting coupling and loss coefficients from a ring resonator. *Optics express*, 17(21), 18971-18982.
17. Delâge, Xu, McKinnon, Post, Waldron, Lapointe, et al. (2009). Wavelength-dependent model of a ring resonator sensor excited by a directional coupler. *Journal of lightwave technology*, 27(9), 1172-1180.
18. Maiti, Hemnani, Amin, Ma, Tahersima, Empante, et al. (2018). Microring resonators coupling tunability by heterogeneous 2d material integration. *arXiv preprint arXiv:1807.03945*.
19. Xue, Jin, Tong, Cui, Yan, & Zhang. (2011). *Quality factor of silicon-on-insulator integrated optical ring resonator*. Paper presented at the Photonic Fiber and Crystal Devices: Advances in Materials and Innovations in Device Applications V.
20. TalebiFard, Schmidt, Shi, Wu, Jaeger, Kwok, et al. (2017). Optimized sensitivity of silicon-on-insulator (soi) strip waveguide resonator sensor. *Biomedical optics express*, 8(2), 500-511.
21. Alasaarela, Korn, Alloatti, Säynätjoki, Tervonen, Palmer, et al. (2011). Reduced propagation loss in silicon strip and slot waveguides coated by atomic layer deposition. *Optics express*, 19(12), 11529-11538.
22. Sparacin, Spector, & Kimerling. (2005). Silicon waveguide sidewall smoothing by wet chemical oxidation. *Journal of lightwave technology*, 23(8), 2455.
23. IMEC (2021). "Photonic integrated circuit prototyping and small volume production." from <https://www.imec-int.com/en/what-we-offer/ic-link/photonic-integrated-circuits>.
24. Littlejohns, Rowe, Du, Li, Zhang, Cao, et al. (2020). Cornerstone's silicon photonics rapid prototyping platforms: Current status and future outlook. *Applied Sciences*, 10(22), 8201.
25. Mou, Boxia, Yan, Yanwei, Zhe, & Fan. (2021). Ultrahigh q soi ring resonator with strip waveguide. *arXiv preprint arXiv:2103.16016*.
26. Biberman, Shaw, Timurdogan, Wright, & Watts. (2012). Ultralow-loss silicon ring resonators. *Optics letters*, 37(20), 4236-4238.

5 Vapour Sensing

Vapour detection is essential in many applications ranging from healthcare, environmental monitoring to security. In particular, gases or vapours emitted from volatile organic compounds (VOCs) are considered as one of the most hazardous and harmful materials to human health [1]. VOCs are widely used in indoor household products such as paints and wax, as well as outdoor industrial processes including petroleum and oil production. This has motivated us to undertake a study on a wide-range of VOCs using the silicon MRR based photonic integrated circuit designs described here. The study incorporates the use of (i) conventional (single waveguide) MRR structures, (ii) slotted (double waveguide) MRRs and (iii) graphene oxide (GO) integrated (slotted) MRRs (from here on referred to as GOMRR), all tested against the following common VOCs; m-xylene, ethylbenzene (EB), water, toluene, ethanol, benzene, hexane, tetrahydrofuran (THF) and acetone. The aim of this study was to determine the effectiveness of each device type as a potential accurate, cost-effective sensing tool with the potential for mass scalability and wide applicability in the various sensing arenas, with the goal of determining both sensitivity and selectivity (the ability to determine the presence of different VOCs).

Figure 5.1 illustrates the schematic structures for all of the sensor types studied here.

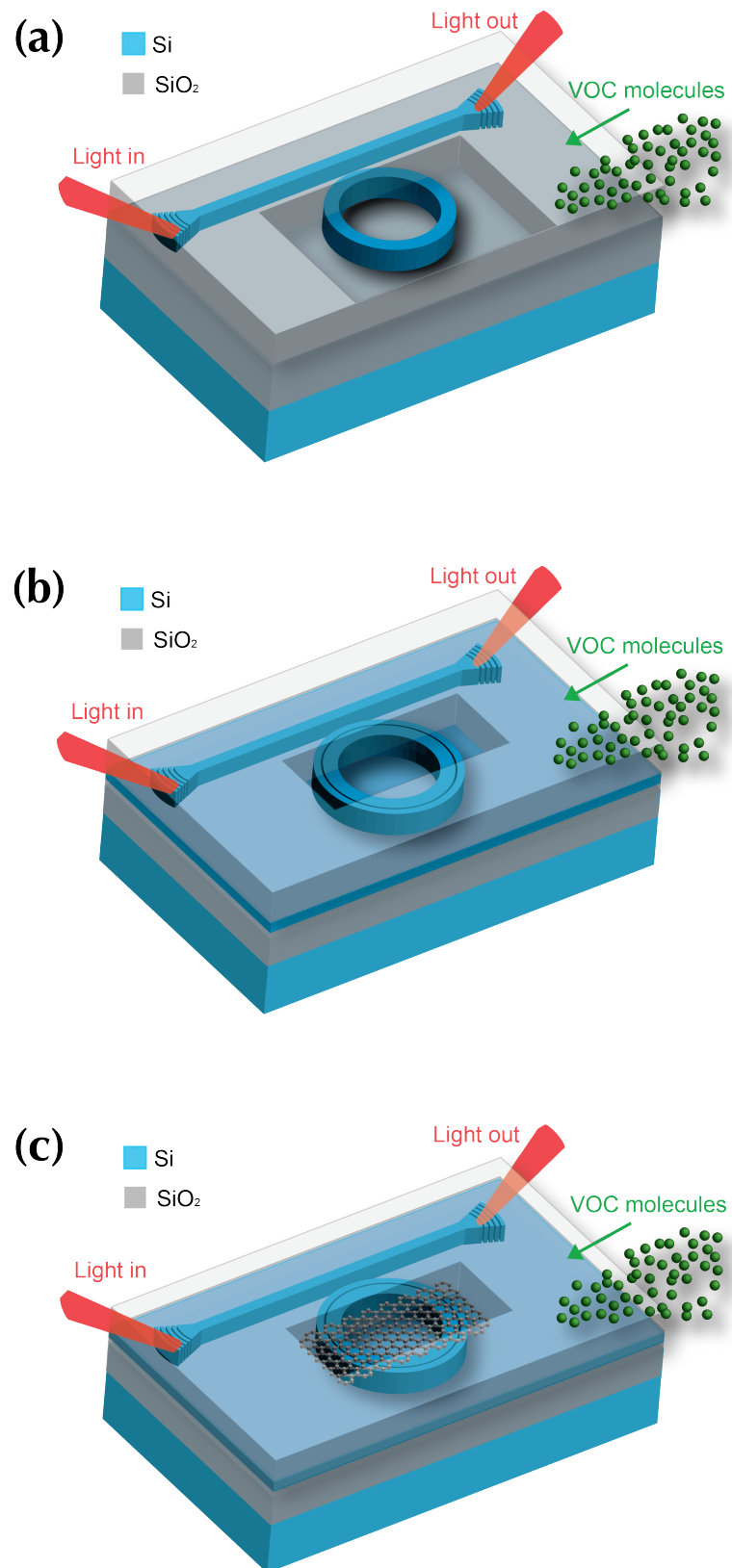
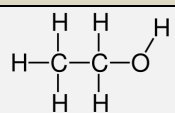
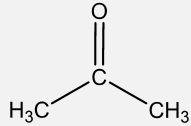
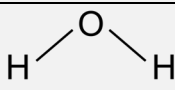
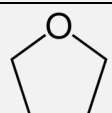
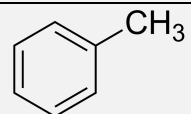
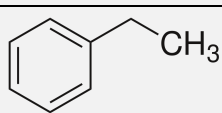
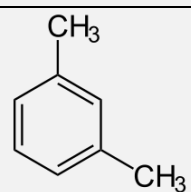
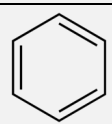
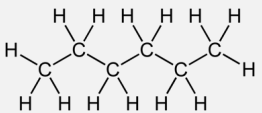


Figure 5.1 Schematic structure of (a) strip-MRR (b) slot-MRR (c) GOMRR

The VOCs in this study can be classified, based on their chemical structure, into three categories: (i) oxygenated VOCs (i.e. ethanol, acetone, water and THF), (ii) aromatic VOCs (i.e. benzene, toluene, EB and m-xylene) and (iii) hydrophobic VOC, namely hexane which lacks both hydroxyl group and the aromatic ring structures. The molecular formula and chemical structure of all VOCs are reported in Table 5.1.

Table 5.1 The molecular formula and chemical structure of all VOCs

Category	VOC	Molecular Formula [2]	Chemical Structure [3]
1	Ethanol	C_2H_6O	
	Acetone	C_3H_6O	
	Water	H_2O	
	Tetrahydrofuran (THF)	C_4H_8O	
2	Toluene	C_7H_8	
	Ethylbenzene (EB)	C_8H_{10}	
	m-xylene	C_8H_{10}	
	Benzene	C_6H_6	
3	Hexane	C_6H_{14}	

physical properties of the VOCs studied are shown, for reference, in Table 5.2. The RI here corresponds to that of the liquid phase of the organic solvents (before evaporation). However, the actual delivered refractive indices (e.g. RI of the vapour phase) are evaluated in section 5.5.

Table 5.2 Physical properties of VOCs tested in this study

VOC	Molecular weight (g/mol) [4]	Kinetic diameter (Å) [5, 6, 7, 8]	Relative Polarity [9]	Refractive index (RI) at 1.55 μm [10, 11]
Hexane	86.18	4.3	0.009	1.369
Benzene	78.11	5.3	0.111	1.479
Ethanol	46.07	4.5	0.654	1.352
Acetone	58.08	4.6	0.335	1.348
Water	18.02	2.6	1	1.318
Tetrahydrofuran (THF)	72.11	6.3	0.207	1.397
Toluene	92.14	5.3	0.099	1.476
Ethylbenzene (EB)	106.17	5.8	0.074	1.476
m-xylene	106.16	6.8	0.074	1.477

The saturated vapour pressures in the unit of a millimetre of mercury (mmHg), which is equivalent to torr, for all VOCs were calculated using Antoine's equation [12]:

$$P = 10^{A - \frac{B}{C+T}} \quad (5.1)$$

Where, A, B and C are substance-specific coefficients (i.e., Antoine coefficients) and T is the temperature in Celsius (°C). These constants with the vapour pressure are tabulated in Table 5.3 [13].

Table 5.3 Antoine coefficients and calculated vapour pressure VOCs.

VOC	A [13]	B [13]	C [13]	Vapour pressure (Torr at 20°C)
Hexane	6.87601	1171.17	224.41	121.39
Benzene	6.90565	1211.033	220.79	75.20
Ethanol	8.32109	1718.1	237.52	44.60
Acetone	7.11714	1210.595	229.664	185.45
Water	-	-	-	17.535
Tetrahydrofuran (THF)	6.99515	1202.29	226.25	129.64
Toluene	6.95464	1344.8	219.48	21.83
Ethylbenzene (EB)	6.95719	1424.255	213.21	7.08
m-xylene	7.00908	1462.266	215.11	6.16

5.1 Experimental and Simulation Details

Before beginning the measurements, the strip-MRR and slot-MRR chips were immersed in acetone solution for one hour then placed in a separate glass container that contains isopropyl alcohol (IPA) for another hour in order to remove any residue from the acetone bath. Deionised (DI) water was then used to rinse the chips from any further contaminations. Finally, the chips were dried using a purified nitrogen flow. This cleaning procedure can clean oils and organic residues that usually exist on glass surfaces. The chip was glued inside the gas cell to prevent any movement during the gas flow.

The schematic of the gas sensing setup shown in Figure 4.1 was used to evaluate the response of the optical sensors to different vapours. A hot plate and temperature controller were used to maintain the temperature of the liquid phase VOC at 20°C. During each measurement, the optical spectrum analyser (OSA) was set to save the optical spectrum every 3 seconds. Initially, three different VOCs, from each VOC category, namely; ethanol, benzene and hexane were tested to assess the sensitivity performance, as well as response and recovery times of each optical sensor. In the real-time measurements for each device, all three VOCs had experienced an additive baseline drift as the flow rate increases which might be due to the adsorption of the molecules on the surface of the sensor [14], localised electric charge trapping [15] or temperature variations [16]. Different approaches were utilised in the past few years to eliminate

this issue and improve the recovery response [14]. This includes, applying continuous ultraviolet (UV) light illumination during detection measurement [17], utilising on-chip micro-heaters to control the device temperature [18] or implementing a p-n junction to reset/control the wavelength position after each flow rate [19]. In this study, the drift baseline, in all real-time measurements, was subtracted using OriginPro software [20].

The first N₂ line (vapour carrier flow) shown in Figure 4.1 was used to vary the vapour delivery rate between 0 and 0.5 litres/min, while the second N₂ line (dilution flow) was fixed at 1 litre/min throughout the experiment. The weights of the VOCs in their liquid phase were measured before opening the vapour carrier flow line and after five minutes of N₂ flow for all flow rates (i.e. 0.05 to 0.5 litres/min). The flow rate showed a linear relationship with the weight difference, indicating that the flow rate is also linearly proportional to the VOC concentration.

The refractive index (RI) of a gas or vapour depends on many factors such as pressure, density, temperature and, more importantly, the frequency of light. The RI can be calculated from the ratio of the velocity of light in a vacuum to the velocity of light in the gas/vapour. In this study, we have determined the RIs of the different VOCs using a simulation approach that combines the use of a Finite Difference Eigenmode (FDE) solver with the homogeneous sensitivity formula (described in section 2.6.1). From this, we have been able to determine the sensitivity of our devices under test, in the commonly employed unit of nm/RIU. For our calculations, the RI of the silicon waveguides and SiO₂ buried oxide (BOX) were set as 3.48 and 1.44, respectively. The bulk (homogeneous) sensitivity and the theoretical peak shift of the MRRs are written again below [21]:

$$S_{Bulk} = \frac{\Delta\lambda_{res}}{\Delta RI} \quad (5.2)$$

$$\Delta\lambda_{res} = \frac{\Delta n_{eff}(\Delta RI, \Delta\lambda_{res})}{n_g(\lambda_{res0})} \lambda_{res0} \quad (5.3)$$

Where, $(\Delta\lambda_{res})$ is the magnitude of the MRR resonance shift with a change, ΔRI of the bulk (top cladding) index, after the introduction of a certain concentration of test VOC. $\Delta n_{eff}(\Delta RI, \Delta\lambda_{res})$ is the effective index change of the optical (guided) mode, which is a function of both the RI change and the resonant peak shift, and $n_g(\lambda_{res0})$ is the group index at the unperturbed resonance wavelength (λ_{res0}) . In our simulations, the unperturbed resonance wavelength λ_{res0} and the group index $n_g(\lambda_{res0})$ were obtained from the experimental data for each MRR.

The theoretical peak shift $(\Delta\lambda_{res})$ was calculated using the iterative method described in [21]. Each initial iteration involves running the FDE simulation twice and recording the effective index of the resonant mode: once for unperturbed condition, and once after introducing an arbitrarily small increment in cladding refractive index (RI) and resonant wavelength (λ_{res}) . The iterative FDE simulation is terminated when the resonant wavelength shift converges within 5×10^{-3} nm. The complete process flow of this iterative approach is described in Figure 5.2. Once the theoretical sensitivity is acquired, the refractive index for each concentration of VOC can be calculated from the linear interpolation with the experimentally determined resonant peak shift $(\Delta\lambda_{res})$.

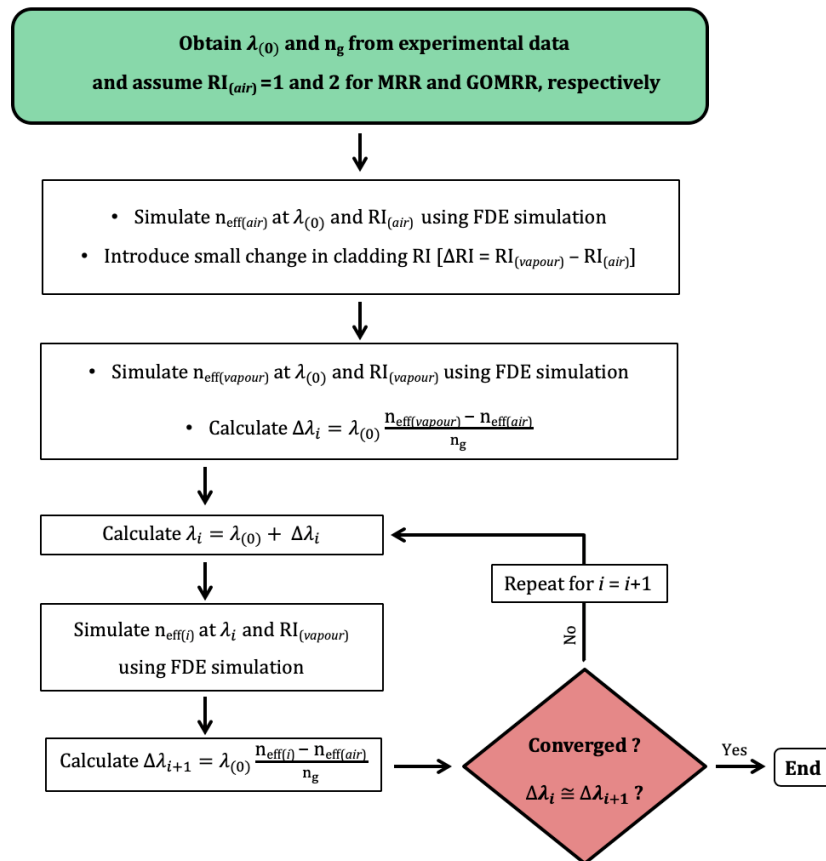


Figure 5.2 Flow chart of the iterative FDE simulation process for determination of the MRR device sensitivity [22]

This iterative technique was verified and validated by comparing it with existing empirical literature results. Sensors employing slotted MRR structures with different platforms; namely SOI and Si_3N_4 were utilised in this validation. Both sensors target aqueous solutions at operational wavelength of 1550nm and 1300nm for SOI and Si_3N_4 , respectively. The percentage errors between the experimental bulk sensitivities and the modelled sensitivity using the proposed iterative method are 7.2% and 2.9% for SOI and Si_3N_4 , respectively as shown in Table 5.4.

Table 5.4 Comparison between empirical sensitivities from literature and the proposed iterative method

VOC	Experimental Bulk Sensitivity (nm/RIU)	Estimated Sensitivity using Iterative Method (nm/RIU)	Error (%)
SOI-based Slotted MRR	298 [23]	321.06	7.2
Si ₃ N ₄ -based Slotted MRR	212.13 [24]	218.48	2.9

5.2 Strip Microring Resonator (Strip-MRR)

The first experiment was performed on an SOI-based conventional (single) strip based MRR with $R = 25\mu\text{m}$, $W = 400\text{nm}$ and $G = 300\text{nm}$. The rationale behind the choice of this specific device, specifically the smaller W , was that it should provide an evanescent field that extends further beyond the waveguide core, permitting a stronger interaction with VOC molecules near the waveguide cladding interface. The 300nm separation gap was chosen for its relatively high Q-factor and extinction ratio, which in principle provides a greater chance of detecting small wavelength shifts in the case of small changes in RI, especially at low VOC vapour concentrations. We studied three different VOCs with this device; ethanol, benzene and hexane.

5.2.1 Strip-MRR Modelling

The unperturbed resonance wavelength (λ_{res0}) and the group index n_g (λ_{res0}) were obtained from the experimental spectrum, shown in Figure 5.3. The unperturbed resonance wavelength was chosen to be 1561.54nm which is shown in the left inset in Figure 5.3. The free spectral range (FSR) was calculated by fitting the Lorentzian line-shape function to the measured resonance peak and estimating the average of five FSRs. The group index was then determined, using Equation (2.7) to be 4.617.

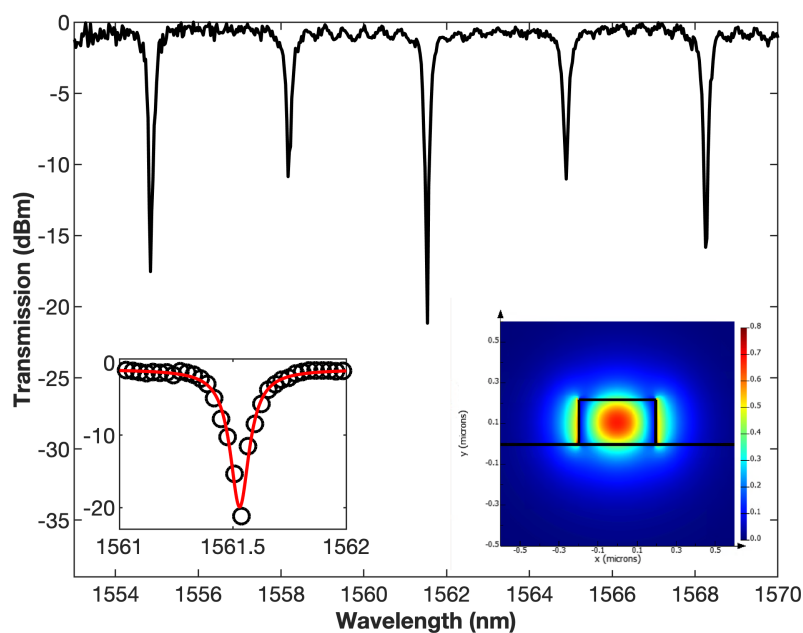


Figure 5.3 Experimental transmission spectrum of the single strip-MRR with the left inset showing a close-up of the unperturbed resonance peak (black circles) and Lorentzian fit (red line). The right inset shows the simulated electric field distribution at the right bend of the 25 μ m strip-MRR

5.2.2 Dynamic (Real-Time) Measurements of the Strip-MRR Sensor

Real-time monitoring of ethanol, benzene and hexane vapours are shown in Figure 5.4. The experiment involves first opening the N₂ dilution flow (no VOC vapour present) followed by opening the N₂ + vapour carrier flow (red shaded areas in the figure). The vapour-dilution flow ratios (F_v/F_d), ranging from 0.05 to 0.5, are illustrated on top of each figure.

For both the benzene and hexane experiments, extremely noisy and unstable resonant peak positions were observed, whereas for ethanol, a smoother more stable detection of the VOC is apparent, as shown in Figure 5.4. We note that both benzene and hexane lack hydrophilic functional groups such as hydroxyl (-OH) or carboxyl (-COOH) groups, which would lead to a lower probability of their molecules being adsorbed on the strip-MRR surface, which is essentially silicon with a $\sim 10\text{\AA}$ hydrophilic native

SiO₂ (oxide) layer (hydroxide being the main termination) [25, 26]. The thin native oxide is naturally formed on the surface of silicon after atmospheric exposure [27]. In contrast, the ethanol is hydroxyl (-OH) terminated, leading to better adsorption on the native oxide/silicon waveguide surface. For this experimental arrangement, we also noted that the observed wavelength shifts ($\Delta\lambda$) were very small (always sub-100pm).

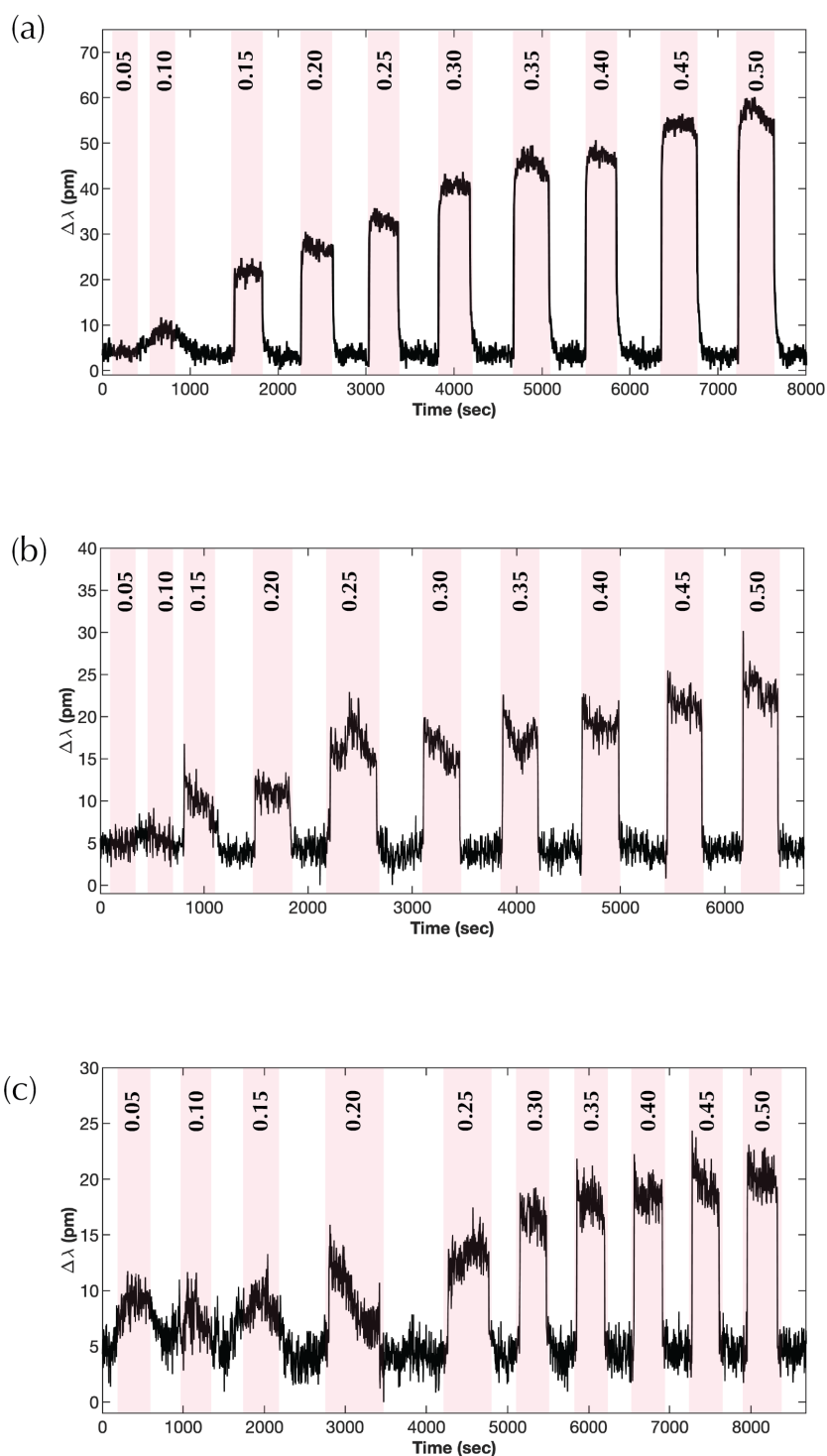


Figure 5.4 Dynamic (real-time) monitoring of spectral response and recovery of the single strip-MRR with exposure to (a) ethanol, (b) benzene and (c) hexane. The red highlighted areas indicate the time range(s) when the N_2 +VOC vapour carrier flow is opened and white regions where it was closed (only N_2 dilution flow open). The vapour-dilution flow ratio (F_v/F_a), ranging from 0.05 to 0.5, are illustrated on top of each figure

5.3 Slotted Microring Resonator (Slot-MRR)

The second experiment was carried out for all nine of the VOCs described in Table 5.1 and 5.2, using an SOI rib-based slotted MRR whereas controlled real-time measurements were performed for one VOC from each group illustrated in Table 5.1, namely ethanol (oxygenated), benzene (aromatic) and hexane (hydrophobic). This device has $R = 25\mu\text{m}$, measured from the centre of the ring(s) to the centre of the slot between the concentric rings. The light is coupled from a bus waveguide with $W = 320\text{nm}$ to the ring waveguide consisting of an outer waveguide, $W = 250\text{nm}$, slot width, $W_{\text{slot}} = 200\text{nm}$ and an inner waveguide, $W = 290\text{nm}$. This structure has an etched opening ('window') over the centre of the ring structure with dimensions of $64\mu\text{m} \times 35\mu\text{m}$.

The slotted structure should allow for improved sensitivity compared with the conventional single strip-MRR because the field maximum of the propagating (guided) optical mode is within the (lower index) slot, implying stronger interaction with VOC molecules there.

5.3.1 Slot-MRR Modelling

Since the slot width ($W_{\text{slot}} = 200\text{nm}$) is much larger than the kinetic diameter of all VOC molecules studied here, we assume it will be (at least partially) filled for the purposes of the iterative simulation. The unperturbed resonance wavelength (λ_{res0}) and the group index $n_g(\lambda_{res0})$ were calculated, as for the single strip-MRR (section 5.2.1) and these were determined, from Figure 5.5, to be 1552.21nm and 3.404 , respectively. The electric field distribution (E_x) shown in the right-hand side inset of Figure 5.5 indeed reveals the maximum to be within the (low index) slot region. However, the rib-based structure also leads to a significant field within the lower slab region beneath the slot. Generally, the Q-factor for such devices tends to be enhanced compared with strip-based structures [28].

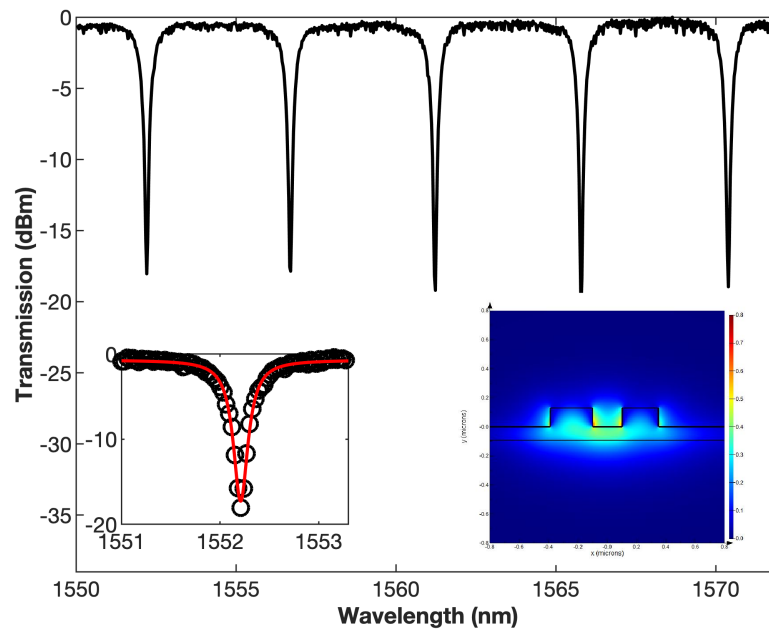


Figure 5.5 Experimental transmission spectra of the slot-MRR with left inset showing a close-up of the unperturbed resonance peak (black circles) and Lorentzian fit (red line). The right inset shows the simulated electric field distribution at the right bend of the 25µm slot-MRR

5.3.2 Real-Time Measurements of Slot-MRR

The real-time measurements of ethanol, benzene and hexane are shown in Figure 5.6. When exposing this device to both ethanol and benzene, it was noted that, when the vapour carrier flow was opened (red shaded areas), after an initial rapid shift, the resonance peak took a longer time to reach steady state, compared with the single strip-MRR. A similar trend was observed after the vapour carrier flow was turned off. The response of this device to hexane was much faster, although some instability in the steady state peak position during vapour flow was again observed, which may be due to the hydrophobic nature of hexane.

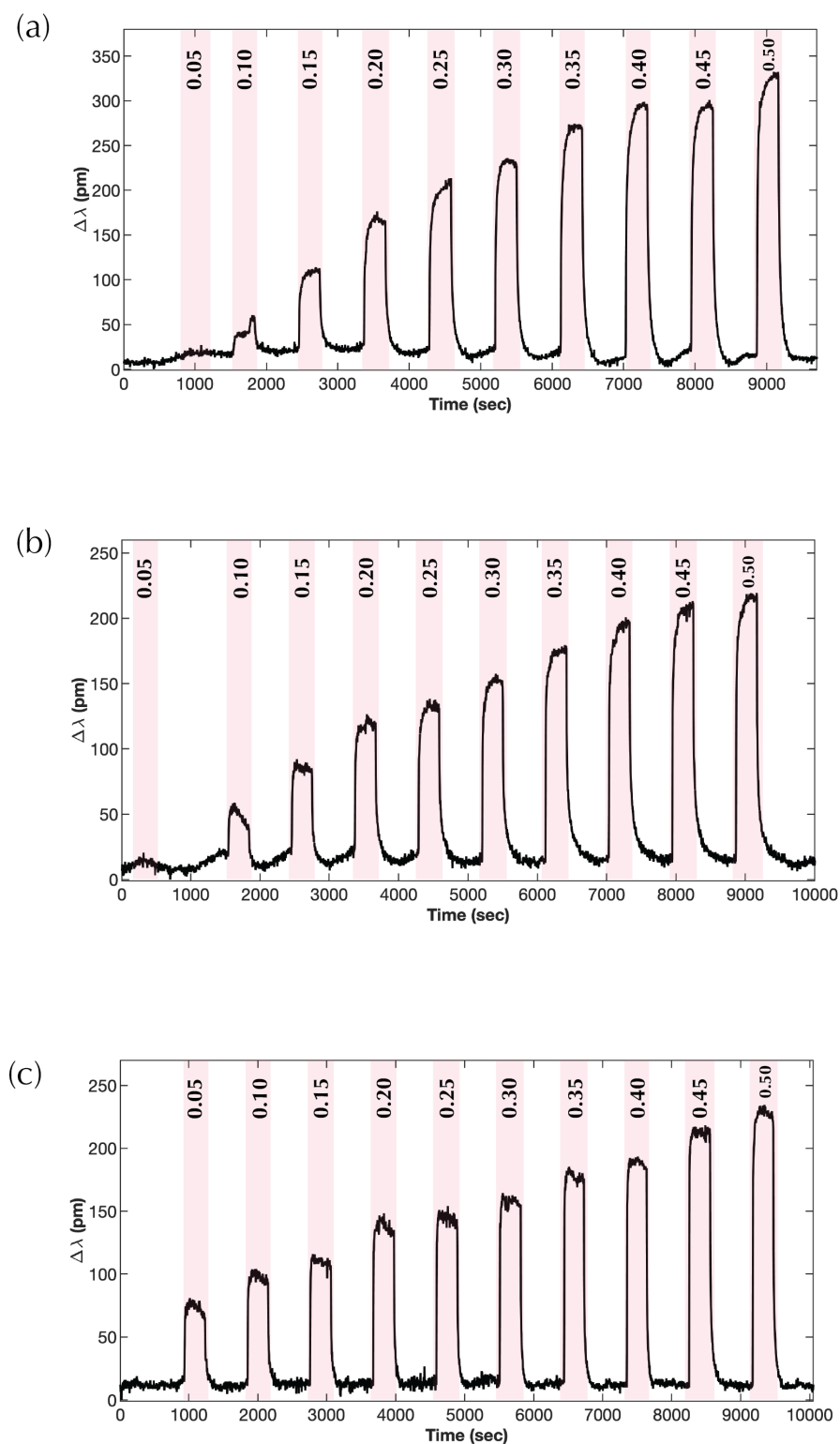


Figure 5.6 Real-time monitoring of spectral response and recovery of slot-MRR for (a) ethanol, (b) benzene and (c) hexane. The red highlighted areas indicate the time range(s) when the $N_2 + VOC$ vapour carrier flow was opened. The vapour carrier-dilution flow ratios are illustrated on top of each plot

5.4 Graphene Oxide Slotted Microring Resonator (GOMRR)

Materials with a high surface-to-volume ratio, such as graphite derivatives can, in principle, offer improved molecular adsorption [29, 30]. In addition, the unique molecular sieving properties of these carbon-based materials have led to numerous applications, including the selective permeability of gas molecules from a mixture of gases [31, 32, 33, 34].

In this section, we exploited graphene oxide (GO), which can be formed by the oxidation of graphite, in an attempt to further enhance the ‘trapping’ and thus sensitivity of the slot-MRR device. The GO offers many advantages over graphite due to the chemical oxidation process, where oxygenated functional groups are introduced on the GO surface, such as hydroxyl ($-OH$), carboxyl ($-COOH$), carbonyl ($-C=O$), epoxy ($-C-O-C-$) and ketone ($-C=O$) groups [35]. These terminations lead to an expansion of the interlayer separation as well as converting the intrinsic hydrophobicity of graphene to a material with hydrophilic properties (e.g. graphene oxide) [36]. Additionally, the existence of oxygen facilitates the GO dispersion in water [37].

5.4.1 Graphene Oxide (GO) Synthesis

The GO utilised in this study was prepared by Mao et al. [38] where they used an adapted procedure from the Hummers method [39]. Pure graphite powder (SP-1 grade 325 mesh, Bay Carbon Inc.) was used to synthesize graphite oxide. A mixture of 10g of graphite flakes and 5g of sodium nitrate ($NaNO_3$) powder were dispersed in 230mL of concentrated sulfuric acid (H_2SO_4) in a 1.5 L beaker. This mixture was cooled down to maintain $0\text{ }^\circ\text{C}$ temperature by immersing the mixture container in an ice-water bath in order to prevent any excess heat that might be generated due to reaction with oxidising agents. With continuous stirring, 30g of potassium permanganate ($KMnO_4$), which acts as a strong oxidising agent, was slowly added to the solution while maintaining the mixture’s temperature below $20\text{ }^\circ\text{C}$. After that, the beaker was placed outside the ice bath where its temperature was allowed to elevate up to $35\text{ }^\circ\text{C}$. In order to complete deep oxidation, the mixture was stirred for 30 minutes at room temperature. Then, 460mL of distilled water was gradually added to the mixture which resulted in a fast exothermic reaction combined with some effervescence. An additional 1.4L of

distilled water was added to dilute the mixture followed by controlled addition of a total of 3% of H₂O₂ solution which changes the mixture colour from reddish brown to light yellow. Hydrogen peroxide compound plays an important role in eliminating the residual oxidants, namely permanganate and manganese dioxide. Microfiltration was achieved using a membrane with a controlled pore size distribution, namely Cyclopore polycarbonate membrane. 3.2L of distilled water was then used to disperse the mixture. Residual salts and ions from the oxidation process were filtered out of the mixture using a two-week dialysis process. The remaining graphite oxide, which was collected from the filtering membrane, was left to dry in a 60 °C furnace. Stable dispersion of graphene oxide (GO) was attained by employing ethanol solvent. An ultrasonication bath for 3h was applied to the suspension, then centrifuged at 3000 rpm for half an hour. The liquid lying above the solid residue (supernatant) was extracted and left to settle for a period of 30 days. A final microfiltration step was performed where only the clear supernatant was utilised in this experiment.

5.4.2 Graphene Oxide (GO) Coating

A total of 0.6µL of 0.05mg/mL graphene oxide (GO) was drop-cast on the surface of the slotted ring resonator (slot-MRR) using a micropipette. The aquatic drop was completely evaporated after a few minutes, leaving only GO flakes coating the entire etched ‘window’ area (64µm × 35µm) over the slotted ring structure.

Raman spectroscopy was employed in order to confirm the successful integration of the GO on the slot-MRR surface. GO can be distinguished by two main Raman spectral bands, namely the D and G bands. The existence of structural distortions such as vacancies or dislocations in the GO structure results in the D band (located near 1350 cm⁻¹) in the GO Raman scattering spectrum. In addition, material defects and impurities which are introduced during GO preparation are also related to this band. The other characteristic peak (G band) appears around 1580 cm⁻¹. This band is related to the in-plane vibration of sp² hybridised carbon atoms [40] and can be used to analyse strain and electronically active defects within the sample [41]. The ratio of the intensities of the D band to that of the G band (I_D/I_G), as well as their Raman peak positions,

are commonly used to determine the oxidation level, strain, stress, disorder and thermal reduction of the GO layer [42, 43, 44, 45]. Raman spectroscopy of the GOMRR was conducted using a Renishaw *inVia* spectrometer equipped with a 633nm laser source and 50x microscope objective lens. A Raman ‘map’ with a spatial resolution of 1 μ m was performed across the whole ‘window’ region, highlighted by the white dashed box in Figure 5.7 (a). The laser power was set below 5% to avoid heating the GO coating. Figure 5.7 (b) illustrates a typical GO Raman scattering spectrum showing the D (left peak) and G (right peak) bands, with I_D/I_G equal to 1.11. The aforementioned spectrum was obtained from the left-hand side bend of the GOMRR, as indicated by the small white circle in Figure 5.7 (a). The Raman mapping result of the I_D/I_G ratio is shown in Figure 5.7 (c). The slightly darker colour in the map, which reveals the underlying ring structure, implies a lower I_D/I_G ratio where the GO is in contact with the device. The statistical histograms displayed in Figure 5.7 (d) indicates that a mean I_D/I_G ratio of 1.14, where the GO is in contact with the ring waveguide, whereas the mean I_D/I_G ratio for the entire ‘window’ area is 1.23. The statistical analysis was derived from around 2200 spectra recorded across the window area. This difference in the I_D/I_G ratios is likely attributed to localised (trapped) charges at the GO/silicon waveguide interface [46, 47].

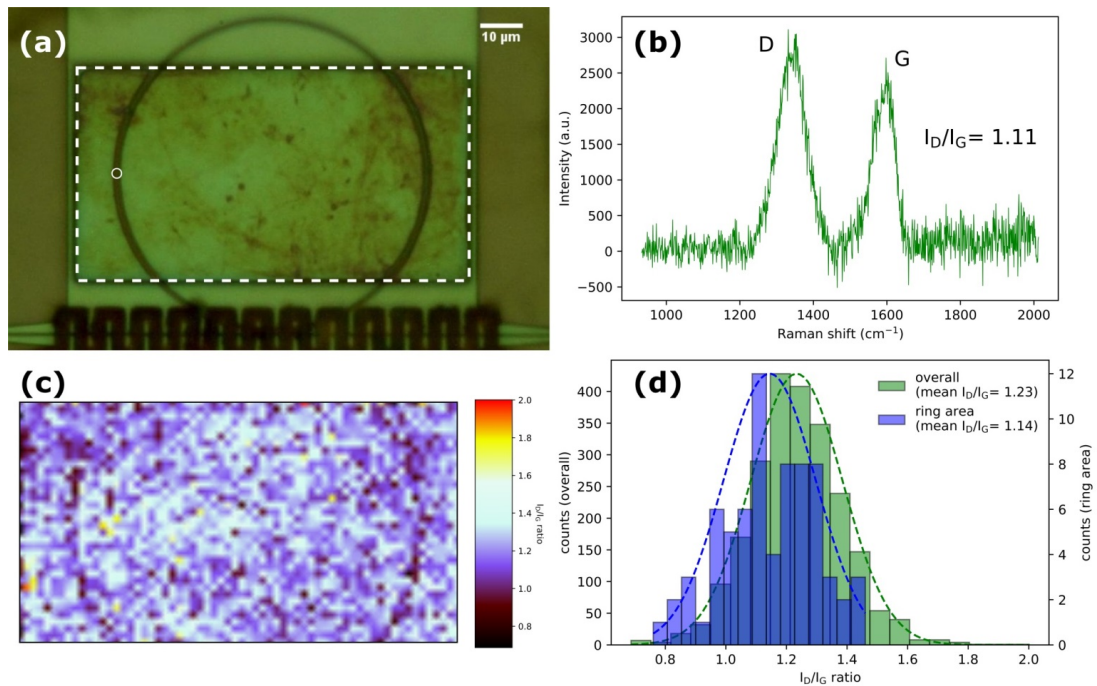


Figure 5.7 (a) Optical microscope image of the GOMRR showing the etched window area highlighted by the white dashed box (b) A typical Raman spectrum obtained from the ring waveguide region, as indicated by the small white circle in (a) with I_D/I_G ratio = 1.11 (c) Raman map of the I_D/I_G ratio for the highlighted window area of the GOMRR with the darker region revealing the underlying ring structure with lower I_D/I_G ratio (d) Histograms and Gaussian fits (dashed lines) of the I_D/I_G ratio, determined from (Lorentzian) fits to the Raman spectral peaks, for each mapped spatial position [22]

5.4.3 GOMRR Modelling

In our simulations, the RI of the bulk GO cladding around 1550nm was assumed to be $RI = 2$, as reported from the near-dispersion-less values in [48, 49]. The lower refractive index contrast between the silicon waveguide ($RI = 3.48$) and bulk GO cladding leads to higher intensities of the evanescent field of the propagating (guided) mode at the interface of silicon/GO, as shown in the right-hand side inset of Figure 5.8. The unperturbed resonance wavelength (λ_{res0}) and the group index n_g (λ_{res0}) were calculated to be 1554.33nm and 3.388, respectively. The Q-factor and ER were slightly reduced after the GO deposition, presumably due to an increase in the propagation loss

associated with absorption by the GO layer. The Q-factor before and after GO deposition was determined to be ~ 9000 and ~ 7500 , respectively. This reduction in the Q-factor however is much smaller than that observed for a similar graphene integrated device [46, 50].

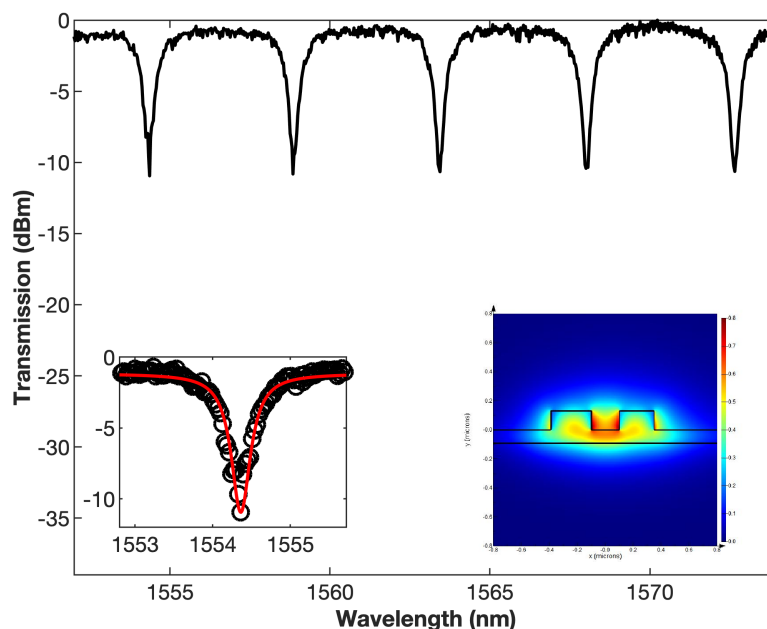


Figure 5.8 Experimental transmission spectrum of the GOMRR with left inset showing a close-up of the unperturbed resonance peak (black circles) and Lorentzian fit (red line). The right inset shows the simulated electric field distribution at the right bend of the 25 μ m GOMRR

5.4.4 Real-Time Measurements of GOMRR

The GO layers have a high surface-to-volume ratio and the formation of capillaries facilitates ‘trapping’ and significant adsorption of the VOC molecules in close proximity to the surface of the ring structure. In this case, the VOC vapours can condense (capillary condensation), forming a liquid. This phenomenon is typically observed in porous materials, especially when a relatively large interlayer space exists, such as is known to be the case for GO. The oxidation process (formation of hydrophilic functional groups) acts to enlarge the space between adjacent GO laminates, which increases the intercalation of molecules [51]. Figure 5.9 reveals continuous measurements for the GOMRR when exposed to ethanol, benzene and hexane.

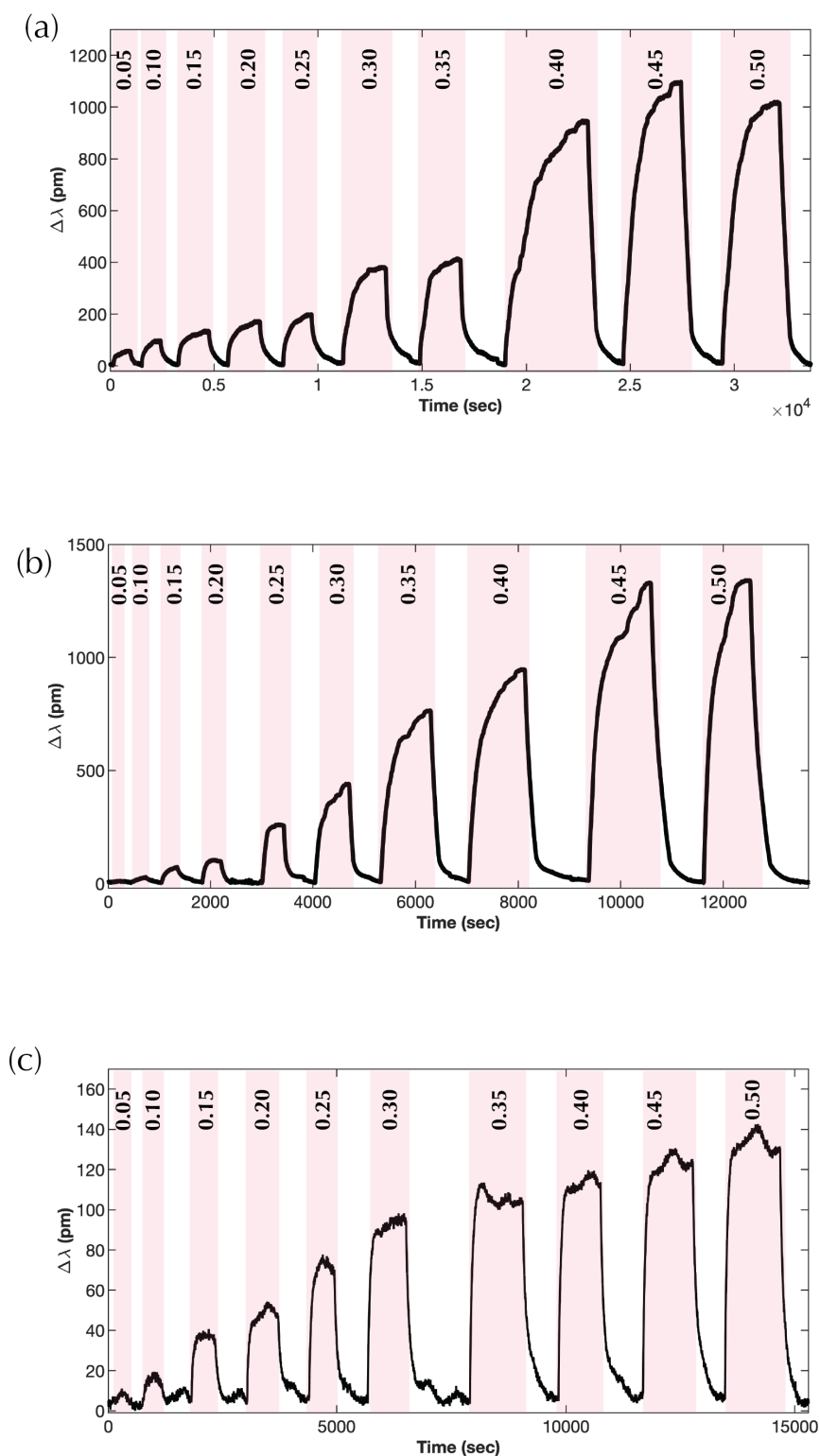


Figure 5.9 Real-time monitoring of the spectral response and recovery of GOMRR for (a) ethanol, (b) benzene and (c) hexane. The red highlighted areas indicate the time range(s) when the N_2+VOC vapour carrier flow is opened. The vapour carrier-dilution flow ratios are illustrated on top of each plot

Once again, we observe a gradual shift of the resonance peak to steady state during vapour delivery for both ethanol and benzene and a rather more rapid increase for hexane. We also note that, for ethanol, a sudden jump in the peak shift appears for $F_v/F_d = 0.40$, which we believe indicates the transition from vapour to capillary condensation. The other striking feature for this data is the much larger peak shift, across the entire range of F_v/F_d , for both ethanol and benzene, compared with hexane, again likely due to the hydrophobic nature of the hexane (the effect being enhanced considerably in this case). In general, although the GOMRR device appears to exhibit superior performance in terms of sensitivity (i.e. enhanced resonance peak shift for the same concentration of delivered VOC), it does exhibit longer response and recovery times. We believe that the mechanism of vapour adsorption, in this case, is a gradual build-up of molecular layer formation, gradually progressing from (possibly) monolayer to multilayer formation and ending with capillary condensation [52]. This process takes longer to permeate through the GO membranes reaching the evanescent field of the propagating (guided) optical mode, close to the silicon/GO interface within the waveguide slot.

5.5 Results and Discussion

The FDE iterative method resulted in sensitivities (S) of 51.13, 52.65 and 114.74 nm/RIU for strip-MRR, slot-MRR and GOMRR, respectively. Although the slot-MRR enables direct interaction between vapours and the guided field, it has a comparable (within experimental error) sensitivity with that of the strip-MRR, possibly because a considerable amount of the mode field is supported under the slot (i.e. slab region).

The limit of detection (LOD) for each of the sensor types was determined, by dividing the measured uncertainty, σ (with 99.73% confidence interval of the unperturbed peak positions) by the device sensitivity (S), according to [53]:

$$\text{LOD} = \frac{3 \sigma}{S} \quad (5.4)$$

The uncertainty of the resonance position (3σ) was determined (from observation of the resonance peak fluctuations, in the absence of vapour flow) to be less than 10pm for all measurements. This leads to an estimate for the LOD of 1.96×10^{-4} , 1.90×10^{-4} and 8.72×10^{-5} RIU for the strip-MRR, slot-MRR and GOMRR, respectively. Table 5.5 compares our strip and slot-MRRs performance (i.e. sensitivity and LOD) with similar previously reported SOI-devices [23, 54]. However, both devices from the aforementioned references are employed to detect aqueous solutions, indicating that the top cladding of these devices will have refractive indices higher than 1.3. This leads to notably longer penetration depth of the evanescent mode (see section 2.2) and improved sensitivity and LOD as compared to our devices that target gas/vapour which usually have refractive indices slightly higher than air. Also, the reported slotted MRR in [23] has strip-based structure (i.e. the waveguides are etched until the BOX layer), indicating that large portion of the confined electric field in the slot can directly interact with the target analytes whereas our slotted device is based on rib-structure where significant amount of the confined electric field is within the slab layer under the slot as depicted in Figure 5.5.

Table 5.5 Comparison of the sensitivity and LOD between different MRR devices.

Device	Target Substance	System Resolution, $\delta\lambda$ (pm)	Sensitivity (nm/RIU)	LOD (RIU)	Ref.
Strip MRR	Aqueous	5	70	7.1×10^{-5}	[54]
Slotted MRR (Strip-based)	Aqueous	12.5	298	4.2×10^{-5}	[23]
Strip MRR	Gas	10	51.13	1.96×10^{-4}	This work
Slotted MRR (Rib-based)	Gas	10	52.65	1.9×10^{-4}	This work
GOMRR (Rib-based)	Gas	10	114.74	8.72×10^{-5}	This work

The resonance shift as a function of flow ratio (F_v/F_d) can be described by a *Hill-Langmuir* type function. This function is commonly used in pharmacological and biochemical sciences to describe the cooperative binding of ligands to enzymes or receptors as a function of ligand concentration [55]. The binding is considered cooperative if the initial binding between a ligand and a macromolecule increases the binding affinity (interaction of ligands with their binding sites) for the next ligand/macromolecule (and negative if the binding affinity is reduced). This leads to nonlinear behaviour in the binding dynamics, such as is observed for the binding of oxygen to haemoglobin molecules [56]. Application of the *Hill-Langmuir* function has been extended to describe interactions such as surface adsorption of gas molecules (e.g. the number of adsorbed molecules per surface site) [57, 58]. In this study, the *Hill* coefficient (n) shown in Equation (5.5) was employed as an indication of the level of cooperative adsorption following exposure of the vapour phase VOCs to the MRR sensors. The *Hill-Langmuir* function can be written as [59]:

$$\Delta\lambda_{eq} = \frac{x^n}{k^n + x^n} \Delta\lambda_{max} \quad (5.5)$$

Where x represents the relative concentration of delivered vapour (in our case determined by the ratio of vapour carrier to the dilution flow, F_v/F_d), n is the *Hill* coefficient, k is the vapour flow ratio at which half the maximum resonance shift is achieved and $\Delta\lambda_{max}$ is the maximum observed resonance shift.

Figure 5.10 presents the steady state (or equilibrium) wavelength shift ($\Delta\lambda_{eq}$) as a function of vapour-dilution flow ratio (F_v/F_d) for all VOCs employed in this study.

The saturated resonance shifts for slot-MRR measurements were in general higher than that for the strip-MRR over the same range of vapour-dilution flow ratio (F_v/F_d). Since these sensors have comparable sensitivities, the higher wavelength shifts observed for the slot-MRR suggest that the vapour concentration (i.e. RI of the VOCs) delivered to the surface of this device is actually higher than that for the strip-MRR for the same F_v/F_d , which might be attributed to the superior trapping mechanism in the slotted device. The fitting of Equation (5.5) confirms this by revealing a relatively higher *Hill* coefficient (n), indicating a greater level of cooperativity for slot-MRR

when compared to strip-MRR device, as shown in Figure 5.10 (a-c). For the GOMRR device, the data follows a rather more sigmoidal shape, consistent with the physisorption of gases that occur in type IV and V isotherm models [60]. These two models are part of six adsorption isotherm models that are classified by the International Union of Pure and Applied Chemistry (IUPAC) [61, 62]. Each model is used to characterise the adsorbent and adsorbate according to their pore structure [62]. Both observed IV and V isotherm models are commonly used to indicate the formation of capillary (or pore) condensation [60, 63]. The GOMRR fits (green dashed curves) in Figure 5.10 are more closely matched with those of the type V isotherm-like relationship, for all VOCs tested, with the exception of ethanol, acetone and water where they show characteristics similar to type IV isotherm (in this case, two distinct underlying mechanisms, each with their own Hill coefficient (n), are required to adequately fit the data). In general, the integration of GO has resulted in higher n for all VOCs, with the exception of Hexane, indicating enhanced cooperativity.

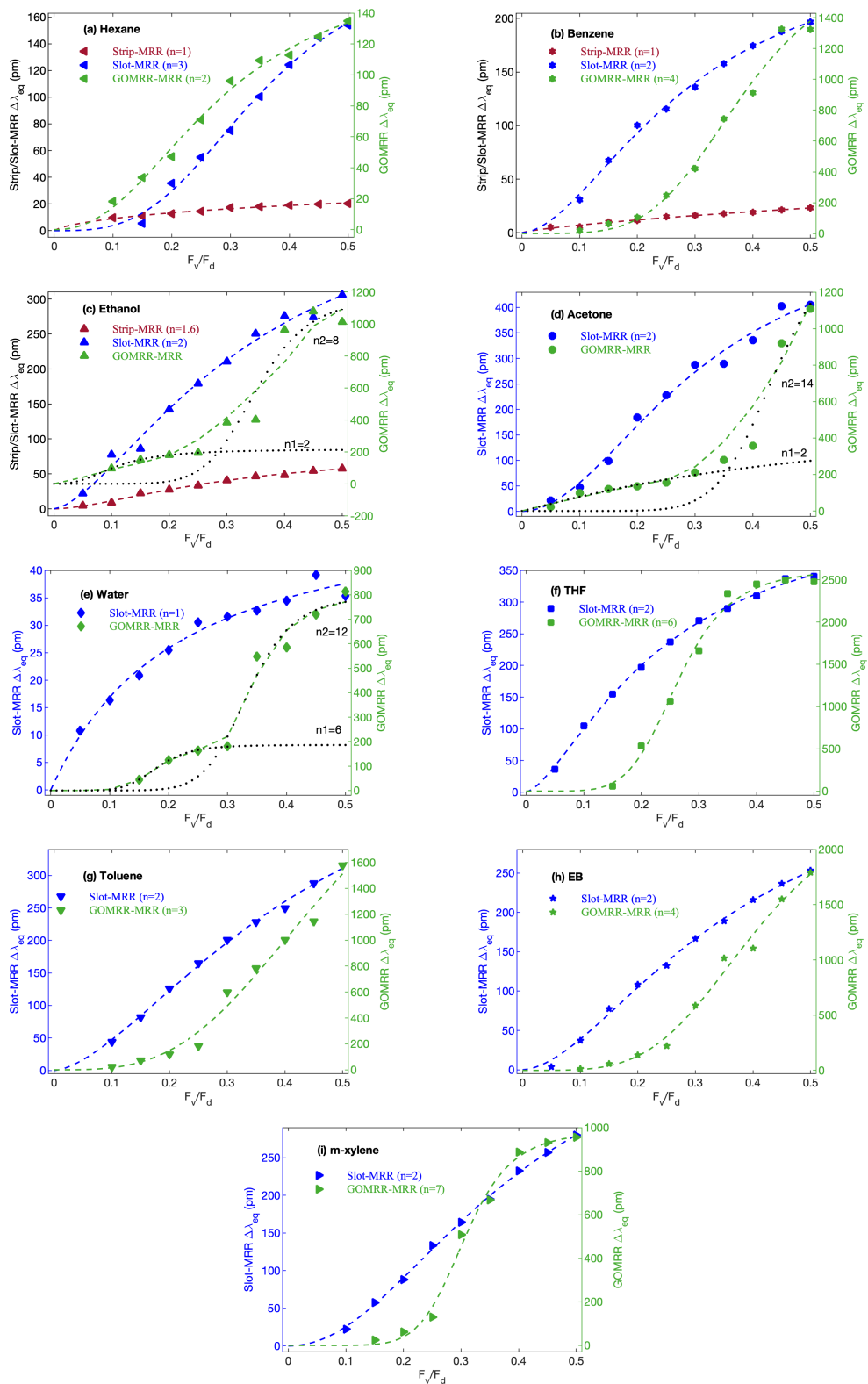


Figure 5.10 Experimental resonance wavelength shift at equilibrium ($\Delta\lambda_{eq}$) as a function of vapour-dilution flow ratio (F_v/F_d) for various VOC vapours for strip-MRR (red) slot-MRR (blue) and GOMRR (green) with the fitting of *Hill-Langmuir* model (dashed lines)

At low concentration levels, the GOMRR device resulted in smaller wavelength shifts ($\Delta\lambda_{\text{eq}}$) for all VOCs, except ethanol, acetone, water and hexane, compared with that of the slot-MRR. This can be attributed to the presence of the GO layer, initially restricting the interaction between VOC molecules and the evanescent field at the Si/GO interface. This ‘blocking’ mechanism is less effective for relatively small molecules (e.g. ethanol, acetone, water and hexane), which can more easily intercalate between GO inter-layers. This leads to a comparable *Hill* coefficient (denoted by n_1 for ethanol, acetone and water) with that observed for the slot-MRR device, at low vapour concentrations. However, as the concentration increases, much larger shifts ($\Delta\lambda_{\text{eq}}$) were observed for almost all VOCs due to the formation of multilayer adsorption, followed by the capillary condensation within the pore structure of the GO. In the case of ethanol, acetone and water, the GOMRR models exhibit the largest *Hill* coefficients at high concentrations (denoted as n_2), as shown in Figure 5.10 (c-e). This suggests significantly increased cooperativity, as well as substantial molecular permeation between the GO interlayers (i.e. complete pore filling) [64]. The measurements in Figure 5.10 were translated to sensitivity measurements in terms of wavelength shifts ($\Delta\lambda_{\text{eq}}$) and changes in the top cladding refractive index (ΔRI), as shown in Figure 5.11. The sensitivities for each device were obtained theoretically using the iterative method described by the flow chart in Figure 5.2, while the $\Delta\lambda_{\text{eq}}$ shifts were measured experimentally for each VOC. Therefore, ΔRI can be calculated from Equation (5.2) for each $\Delta\lambda_{\text{eq}}$, indicating the level of actual concentration delivered to each sensor. The range of ΔRI increases as a result of this trapping mechanism, where the GOMRR device exhibits the largest range for almost all measurements (with the strip-MRR having the smallest). This would indicate that the vapour concentration delivered to the GOMRR is significantly higher than for the other devices, despite the same vapour-dilution flow ratio. The sudden jump in ΔRI for ethanol, acetone and water, as shown in Figure 5.11 (c-e), correlates well with the occurrence of cooperative binding at higher concentrations, which is likely explained by the onset of microscopic capillary condensation (i.e. liquid formation in the saturated GO pore structure). These three VOCs share common characteristics where they all have relatively small molecular weight and kinetic diameter as well as relatively high polarity, compared with the other VOCs tested (see Table 5.2). This could explain this potential selective behaviour [31]. Hexane was

the only VOC that exhibited a rather weak interaction with the GOMRR device, which we attribute to the lack of hydroxyl or carboxyl functional groups, and absence of an aromatic ring structure, such as that of the hydrocarbon compounds (e.g. m-xylene, toluene and benzene). This can form π - π stacking with the basal plane of GO [65, 66] and might explain why the interaction between these VOCs and the GOMRR is stronger than hexane.

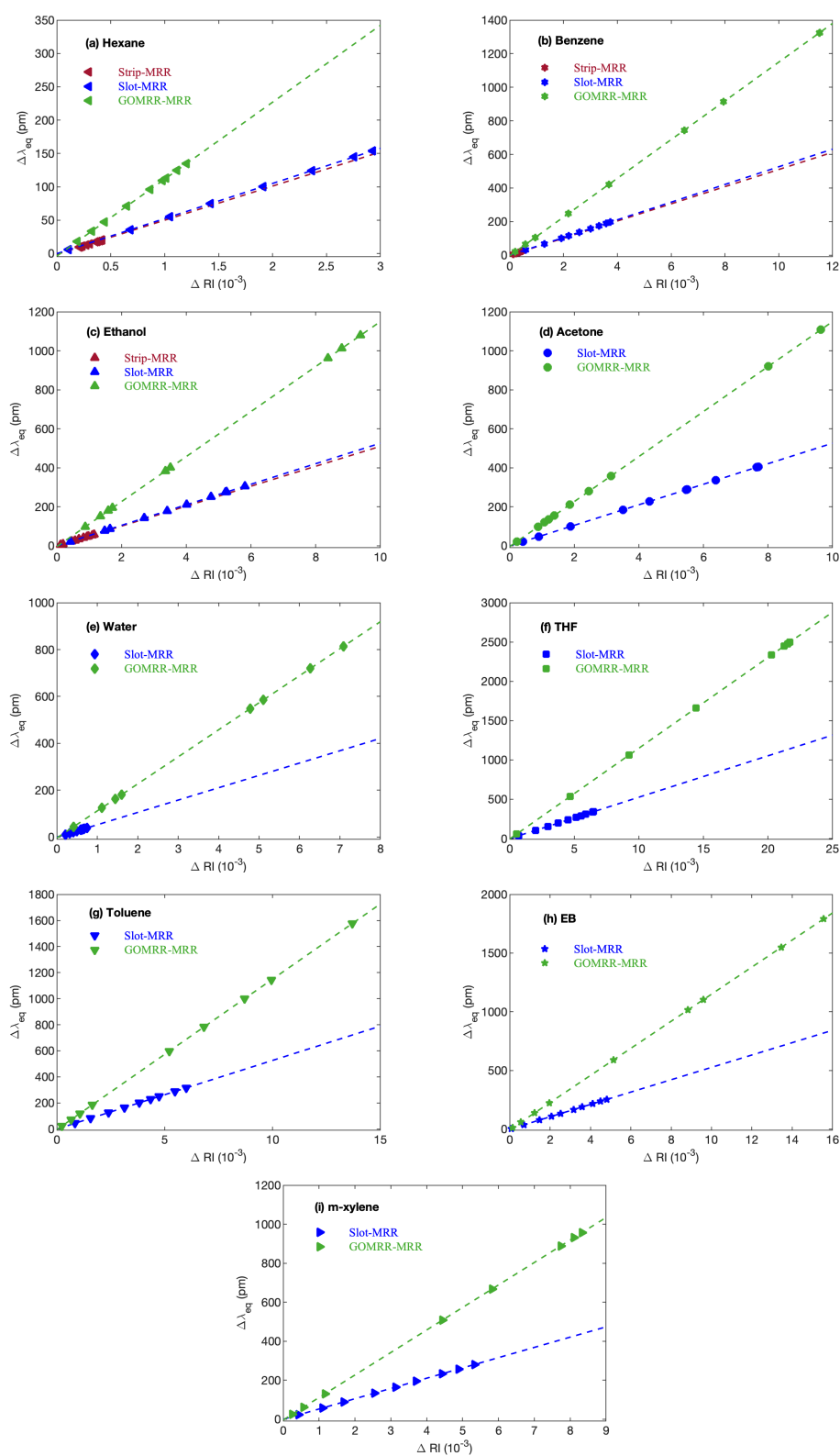


Figure 5.11 Sensitivity measurements showing equilibrium resonance shift ($\Delta\lambda_{eq}$) as a function of change in refractive index (ΔRI) for various VOC vapours for strip-MRR (red) slot-MRR (blue) and GOMRR (green)

In this context, routes towards determining the relative molecular selectivity of GOMRR as compared with slot-MRR can be described in terms of cooperativity level, namely the ratio of *Hill* coefficients ($n_{\text{GOMRR}}/n_{\text{slot-MRR}}$). It was noted that the combined effect of relative polarity and kinetic diameter of VOCs is strongly correlated with molecular permeation within GO layers, which lead to a high capillary condensation rate in the confined pore structure of GO. Figure 5.12 shows this cooperativity ratio ($n_{\text{GOMRR}}/n_{\text{slot-MRR}}$) as a function of molecular polarity relative to kinetic diameter. The error bars indicate the standard fitting error for the parameter n_{GOMRR} and $n_{\text{slot-MRR}}$.

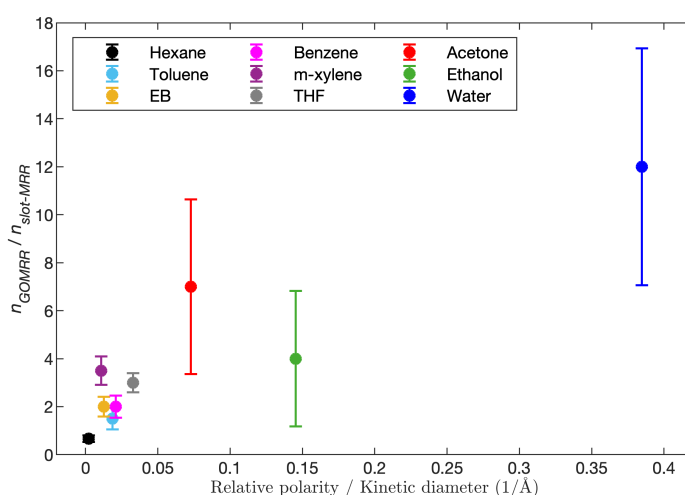


Figure 5.12 *Hill* coefficient ratio ($n_{\text{GOMRR}}/n_{\text{slot-MRR}}$) as a function of the relative polarity - kinetic diameter ratio for all VOCs tested, green dashed line is a guide to the eye [22]

5.6 Summary and Future Work

In summary, the integration of the GO layer resulted in an enhanced VOC vapour detection when compared to an identical, uncoated (control) device. Here the GO layer can act as very precise molecular sieve [67]. The characteristic sigmoidal behaviour of the GOMRR device suggests that most of the tested VOCs experience capillary condensation within the graphene oxide interlayers [60]. The extracted *Hill* coefficients showed that: $n_{\text{GOMRR}} > n_{\text{slot-MRR}} > n_{\text{strip-MRR}}$ for almost all VOCs with the exception of Hexane where n_{GOMRR} is actually lower than $n_{\text{slot-MRR}}$ due to Hexane's inherent

incapability of forming multilayers on GO. In general, the oxygenated VOCs, especially ethanol, acetone and water, demonstrated the highest n_{GOMRR} , suggesting that their molecules are adsorbed on the GO layers. The remaining oxygenated VOC, namely THF, has shown slightly lower n_{GOMRR} as compared to the same VOCs category, which might indicate its inability to permeate through the GO interlayers due to its large kinetic diameter, as shown in Table 5.2. The relationship between the molecular characteristics (i.e. relative polarity and kinetic diameter) and the ratio of Hill coefficients ($n_{\text{GOMRR}}/n_{\text{slot-MRR}}$) provides a potential route to discriminating between different VOCs.

In future work, we aim to design and fabricate strip-based slotted MRRs with a fixed (unetched) over-coupled region. Unlike the rib-based slotted MRR (described in this chapter), where a large portion of the confined fields are located under the slot, the strip structure allows the electric field to be fully concentrated within the slot region, allowing improved sensitivities. The over-coupled region between the bus and MRR should be carefully designed in order to ensure that the deposited GO can actually increase the ER of the MRR notches, as explained in section 4.6.2. In addition, we aim to adopt techniques to precisely measure and control the number of the GO layers [68, 69] and study their effect on the device sensitivity and selectivity.

5.7 References

1. "Volatile organic compounds' impact on indoor air quality." Retrieved 4 July 2020, from <https://www.epa.gov/indoor-air-quality-iaq/volatile-organic-compounds-impact-indoor-air-quality>.
2. Kim, Chen, Cheng, Gindulyte, He, He, et al. (2021). Pubchem in 2021: New data content and improved web interfaces. *Nucleic acids research*, 49(D1), D1388-D1395.
3. "Wikiwand website." from <https://www.wikiwand.com>.
4. Linstrom, & Mallard. (2001). The nist chemistry webbook: A chemical data resource on the internet. *Journal of Chemical & Engineering Data*, 46(5), 1059-1063.
5. Wu, Gong, Olson, & Li. (2012). Commensurate adsorption of hydrocarbons and alcohols in microporous metal organic frameworks. *Chemical reviews*, 112(2), 836-868.
6. Gales, Mendes, & Costa. (2000). Hysteresis in the cyclic adsorption of acetone, ethanol and ethyl acetate on activated carbon. *carbon*, 38(7), 1083-1088.
7. Lashaki, Fayaz, Niknaddaf, & Hashisho. (2012). Effect of the adsorbate kinetic diameter on the accuracy of the dubinin–radushkevich equation for modeling adsorption of organic vapors on activated carbon. *Journal of hazardous materials*, 241, 154-163.
8. Shah, Kissick, Ghorpade, Hannah, & Bhattacharyya. (2000). Pervaporation of alcohol–water and dimethylformamide–water mixtures using hydrophilic zeolite naa membranes: Mechanisms and experimental results. *Journal of Membrane Science*, 179(1-2), 185-205.
9. Reichardt. (1994). Solvatochromic dyes as solvent polarity indicators. *Chemical reviews*, 94(8), 2319-2358.
10. Saunders, Sanders, Chen, & Loock. (2016). Refractive indices of common solvents and solutions at 1550 nm. *Applied optics*, 55(4), 947-953.
11. Hale, & Querry. (1973). Optical constants of water in the 200-nm to 200- μ m wavelength region. *Applied optics*, 12(3), 555-563.
12. Thomson. (1946). The antoine equation for vapor-pressure data. *Chemical reviews*, 38(1), 1-39.
13. Dean. (1992). *Lange's handbook of chemistry* (Vol. 15): McGraw-Hill New York.

14. Liu, Liu, Chu, Hayasaka, Joshi, Cui, et al. (2018). Ac phase sensing of graphene fets for chemical vapors with fast recovery and minimal baseline drift. *Sensors and Actuators B: Chemical*, 263, 94-102.
15. Zhang, Chen, & Hu. (2015). Organic field-effect transistor-based gas sensors. *Chemical Society Reviews*, 44(8), 2087-2107.
16. Peterson, Aujla, Grant, Brundle, Thompson, Vande Hey, et al. (2017). Practical use of metal oxide semiconductor gas sensors for measuring nitrogen dioxide and ozone in urban environments. *Sensors*, 17(7), 1653.
17. Chen, Paronyan, & Harutyunyan. (2012). Sub-ppt gas detection with pristine graphene. *Applied Physics Letters*, 101(5), 053119.
18. Choi, Choi, Kim, Choe, Chung, Shin, et al. (2014). Flexible and transparent gas molecule sensor integrated with sensing and heating graphene layers. *small*, 10(18), 3685-3691.
19. Wang, Paez, Abd El-Rahman, Wang, Dow, Cartledge, et al. (2017). Resonance control of a silicon micro-ring resonator modulator under high-speed operation using the intrinsic defect-mediated photocurrent. *Optics express*, 25(20), 24827-24836.
20. "Originpro." (2020). from <https://www.originlab.com/origin>.
21. Barrios. (2009). *Analysis and modeling of a silicon nitride slot-waveguide microring resonator biochemical sensor* (Vol. 7356): SPIE.
22. Tsui, Alsalman, Mao, Alodhayb, Albrithen, Knights, et al. (2020). Graphene oxide integrated silicon photonics for detection of vapour phase volatile organic compounds. *Scientific reports*, 10(1), 1-11.
23. Claes, Molera, De Vos, Schacht, Baets, & Bienstman. (2009). Label-free biosensing with a slot-waveguide-based ring resonator in silicon on insulator. *IEEE Photonics journal*, 1(3), 197-204.
24. Barrios, Banuls, Gonzalez-Pedro, Gylfason, Sanchez, Griol, et al. (2008). Label-free optical biosensing with slot-waveguides. *Optics letters*, 33(7), 708-710.
25. Rye, Nelson, & Dugger. (1997). Mechanistic aspects of alkylchlorosilane coupling reactions. *Langmuir*, 13(11), 2965-2972.
26. Liu, Michalak, Chopra, Pujari, Cabrera, Dick, et al. (2016). Surface etching, chemical modification and characterization of silicon nitride and silicon oxide—selective functionalization of si₃n₄ and sio₂. *Journal of Physics: Condensed Matter*, 28(9), 094014.

27. Vorathamrong, Panyakeow, Ratanathamphan, & Praserttham. (2019). Surface evolution of native silicon oxide layer and its effects on the growth of self-assisted vls gaas nanowires. *AIP Advances*, 9(2), 025318.
28. Vivien, Grillot, Cassan, Pascal, Lardenois, Lupu, et al. (2005). Comparison between strip and rib soi microwaveguides for intra-chip light distribution. *Optical materials*, 27(5), 756-762.
29. Yu, Wang, Xu, Chen, Fu, Wu, et al. (2018). Adsorption of vocs on reduced graphene oxide. *Journal of Environmental Sciences*, 67, 171-178.
30. Chen, & Chen. (2015). Macroscopic and spectroscopic investigations of the adsorption of nitroaromatic compounds on graphene oxide, reduced graphene oxide, and graphene nanosheets. *Environmental science & technology*, 49(10), 6181-6189.
31. Yang, Su, Chi, Cherian, Huang, Kravets, et al. (2017). Ultrathin graphene-based membrane with precise molecular sieving and ultrafast solvent permeation. *Nature materials*, 16(12), 1198-1202.
32. Sun, Zhu, Liu, Shen, & Bai. (2019). Selective molecular sieving through a large graphene nanopore with surface charges. *The Journal of Physical Chemistry Letters*, 10(22), 7188-7194.
33. Li, Song, Zhang, Huang, Li, Mao, et al. (2013). Ultrathin, molecular-sieving graphene oxide membranes for selective hydrogen separation. *science*, 342(6154), 95-98.
34. Alen, Nam, & Dastgheib. (2019). Recent advances in graphene oxide membranes for gas separation applications. *International journal of molecular sciences*, 20(22), 5609.
35. Yaragalla, Mishra, Thomas, Kalarikkal, & Maria. (2019). *Carbon-based nanofillers and their rubber nanocomposites: Fundamentals and applications*: Elsevier.
36. Munz, Giusca, Myers-Ward, Gaskill, & Kazakova. (2015). Thickness-dependent hydrophobicity of epitaxial graphene. *Acs Nano*, 9(8), 8401-8411.
37. Wang, Wang, Park, Yang, Shen, & Yao. (2009). Synthesis of enhanced hydrophilic and hydrophobic graphene oxide nanosheets by a solvothermal method. *carbon*, 47(1), 68-72.
38. Mao, Calatayud, Mirabello, Hodges, Martins, Botchway, et al. (2016). Interactions between an aryl thioacetate-functionalized zn (ii) porphyrin and graphene oxide. *Advanced Functional Materials*, 26(5), 687-697.

39. Hummers Jr, & Offeman. (1958). Preparation of graphitic oxide. *Journal of the american chemical society*, 80(6), 1339-1339.
40. Muzyka, Drewniak, Pustelny, Chrubasik, & Gryglewicz. (2018). Characterization of graphite oxide and reduced graphene oxide obtained from different graphite precursors and oxidized by different methods using raman spectroscopy. *Materials*, 11(7), 1050.
41. Yeh, Hsu, Teague, Wang, Boyd, & Chen. (2016). Nanoscale strain engineering of graphene and graphene-based devices. *Acta Mechanica Sinica*, 32(3), 497-509.
42. Ferrari, & Basko. (2013). Raman spectroscopy as a versatile tool for studying the properties of graphene. *Nature nanotechnology*, 8(4), 235-246.
43. Proctor, Gregoryanz, Novoselov, Lotya, Coleman, & Halsall. (2009). High-pressure raman spectroscopy of graphene. *Physical Review B*, 80(7), 073408.
44. Cançado, Jorio, Ferreira, Stavale, Achete, Capaz, et al. (2011). Quantifying defects in graphene via raman spectroscopy at different excitation energies. *Nano letters*, 11(8), 3190-3196.
45. Wróblewska, Dużyńska, Judek, Stobiński, Żerańska, Gertych, et al. (2017). Statistical analysis of the reduction process of graphene oxide probed by raman spectroscopy mapping. *Journal of Physics: Condensed Matter*, 29(47), 475201.
46. Hussein, Crowe, Clark, Milosevic, Vijayaraghavan, Gardes, et al. (2017). Raman mapping analysis of graphene-integrated silicon micro-ring resonators. *Nanoscale research letters*, 12(1), 1-8.
47. Gupta, Carrizosa, Jasinski, & Dimakis. (2018). Charge transfer dynamical processes at graphene-transition metal oxides/electrolyte interface for energy storage: Insights from in-situ raman spectroelectrochemistry. *AIP Advances*, 8(6), 065225.
48. Kravets, Marshall, Nair, Thackray, Zhukov, Leng, et al. (2015). Engineering optical properties of a graphene oxide metamaterial assembled in microfluidic channels. *Optics express*, 23(2), 1265-1275.
49. Zheng, Lin, Yang, & Jia. (2017). Laser trimming of graphene oxide for functional photonic applications. *Journal of Physics D: Applied Physics*, 50(7), 074003.
50. Crowe, Clark, Hussein, Towlson, Whittaker, Milosevic, et al. (2014). Determination of the quasi-te mode (in-plane) graphene linear absorption coefficient via integration with silicon-on-insulator racetrack cavity resonators. *Optics express*, 22(15), 18625-18632.

51. Liu, Gong, Zhang, & Lee. (2017). Graphene oxide papers with high water adsorption capacity for air dehumidification. *Scientific reports*, 7(1), 1-9.
52. Horikawa, Do, & Nicholson. (2011). Capillary condensation of adsorbates in porous materials. *Advances in colloid and interface science*, 169(1), 40-58.
53. Guider, Gandolfi, Chalyan, Pasquardini, Samusenko, Pederzolli, et al. (2015). Sensitivity and limit of detection of biosensors based on ring resonators. *Sensing and bio-sensing research*, 6, 99-102.
54. De Vos, Bartolozzi, Schacht, Bienstman, & Baets. (2007). Silicon-on-insulator microring resonator for sensitive and label-free biosensing. *Optics express*, 15(12), 7610-7615.
55. Stefan, & Le Novère. (2013). Cooperative binding. *PLoS Comput Biol*, 9(6), e1003106.
56. Wool, & Sun. (2011). *Bio-based polymers and composites*: Elsevier.
57. Ringot, Lerzy, Chaplain, Bonhoure, Auclair, & Larondelle. (2007). In vitro biosorption of ochratoxin a on the yeast industry by-products: Comparison of isotherm models. *Bioresource technology*, 98(9), 1812-1821.
58. Swenson, & Stadie. (2019). Langmuir's theory of adsorption: A centennial review. *Langmuir*, 35(16), 5409-5426.
59. Gesztelyi, Zsuga, Kemeny-Beke, Varga, Juhasz, & Tosaki. (2012). The hill equation and the origin of quantitative pharmacology. *Archive for history of exact sciences*, 66(4), 427-438.
60. Buttersack. (2019). Modeling of type iv and v sigmoidal adsorption isotherms. *Physical Chemistry Chemical Physics*, 21(10), 5614-5626.
61. Union, & Pure. (1985). *Chemistry. A., Divisions, PC, Working, I., For, P., Of, H., Assurance, Q., For, S., Laboratories, A., Thompson, M., Ellison, SLR and Wood*, 835-855.
62. Thommes, Kaneko, Neimark, Olivier, Rodriguez-Reinoso, Rouquerol, et al. (2015). Physisorption of gases, with special reference to the evaluation of surface area and pore size distribution (iupac technical report). *Pure and Applied Chemistry*, 87(9-10), 1051-1069.
63. Reedijk, & Poeppelmeier. (2013). Comprehensive inorganic chemistry ii: From elements to applications. In *V1 main-group elem., incl. Noble gases v2 transition elem., lanthanides and actinides v3 bioinorganic fundam. And appl.: Metals in nat. Living syst. And metals in toxicology and med. V4 solid-state mater., incl. Ceramics and minerals v5 porous mater. And nanomaterials v6 homogeneous catal. Appl. V7 surf. Inorganic chem. And heterog. Catal. V8*

coord. And organometallic chem. V9 theory and methods (pp. 1-7196): Elsevier Ltd.

64. Lipatov, Varezchnikov, Wilson, Sysoev, Kolmakov, & Sinitskii. (2013). Highly selective gas sensor arrays based on thermally reduced graphene oxide. *Nanoscale*, 5(12), 5426-5434.
65. Georgakilas, Tiwari, Kemp, Perman, Bourlinos, Kim, et al. (2016). Noncovalent functionalization of graphene and graphene oxide for energy materials, biosensing, catalytic, and biomedical applications. *Chemical reviews*, 116(9), 5464-5519.
66. Tang, Zhao, Shan, Yang, Liu, Cui, et al. (2018). Theoretical insight into the adsorption of aromatic compounds on graphene oxide. *Environmental Science: Nano*, 5(10), 2357-2367.
67. Joshi, Carbone, Wang, Kravets, Su, Grigorieva, et al. (2014). Precise and ultrafast molecular sieving through graphene oxide membranes. *science*, 343(6172), 752-754.
68. Wu, Ren, Gao, Liu, Jiang, & Cheng. (2009). Synthesis of high-quality graphene with a pre-determined number of layers. *carbon*, 47(2), 493-499.
69. Shearer, Slattery, Stapleton, Shapter, & Gibson. (2016). Accurate thickness measurement of graphene. *Nanotechnology*, 27(12), 125704.

6 Novel Sensor Design based on Directional Coupler Integrated MRR (DC-MRR) with Ultra-Large FSR

In this chapter, a novel and simple design with an ultra-large free spectral range (FSR) and high detection sensitivity is reported. The structure consists of a single racetrack-type micro-ring resonator (MRR) connected to double directional couplers (DCs). This device can be employed as a powerful refractive index sensor based on Vernier effect. The device bulk sensitivity can reach values greater than 14,000nm/RIU which is about 47 times higher than the sensitivity of a single slotted ring resonator [1]. In addition, FSRs larger than 232nm can be achieved by optimising the length of the double DCs.

6.1 Directional Couplers (DCs)

DCs are a standard component in PICs for applications in broadband optical routing. The DC consists of two waveguides (WGs) brought into close proximity, as shown in the schematic in Figure 6.1. Light coupled to the device via port, P_1 can efficiently be split to deliver an output optical signal at the two ports; P_2 and P_3 . The length for which maximum energy transfer between the two waveguide cores is achieved is called the beating, or coupling length, L_c . This length is highly dependent on the effective index for the propagating mode. A coupling coefficient, κ , is used to describe the coupling strength between the two waveguides, which is itself a function of several parameters of the device: exact WG dimensions, WG and cover refractive indices, WG separation, G etc. The coupling length, L_c can be controlled by design to achieve, for instance, fraction of input/output power splitting/combining [2], polarisation splitting [3] and biochemical sensing [4].

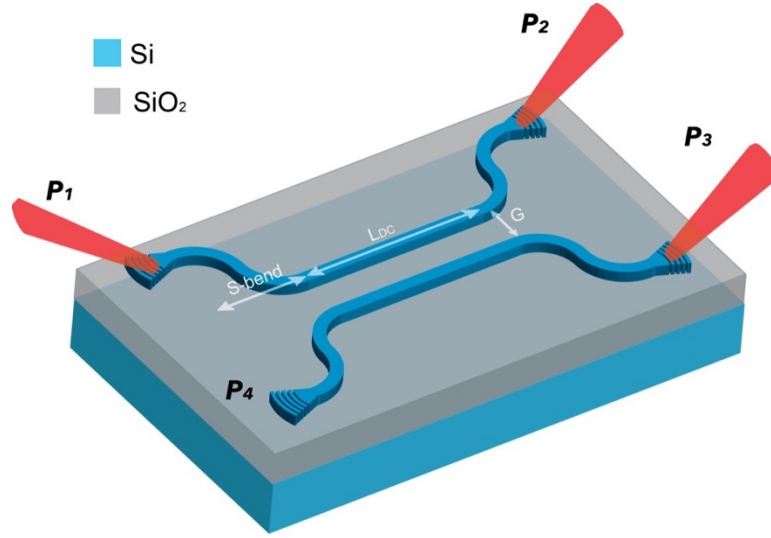


Figure 6.1 A schematic diagram of the directional coupler

Assuming the coupling contributions from S-bends are very small, the through (P_2) and coupled (P_3) powers can be expressed using coupled-mode theory (CMT) [5]:

$$P_2 = P_1 \cos^2 \left(\frac{\pi L_{DC} \Delta n_{eff}}{\lambda} \right) = P_1 \cos^2 \left(\frac{\pi L_{DC}}{2L_c} \right) \quad (6.1)$$

$$P_3 = P_1 \sin^2 \left(\frac{\pi L_{DC} \Delta n_{eff}}{\lambda} \right) = P_1 \sin^2 \left(\frac{\pi L_{DC}}{2L_c} \right) \quad (6.2)$$

Where L_{DC} is the total length of the DC, Δn_{eff} is the difference between the effective indices of even n_{even} (symmetric) and odd n_{odd} (anti-symmetric) supermodes, λ is the wavelength of the input light. The supermodes (n_{even} and n_{odd}) can be calculated from the cross-section of the DC using FDE simulations with fine mesh grid size. The coupling length L_c can be obtained using simulations such as 3D FDTD and EME or theoretically by solving Equation (6.1) or (6.2). The expression for coupling length can be written as [6]:

$$L_c = \frac{\lambda}{2 \Delta n_{eff}} \quad (6.3)$$

Figure 6.2 shows how the effective indices, for the even (red curve) and odd (blue curve) supermodes, vary with the coupling gap ($50 \leq G \leq 800\text{nm}$) for a DC with width, $W = 350\text{nm}$ and height, $H = 220\text{nm}$. In this chapter, all dimensions of each individual WG of the DC are 350nm and 220nm for the width and height, respectively. The refractive indices are 3.48 and 1.44 for the silicon core and buried oxide (BOX), respectively [7, 8] with upper cladding as water (RI = 1.318) at 1550nm [9].

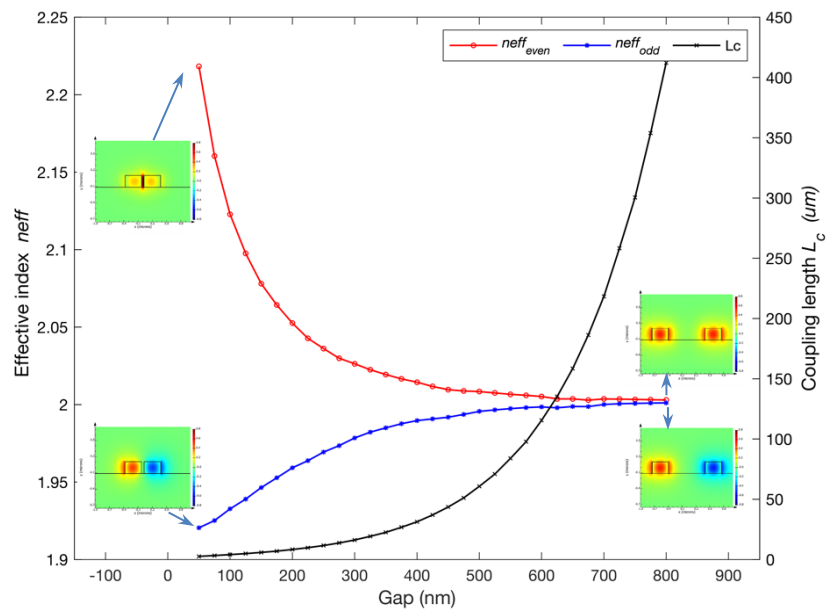


Figure 6.2 Effective indices of the even (red curve) and odd (blue curve) modes for directional coupler with identical waveguide dimensions ($350 \times 220\text{nm}$). The coupling length (black curve) as a function of the coupling gap is displayed in the secondary y-axis. Insets show the even (upper) and odd (lower) modes profile for 50nm (left) and 800nm (right) coupling gaps

The corresponding L_c (to achieve maximum power transfer) is also shown (black curve, right axis). The insets show the modelled electric field (E_x) profiles of the fundamental TE mode. The left-hand side insets show the even (upper inset) and odd (lower inset) super mode profiles for $G = 50\text{nm}$ and the right-hand side insets show even (upper inset) and odd (lower inset) profiles for $G = 800\text{nm}$. For a sufficiently

large separation gap, the even and odd effective indices tend towards the effective index of an isolated waveguide, leading to the requirement for much larger coupling lengths (to achieve efficient power transfer).

Using CMT, the power exchange between two waveguides can be obtained, as shown in Figure 6.3.

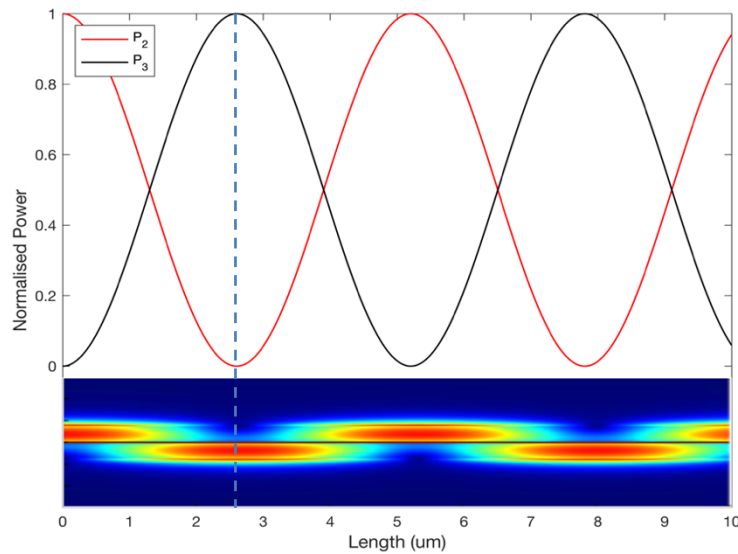


Figure 6.3 Through and coupled powers as a function of DC length with inset of electric field distribution of identical SOI waveguides with gap (G), width and height of 50nm, 350nm and 220nm, respectively. The dashed line indicates the coupling length L_c

With the power coupling (normalised to the input, P_1), Δn_{eff} was obtained using FDE simulations. The inset (bottom) shows the electric field distribution of the two identical waveguides with gap (G), width (W) and height (H) of 50nm, 350nm and 220nm, respectively using EME simulation, where light at 1550nm is injected into P_1 of the DC upper arm at $L = 0$. It is worth noting that for very small gaps such as 50nm, the electric field maximum of the propagating mode is often confined to the low index medium (between the coupled waveguides), which explains the efficient power transfer, even for very small L_c . In this case, the EME simulation derived $L_c (= 2.67\mu\text{m})$ is in close agreement with that calculated using FDE and Equation (6.3) (i.e. $= 2.60\mu\text{m}$).

6.2 DC biochemical sensing

The periodic nature of the output power as a function of distance or wavelength and the dependence of the coupling length on the cover refractive index provides a potential application of the DC as a sensor. The interaction between the evanescent field of the propagating mode and a target analyte will dictate the sensitivity of such a sensor. The refractive index contrast (between the silicon waveguide core and upper cladding) determines the mode confinement (or depth of evanescent wave penetration into the low index cladding) and effective index of the even and odd modes of the DC. The sensing modality can be realised by exploiting the fact that L_c (for maximum power transfer) is a function of the cover refractive index. If this changes, say as a result of the presence of a small perturbation, ΔRI (due to the presence of a target analyte), this can be detected, either by monitoring a change in (coupled) output power (intensity interrogation [10]) at a particular wavelength (with the unit of dB/RIU) or by the more traditional spectral interrogation [10], which determines the wavelength shift ($\Delta\lambda$) in relation to the change in refractive index, ΔRI (with the unit of nm/RIU).

6.2.1 Intensity Interrogation

This technique relies on comparing the output intensity, of either the through or coupled ports, when there is a change in the cover RI. When both arms of the DC are exposed to a small variation of ΔRI , their associated transmitted powers, as a function of DC length or wavelength, propagate with slightly different frequencies. The two signals gradually move out of phase until they reach a maximum phase difference of 180° , leading to the highest sensitivity in dB/RIU. After this point, they start to move back into phase. The minimum DC length (L_{orth}) at which the two signals are nearly orthogonal for an arbitrary wavelength can be obtained from [10]:

$$L_{\text{orth}} = \frac{1}{2} \left(\frac{FSR_0 FSR_1}{|FSR_0 - FSR_1|} \right) = \frac{L_{c_0} L_{c_1}}{|L_{c_0} - L_{c_1}|} \quad (6.4)$$

Where FSR_0 and L_{c0} represent the free spectral range and coupling length for the unperturbed DC and FSR_1 and L_{c1} are those parameters for the same DC with $\Delta RI \neq 0$. When the DC is operated at a fixed, single wavelength, the period or FSR of the transmitted or coupled power can be expressed as: $FSR = 2L_c$.

Since the output signals (with small L_c discrepancy) travel with similar frequency, it is possible to define a phase shift (or ΔL_{DC}) between the two signals. Assuming the phase of P_2 (when $\Delta RI = 0$) to be zero, then the phase of P_2 (when $\Delta RI \neq 0$) lags or advances by ΔL_{DC} according to:

$$\Delta L_{DC} = \left(\frac{L_{c1} - L_{c0}}{L_{c1}} \right) L_{DC} \quad 0 \leq L_{DC} \leq L_{orth} \quad (6.5)$$

In Figure 6.4, the transmitted power, with respect to the input, (P_2/P_1) for $\Delta RI = 0.02$ were extracted using 3D EME solver. The length of the DC was swept from 0 to $100\mu\text{m}$ at a wavelength of 1550nm for $G = 50, 100, 200$ and 300nm . The unperturbed and perturbed output signals tend to a 180° phase shift for DC lengths of $307.1, 404.1, 820.2$ and $1688.7\mu\text{m}$ for $G = 50, 100, 200$ and 300nm , respectively.

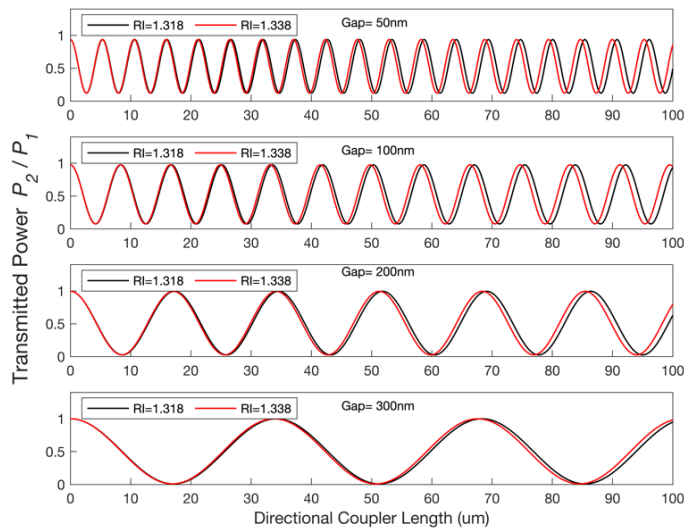


Figure 6.4 Transmitted power for RI = 1.318 (black) and 1.338 (red) as a function of the DC length for different separation gaps, G

6.2.2 Wavelength Interrogation

When a broadband light source is coupled to one arm of the DC, the transmitted or coupled power, at a fixed DC length, varies sinusoidally with wavelength. The expression for the FSR of the transmitted and coupled powers are no longer independent of length and can be expressed as:

$$FSR_{DC}(\lambda) = \frac{\lambda^2}{L_{DC} \Delta n_{eff}} = \left(\frac{2L_c}{L_{DC}} \right) \lambda \quad (6.6)$$

Where Δn_{eff} is the difference of the effective indices of the even and odd supermodes. The wavelength shift ($\Delta\lambda$), due to a change in RI, is evaluated in a similar manner as ΔL_{DC} . The expression for $\Delta\lambda$ can be written as [11]:

$$\Delta\lambda_{DC} = \left(\frac{\partial n_{even}}{\partial RI} - \frac{\partial n_{odd}}{\partial RI} \right) \frac{\lambda_0}{\Delta n_{g0}} \quad (6.7)$$

Where λ_0 is the unperturbed wavelength, $\frac{\partial n_{even}}{\partial RI}$ and $\frac{\partial n_{odd}}{\partial RI}$ represent the change of effective index due to a change in RI for the even and odd supermodes, respectively and Δn_{g0} is the difference of the group index of the even and odd modes of the unperturbed DC. The device sensitivity can be obtained, as described in section 2.6.1, from $S = \Delta\lambda_{DC}/\Delta RI$.

Figure 6.5 demonstrates the wavelength shift due to a change, ΔRI . The device sensitivities were found to be 177, 159, 113 and 86nm/RIU for $G = 50, 100, 200$ and 300nm, respectively.

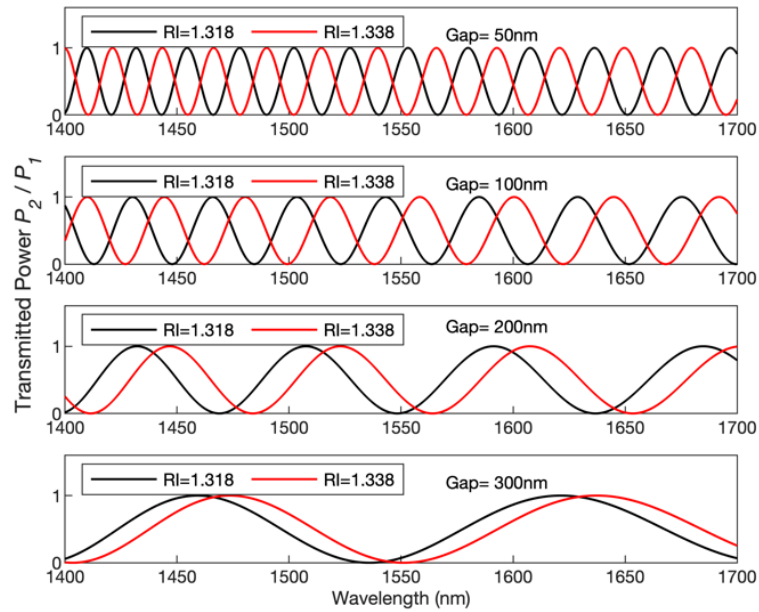


Figure 6.5 Transmitted power for RI = 1.318 (black) and 1.338 (red) as a function of wavelength for different separation gap, G

6.3 Novel DC coupled racetrack-type MRR

Here we describe a novel approach by coupling a relatively long DC to a racetrack-type MRR, Figure 6.6. This device can achieve an ultra-large FSR, compared with either the isolated DC or MRR sensors described earlier. This novel device exploits and combines the sensing and operation mechanism of the DC described by Uchiyama et al [4] and the powerful behaviour of the ring resonator [12].

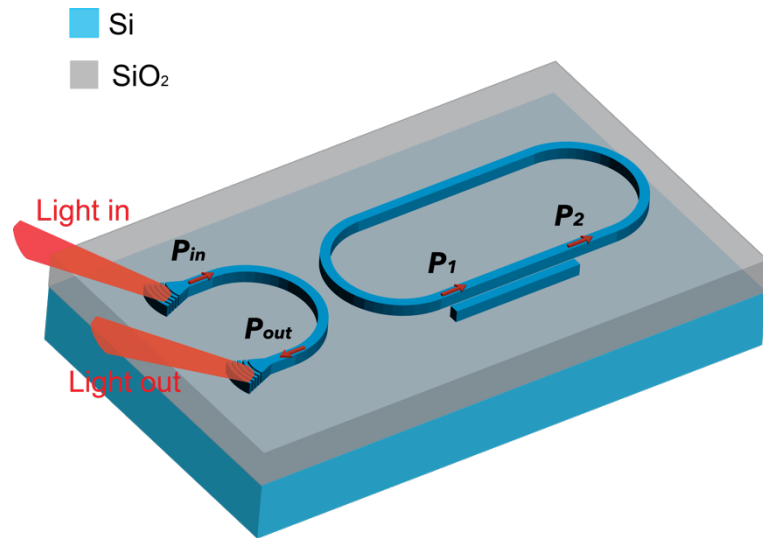


Figure 6.6 Schematic diagram of the proposed DC coupled MRR sensor illustrating input and output ports

A similar design, which merges a strip-based and a slot WG via a strip-to-slot mode-converter, was presented by Steglich et al. in which the input light was coupled to the MRR cavity via straight coupling section [13], whereas our proposed device couples the input signal via single-point coupler and introduce the slot WG (or DC) abruptly (i.e. without mode-converter). The main objective in that work was to enhance the MRR Q-factor, enhancing spectral sensitivity, whereas the design proposed here is based on MRR cavity ‘loss modulation’, enabling a sensing modality based on detection of signal amplitude (rather than spectral) changes.

One of the critical aspects of this design is the extension of the FSR, which the DC provides. Large FSRs are essential in many applications, such as filters and sensing, especially when a large tuning range (dynamic range) is required. A straightforward method to increase the FSR of a microring resonator (MRR) is by directly reducing the overall roundtrip length for the light because the FSR is inversely proportional to cavity circumference, as shown in Equation (2.7). However, resonators with very small radii (less than 4 μ m) can lead to significant radiation (bend) losses, as shown in Figure 6.7. These radiation losses were obtained directly from FDE Lumerical simulation.

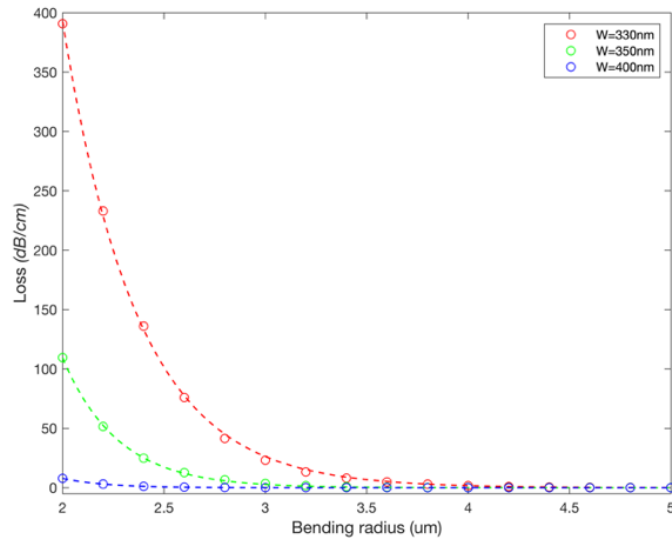


Figure 6.7 Simulations of the attenuation losses of the fundamental mode as a function of the bend radius for different waveguide widths (circles) with its exponential fit (dashed line)

This has motivated many researchers to design novel structures that are capable of extending the FSR of a given MRR without reducing its physical roundtrip length. Li et al. had demonstrated a ring connected to a Mach–Zehnder interferometer (MZI) and a Sagnac mirror which is capable of producing 150 nm FSR due to internal reflection inside the ring [14]. Another well-known approach to extend the FSR is by exploiting the Vernier effect where dual ring resonators with slightly different cavity lengths are connected together to generate an envelope signal with a wider FSR [15, 16, 17]. The drawback of the first device is its (still) limited FSR. The second approach lacks design flexibility where any fabrication error on the dual cavity lengths can modify or cancel the Vernier effect.

6.3.1 Single DC coupled MRR - modelling

In Figure 6.8, the input light (E1) is coupled to the racetrack MRR via a single-point coupler in order to minimise the dependency of the transmission coefficient (t_l) on

wavelength [18]. On the other hand, the long(er) coupling length associated with the DC-MRR means that the transmission coefficient (t_2) will exhibit a strong wavelength dependence [19]. In other words, if the structure includes only a lossless single-point coupler (k_1) without the attachment of the DC (k_2), the output light, in theory, will reveal “notches” or peaks with approximately equal extinction ratio (ER). However, the attachment of the DC will cause the resonant light to be modelled by a sinusoidal function. These resonant light will eventually couples back to the output port displaying peaks with unequal ER.

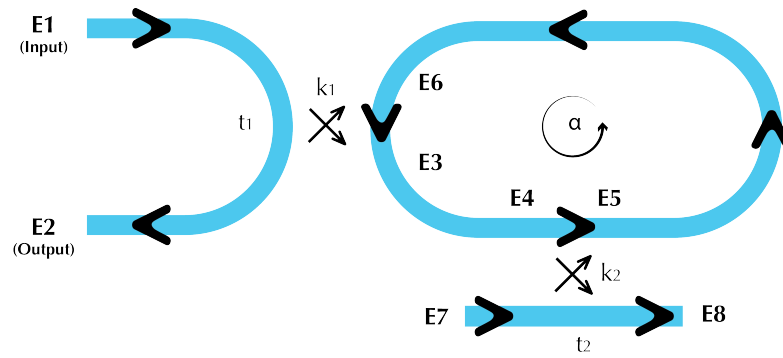


Figure 6.8 Schematic illustration of the single DC coupled MRR model

The proposed device can be described using the well-known matrix analysis of an MRR [20], where the output fields can be related to the input fields via the following:

$$\begin{pmatrix} E2 \\ E3 \end{pmatrix} = \begin{pmatrix} t_1 & i\kappa_1 \\ i\kappa_1 & t_1 \end{pmatrix} \begin{pmatrix} E1 \\ E6 \end{pmatrix} \quad (6.8)$$

$$\begin{pmatrix} E5 \\ E8 \end{pmatrix} = \begin{pmatrix} t_2 & i\kappa_2 \\ i\kappa_2 & t_2 \end{pmatrix} \begin{pmatrix} E4 \\ E7 \end{pmatrix} \quad (6.9)$$

$$\begin{pmatrix} E4 \\ E6 \end{pmatrix} = \begin{pmatrix} \alpha e^{i\frac{\theta}{4}} & 0 \\ 0 & \alpha e^{i\frac{3\theta}{4}} \end{pmatrix} \begin{pmatrix} E3 \\ E5 \end{pmatrix} \quad (6.10)$$

Where t_1 and k_1 represent the transmission and coupling coefficients of the single-point coupler and t_2 and k_2 correspond to the DC, respectively. The loss factor α accounts for all cavity losses and θ represents the phase delay around the racetrack MRR and can be written as:

$$\theta = \frac{2\pi L \bar{n}_{eff}}{\lambda} \quad (6.11)$$

Where, L is the total roundtrip length and \bar{n}_{eff} is the weighted average of the effective indices of DC, radial and straight waveguides of the racetrack MRR as follows [13]:

$$\bar{n}_{eff} = \left(\frac{L_{DC}}{L}\right) n_{effs} + \left(\frac{2\pi R}{L}\right) n_{effb} + \left(\frac{L_{DC}}{L}\right) n_{eff(DC)} \quad (6.12)$$

Where R is the radius of the cavity, n_{effs} and n_{effb} represent the individual effective indices of the straight and bent (radial) waveguide sections, respectively and $n_{eff(DC)}$ is the difference between the effective index of the straight waveguide and the mean value of the even and odd supermodes and can be expressed as [21]:

$$n_{eff(DC)} = n_{effs} - \left(\frac{n_{even} + n_{odd}}{2}\right) \quad (6.13)$$

Assuming $E1 = 1$, $E7 = 0$ and a lossless single-point coupler (i.e. $\kappa_1^2 + t_1^2 = 1$), then the output power (at E2) can be obtained by solving equations (6.8 - 6.10) using a Matlab program, as shown in Listing 6.5.1, The output power can be written as:

$$P_{out} = \left| \frac{t_2 e^{i\theta} \alpha^2 - t_1}{t_1 t_2 e^{i\theta} \alpha^2 - 1} \right|^2 \quad (6.14)$$

The transmission coefficient t_2 is strongly dependent on the physical DC length (L_{DC}) and the coupling length (L_c), as shown in the following equation [19, 21]:

$$t_2 = \cos\left(\frac{\pi L_{DC}}{2L_c}\right) e^{i\left(\frac{2\pi n_{eff}(DC)}{\lambda}\right)L_{DC}} \quad (6.15)$$

Integration of the DC here enables the (isolated) MRR FSR to be extended significantly. The proposed structure can be designed to have a periodic envelope output spectrum (P_{out}) comprising of constituent peaks where the envelope FSR is the same as the DC FSR illustrated in Equation (6.6).

An ultra-large FSR response for a DC coupled racetrack MRR with $L_{DC} = 20.7\mu\text{m}$ and $R = 10\mu\text{m}$ is shown in Figure 6.9. The mean group effective index (\bar{n}_g) was used in the model in order to account for dispersion and can be expressed as [13, 21]:

$$\bar{n}_g = \bar{n}_{eff} - \lambda \left(\frac{\partial \bar{n}_{eff}}{\partial \lambda} \right) \quad (6.16)$$

In Figure 6.9 (a), the cavity losses were assumed to be $\alpha = 0.80$ (i.e. higher) than losses of Figure 6.9 (b) which was assumed to be $\alpha = t_1 = 0.95$. This resulted in deeper notches and slightly narrower FWHM of the envelope output for the latter.

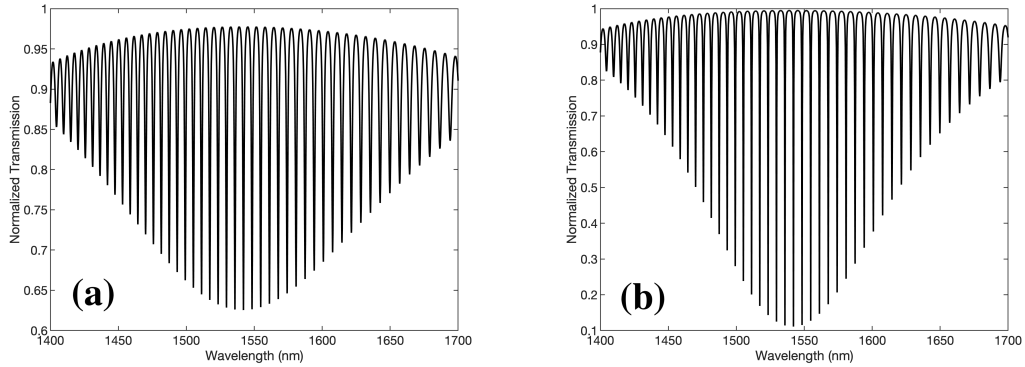


Figure 6.9 Normalised transmission (P_{out}) for a DC coupled racetrack MRR with $L_{DC} = 20.7\mu\text{m}$, $t_1 = 0.95$ and (a) $\alpha = 0.80$ (b) $\alpha = 0.95$

The wavelength shift of the envelope ($\Delta\lambda_{env}$), due to a change of cover RI, for a fixed DC length can be simply derived from the phase shift of the DC, leading to:

$$\Delta\lambda_{env} = \Delta\lambda_{DC} \quad (6.17)$$

For the aforementioned device parameters, the sensitivity and FSR can reach up to 183nm/RIU and 390nm at 1550nm wavelength, respectively. These values can be further enhanced when the DC length is optimised, or by using Vernier cascaded DCs, as will be described in the next section.

6.4 Vernier Cascaded DCs

This section aims to demonstrate a novel design consisting of a double DC integrated racetrack MRR so as to produce a Vernier effect. One of the DCs in this design acts as a reference and the other as a sensor. The sensor DC is exposed to the environment in order to detect variations in the near field refractive index, whereas the reference DC is protected from these changes by a cover SiO₂ cladding, as shown in Figure 6.10.

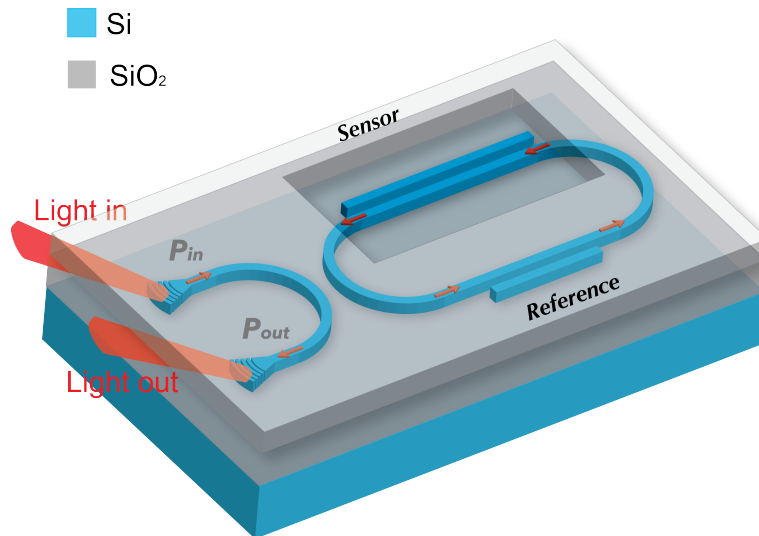


Figure 6.10 Schematic diagram of the double DC coupled MRR

As the input light couples to the racetrack cavity and passes both DCs (reference and sensor), the overall output spectrum (P_{out}) will be a complex combination of the total transmission and coupling coefficients. The Vernier effect is achieved by having dissimilar (reference and sensor) DC transmission coefficients, e.g. by ensuring a difference in the gap (G) or length (L_{DC}) between the reference and sensor DCs.

6.4.1 Double DC coupled MRR - modelling

The schematic illustration of the model is shown in Figure 6.11.

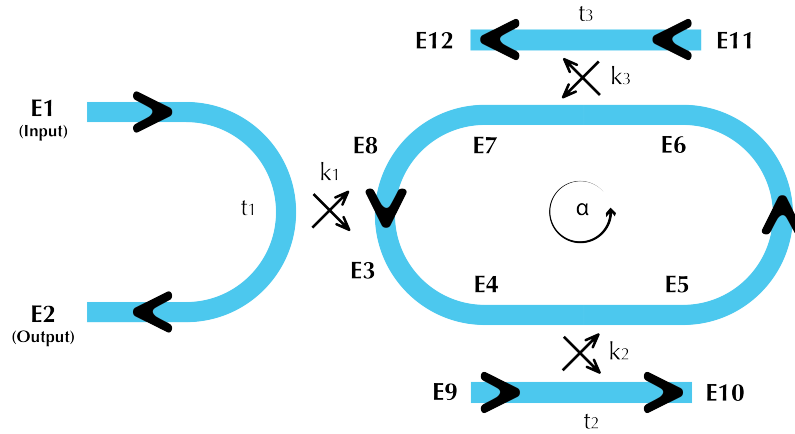


Figure 6.11 Schematic illustration of the ring with DC model

Analogous to the previous section, an analytical expression for the device output power can be obtained by solving the following matrices:

$$\begin{pmatrix} E2 \\ E3 \end{pmatrix} = \begin{pmatrix} t_1 & i\kappa_1 \\ i\kappa_1 & t_1 \end{pmatrix} \begin{pmatrix} E1 \\ E8 \end{pmatrix} \quad (6.18)$$

$$\begin{pmatrix} E5 \\ E10 \end{pmatrix} = \begin{pmatrix} t_2 & i\kappa_2 \\ i\kappa_2 & t_2 \end{pmatrix} \begin{pmatrix} E4 \\ E9 \end{pmatrix} \quad (6.19)$$

$$\begin{pmatrix} E7 \\ E12 \end{pmatrix} = \begin{pmatrix} t_3 & i\kappa_3 \\ i\kappa_3 & t_3 \end{pmatrix} \begin{pmatrix} E6 \\ E11 \end{pmatrix} \quad (6.20)$$

$$\begin{pmatrix} E4 \\ E6 \\ E8 \end{pmatrix} = \begin{pmatrix} \alpha e^{i\frac{\theta}{4}} & 0 & 0 \\ 0 & \alpha e^{i\frac{\theta}{2}} & 0 \\ 0 & 0 & \alpha e^{i\frac{\theta}{4}} \end{pmatrix} \begin{pmatrix} E3 \\ E5 \\ E7 \end{pmatrix} \quad (6.21)$$

The normalised output power was obtained using Matlab, as shown in Listing 6.5.2, and can be written as:

$$P_{out} = \left| \frac{t_2 t_3 e^{-i\theta} \alpha^3 - t_1}{t_2 t_3 e^{-i\theta} \alpha^3 t_1 - 1} \right|^2 \quad (6.22)$$

Where t_1 , t_2 and t_3 correspond to the transmission coefficients of the single-point coupler, reference and sensor DCs, respectively.

Variational FDTD (varFDTD) solver from Lumerical software was utilised to verify the accuracy of our model. The employed parameters in the simulation and model were: $R=3.1\mu\text{m}$, $L_{DC_{ref}} = L_{DC_{sensor}} = 100\mu\text{m}$. The transmission spectrum of the model showed a good fit to the varFDTD result, as depicted in Figure 6.12.

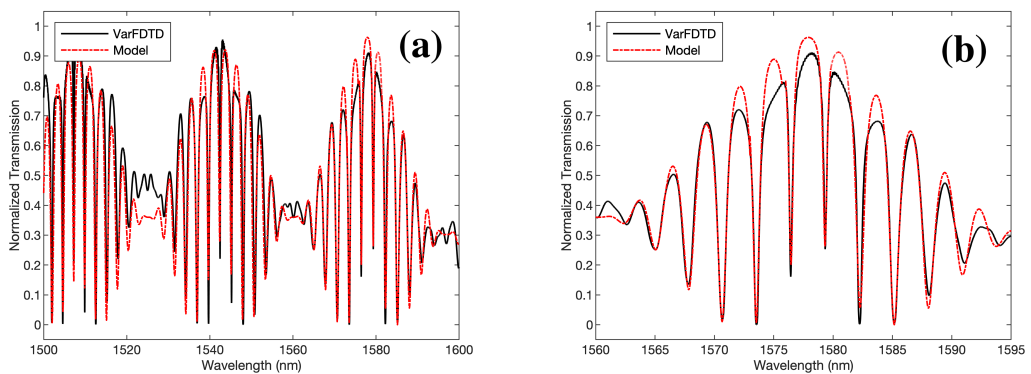


Figure 6.12 The transmission spectrum of the varFDTD simulation (black curve) and our model (red curve) for (a) wide wavelength range and (b) zoomed wavelength range of 1560-1595nm

When the periods of the transmitted powers from reference and sensor DCs are imbalanced, the Vernier effect is realised. Under these conditions, the FSR and sensitivity of this device (compared to the single DC coupled racetrack MRR) are improved by a factor called the Vernier coefficient (C):

$$C = \frac{\text{FSR}_{ref}}{\text{FSR}_{ref} - \text{FSR}_{sensor}} \quad (6.23)$$

Where FSR_{ref} and FSR_{sensor} represent the individual FSRs of the reference and sensor DCs. The overall wavelength shift ($\Delta\lambda_{Vernier}$) and sensitivity ($S_{Vernier}$), due to a change, ΔRI , can be written as:

$$\Delta\lambda_{Vernier} = C \cdot \Delta\lambda_{sensor} \quad (6.24)$$

$$S_{Vernier} = \frac{\Delta\lambda_{Vernier}}{\Delta\text{RI}} \quad (6.25)$$

Where $\Delta\lambda_{sensor}$ is the wavelength shift of the sensor DC. The Vernier sensitivity ($S_{Vernier}$) can be extremely high by designing a large C . Although large C is usually desirable, this can very quickly push the wavelength shift outside of the transparency range of the SOI platform, or detection instrumentation, even for relatively small changes in RI. Hence, C must be chosen to achieve high sensitivities simultaneously with reasonable Vernier FSR. The overall FSR ($\text{FSR}_{Vernier}$), neglecting dispersion, can be written as [15]:

$$\text{FSR}_{Vernier} = \frac{\text{FSR}_{ref} \cdot \text{FSR}_{sensor}}{|\text{FSR}_{ref} - \text{FSR}_{sensor}|} \quad (6.26)$$

In Figure 6.13, the $S_{Vernier}$ (black curve) and $\text{FSR}_{Vernier}$ (red curve) were calculated, using Equation (6.25) and (6.26) as a function of $L_{DC_{sensor}}$ for the double DC coupled

MRR with $L_{DC_{ref}} = 2590\mu\text{m}$. The inset shows the zoomed-in range of $L_{DC_{sensor}}$ which produces a practical $FSR_{Vernier}$.

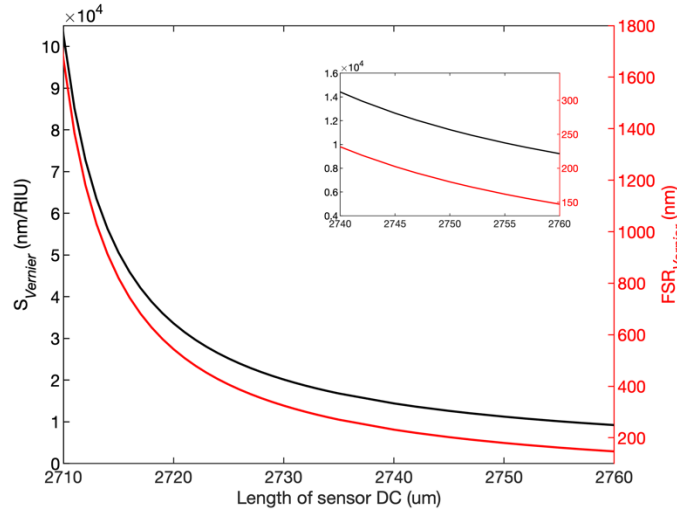


Figure 6.13 The Vernier sensitivity, $S_{Vernier}$, (black curve) and free spectral range, $FSR_{Vernier}$, (red curve) as a function of the length of the sensor DC, $L_{DC_{sensor}}$. The inset shows the zoomed range of $L_{DC_{sensor}}$

At $L_{DC_{sensor}} = 2740\mu\text{m}$, $S_{Vernier}$ reaches values larger than 14,000 nm/RIU with $FSR_{Vernier} = 232\text{nm}$. Hence, this novel SOI device can be employed as a powerful sensor for a system operating around the range of 1400 to 1700nm. In this study, the Vernier coefficient was improved by decreasing the FSR difference between reference and sensor DC (i.e. $|FSR_{ref} - FSR_{sensor}|$) which increased both $S_{Vernier}$ and $FSR_{Vernier}$. However, the $S_{Vernier}$ can be further enhanced by optimising the sensor DC parameters (e.g. width, depth and separation gap G).

6.5 Code Listings

Listing 6.5.1 Output of single DC coupled MRR

```
i= sqrt(-1);
syms E1 E2 E3 E4 E5 E6 E7 E8 t1 t2 k1 k2 alpha theta
%assume E1=1 and E7=0
E1=1;
E7=0;

eqn1= E2 - E1*t1 - E6*k1*i;
eqn2= E3 - E6*t1 - E1*k1*i;
eqn3= E4 - E3*alpha*exp(i*theta/4);
eqn4= E5 - E4*t2 - E7*k2*i;
eqn5= E6 - E5*alpha*exp(i*theta*0.75);
eqn6= E8 - E7*t2 - E4*k2*i;

sol=solve(eqn1,eqn2,eqn3,eqn4,eqn5,eqn6,E2,E3,E4,E5,E6,E8)
sol.E2
```

Listing 6.5.2 Output of double DC coupled MRR

```
i= sqrt(-1);
syms E1 E2 E3 E4 E5 E6 E7 E8 E9 E10 E11 E12 t1 t2 t3 k1 k2 k3 al-
pha theta
E1=1;
E9=0;
E11=0;

eqn1= E2 - E1*t1 - E8*k1*i;
eqn2= E3 - E8*t1 - E1*k1*i;
eqn3= E4 - E3*alpha*exp(i*theta/4);
eqn4= E5 - E4*t2 - E9*k2*i;
eqn5= E6 - E5*alpha*exp(i*theta/2);
eqn6= E7 - E6*t3 - E11*k3*i;
eqn7= E8 - E7*alpha*exp(i*theta/4);
eqn8= E10 - E9*t2 - E4*k2*i;
eqn9= E12 - E11*t3 - E6*k3*i;

sol=solve(eqn1,eqn2,eqn3,eqn4,eqn5,eqn6,eqn7,eqn8,eqn9,E2,E3,E4,E
5,E6,E7,E8,E10,E12)

sol.E2
```

6.6 References

1. Claes, Molera, De Vos, Schacht, Baets, & Bienstman. (2009). Label-free biosensing with a slot-waveguide-based ring resonator in silicon on insulator. *IEEE Photonics journal*, 1(3), 197-204.
2. Han, Kuo, Alic, & Radic. (2018). Ultra-broadband multimode 3db optical power splitter using an adiabatic coupler and a y-branch. 26(11), 14800-14809.
3. Soudi, & Rahman. (2016). Design of a compact polarization splitter by using identical coupled silicon nanowires. 34(17), 4169-4178.
4. Uchiyamada, Okubo, Yokokawa, Carlen, Asakawa, & Suzuki. (2015). Micron scale directional coupler as a transducer for biochemical sensing. *Optics express*, 23(13), 17156-17168.
5. Xing, Khan, Alves Júnior, & Bogaerts. (2017). *Behavior model for directional coupler*. Paper presented at the Proceedings Symposium IEEE Photonics Society Benelux.
6. Stegmaier, & Pernice. (2013). Broadband directional coupling in aluminum nitride nanophotonic circuits. 21(6), 7304-7315.
7. Li, & Data. (1980). Refractive index of silicon and germanium and its wavelength and temperature derivatives. 9(3), 561-658.
8. Malitson. (1965). Interspecimen comparison of the refractive index of fused silica. 55(10), 1205-1209.
9. Hale, & Querry. (1973). Optical constants of water in the 200-nm to 200- μ m wavelength region. 12(3), 555-563.
10. Jin, Li, & He. (2012). Analysis of wavelength and intensity interrogation methods in cascaded double-ring sensors. *Journal of lightwave technology*, 30(12), 1994-2002.
11. Li, Zhang, Zhang, Zhang, Liu, & Wei. (2018). Spectral characteristics and ultrahigh sensitivities near the dispersion turning point of optical microfiber couplers. *Journal of lightwave technology*, 36(12), 2409-2415.
12. Bogaerts, De Heyn, Van Vaerenbergh, De Vos, Kumar Selvaraja, Claes, et al. (2012). Silicon microring resonators. *Laser & Photonics Reviews*, 6(1), 47-73.
13. Steglich, Villringer, Pulwer, Heinrich, Bauer, Dietzel, et al. (2017). Hybrid-waveguide ring resonator for biochemical sensing. 17(15), 4781-4790.

14. Li, Huang, & Bogaerts. (2016). Design of a single all-silicon ring resonator with a 150 nm free spectral range and a 100 nm tuning range around 1550 nm. *Photonics Research*, 4(2), 84-92.
15. Claes, Bogaerts, & Bienstman. (2011). *Vernier-cascade silicon photonic label-free biosensor with very large sensitivity and low-cost interrogation*. Paper presented at the Biosensing and Nanomedicine IV.
16. Claes, Bogaerts, & Bienstman. (2010). Experimental characterization of a silicon photonic biosensor consisting of two cascaded ring resonators based on the vernier-effect and introduction of a curve fitting method for an improved detection limit. *Optics express*, 18(22), 22747-22761.
17. Kim, & Yu. (2016). Cascaded ring resonator-based temperature sensor with simultaneously enhanced sensitivity and range. *Optics express*, 24(9), 9501-9510.
18. McKinnon, Xu, Storey, Post, Densmore, Del age, et al. (2009). Extracting coupling and loss coefficients from a ring resonator. *Optics express*, 17(21), 18971-18982.
19. Del age, Xu, McKinnon, Post, Waldron, Lapointe, et al. (2009). Wavelength-dependent model of a ring resonator sensor excited by a directional coupler. *Journal of lightwave technology*, 27(9), 1172-1180.
20. Rabus. (2007). Ring resonators: Theory and modeling. *Integrated Ring Resonators: The Compendium*, 3-40.
21. Masi, Orobtcchouk, Fan, Fedeli, & Pavesi. (2010). Towards a realistic modelling of ultra-compact racetrack resonators. *Journal of lightwave technology*, 28(22), 3233-3242.

7 Tuneable Superluminal and Slow Light in coupled ring resonators

In this chapter, a full control of resonance splitting, as well as tuneable fast and slow light are demonstrated using SOI-based coupled ring resonators (CRRs). Comprehensive analytical modelling combined with FDTD simulations were employed to study the nonlinear characteristics of the fabricated devices.

7.1 Introduction

It is well known that light travels at a constant speed ($c = 2.99792458 \times 10^8$ m/s) in a vacuum [1]. In general, the velocity of light propagating in a dispersive medium is usually described by the phase velocity ($V_p = c/n$) for a monochromatic beam and group velocity ($V_g = c/n_g$) for a beam, consisting of a finite spread of wavelengths, where n and n_g represent the material refractive index and group index, respectively. Recent studies have shown that the group velocity (V_g) can be manipulated, achieving superluminal (fast) and subluminal (slow) propagation in the same material [2, 3, 4, 5]. This concept was also recently observed in single and coupled optical ring resonators where the resonant modes can experience a significant time delay (i.e. $V_g < c$) [6, 7]. The observation of ‘fast’ light (i.e. $V_g > c$ or $V_g < 0$) is usually achieved under conditions of anomalous dispersion [8, 9]. The device dispersion can be controlled by manipulating the coupling strength and the overall cavity loss (α). Normal dispersion usually occurs in over-coupled ring resonators (i.e. the coupling coefficient (κ) is large compared with the cavity loss), whereas anomalous dispersion occurs in under-coupled cavities where $\kappa < \alpha$ [10]. It is worth mentioning that the ‘fast’ light phenomenon does not violate the ‘Einstein Causality’ where a cause must precede its effect [4, 11, 12]. When V_g exceeds the speed of light (or is negative), the centre of the transmitted peak signal arrives at the output port before the input signal, as shown in Figure 7.1. This unusual peak advancement is attributed to the nonlinear pulse reshaping or rephasing effect caused by the anomalous dispersion ($n_g < 0$) [4, 13, 14, 15]. However,

the true information is carried by the nonanalytical points (i.e. the front edge of the pulse) and can be described by the front velocity (V_f) [16]. This velocity is always \leq the speed of light in vacuum, as described by Sommerfeld and Brillouin [12].

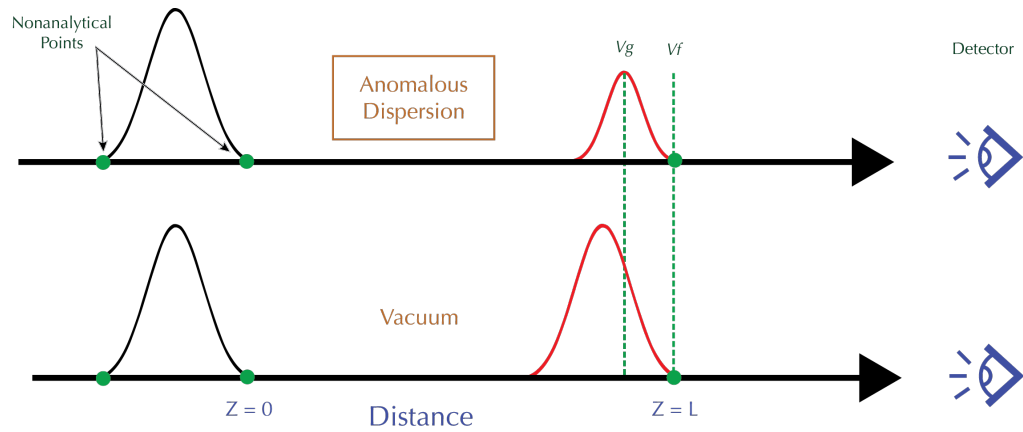


Figure 7.1 Schematic illustration of pulse propagation from $Z = 0$ to $Z = L$ in Vacuum and in a medium with anomalous dispersion. The front edges of the pulses (i.e. the non-analytical points in the leading edge of the peaks) always propagate with $V_f = c$, whereas the centre of the peak passing a medium with anomalous dispersion propagates with superluminal group velocity (i.e. $V_{g(\text{Anomalous})} > V_{g(\text{Vacuum})} = c$)

The characteristics of fast and slow light, which are commonly described by the group delay (τ_g), can be enhanced considerably in devices exhibiting high nonlinearity. Such nonlinearity is observed in strongly coupled resonators, characterised by a signature electromagnetic induced transparency (EIT)-like effect [17, 18, 19]. This interesting fundamental phenomenon was first observed in the gas-phase atomic media [20]. It originates from the quantum interference of optical transitions, induced by coherent interference in atomic systems [21]. In the last decade, the realisation of the optical analogue of EIT has drawn a considerable amount of attention due to the various potential applications; in sensing [22, 23], slow light/optical storage [24], optical switches, modulators [25, 26], gyroscopes [27] and enhanced nonlinear optics [28]. Different platforms and structures were developed to generate the EIT-like effect, such as optical coupled ring resonators (CRR) [29, 30], metamaterials [31] and hybrid configurations [32]. Among the different platforms, SOI coupled ring resonators have

proven to be an excellent platform due to their small footprint, ultra-high index contrast and compatibility with CMOS. Recent approaches have been able to generate and dynamically tune the EIT-like effect in indirectly CRRs [29], directly CRRs [33] and even graphene-based CRRs [26], all of which have the common feature of dynamically introducing small differences between the two CRR optical path lengths to detune their resonances.

7.2 3×3 Coupler based dual (Coupled) Ring Resonator (CRR)

In this chapter, we present a novel design comprised of a set of coupled ring resonators (CRRs), each with the same (designed) geometry (ring radius) with independent thermal tuning capability, with which it is possible to demonstrate EIT-like (and resulting Fano-like resonant spectral line-shapes).

The light is coupled to the device using a common grating coupler and split (3dB) using a y-splitter, which feeds two bus waveguides for delivery of (in theory) half of the power to each of the rings of the CRR, simultaneously. An output (transmitted/through) signal may be measured independently from these two bus waveguides via grating couplers (T_1 , T_2). The rings forming the CRR are coupled, via a third bus waveguide, which serves as a common ‘drop port’, also incorporating a grating coupler for measurement (D_1), as illustrated in the schematic diagram in Figure 7.2.

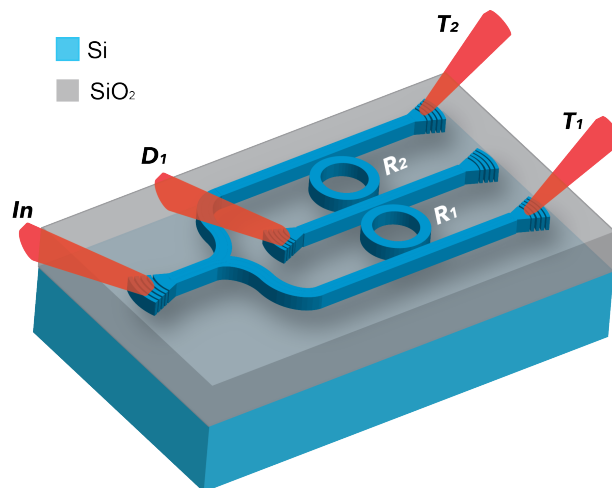


Figure 7.2 Schematic of the 3x3 coupler based CRR design, with rings (R_1 , R_2), coupled via common drop port. Optical Input (In) and Output (T_1 , T_2 and D_1) ports are labelled

Utilising this design, we demonstrated on-chip thermo-optic tuning of an EIT-like effect using integrated titanium nitride (TiN) micro-heaters. The thermo-optic tuning of one of the MRRs (with the other being static) reveals an anti-crossing behaviour and a controllable group delay. We show that, by tuning the device in this way, we can control the group delay over the range -239.2ps to 16.3ps. In this section, we discuss the device operation in more detail and explore the potential applications in e.g. low power optical switching, modulation, optical memory/storage, gyroscopes and sensing. Analytical modelling and FDTD simulations support the experimental data.

7.2.1 Experimental and Modelling Methods

The proposed coupler system was fabricated on an SOI platform via CORNERSTONE foundry. All fabricated waveguides are 220 ± 20 nm strip-based waveguides with underlying buried oxide (BOX) layer of $2\mu\text{m}$ and a $1\mu\text{m}$ thick top cladding oxide layer. For the purpose of the thermo-optic tuning, 60nm-thick titanium nitride (TiN) heaters were deposited on top of the SiO_2 top cladding layer. The full fabrication process is shown in section 3.3.

Both rings (R_1 and R_2), which were illustrated in Figure 7.2, have (nominally, by design) radii of $25\mu\text{m}$ with a waveguide width of 400nm and (bus-to-ring) coupling gaps of 250nm.

Light from either an SLD (model: S5FC1005S Thorlabs, Inc.) or tuneable (external cavity) laser (model: TLK-L1550M, Thorlabs, Inc.) with 3pm wavelength tuning resolution, was coupled into the chip via grating coupler (with a designed centre wavelength of 1550nm) and collected (from the output ports), using a fibre coupled optical spectrum analyser (OSA 203B, Thorlabs), as demonstrated in section 4.2.2. Independent thermo-optic tuning of resonator, R_2 was realised by using electrical probes connected to a 30V power supply unit. A DC current in the micro-heaters dissipates energy, locally, in the form of heat which alters the mode effective index in the tuned resonator, thus shifting its resonance spectrum (with respect to that of the static resonator, R_1).

The CRR design can be modelled using the scattering matrix method (SMM) which describes the behaviour of travelling light in a system where each electric field in each section of the device is modified when it gets transmitted, coupled or attenuated [34]. The schematic in Figure 7.3 illustrates all inputs, outputs and circulating electric fields (E1 to E14), as well as the transmission coefficient, t , coupling coefficient, κ and the loss factor, α (which includes all cavity losses) [35].

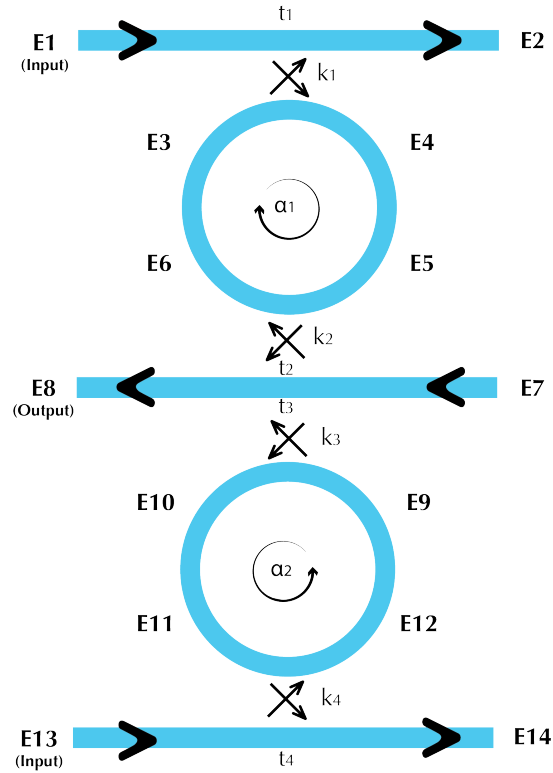


Figure 7.3 Schematic diagram of the 3x3 coupler model as used in the SMM approach

A set of matrices can also be employed to describe the relationship between input and output electric fields in a similar manner, as described in section 3.1.5. The uppermost and lowermost couplers define the through ports (T_1 or E2 and T_2 or E14) with their corresponding inputs (E1 and E13). This relationship is described by the 2x2 matrices, as shown in Equation (7.1) and (7.2):

$$\begin{pmatrix} E2 \\ E4 \end{pmatrix} = \begin{pmatrix} t_1 & i\kappa_1 \\ i\kappa_1 & t_1 \end{pmatrix} \begin{pmatrix} E1 \\ E3 \end{pmatrix} \quad (7.1)$$

$$\begin{pmatrix} \text{E12} \\ \text{E14} \end{pmatrix} = \begin{pmatrix} t_4 & i\kappa_4 \\ i\kappa_4 & t_4 \end{pmatrix} \begin{pmatrix} \text{E11} \\ \text{E13} \end{pmatrix} \quad (7.2)$$

The output of the centre waveguide (D₁ or E8) can be modelled by a 3x3 matrix since it contains two couplers. The following matrix describes the coupled and transmitted fields at the shared drop port:

$$\begin{pmatrix} \text{E6} \\ \text{E8} \\ \text{E10} \end{pmatrix} = \begin{pmatrix} t_2 & i\kappa_2 & i\kappa_2 i\kappa_3 \\ i\kappa_2 & \sqrt{1 - \kappa_2^2 - \kappa_3^2} & i\kappa_3 \\ i\kappa_2 i\kappa_3 & i\kappa_3 & t_3 \end{pmatrix} \begin{pmatrix} \text{E5} \\ \text{E7} \\ \text{E9} \end{pmatrix} \quad (7.3)$$

The cavity loss contributions (α_1, α_2) are incorporated into the entire coupled system by defining the fields (E3, E5, E9 and E11), as shown in Equation (7.4) and (7.5).

$$\begin{pmatrix} \text{E3} \\ \text{E5} \end{pmatrix} = \begin{pmatrix} \alpha_1 e^{i\frac{\theta_1}{2}} & 0 \\ 0 & \alpha_1 e^{i\frac{\theta_1}{2}} \end{pmatrix} \begin{pmatrix} \text{E6} \\ \text{E4} \end{pmatrix} \quad (7.4)$$

$$\begin{pmatrix} \text{E9} \\ \text{E11} \end{pmatrix} = \begin{pmatrix} \alpha_2 e^{i\frac{\theta_2}{2}} & 0 \\ 0 & \alpha_2 e^{i\frac{\theta_2}{2}} \end{pmatrix} \begin{pmatrix} \text{E12} \\ \text{E10} \end{pmatrix} \quad (7.5)$$

Where, (α_1, α_2) represent the half round-trip loss coefficients of the upper and lower ring resonators, respectively and θ_1 and θ_2 are the corresponding phase delays in the rings. The last two terms were divided by two because their associated fields only complete half-circular trips.

The phase delay around each ring (θ) can be expressed in terms of wavelength (λ) or angular frequency (ω) by:

$$\theta = \frac{\omega(2\pi R) n_{eff}}{c} = \frac{4\pi^2 R n_{eff}}{\lambda} \quad (7.6)$$

Where, n_{eff} is the mode effective index, R is the radius of the ring measured from the centre of the ring to the centre of the circular waveguide and c is the vacuum speed of light (equal to 2.99792458×10^8 m/s).

Utilising the law of conservation of energy, we can define the relationship between the transmission and coupling coefficients as $t^2 + \kappa^2 = 1$. Exploiting this and assuming the input fields $E1 = E13 = 1$ and $E7 = 0$, then solving Equations (7.1–7.6), the power output of the shared drop port can be written as:

$$\left| \frac{E8}{E1} \right|^2 = \left| \frac{e^{i\pi} e^{i\frac{\theta_1}{2}} e^{i\frac{\theta_2}{2}} \left(-Ae^{i\frac{\theta_1}{2}} - Be^{i\frac{\theta_1}{2}} - Ce^{i\frac{\theta_2}{2}} - De^{i\frac{\theta_2}{2}} - Ee^{-i\frac{\theta_2}{2}} - Fe^{-i\frac{\theta_1}{2}} \right)}{Ge^{i\theta_1} e^{i\theta_2} + He^{i\theta_1} e^{i\theta_2} + Ie^{i\theta_1} + Je^{i\theta_2} - 1} \right|^2 \quad (7.7)$$

Where,

$$A = -t_1 t_2 \kappa_3 \kappa_4 \alpha_1^2 \alpha_2$$

$$B = -t_1 \kappa_2^2 \kappa_3 \kappa_4 \alpha_1^2 \alpha_2$$

$$C = -t_3 t_4 \kappa_1 \kappa_2 \alpha_1 \alpha_2^2$$

$$D = -t_4 \kappa_1 \kappa_2 \kappa_3^2 \alpha_1 \alpha_2^2$$

$$E = \alpha_1 \kappa_1 \kappa_2$$

$$F = \alpha_2 \kappa_3 \kappa_4$$

$$G = -t_1 t_2 t_3 t_4 \alpha_1^2 \alpha_2^2$$

$$H = -\alpha_1^2 \alpha_2^2 t_1 t_4 \kappa_2^2 \kappa_3^2$$

$$I = \alpha_1^2 t_1 t_2$$

$$J = \alpha_2^2 t_3 t_4$$

This lengthy equation expressing the complex fields at the shared drop port (D_1) was solved by hand and confirmed by Matlab symbolic math toolbox [36].

The effective phase shift (Φ) is described as the argument of the complex transmitted field intensity. The phase shift of the drop port can be expressed as:

$$\Phi = \arg \left(\frac{E8}{E1} \right) \quad (7.8)$$

The group delay (τ_g) is determined from the rate of change of the phase shift (Φ) with respect to the angular-frequency, as [37]:

$$\tau_g = \frac{d\Phi}{d\omega} \quad (7.9)$$

7.2.2 Device Characterisation

In order to determine the CRR device output spectral characteristics, from either the drop (D_1) or through (T_1, T_2) ports, the input wavelength (initially using the tuneable laser) was varied across approximately a single free spectral range, FSR (expected for an isolated ring of $25\mu\text{m}$). Spectral measurements were combined with imaging, using a purpose-built microscope (including IR camera and 24x zoom lens) in order to correlate the spectra with scattered light in the waveguides. Figure 7.4 shows the unperturbed (i.e. no thermal tuning, $I = 0\text{mA}$) transmission spectrum (top) and (inset) the scattered IR image from the device for three wavelengths across the spectrum. The red dashed circles and lines indicate the location of the CRRs and the shared drop port.

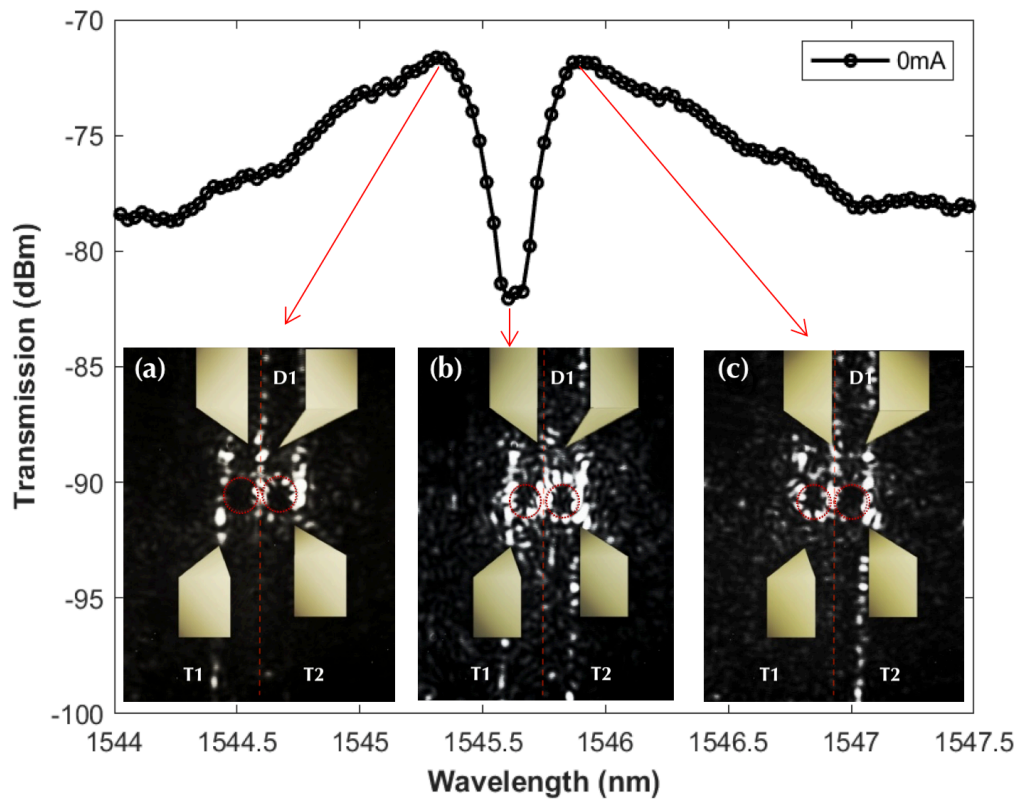


Figure 7.4 (top) Combined experimental unperturbed drop port spectrum with (inset, bottom) IR scattered light microscope images of the CRRs (TiN electrical contacts in Gold and CRR with their shared drop port positions are illustrated by the dashed red circles and lines) at a wavelength of (a) 1545.31nm, (b) 1545.68nm and (c) 1545.94nm

The combined drop spectrum reveals a broad background with a deep, narrow notch at its centre. It is noteworthy that the background signal is much broader than would be expected from a mixture of the two isolated resonators. The much narrower (and deep) notch appears at a wavelength of 1545.68nm and the central (inset) image reveals that, at this wavelength, the driving signal is coupled equally into both rings of the CRR, evidenced by the strong, approximately equal, scattering in both. We also note that the corresponding return signal to the drop port, D_1 is small (or near absent), which explains the ‘notch’ depth, whereas scattered light (of broadly equivalent intensity) can still be observed in both the through ports (to outputs T_1 , T_2) of the device. This suggests that, for this wavelength, the dual resonator system is strongly ‘coupled’

and light can pass from one ‘arm’ of the device to the other (via the ‘drop’ bus), and vice versa, with little ‘resistance’. In this condition, we can also see that there should be a strong interaction between counter-propagating modes in the dual resonator system. For the shorter (longer) wavelength of 1545.31nm (1545.94nm), the corresponding images (insets – bottom left, right) reveal that the light is preferentially coupled to resonator, R_2 (R_1), with the light level at T_2 (T_1) approaching zero. In comparison, the scattered light levels in R_1 (R_2) are much lower/near zero, indicating no coupling of light to this ring, with correspondingly high light levels passing to T_1 (T_2). In either of these latter cases, the resulting signal at D_1 is therefore predominantly associated with light ‘dropped’ from R_2 (R_1).

The modelling described in the previous section shows that the EIT-like spectrum can be produced for identical rings in such a CRR system by: (i) introducing a relative difference in cavity loss between the individual rings, (ii) slightly detuning the resonance wavelength for one ring with respect to the other, i.e. by modifying the mode effective index (n_{eff}) or (iii) varying the coupling or transmission coefficients.

In case (i) small differences in the cavity losses could arise from even small variations in fabrication, e.g. etch non-uniformity and variations in surface roughness. Differences in loss can lead to slight differences in the effective index of the resonant mode; thus, transmission transparency can be observed due to the relative difference in resonant position between the two MRRs. Just a few nanometres difference in waveguide depth (or width) between the two rings can lead to EIT-like effects. Finite-Difference Time-Domain (FDTD) from Lumerical software was utilised to compare the behaviour of the electric field distribution when small differences in cavity loss are present. Figure 7.5 shows the transmission spectra and electric field distribution for two, nearly identical coupled rings (each with 5 μ m radius, for computational efficiency) when a 2nm difference is introduced to their waveguide widths. The results in Figure 7.5 (b-d) were captured at the different wavelengths across the EIT-like spectrum. The electric field distribution in FDTD shows a similar pattern to that observed experimentally in Figure 7.4.

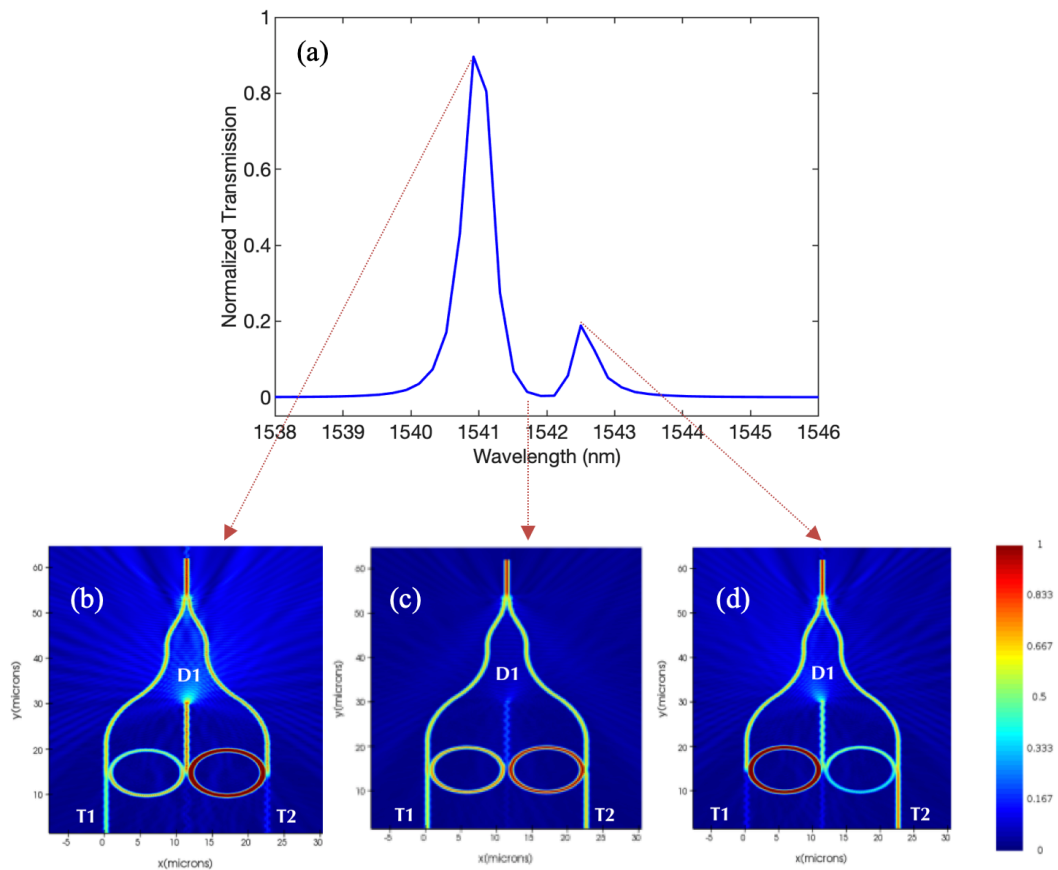


Figure 7.5 FDTD simulation for a CRR system with rings of $5\mu\text{m}$ radius and a small (2nm) difference in the waveguide width. (a) D_1 output spectrum and E-field distribution in the CRR system for (b) the shorter wavelength peak, (c) the central transparency and (d) the longer wavelength peak

In order to overcome the limitations of FDTD for the actual ($25\mu\text{m}$ radius ring) CRR system, the analytical model (proposed in Equation (7.7)) was used to investigate cases (ii) and (iii). Figure 7.6 (a-c) shows the effect of changing the individual parameters of one ring with respect to the other; ring radius, R , effective index, n_{eff} and transmission coefficient, t on the combined drop port (D_1) spectrum.

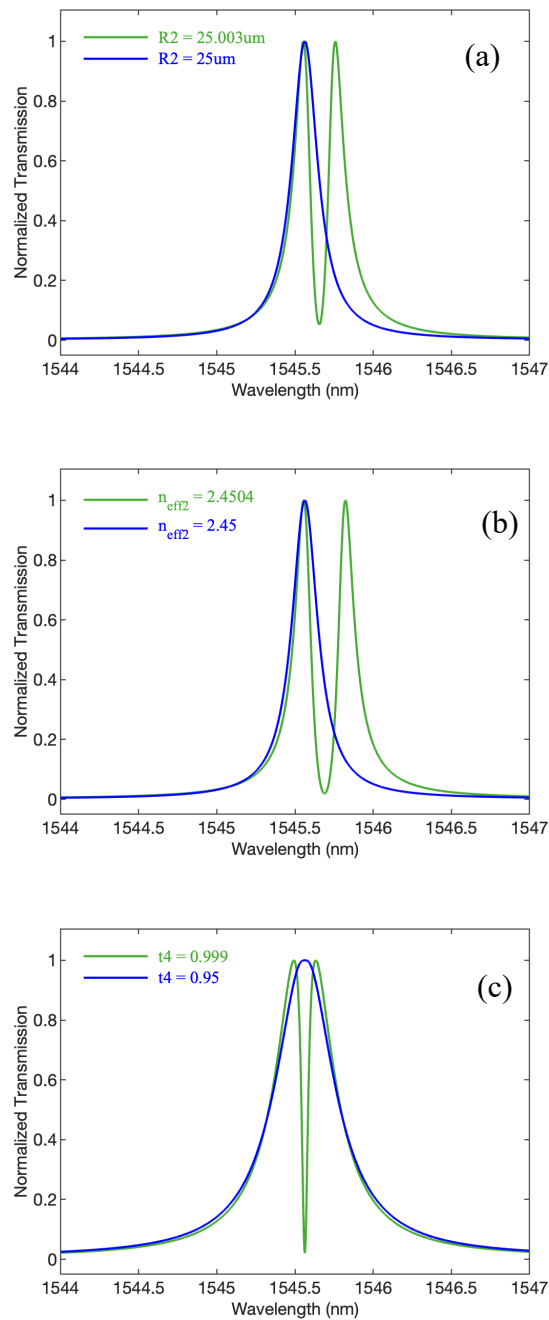


Figure 7.6 Analytical modelling of 3x3 CRR for (a) $R_1 = 25\mu\text{m}$, $n_{\text{eff}1} = n_{\text{eff}2} = 2.45$, $\alpha_{1,2} = 0.99$ and $t_{1,2,3,4} = 0.98$ (b) $R_1 = R_2 = 25\mu\text{m}$, $n_{\text{eff}1} = 2.45$, $\alpha = 0.99$ and $t_{1,2,3,4} = 0.98$ (c) $R_1 = R_2 = 25\mu\text{m}$, $n_{\text{eff}1} = n_{\text{eff}2} = 2.45$, $\alpha_{1,2} = 0.98$, $t_{1,2} = 0.99$ and $t_3 = 0.90$

In Figure 7.6 (a) and (b), the transparency peak can be turned on and off by increasing the radius of the upper ring (R_2) by 3nm or by slightly altering the effective refractive index of mode of R_2 . This implies that this structure can be used as a very sensitive

sensor if only one ring is exposed to analytes and the other ring is used as a reference ring. Furthermore, the mode splitting was also observed when manipulating the coefficients of only one coupler, as illustrated in Figure 7.6 (c).

7.2.3 Thermo-Optic Tuning

The integration of TiN heaters in our device allows us to induce perturbations in the effective index of either ring with respect to the other. This was simulated using the HEAT transport solver (HT) from Lumerical. The heater can be modelled as a uniform power source located at $\sim 1\mu\text{m}$ above the waveguide. A simulation sweep, from 0 to 21mA was implemented and the thermo-optic coefficient for silicon, $dn/dT = 1.8 \times 10^{-4} \text{ K}^{-1}$ at 1550nm [38] was used to convert the temperature map into a change in the effective refractive index of the mode. The temperature profiles for the different input heater powers in the proximity of the buried waveguide are shown in Figure 7.7.

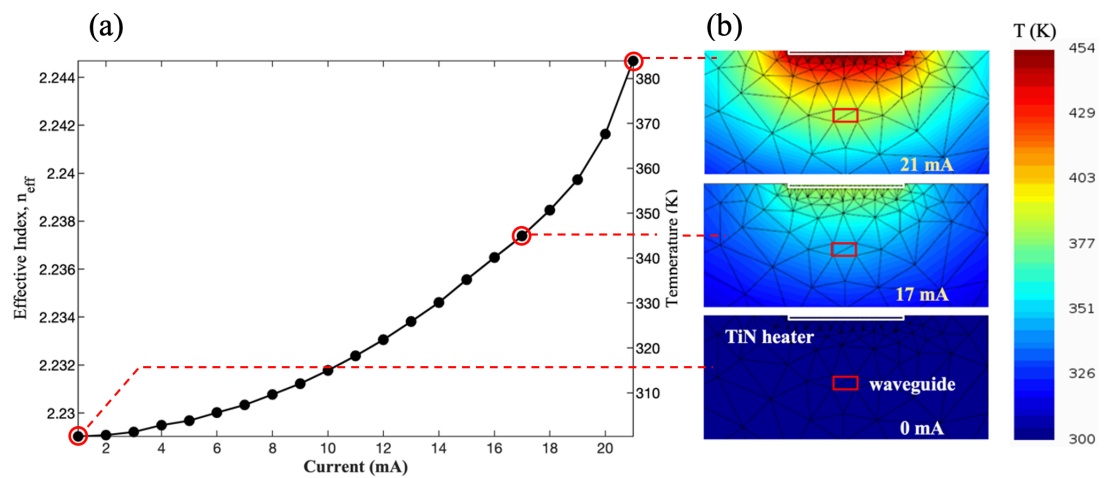


Figure 7.7 (a) Effective index (n_{eff}) and local temperature close to the waveguide as a function of injected (heater) power and (b) thermal distribution close to the waveguide (red box) for heater powers; 0, 17 and 21mA (colour bar labels are temperature in K)

Tuning the resonance wavelength of one of the rings (R_2) reveals changes in the EIT-like effect at the drop port (D_1), as shown in Figure 7.8.

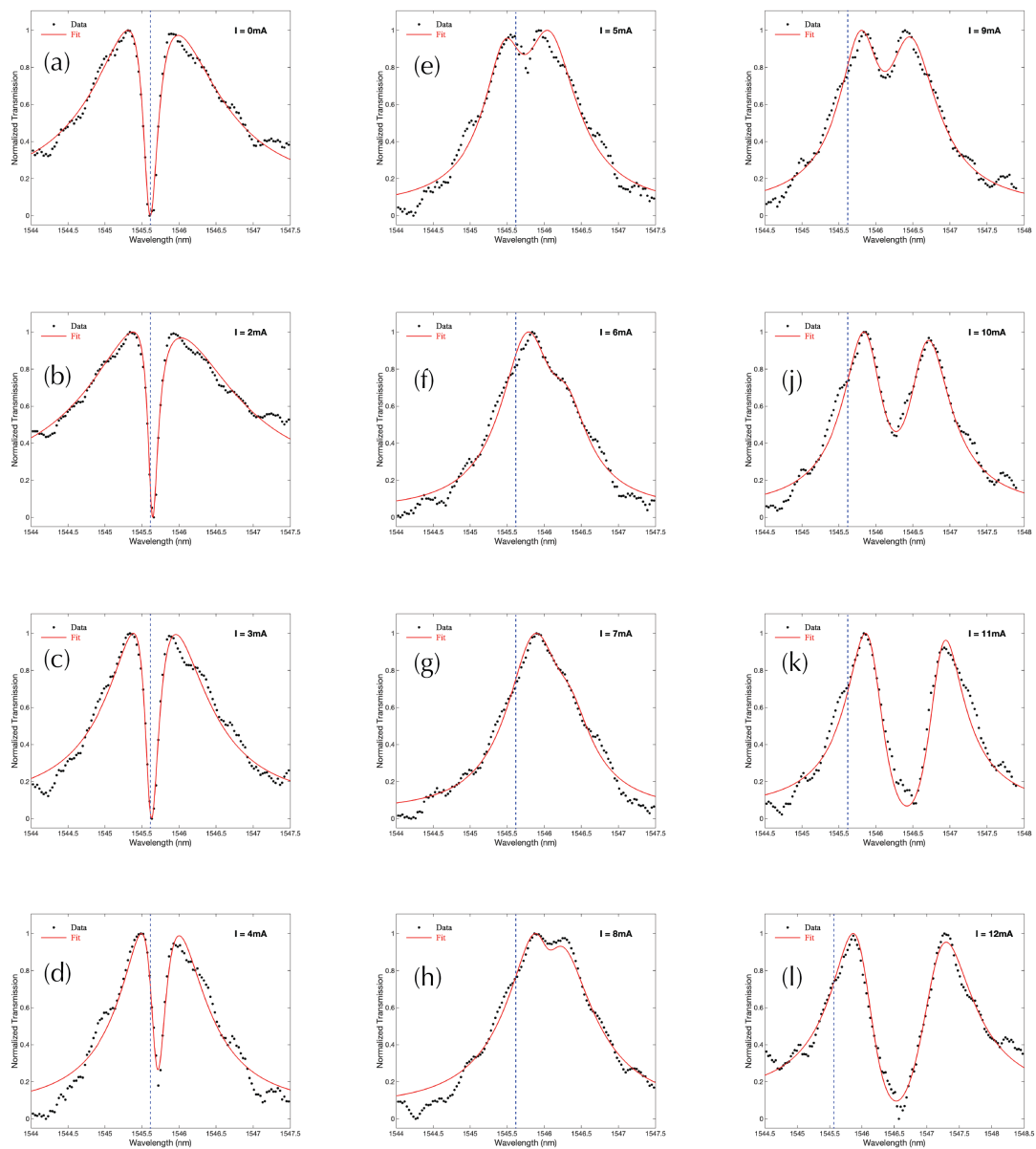


Figure 7.8 Experimental vs modelled drop port (D_1) spectra as a function of R_2 heater currents in the range 0 to 12mA (as indicated in (a) to (l)). The dashed blue line indicates the original position of the transparency

As the heater current is increased, the ‘transparency’ in the drop spectrum initially narrows (at $I = 2$ mA) before becoming shallower and broader ($I = 4$ mA) and eventually disappearing as the background turns into a single peak at $I = 6$ mA, Figure 7.8 (f). We note that, for this heater current, the single peak in the combined spectrum is shifted up in wavelength, from the original position of the transparency, by 0.23nm.

For larger heater currents, $I > 8\text{mA}$, a much wider ‘notch’ re-appears in the combined drop spectrum, and the system begins to resemble two distinct (isolated) resonances (one from each ring). As the heater current is further increased, the longer wavelength peak (associated with R_2) continues to move further away from the ‘static’, shorter wavelength peak associated with R_1 . There are a number of curious aspects associated with this data; firstly, for zero (or very low heater currents), when the two rings are strongly coupled, the background signal (at the wavelength extrema) is rather high ($\sim 40\%$ of the peak amplitude), whereas for larger heater currents (when the rings are apparently de-coupled), the background signal level at the wavelength extrema is much lower, i.e. the bandwidth of the individual (uncoupled) resonances appears to be smaller than when they are combined (coupled), suggesting that the two resonant modes (i.e. R_1 and R_2) hybridize to form “supermodes” for the strongly coupled system [39]. Secondly, the (apparent) steady-state position of the un-tuned ring, R_1 (for $I = 12\text{mA}$ on R_2) is at the wavelength of the combined peak (for $I = 6\text{mA}$), i.e. shifted (up in wavelength) by $\sim 0.23\text{nm}$ from the position of the transparency (at $I = 0\text{mA}$)

The net effect of this is that, as the detuning decreases (i.e. as the resonant modes of the individual rings are brought closer together, by reducing the heater current on R_2) the coupling increases, until, for very small detuning, the combined resonance spectrum rather describes that of a super-mode, consisting of symmetric and anti-symmetric modes at the frequency (ω_s) and (ω_{as}), respectively (which explains the broad background signal with the narrow transparency). In general, the overall CRR cavity response can be described by [40]:

$$\omega_{s,as} = \frac{\omega_{R1} + \omega_{R2}}{2} \pm \sqrt{\frac{(\omega_{R1} - \omega_{R2})^2}{4} + \gamma^2} \quad (7.10)$$

Where, ω_{R1} and ω_{R2} are the resonance frequencies of the stationary (un-tuned) (R_1) and travelling (tuned) (R_2), respectively and γ is the coupling rate between the rings. Increasing the heater current (I) on the tuned ring (R_2) causes a redshift for both resonances, according to $\omega_{R1,R2} = \omega_{0R1,R2} - (\eta_{R1,R2} \times I)$, where $\omega_{0R1,R2}$ is the un-tuned

resonant frequency and $\eta_{R1,R2}$ is the tuning efficiency of both rings. The measured peak positions were fitted with the anti-crossing model, as shown in Figure 7.9.

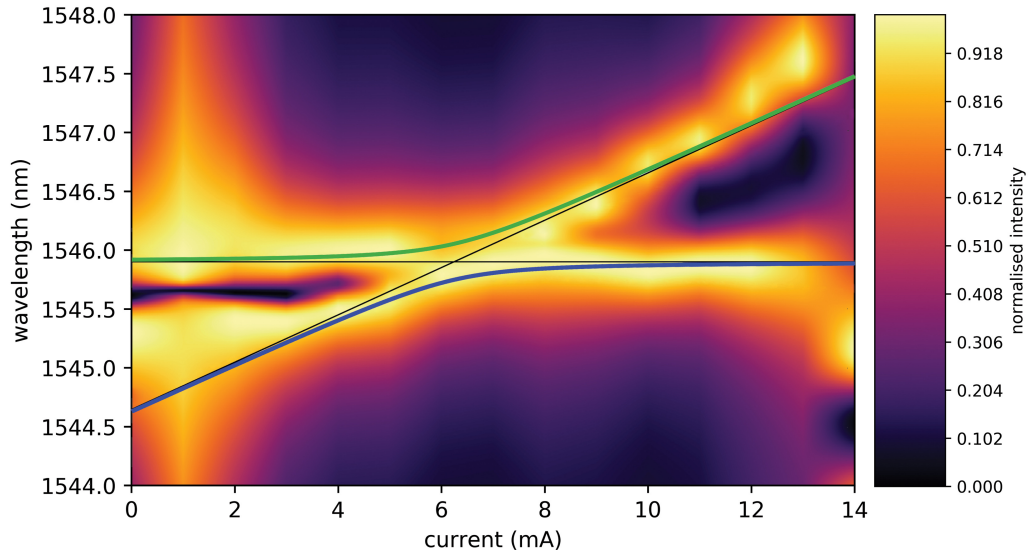


Figure 7.9 Contour plot showing the spectral intensity of the CRR as a function of heater current on R_2 . The black lines represent the uncoupled system, whereas the green and blue curves correspond to the theoretical fit of the stationary and travelling peak positions, respectively using the avoided crossing model, Equation (7.10)

The black lines correspond to CRR with $\gamma = 0$ whereas the green and blue curves resemble the theoretical fit for a strongly coupled system with $\gamma = 2\pi \times 19$ GHz. The tuning efficiencies were extracted from the model. The tuned ring (R_2) exhibited a tuning efficiency (η_{R2}) of $2\pi \times 25$ GHz/A whereas the un-tuned ring (R_1) has $\eta_{R1} = 0$, suggesting that heat, due to injected current, is localised on R_2 and thermal crosstalk between the CRR can be neglected.

Figure 7.10 shows the phase relationship with thermo-optic tuning for the CRR modes. We note that, for small heater currents ($I < 5$ mA), where the coupling regime is strong, an abrupt π phase shift occurs near each cavity resonance, as well as at the transparency wavelength. For heater currents, $4 \text{ mA} < I < 10 \text{ mA}$, only a single π phase shift is observed, similar to that which would be expected across the resonance of a single MRR [41].

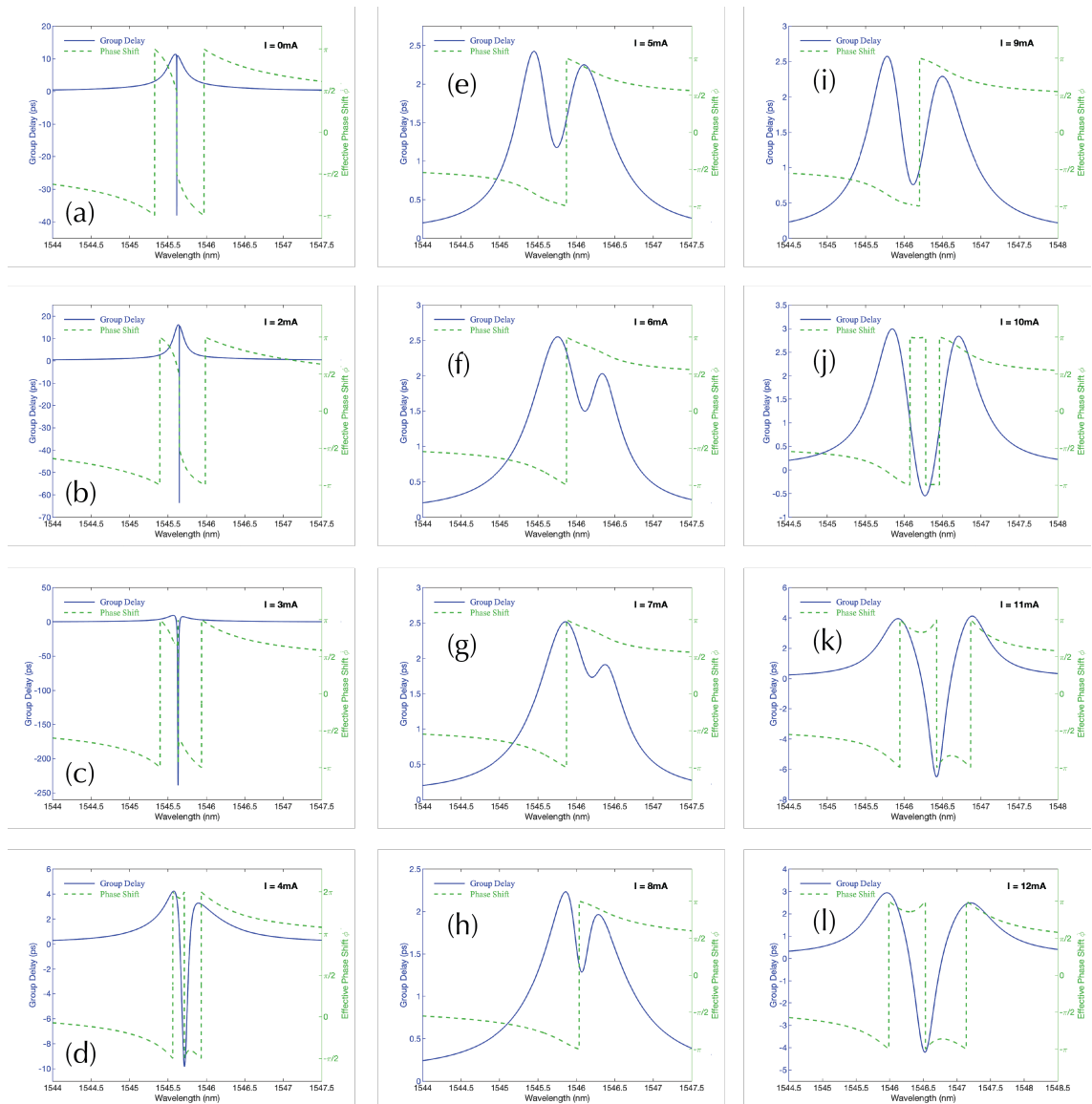


Figure 7.10 Effective phase shift, Φ , (green dashed curves) and group delay, τ_g , (blue curves) of the output signal collected by the shared drop port for heater current on R2 of $I = 0\text{mA}$ to 12mA (as indicated)

By taking the first derivative of the phase, the group delay can be obtained using Equation (7.9). The group delays (τ_g), shown by the blue curves in Figure 7.10, reveal negative τ_g (i.e. fast light) at the transparency wavelength for $I < 5\text{mA}$ whereas only positive τ_g (i.e. slow light) was observed for $4\text{mA} < I < 10\text{mA}$. At the transparency,

the minimum τ_g was realised for $I = 3\text{mA}$ where $\tau_g = -239.2\text{ps}$. Beyond this tuning current, the light near the transparency started to slow down, with τ_g reaching a maximum of 1.6ps at $I = 6\text{mA}$. However, higher group delays were observed near each cavity resonance where the slowest light was found near the left (travelling) peak for $I = 2\text{mA}$ with $\tau_g = 16.2\text{ps}$. Thus, the drop port can realise a controllable τ_g over the range of -239.2ps to 16.2ps by only 3mA tuning current on R_2 , suggesting that this device can be utilised in a range of applications, including optical telecommunication, where the controllable slow light can act as an optical buffer [11, 42], and interferometry, where careful engineering of the group index (n_g) can lead to significant improvements in the spectral sensitivity [43, 44]. Also, the on/off control of the EIT-like resonance peak suggests a great potential in switching applications. The off state (zero tuning current) is represented by the sharp EIT peak whereas the disappearance of the EIT resonance indicates the on state. This state can be acquired by tuning one MRR by 6mA (i.e. the tuned MRR should be heated to 305.6K , as shown in Figure 7.7). We have modelled the heat flow from the on-chip microheaters through the $1\text{-}\mu\text{m}$ SiO_2 cover using the HEAT solver from Lumerical. The temperature profile near the waveguide's surface was monitored as a function of time, as shown in Figure 7.11. The steady-state time (i.e. time required to turn on the EIT resonance) is around $50\mu\text{s}$. This speed can be significantly improved by employing p-n junctions around the cavity waveguide [45], allowing fast modulation (typically $\leq 1\text{ns}$ [46]).

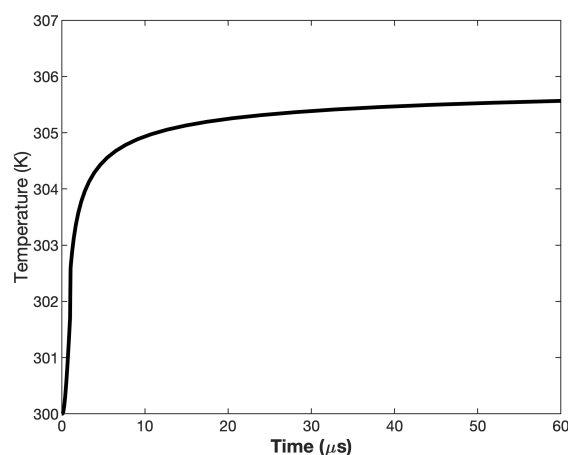


Figure 7.11 Simulation of the temperature rise as function of time at the waveguide's surface

7.3 References

1. Baird, Smith, & Whitford. (1979). Confirmation of the currently accepted value 299 792 458 metres per second for the speed of light. *Optics Communications*, 31(3), 367-368.
2. Liu, Zhu, Chen, & Wu. (2002). Superluminal pulse propagation through one-dimensional photonic crystals with a dispersive defect. *Physical Review E*, 65(4), 046607.
3. Bortman-Arbiv, Wilson-Gordon, & Friedmann. (2001). Phase control of group velocity: From subluminal to superluminal light propagation. *Physical Review A*, 63(4), 043818.
4. Boyd, & Gauthier. (2002). " Slow"and" fast"light.
5. Bigelow, Lepeshkin, & Boyd. (2003). Superluminal and slow light propagation in a room-temperature solid. *science*, 301(5630), 200-202.
6. Heebner, Wong, Schweinsberg, Boyd, & Jackson. (2004). Optical transmission characteristics of fiber ring resonators. *IEEE Journal of Quantum Electronics*, 40(6), 726-730.
7. Heebner, & Boyd. (2002). Slow and stopped light'slow'and'fast'light in resonator-coupled waveguides. *Journal of modern optics*, 49(14-15), 2629-2636.
8. Lin, Liu, Zhang, Li, Zhao, Jin, et al. (2016). Theoretical analyses of resonant frequency shift in anomalous dispersion enhanced resonant optical gyroscopes. *Scientific reports*, 6, 38759.
9. Li, Zhang, Wang, Qiu, & Su. (2009). Fast light in silicon ring resonator with resonance-splitting. *Optics express*, 17(2), 933-940.
10. Totsuka, & Tomita. (2006). Slow and fast light in a microsphere-optical fiber system. *JOSA B*, 23(10), 2194-2199.
11. Boyd, & Gauthier. (2009). Controlling the velocity of light pulses. *science*, 326(5956), 1074-1077.
12. Brillouin. (2013). *Wave propagation and group velocity* (Vol. 8): Academic press.
13. Talukder, Haruta, & Tomita. (2005). Measurement of net group and reshaping delays for optical pulses in dispersive media. *Physical Review Letters*, 94(22), 223901.

14. Mitchell, & Chiao. (1998). Causality and negative group delays in a simple bandpass amplifier. *American Journal of Physics*, 66(1), 14-19.
15. Dogariu, Kuzmich, Cao, & Wang. (2001). Superluminal light pulse propagation via rephasing in a transparent anomalously dispersive medium. *Optics express*, 8(6), 344-350.
16. Morita, & Tomita. (2019). Development of superluminal pulse propagation in a serial array of high-q ring resonators. *Scientific reports*, 9(1), 1-9.
17. Li, & Bogaerts. (2017). Tunable electromagnetically induced transparency in integrated silicon photonics circuit. *Optics express*, 25(25), 31688-31695.
18. Keleshtery, Kaatuzian, Mir, & Zandi. (2017). Method proposing a slow light ring resonator structure coupled with a metal–dielectric–metal waveguide system based on plasmonic induced transparency. *Applied optics*, 56(15), 4496-4504.
19. Wang, Hu, Du, & Long. (2019). Multiple eit and eia in optical microresonators. *Optics express*, 27(5), 7344-7353.
20. Boller, Imamoglu, & Harris. (1991). Observation of electromagnetically induced transparency. *Physical Review Letters*, 66(20), 2593.
21. Fleischhauer, Imamoglu, & Marangos. (2005). Electromagnetically induced transparency: Optics in coherent media. 77(2), 633.
22. Du, Li, Yang, & Lu. (2019). High-performance optical sensing based on electromagnetically induced transparency-like effect in tamm plasmon multilayer structures. 58(17), 4569-4574.
23. Tomita, Totsuka, Hanamura, & Matsumoto. (2009). Tunable fano interference effect in coupled-microsphere resonator-induced transparency. 26(4), 813-818.
24. Li, & Bogaerts. (2017). Tunable electromagnetically induced transparency in integrated silicon photonics circuit. 25(25), 31688-31695.
25. Scheuer, Sukhorukov, & Kivshar. (2010). All-optical switching of dark states in nonlinear coupled microring resonators. 35(21), 3712-3714.
26. Zhou, Zhang, Yin, Chen, & Li. (2017). Dynamically tunable electromagnetically induced transparency in graphene-based coupled micro-ring resonators. 9(2), 1-9.
27. Zhang, Wang, Tian, Wang, Qiu, Wang, et al. (2008). A high sensitivity optical gyroscope based on slow light in coupled-resonator-induced transparency. 372(36), 5848-5852.

28. Zhou, Zhang, Armani, Beausoleil, Willner, & Pang. (2013). Power enhancement and phase regimes in embedded microring resonators in analogy with electromagnetically induced transparency. *21*(17), 20179-20186.
29. Xu, Sandhu, Povinelli, Shakya, Fan, & Lipson. (2006). Experimental realization of an on-chip all-optical analogue to electromagnetically induced transparency. *96*(12), 123901.
30. Wang, Lu, Wang, Xia, & Huang. (2017). Electromagnetically induced transparency and absorption in a compact silicon ring-bus-ring-bus system. *25*(13), 14368-14377.
31. Zhang, Genov, Wang, Liu, & Zhang. (2008). Plasmon-induced transparency in metamaterials. *101*(4), 047401.
32. Weis, Garcia-Pomar, Beigang, & Rahm. (2011). Hybridization induced transparency in composites of metamaterials and atomic media. *19*(23), 23573-23580.
33. Miller, Okawachi, Ramelow, Luke, Dutt, Farsi, et al. (2015). Tunable frequency combs based on dual microring resonators. *23*(16), 21527-21540.
34. Yariv. (2000). Universal relations for coupling of optical power between microresonators and dielectric waveguides. *36*(4), 321-322.
35. Rabus. (2007). *Integrated ring resonators*: Springer.
36. "Symbolic math toolbox." Retrieved 01 Dec 2019, from <https://uk.mathworks.com/help/symbolic/solve-an-algebraic-equation.html>.
37. Zhang, Wang, Ju, Yuan, Zhang, & Qiang. (2010). Observation of the phase shift and group delay in nested optical fiber ring resonator. *PIERS Online*, *6*(6), 514-517.
38. Komma, Schwarz, Hofmann, Heinert, & Nawrodt. (2012). Thermo-optic coefficient of silicon at 1550 nm and cryogenic temperatures. *Applied Physics Letters*, *101*(4), 041905.
39. Miller, Okawachi, Ramelow, Luke, Dutt, Farsi, et al. (2015). Tunable frequency combs based on dual microring resonators. *Optics express*, *23*(16), 21527-21540.
40. Lee, Zhang, Barbosa, Miller, Mohanty, St-Gelais, et al. (2017). On-chip thermo-optic tuning of suspended microresonators. *25*(11), 12109-12120.
41. Chang, Li, Zhang, Qiu, Ye, & Su. (2008). A tunable broadband photonic rf phase shifter based on a silicon microring resonator. *IEEE photonics technology letters*, *21*(1), 60-62.

-
42. Khurgin, & Tucker. (2018). *Slow light: Science and applications*: CRC press.
 43. Shi, Boyd, Gauthier, & Dudley. (2007). Enhancing the spectral sensitivity of interferometers using slow-light media. *Optics letters*, 32(8), 915-917.
 44. Qin, Hu, Retterer, Kravchenko, & Weiss. (2016). Slow light mach–zehnder interferometer as label-free biosensor with scalable sensitivity. *Optics letters*, 41(4), 753-756.
 45. Xu, Schmidt, Pradhan, & Lipson. (2005). Micrometre-scale silicon electro-optic modulator. *Nature*, 435(7040), 325-327.
 46. Atabaki, Hosseini, Eftekhar, Yegnanarayanan, & Adibi. (2010). Optimization of metallic microheaters for high-speed reconfigurable silicon photonics. *Optics express*, 18(17), 18312-18323.

8 Conclusions and Future Work

8.1 Summary

Silicon photonics-based devices have tremendous potential in areas as diverse as healthcare, food safety, environment and security [1]. The Silicon-On-Insulator (SOI) platform can provide major advantages, especially regarding device portability, cost and accuracy. In the present work, we have been able to demonstrate novel structures based on the established SOI optical microring resonator (MRR), which can be utilised in different applications, including sensing [2] and telecommunications [3].

Firstly, we have designed and experimentally presented simple strip-based MRRs with different coupling conditions. The photonic components (e.g. grating couplers, and waveguides) were fabricated based on the simulation results. The q-factors of these MRRs reveal a competitive performance as compared to literature [4, 5]. By fixing all MRR's parameters and only increasing the coupling gaps gradually from 200nm to 300nm, over-coupled ($\alpha > t$), almost critically-coupled ($\alpha \approx t$) and under-coupled ($\alpha < t$) resonators were demonstrated. Each coupling condition is designated for different applications. The over-coupled resonators are suitable for application requiring implantation or surface modification whereas critically-coupled resonators are practical for application requiring high extinction ratio (ER). The under-coupled devices are usually realised for areas that demand anomalous dispersion [6].

Secondly, we have employed the aforementioned MRRs, as well as slotted MRR structures in an attempt to demonstrate detection of volatile organic compounds (VOCs) using an appropriate setup for gas/vapour delivery. We showed that integrating two-dimensional (2D) materials, namely graphene oxide (GO) on the sensor surface, GOMRR, can improve the spectral sensitivity by a factor of ~ 2 , which we attribute to the GO's ability to efficiently trap the VOC molecules within its interlayer structure [7]. This leads to a capillary condensation, which depends on the VOC's specific attributes, hinting at a potential route to selectivity in optical detection. The optical responses against different flow rates were analysed based on the *Hill-Langmuir* absorption isotherm [8]. The degree of cooperative molecular binding is determined by the *Hill* coefficient (n). Here the modelling reveals that this cooperativity is significantly

enhanced for GOMRR as compared to control slot-MRR and strip-MRR ($n_{\text{GOMRR}} > n_{\text{slot-MRR}} > n_{\text{strip-MRR}}$) for all VOCs with the exception of Hexane. In case of GOMRR, the oxygenated VOCs exhibited the highest *Hill* coefficient. Also, it was shown that cooperativity is enhanced for molecules with a polarity that is high relative to their size (kinetic diameter).

Thirdly, a novel device incorporating single or double DC coupled MRRs was presented. The supported multiple resonances inside the cavity combined with the sinusoidal behaviour of the DC can provide a unique and improved optical output. Using only one DC produces a substantial improvement in the device's FSR while employing two DCs, with one covered (unetched) and the other being exposed to the surrounded environment, demonstrated a Vernier effect. In the latter device, the analytical modelling using SMM approach, combined with FDTD revealed a significant enhancement of both FSR and device sensitivity, compared with conventional or slotted MRRs. In our study, we have shown that the device sensitivity and FSR can reach values large than 14,000nm/RIU and 232nm, respectively.

Finally, an electromagnetically induced transparency (EIT)-like effect and controllable group delay (τ_g) was achieved in a 3×3 coupler based dual (coupled) ring resonator (CRR). This EIT-like effect was observed in the output spectrum of the shared drop port of an identical MRRs where both rings are strongly coupled and acts as one whole system [9]. Using mathematical modelling combined with FDTD, it was shown that EIT can arise when: (i) a relative difference in cavity loss between the individual rings is introduced, (ii) the mode effective index (n_{eff}) is modified or (iii) the coupling or transmission coefficients are varied. By applying an electrical current on the integrated micro-heaters of only one of the MRRs, we were able to switch the EIT transparency on and off and demonstrate an anti-crossing behavior. The time required to switch on the device, using thermo-optic effect, is around 50μs. Also, The general nature of the anomalous dispersion in this CRR system can greatly influence the group index (n_g) near the resonance wavelengths. This leads to tuneable group delays where we demonstrated a τ_g ranging from -239.2ps to 16.2ps.

8.2 Future Work

The promising results and outcomes of this study have real potential in sensing and telecommunication applications and pave the way for numerous future works. Hundreds of optical SOI-based devices have been designed and fabricated during my PhD study, although here the focus has only been on a selection of them, with potential for the remaining for future research. The sensing aspects of the research can be extended further to investigate the detection of other, relevant molecules and the nonlinear behaviour of the devices can be investigated with specific applications in mind; notably four-wave-mixing (FWM), e.g. for frequency comb generation.

In this study, the integration of graphene oxide (GO) was performed on critically coupled resonators, where we noticed a slight decrease in ER and q-factor after GO deposition due to absorption loss, suggesting that the device has switched to under-coupled regime [10]. However, the integration of a lossy material on an over-coupled resonators can actually switch the device to critical coupling region (i.e. when cavity loss factor, $\alpha = \text{transmission coefficient, } t$), resulting in an increased in the ER.

Our study of GO integrated MRR sensors motivates further exploration of the capabilities of other 2D materials such as ZnO and MoS₂, where, for example, one might consider an array of optical sensors, coated with different functional materials, that is capable of distinguishing between a wide range of different target molecules.

The current optical gas sensing setup can be further improved by incorporating a temperature controller along with two electrical probes inside the gas cell which allow thermo-optic tuning via integrated on-chip micro-heaters during the gas measurements. This provides further controlled environment and precise results.

The thermo-optic setup can be upgraded to be compatible with techniques that offer high coupling efficiencies between the optical fibre and the sub-micron waveguides such as butt or end-fire coupling [11, 12] especially for devices with multiple coupling sections and relatively long dimensions such as the double DC coupled MRR (explained in chapter 6). These devices need to be fabricated with spot-size converter and cleaved facets to enable the edge coupling.

Further optimisation needs to be performed on the coupling gap, G , and style between the bus waveguide and MRR. In this thesis, all MRR designs were replicated three times with $G = 200\text{nm}$, 250nm and 300nm . However, for future work, the gap distance,

G, and style (e.g. single-point and pulley-type couplers) need to be carefully designed, by including the effect of waveguide's surface roughness, using FDTD simulations in order to produce devices with improved q-factors and ERs.

Along with the careful optimisation, high standard lithography process needs to be employed in order to improve our devices' performance especially when long waveguides are utilized.

In this thesis, only the near-IR spectral range was considered due to the restricted transparency range of conventional SOI platforms, as well as the limited bandwidth of the fabricated grating couplers. However, the study can be extended to the mid-infrared range. This wavelength range is interesting since oscillation frequencies of light waves in the mid-infrared region match the frequencies of characteristic vibrations of molecular bonds [13], which provides a method for unambiguous fingerprinting of particular gases/vapours. In order to realise this sensing range, the current equipment such as input laser source, optical spectrum analyser (OSA) and camera need to be changed. Also, mid-IR compatible materials, such as germanium and under-cut silicon can be employed as the photonic integrated circuit components, the fabrication of which is now readily accessible under the EPSRC CORNERSTONE 2 programme at the University of Southampton [14].

Alternative detection schemes such as on-chip Raman scattering [15] may also be employed with the current device designs, applied to materials capable of guiding higher energy (visible) light, e.g. silicon nitride, also accessible through various multi-project wafer fabrication facilities (Southampton and IMEC). On-chip (guided) Raman has a number of advantages in PIC-based sensing (e.g. scattering efficiency and specificity of molecular detection) and may be a natural extension of the work described here.

8.3 References

1. Shahine. (2021). *Optoelectronics: BoD–Books on Demand*.
2. Tsui, Alsalman, Mao, Alodhayb, Albrithen, Knights, et al. (2020). Graphene oxide integrated silicon photonics for detection of vapour phase volatile organic compounds. *Scientific reports*, 10(1), 1-11.
3. Naghizade, & Sattari-Esfahlan. (2020). Tunable high performance 16-channel demultiplexer on 2d photonic crystal ring resonator operating at telecom wavelengths. *Journal of Optical Communications*, 41(3), 249-256.
4. Xue, Jin, Tong, Cui, Yan, & Zhang. (2011). *Quality factor of silicon-on-insulator integrated optical ring resonator*. Paper presented at the Photonic Fiber and Crystal Devices: Advances in Materials and Innovations in Device Applications V.
5. TalebiFard, Schmidt, Shi, Wu, Jaeger, Kwok, et al. (2017). Optimized sensitivity of silicon-on-insulator (soi) strip waveguide resonator sensor. *Biomedical optics express*, 8(2), 500-511.
6. Totsuka, & Tomita. (2006). Slow and fast light in a microsphere-optical fiber system. *JOSA B*, 23(10), 2194-2199.
7. Joshi, Carbone, Wang, Kravets, Su, Grigorieva, et al. (2014). Precise and ultrafast molecular sieving through graphene oxide membranes. *science*, 343(6172), 752-754.
8. Gesztelyi, Zsuga, Kemeny-Beke, Varga, Juhasz, & Tosaki. (2012). The hill equation and the origin of quantitative pharmacology. *Archive for history of exact sciences*, 66(4), 427-438.
9. Miller, Okawachi, Ramelow, Luke, Dutt, Farsi, et al. (2015). Tunable frequency combs based on dual microring resonators. *Optics express*, 23(16), 21527-21540.
10. Choi, Lee, & Yariv. (2001). Control of critical coupling in a ring resonator–fiber configuration: Application to wavelength-selective switching, modulation, amplification, and oscillation. *Optics letters*, 26(16), 1236-1238.
11. Marchetti, Lacava, Carroll, Gradkowski, & Minzioni. (2019). Coupling strategies for silicon photonics integrated chips. *Photonics Research*, 7(2), 201-239.
12. Sun, Chen, Sun, Liu, & Cao. (2021). *Novel low-loss fiber-chip edge coupler for coupling standard single mode fibers to silicon photonic wire waveguides*. Paper presented at the Photonics.

-
13. Lin, Luo, Gu, Kimerling, Wada, Agarwal, et al. (2017). Mid-infrared integrated photonics on silicon: A perspective. *Nanophotonics*, 7(2), 393-420.
 14. "Epsrc." (2021). from <https://gow.epsrc.ukri.org/NGBOViewGrant.aspx?GrantRef=EP/T019697/1>.
 15. Coucheron, Wadduwage, Murugan, So, & Ahluwalia. (2019). Chip-based resonance raman spectroscopy using tantalum pentoxide waveguides. *IEEE photonics technology letters*, 31(14), 1127-1130.